Radium and Mercury Dynamics in the Arctic: Investigating Terrestrial Inputs, Groundwater Discharge, and Chemical Cycling in a Changing Climate

by

Emma Jacqueline Bullock

B.S. Chemistry, Haverford College, 2019

Submitted to the Earth, Atmospheric, and Planetary Sciences Department in partial fulfillment of the requirements for the degree of

Doctor of Philosophy

at the

MASSACHUSETTS INSTITUTE OF TECHNOLOGY

and the

WOODS HOLE OCEANOGRAPHIC INSTITUTION

February 2025

Signature of Author

Joint Program in Oceanography/Applied Ocean Science and Engineering
Massachusetts Institute of Technology
and Woods Hole Oceanographic Institution
October 11, 2024

Certified by

Dr. Matthew A. Charette
Thesis Supervisor
Woods Hole Oceanographic Institution

Accepted by

Dr. Colleen Hansel
Chair, Joint Committee for Chemical Oceanography
Massachusetts Institute of Technology/
Woods Hole Oceanographic Institution

Radium and Mercury Dynamics in the Arctic: Investigating Terrestrial Inputs, Groundwater Discharge, and Chemical Cycling in a Changing Climate

by

Emma Jacqueline Bullock

Abstract

The Arctic Ocean is distinctive due to its extreme seasonal variations in temperature and significant terrestrial inputs, including freshwater, carbon, nutrients, and toxins. Of particular concern is mercury (Hg) in its neurotoxic form, methylmercury (MeHg), which is already beginning to adversely affect Arctic human populations and wildlife. However, the region's harsh conditions and remoteness have made conducting seasonal chemical and hydrological studies challenging. Tracers of boundary inputs, such as the radium (Ra) isotope quartet, offer potential for tracking and quantifying riverine and submarine groundwater discharge (SGD) of species like Hg into the Arctic Ocean. This thesis employs seasonal data and laboratory experiments to investigate the factors influencing terrestrial Ra inputs to the Arctic Ocean, quantifies SGD and associated Hg inputs to an Arctic coastal lagoon, and elucidates the chemical and geological factors influencing Hg cycling in Arctic groundwater.

Using historical and unpublished datasets combined with new laboratory investigations, differences in inputs of riverine Ra isotopes between the North American and Eurasian land masses were identified. The findings revealed higher Ra fluxes from the North American continent, attributed to greater sediment loads and lower organic matter in rivers compared to those on the Eurasian land mass. Subsequently, Ra data from five extensive field campaigns to Simpson Lagoon, Alaska, provided insights into Ra cycling on a more localized scale. These campaigns offered the first seasonal perspective on supra-permafrost SGD along an Arctic coastline, suggesting that SGD fluxes may rival those of rivers along the Beaufort Sea coast. Concurrently collected Hg groundwater concentrations allowed for the development of the first estimates of Hg fluxes from groundwater to the Arctic Ocean. If these estimates hold true along the rest of the Pan-Arctic coastline, they could significantly alter our understanding of microbial MeHg uptake in the Arctic Ocean. Finally, sediment cores from Simpson Lagoon and two other locations along the Beaufort Sea coast were used to examine how changing groundwater conditions, such as changing salinity, temperature, and redox conditions, influence Hg cycling. These experiments, alongside findings from Simpson Lagoon groundwater, indicate that Hg cycling in recently thawed permafrost sediments involves a complex interplay between organic material, metal oxides, and sulfide species, with groundwater conditions and soil carbon content playing crucial roles in Hg mobilization.

Thesis supervisor: Dr. Matthew A. Charette

Title: Senior Scientist, Woods Hole Oceanographic Institution

Acknowledgements

I would like to thank the following for their tremendous support over the course of my graduate studies. Whether it was answering questions or keeping me sane, these people have been instrumental to my success writing this thesis.

First, my advisor, Matthew Charette, who guided me through my research and studies. His encouragement and flexibility in mentoring allowed me to branch into new areas of research that interested me. His patient editing of my papers has helped me become a more effective scientific writer and his guidance is directly responsible for my ability to publish articles during my studies. I am also grateful for the opportunities he provided to do field research which, despite my frequent complaints of being cold, were incredible experiences that I am honored to have taken part in.

Paul Henderson and Emilie le Roy also deserve recognition for taking a first year student who had never worked with radium and teaching her how everything worked. Paul was always willing to give me a hand or help me figure out a solution, both in the lab and in the field. He is the most efficient person I have ever met and I aspire to use my time as well as him. Emilie was a joy to be around in my first few years, particularly since the COVID pandemic made it hard to meet anyone outside of the lab.

My committee has been essential to the success of this thesis: Robert Mason, Phil Gschwend, and Julia Guimond. Rob was willing to step in and make my final two chapters that center around mercury possible, both with his expertise and by allowing me to use his lab to run samples. Phil was always genuinely interested in my research and his questions pushed me to challenge my assumptions and made my papers the best they could be. Julia has been both a scientific mentor and a professional one, helping me navigate the challenges of graduate school and the application process for afterwards. Because she went on many of our Arctic field campaigns, she has seen me at my most exhausted and deranged. Her enthusiasm for science and energy in the field was a key reason I was able to remember why we were out there.

I would also like to thank everyone else who went to the Arctic multiple times with me: Jim McClelland and Bayani Cardenas, who were amazing mentors, as well as fellow graduate students Cansu Demir, Emily Bristol, and Isabel Schaal. When you're working long days in hard conditions, it can either spur lifelong friendships or eternal resentment. I'm very happy to say that in our case, it's the former. I will always remember our drive from Fairbanks to Deadhorse in particular, especially gazing out at the magnificent Brooks Range together. Cansu and Emily, I consider both of you role-models. I hope one day we get to collaborate together on a project of our own. Isabel, you were also my lab mate and friend. Knowing you would be in the office made coming into work enjoyable and fun.

There are also numerous people who helped me get through this process from a non-scientific angle. I started my graduate experience in the depths of the COVID pandemic. I remember walking into Clark for the first time in September 2020: the lights were dim and all the calendars still said March. My chemistry cohort that year became my lifeline: Luciana Villarroel, Erica Herrera, Ellen Park, Solomon Chen, Sabrina Elkassas, and Annaliese Meyer. Luciana, you were the glue sticking us all together and making sure we socialized. Sabrina, you made the best meals and we had so much fun sitting around your dinner table for hours. Solomon, you're the most laid back graduate student I've ever met and you reminded me to that not everything

has to be work related. Ellen, I feel like every time we got to hang out, we ended up having a conversation that made me go away feeling better about life. Annaliese, I loved that we discovered our shared passion of writing and were able to share that with each other. Finally, Erica, your enduring ability to remain true to yourself is something I admire so much. You are both a friend and a role model and this past year would have been much harder without you in it.

My partner, Ben, has been my rock throughout this whole process. From before I started graduate school and said I was going to Germany for a year to get experience, he has been nothing but supportive and encouraging. He celebrates my successes and reminds me I can keep going when I fail. I am incredibly thankful for all of his support and humor. I know, without a doubt, that this next chapter in our lives will be amazing.

Finally, my parents, who knew I was going to be a scientist from the time I was five and my favorite t-shirt had a bacteriophage on it. I'd say that all of those science camps and trips to children's and natural history museums definitely paid off. I know how much you sacrificed to give me those opportunities and to make sure I had the best education possible. I want to thank you, both for setting me up to be academically successful, but also for giving me the confidence to go after my dreams. You're both amazing role models and I am lucky to have you as my parents.

Financial Support

The Arctic Rivers project was a broad, collaborative effort that would not have been possible without contributions from numerous funding sources, including the National Science Foundation (NSF-0751525, NSF-1736277, NSF-1458305, NSF-1938873, NSF-2048067, NSF-2134865), the NERC-BMBF project CACOON [NE/R012806/1] (UKRI NERC) and BMBF-03F0806A, and an EU Starting Grant (THAWSOME-676982). The Simpson Lagoon radium work was supported by the National Science Foundation's Office of Polar Programs through grants 1938873 (Charette), 1938820 (Cardenas and McClelland), and 1656026 (McClelland). The Simpson Lagoon mercury work was supported by the National Science Foundation's Office of Polar Programs through grants 2134865 (Bullock and Charette), 1938873 (Charette), 1938820 (Cardenas and McClelland), 1656026 (McClelland), and 1854454 (Mason). For all Simpson Lagoon research, Hillcorp Alaska provided access to field sites and Battelle Arctic Research Operations (via Polar Field Services) provided logistical support. We also thank the Beaufort Lagoon Ecosystems Long Term Ecological Research program, including the captain and crew of the *R/V Proteus*, for sharing lab and field resources.

Table of Contents

List of Figures

List of Tables

Chapter 1: Introduction

1.1 Terrestrial Inputs to a Changing Arctic Ocean

The Arctic Ocean is a unique, semi-contained basin, half of which is underlain by continental shelves (Jakobsson, 2002). It receives 10% of the global river discharge despite making up just 1% of the ocean's volume (McClelland et al. 2012). As a result, terrestrial inputs exert a significant biogeochemical influence on the upper water column of the Arctic Ocean (Klunder et al. 2012, Kipp et al. 2020). Rivers in the Arctic transport large quantities of organic matter (OM) (Wheeler et al. 1997), trace metals such as iron (Fe) and manganese (Mn) (Middag et al. 2011, Klunder et al. 2012, Charette et al. 2020), and sediment (Amon et al. 2012) to the Arctic Ocean. Submarine groundwater discharge (SGD) is also beginning to be recognized as a notable source of greenhouse gases (Lecher et al. 2015), nutrients, and dissolved organic matter (DOM) (Lecher et al. 2016; Connolly et al. 2020) to the Arctic Ocean as supra-permafrost SGD, which is limited to the near-shore coastal zone and flows through the seasonally thawed active layer. These substantial terrestrial inputs are just beginning to be fully quantified and understood in the context of their impacts on Arctic biogeochemistry.

Because the Arctic is warming four times faster than the rest of the globe (Rantanen et al. 2022) the hydrological cycle has been intensified, causing increases in precipitation and river discharge (Rawlins et al., 2010, Déry et al., 2016, Andreson et al., 2020, Wang et al., 2021), along with processes such as permafrost thaw (Biskaborn et al., 2019, IPCC, 2021) and coastal erosion (Günther et al., 2013; Irrgang et al., 2022). As a result, baseline estimates of water and material fluxes to the Arctic Ocean are needed in order to understand changing inputs in the future. Chemical tracers that are used to track and quantify terrestrial inputs, such as radium (Ra) isotopes, have shown promise as a method to trace riverine (Kipp et al. 2018, Kipp et al. 2020) and SGD inputs (Charkin et al. 2017) in the Arctic. These tracers can then be used to assess changing fluxes of materials that pose a risk to humans and wildlife, such as mercury, which has accumulated in frozen Arctic soils (Dastoor et al. 2022) and may be released as permafrost degradation intensifies (Nielsen et al. 2022).

1.2 Radium as a Tracer of Arctic Coastal Processes

There are four Ra isotopes commonly used to trace coastal processes (Moore 2008): ^{224}Ra ($t_{1/2}$ = 3.66 d), ^{223}Ra ($t_{1/2}$ = 11.4 d), ^{228}Ra ($t_{1/2}$ = 5.75 y), and ^{226}Ra ($t_{1/2}$ = 1600 y). Ra isotopes are sourced from crustal rocks and sediment as part of the U/Th decay series. When these sediments encounter solutions of high ionic strength, such as brackish or saline water, Ra partitions preferentially from the sediment particles into the dissolved phase. Of relevance to this thesis, this process occurs in the subterranean estuary–the coastal mixing zone where fresh groundwater mixes with recirculated saline water to form SGD (Garcia-Orellana et al. 2021)–as well as in river estuaries where suspended sediments encounter higher salinity waters (Li et al., 1977; Rutgers van der Loeff et al., 2003). As a result of these estuarine enrichment processes, Ra has often been used to estimate fluxes from SGD (Moore 1996, Moore 2008, Rapaglia et al. 2010, Zhang et al. 2017, Garcia-Orellana et al. 2021) and to trace riverine inputs as they move away from the coast (Moore et al., 1986; Moore & Krest, 2004).

The Arctic Ocean has notable salinity-driven stratification (Serreze et al. 2007), allowing river plumes to carry important nutrients and trace metals into the central Arctic basin (Klunder et al. 2012) and to supply up to 25% of the dissolved organic carbon (DOC) in this region

(Wheeler et al. 1997). Given the changing hydrological cycle in the Arctic, which may include increasing river discharge (Rawlins et al. 2010) and changing mixing regimes over continental shelves (Schulz et al. 2021), tracking these plumes using radium isotopes has provided important advances in our understanding of how Arctic Ocean circulation transports biogeochemically relevant species (Rutgers van der Loeff et al. 2003, Kipp et al. 2018, Rutgers van der Loeff et al. 2018, Charette et al. 2020, Kipp et al. 2020, Kipp et al. 2023). However, due to the difficulty of sampling in the Arctic, many questions remain regarding inputs of Ra from Arctic rivers, particularly when it comes to differences in Ra activities and behavior between the North American rivers and Eurasian rivers, which drain dramatically different landscapes (Amon et al. 2012, Holmes et al. 2012).

Ra isotopes are also a valuable tool for quantifying SGD, which is defined as the mix of fresh, brackish, and saline water discharging into coastal waters from margin sediments. Processes driving SGD can include terrestrial hydraulic gradients, water level fluctuations, wind speed and direction, wave set-up and tidal pumping, density driven convection, and more (Garcia-Orellana et al. 2021). In the Arctic, SGD is increasingly recognized as a potentially significant source of carbon (Connolly et al. 2020), nutrients (Lecher et al. 2017), and methane (Lecher et al. 2015) to the Arctic Ocean. Despite this, few studies have explored coastal groundwater dynamics in the Arctic (Deming et al. 1992, Dimova et al. 2015, Frederick and Buffet, 2015, Lecher et al. 2015, Connolly et al. 2020, Guimond et al. 2023) and even fewer have used Ra to track SGD in Arctic environments (Lecher et al. 2016, Charkin et al. 2017). Notably, none of these studies addresses the seasonality on Ra cycling in the Arctic or how SGD fluxes vary over the course of the ice-free season. Addressing these gaps is crucial for effectively using Ra isotopes to monitor SGD in a warming Arctic.

1.3 Mercury in the Arctic

Mercury (Hg) exposure can cause neurotoxicity in humans and wildlife, with pregnant women and children being particularly vulnerable due to the developmental impacts of Hg (US EPA, 1997). Atmospheric circulation patterns cause much of the Hg emitted in the northern hemisphere to be transported to the Arctic, where it is often deposited in tundra soils or transported to the Arctic Ocean via terrestrial runoff (Halbach et al. 2017, Obrist et al. 2017). In its methylated form (CH_3Hg^+), Hg can be taken up into food chains, resulting in high and increasing Hg concentrations in the blood and tissues of animals in the Arctic and the human communities who depend on these creatures to survive (Dietz et al. 2013). The practice of subsistence hunting by communities in the Arctic is not only of cultural importance, but is vital to the survival of indigenous populations living along the Arctic coastline (Dietz et al. 2013, UN-Environment, 2019). Indigenous knowledge holders across the Arctic have reported animals appearing distressed or exhibiting unusual behavior (UN-Environment, 2019). These are often physical manifestations of Hg neurotoxicity, as verified by researchers (Dietz et al. 2013, AMAP, 2021). Without alternative food sources, indigenous communities who rely on fish and marine mammals are also showing elevated levels of Hg in their blood, often exceeding the 5.8 µg Hg/L safety limit (Sundseth et al. 2015).

Although atmospheric emissions of Hg have decreased in recent decades, the accumulation of Hg in Arctic soils makes them a potentially large source of new Hg to Arctic ecosystems (Soerensen et al. 2016; Obrist et al. 2017; Sonke et al. 2018; UN-Environment, 2019). Notably, the transport of Hg through Arctic soils and groundwater has been largely ignored, despite its potential to impact multiple inputs to the Arctic Ocean: riverine concentrations (Sonke et al. 2018; Mu et al. 2019; Zolkos et al. 2020), direct inputs from groundwater discharge (Outridge et al. 2008), and remobilization of Hg in sediments (Soerensen et al. 2016). Part of the reason for this is that groundwater discharge pathways and seasonality in the Arctic are globally unique, largely due to the presence of permafrost, which limits flow through seasonally thawed, shallow active layers (Neilson et al. 2018; Connolly et al. 2020). The seasonally dynamic structure of Arctic aquifers, combined with soil stratification ranging from high organic matter (OM) peat overlaying mineral-rich soils (Obrist et al. 2017; Connolly et al. 2020), will undoubtedly impact the retention, speciation, and discharge of Hg into coastal regions. Understanding how the uncommon conditions within Arctic coastal aquifers impact Hg mobilization is essential for future risk and mitigation assessments.

1.4 Introduction to the Thesis

This thesis investigates the hydrological and chemical processes influencing Ra and Hg cycling in the Arctic coastal region, beginning with Ra. In the second chapter, riverine inputs of long-lived Ra isotopes to the Arctic Ocean are explored using a combination of historical datasets and laboratory desorption experiments, providing the first pan-Arctic estimates of ^{226}Ra from rivers and refining estimates for ^{228}Ra. Key differences in Ra behavior were found between the major North American Mackenzie and Yukon rivers, compared to the major Eurasian Ob and Lena rivers, which is important to take into account when using Ra to trace riverine inputs in the Arctic Ocean.

In the third chapter, Ra isotopes are used to investigate SGD inputs to an Arctic coastal lagoon. Data from five sampling campaigns in Simpson Lagoon, Alaska–conducted in August 2021, June, July, and October 2022, and July 2023–were analyzed to elucidate the factors influencing SGD and Ra cycling throughout the open water season. This study represents the first seasonal investigation of SGD in the Arctic to utilize Ra isotopes, exploring the processes that impact Ra cycling in Arctic tundra environments. The short-lived isotopes, ^{223}Ra and ^{224}Ra, were the only ones with a large enough signal to trace SGD in Simpson Lagoon, highlighting the predominance of short-term processes, such as wave pumping, on SGD. Comparing the seasonal Ra isotope data with concurrent physical measurements underscored the importance of wind-driven water levels on SGD at this site. The chapter emphasizes the need for seasonal and interannual studies to fully understand the driving forces behind SGD in new study locations.

The fourth chapter uses the SGD results found in chapter 3 and Hg measurements taken during concurrent sampling campaigns to estimate total Hg (THg) and methyl-Hg (MeHg) inputs to Simpson Lagoon and the Arctic Ocean from supra-permafrost groundwater. This is the first estimate of coastal groundwater inputs of Hg to the Arctic Ocean, despite Arctic soils being the largest sink of Hg in the polar region (Dastoor et al. 2022). The combination of high THg and MeHg concentrations in Arctic groundwater, as well as substantial SGD rates occurring in the summer and early autumn, result in estimated pan-Arctic annual inputs of MeHg from SGD that rival inputs from Arctic rivers. This finding draws attention to this understudied process and highlights the need for more measurements of SGD and Hg along Arctic coastlines.

The fifth chapter builds on the fourth by investigating the chemical processes within the subterranean estuary that influence Hg cycling in Arctic active layer soils and permafrost. This is accomplished through statistical analyses that compare THg and MeHg concentrations from three Simpson Lagoon groundwater transects and soil plug flow-through experiments with various parameters known to affect Hg cycling in soils. The cores used in the plug flow-through experiments come from Simpson Lagoon's peat-dominated active layer soils and permafrost, Elson Lagoon's lacustrine mineral permafrost, and Drew Point's lacustrine mineral permafrost. Additionally, operationally-defined leaches were employed to identify the types of associations Hg forms with Simpson Lagoon soil matrices. Together, these field measurements and laboratory experiments provide a robust foundation for understanding how different types of Arctic permafrost will release Hg and MeHg upon thawing. Finally, Chapter 6 presents a summary of the results from the four studies presented in this thesis, as well as suggested future directions.

References

AMAP, 2021. AMAP Assessment 2021: Mercury in the Arctic. Arctic Monitoring and Assessment Programme (AMAP), Tromsø, Norway. pg: viii - 324.

Amon, R. M. W., Rinehart, A. J., Duan, S., Louchouarn, P., Prokushkin, A., Guggenberger, G. et al. (2012). Dissolved organic matter sources in large Arctic rivers. *Geochimica et Cosmochimica Acta, 94,* 217-237. https://doi.org/10.1016/j.gca.2012.07.015

Andresen, C. G., Lawrence, D. M., Wilson, C. J., McGuire, A. D., Koven, C., Schaefer, K. et al. (2020). Soil moisture and hydrology projections of the permafrost region - a model intercomparison. *The Cryosphere, 14,* 445-459. https://doi.org/10.5194/tc-14-445-2020

Biskaborn, B. K., Smith, S. L., Noetzli, J., Matthes, H., Vieira, G., Streletskiy, D. A. et al. (2019). Permafrost is warming at a global scale. *Nature Communications, 10,* 264. https://doi.org/10.1038/s41467-018-08240-4

Charette, M. A., Kipp, L. E., Jensen, L. T., Dabrowski, J. S., Whitmore, L. M., Fitzsimmons, J. N., et al. (2020). The Transpolar Drift as a Source of Riverine and Shelf-Derived Trace Elements to the Central Arctic Ocean. *Journal of Geophysical Research: Oceans, 125* (5), e2019JC015920. https://doi.org/10.1029/2019JC015920

Charkin, A. N., van der Loeff, M. R., Shakhova, N. E., Gustafsson, Ö., Dudarev, O. V., Cherepnev, M. S. et al. (2017). Discover and characterization of submarine groundwater discharge in the Siberian Arctic seas: a case study in the Buor-Khaya Gulf, Laptev Sea. *The Cryosphere, 11,* 2305-2327. https://doi.org/10.5194/tc-11-2305-2017

Connolly, C. T., M. B. Cardenas, G. A. Burkart, R. G. M. Spencer, and J. W. McClelland. (2020). Groundwater as a major source of dissolved organic matter to Arctic coastal waters. Nature Communications, 11, 1479. https://doi.org/10.1038/s41467-020-15250-8

Dastoor, A., Angot, H., Bieser, J., Christensen, J. H., Douglas, T. A., Heimbürger-Boavida, L-E., et al. (2022). Arctic mercury cycling. *Nature Reviews Earth & Environment, 3,* 270-286. https://doi.org/10.1038/s43017-022-00269-w

Deming, D., J. H. Sass, A. H. Lachenbruch, and R. F. De Rito (1992). Heat flow and subsurface temperature as evidence for basin - scale ground - water flow, North Slope of Alaska. *Geological Society of America Bulletin, 104*, 528 - 542.

Déry, S. J., Stadnyk, T. A., MacDonald, M. K., Gauli-Sharma, B. (2016). Recent trends and variability in river discharge across northern Canada. *Hydrological Earth Systems, 20,* 4801-4818. https://doi.org/10.5194/hess-20-4801-2016

Dietz, R., Sonne, C., Basu, N., Braune, B., O'Hara, T., Letcher, R. J. et al. (2013). What are the toxicological effects of mercury in Arctic biota? *Science of the Total Environment*, *443*, 775 - 790. https://doi.org/10.1016/j.scitotenv.2012.11.046

Dimova, N. T., Paytan, A., Kessler, J. D., Sparrow, K. J., Kodovska, F. G.-T., Lecher, A. L., Murray, J., Tulaczyk, S. M. (2015). Current magnitude and mechanisms of groundwater discharge in the Arctic: Case Study from Alaska. *Environmental Science & Technology, 49,* 12036 -12043. www.doi.org/10.1021/acs.est.5b02215

Frederick, J. M., Buffet, B. A. (2015). Effects of submarine groundwater discharge on the present day extent of relict submarine permafrost and gas hydrate stability on the Beaufort Sea continental shelf. *Journal of Geophysical Research Earth Surface, 120,* 417-432. www.doi.org/10.1002/2014JF003349

Garcia-Orellana, J., Rodellas, V., Tamborski, J., Diego-Feliu, M., van Beek, P., Weinstein, Y., Charette, M., Alorda-Kleinglass, A., Michael, H. A., Stieglitz, T., Scholten, J. (2021). Radium isotopes as submarine groundwater discharge (SGD) tracers: Review and recommendations. *Earth Science Reviews, 220,* 103681. www.doi.org/10.1016/j.earscirev.2021.103681

Guimond, J.A., Demir, C., Kurylyk, B. L., Walvoord, M. A., McClelland, J. W., Cardenas, M. B. (2023). Wind - modulated groundwater discharge along a microtidal Arctic coastline. *Environmental Research Letters, 18*(9), 094042. https://doi.org/10.1088/1748-9326/acf0d8

Günther, F., Overduin, P. P., Sandakov, A. V., Grosse, G., Grigoriev, M. N. (2013). Short- and long-term thermo-erosion of ice-rich permafrost coasts in the Laptev Sea region. *Biogeosciences, 10,* 4297-4318. https://doi.org/10.5194/bg-10-4297-2013

Halbach, K., Mikkelsen, Ø., Berg, T., Steinnes, E. (2017). The presence of mercury and other trace metals in surface soils in the Norwegian Arctic. *Chemosphere, 188,* 567-574. https://doi.org/10.1016/j.chemosphere.2017.09.012

Holmes, R. M., McClelland, J. W., Peterson, B. J., Tank, S. E., Bulygina, E., Eglinton, T. I., et al. (2012). Seasonal and Annual Fluxes of Nutrients and Organic Matter from Large Rivers to the Arctic Ocean and Surrounding Seas. *Estuaries and Coasts, 35,* 369-382. https://doi.org/10.1007/s12237-011-9386-6

IPCC. (2019). IPCC Special Report on the Ocean and Cryosphere in a Changing Climate [H.-O. Pörtner, D.C. Roberts, V. Masson-Delmotte, P. Zhai, M. Tignor, E. Poloczanska, K. Mintenbeck, A. Alegría, M. Nicolai, A. Okem, J. Petzold, B. Rama, N.M. Weyer (eds.)]. In press.

Irrgang, A. M., Bendixen, M., Farquharson, L. M., Baranskaya, A. V., Erikson, L. A., Gibbs, A. E., et al. (2022). Drivers, dynamics, and impacts of changing Arctic coasts, *Nature reviews Earth & Environment, 3,* 39-54. https://doi.org/10.1038/s43017-021-00232-1

Jakobsson, M. (2002). Hypsometry and volume of the Arctic Ocean and its constituent seas. *Geochemistry, Geophysics, Geosystems, 3*(5), 1-18. https://doi.org/10.1029/2001GC000302

Kipp, L. E., Charette, M. A., Moore, W. S., Henderson, P. B., Rigor, I. G. (2018). Increased fluxes of shelf-derived materials to the central Arctic Ocean. *Science Advances, 4*. https://doi.org/10.1126/sciadv.aao1302

Kipp, L. E., Henderson, P. B., Wang, Z. A., Charette, M. A. (2020). Deltaic and Estuarine Controls on Mackenzie River Solute Fluxes to the Arctic Ocean. *Estuaries and Coasts, 43,* 1992-2014. https://doi.org/10.1007/s12237-020-00739-8

Kipp, L., Charette, M., Robbins, A., Pnyushkov, A., Polyakov, I., Whitmore, L. (2023). Radium Isotopes as Tracers of Shelf-Basin Exchange Processes in the Eastern Arctic Ocean. *Journal of Geophysical Research: Oceans, 128* (12), e2023JC020303. https://doi.org/10.1029/2023JC020303

Klunder, M. B., Bauch, D., Laan, P., de Baar, H. J. W., van Heuven, S., Ober, S. (2012). Dissolved iron in the Arctic shelf seas and surface waters of the central Arctic Ocean: Impact of Arctic river water and ice-melt. *Journal of Geophysical Research: Oceans, 117* (C1). https://doi.org/10.1029/2011JC007133

Lecher, A. L. (2017). Groundwater Discharge in the Arctic: A Review of Studies and Implications for Biogeochemistry. *Hydrology, 4* (3), 41. www.doi.org/10.3390/hydrology4030041

Lecher, A. L., Chien, C.-T., Paytan, A. (2016). Submarine groundwater discharge as a source of nutrients to the North Pacific and Arctic coastal ocean. *Marine Chemistry, 186,* 167-177. www.doi.org/10.1016/j.marchem.2016.09.008

Lecher, A. L., Kessler, J., Sparrow, K., Kodovska, G.-T., Dimova, N., Murray, J., Tulaczyk, S., Paytan, A. (2015). Methane transport through submarine groundwater discharge to the North Pacific and Arctic Ocean at two Alaskan sites. *Limnology and Oceanography, 61,* S344-S355. www.doi.org/10.1002/lno.10118

Li, Y-H., Mathieu, G., Biscaye, P., Simpson, H. J. (1977). The Flux of ^{226}Ra from Estuarine and Continental Shelf Sediments. *Earth and Planetary Sciences, 37,* 237-241.

McClelland, J. W., Holmes, R. M., Dunton, K. H., Macdonald, R. W. (2012). The Arctic Ocean Estuary. *Estuaries and Coasts, 35,* 353-368. https://doi.org/10.1007/s12237-010-9357-3

Middag, R., de Baar, H. J. W., Laan, P., Klunder, M. B. (2011). Fluvial and hydrothermal input of manganese into the Arctic Ocean. *Geochimica et Cosmochimica Acta, 75* (9), 2393-2408. https://doi.org/10.1016/j.gca.2011.02.011

Moore, W. S. (1996). Large groundwater inputs to coastal waters revealed by 226Ra enrichments. *Nature, 380*, 612 - 614. www.doi.org/10.1038/380612a0

Moore, W. S. (2008). Fifteen years experience in measuring 224Ra and 223Ra by delayed - coincidence counting. *Marine Chemistry, 109*, 188 -197.

Moore, W. S., Krest, J. (2004). Distribution of 223Ra and 224Ra in the plumes of the Mississippi and Atchafalaya Rivers and the Gulf of Mexico. *Marine Chemistry, 86*, 105-119.

Moore, W. S., Scott, M. R. (1986). Behavior of ^{226}Ra in the Mississippi River mixing zone. *Journal of Geophysical Research: Oceans, 91* (C12), 14317-14329. https://doi.org/10.1029/JC091iC12p14317

Mu, C., Zhang, F., Chen, X., Ge, S., Mu, M., Jia, L., Wu, Q., Zhang, T. (2019). Carbon and mercury export from the Arctic rivers and response to permafrost degradation. *Water Research, 161,* 54-60. https://doi.org/10.1016/j.watres.2019.05.082

Neilson, B. T., Cardenas, M. B., O'Connor, M. T., Rasmussen, M. T., King, T. V., Kling, G. W. (2018). Groundwater Flow and Exchange Across the Land Surface Explain Carbon Export

Patterns in Continuous Permafrost Watersheds. *Geophysical Research Letters, 45* (15), 7596-7605. https://doi.org/10.1029/2018GL078140

Obrist, D., Agnan, Y., Jiskra, M., Olson, C. L., Colegrove, D. P., Hueber, J., Moore, C. W., Sonke, J. E., Helmig, D. (2017) Tundra uptake of atmospheric elemental mercury drives Arctic mercury pollution. *Nature, 547*, 201–204. https://doi.org/10.1038/nature22997

Outridge, P. M., Macdonald, R. W., Wang, F., Stern, G. A., Dastoor, A. P. (2008). A mass balance inventory of mercury in the Arctic Ocean. *Environmental Chemistry, 5* (2), 89-111. https://doi.org/10.1071/EN08002

Rantanen, M., Karpechko, A. Y., Lipponen, A., Nordling, K., Hyvärinen, O., Ruoseenoja, K., Vihma, T., Laaksonen, A. (2022). The Arctic has warmed nearly four times faster than the globe since 1979. *Earth and Environment Communications, 3,* 168. www.doi.org/10.1038/s43247-022-00498-3

Rapaglia, J., Ferrarin, C., Zaggia, L., Moore, W. S., Umgiesser, G., Garcia-Solsona, E., Garcia-Orellana, J., Masqué, P. (2010). Investigation of residence time and groundwater flux in Venice Lagoon: comparing radium isotope and hydrodynamical models. *Journal of Environmental Radioactivity, 101* (7), 571-581. https://doi.org/10.1016/j.jenvrad.2009.08.010

Rawlins, M. A., Steele, M., Holland, M. M., Adam, J. C., Cherry, J. E., Francis, J. A., et al. (2010). Analysis of the Arctic system for freshwater cycle intensification: Observations and expectations. *Journal of Climate, 23*(21), 5715–5737. https://doi.org/10.1175/2010JCLI3421.1

Rutgers van der Loeff, M., Kühne, S., Wahsner, M., Höltzer, H., Frank, M., Ekwurzel, B., et al. (2003). ^{228}Ra and ^{226}Ra in the Kara and Laptev seas. *Continental Shelf Research, 23*(1), 113–124. https://doi.org/10.1016/S0278-4343(02)00169-3

Rutgers van der Loeff, M., Kipp, L. E., Charette, M. A., Moore, W. S., Black, E., Ingrid, S., et al. (2018). Radium isotopes across the Arctic Ocean show time scales of water mass ventilation and increasing shelf inputs. *Journal of Geophysical Research: Oceans, 123*(7), 4853–4873. https://doi.org/10.1029/2018JC013888

Schultz, C., Doney, S. C., Hauck, J., Kavanaugh, T., Schofield, O. (2021). Modeling Phytoplankton Blooms and Inorganic Carbon Responses to Sea-Ice Variability in the West Antarctic Peninsula. *Journal of Geophysical Research: Biogeosciences, 126* (4), e2020JG006227. https://doi.org/10.1029/2020JG006227

Serreze, M. C., Barret, A. P., Slater, A. G., Woodgate, R. A., Aagaard, K., Lammers, R. B., et al. (2007). The large-scale freshwater cycle of the Arctic. *Journal of Geophysical Research, 111*(C11), C11010. https://doi.org/10.1029/2005JC003424

Soerensen, A. L., Jacob, D. J., Schartup, A. T., Fisher, J. A., Lehnherr, I., St. Louis, V. L., Heimbürger, L-E., Sonke, J. E., Krabbenhoft, D. P., Sunderland, E. M. (2016). A mass budget for mercury and methylmercury in the Arctic Ocean. *Global Biogeochemical Cycles*, *30* (4), 560-575.

Sonke, J. E., Teisserenc, R., Heimbürger-Boavida, L., Petrova, M. V., Marusczak, N., Le Dantec, T., Chupakov, A. V., Li, C., Thackray, C. P., Sunderland, E. M., Tananaev, N., Pokrovsky, O. S. (2018). Eurasian river spring flood observations support net Arctic Ocean mercury export to the atmosphere and Atlantic Ocean. *PNAS*, *115*(50), E11586-E11594. https://doi.org/10.1073/pnas.1811957115

Sundseth, K., Pacyna, J. M., Banel, A., Pacyna, E. G., Rautio, A. (2015). Climate Change Impacts on Environmental and Human Exposure to Mercury in the Arctic. *International Journal of Environmental Research and Public Health, 12* (4), 3579-3599. https://doi.org/10.3390/ijerph120403579

UN-Environment. Global Mercury Assessment 2018. UN-Environment Programme, Chemicals and Health Branch, Geneva, Switzerland, 2019.

US EPA. (1997). Inventory of anthropogenic mercury emissions in the United States. In The Mercury Study Report to Congress, vol. 2. US Environmental Protection Agency, EPA-452/R-96-001a.

Wang, P., Huang, Q., Pozdniakov, S. P., Liu, S., Ma, N., Wang, T., et al. (2021). Potential role of permafrost thaw on increasing Siberian river discharge. *Environmental Research Letters, 16*(3), 034046. https://doi.org/10.1088/1748-9326/abe326

Wheeler, P. A., Watkins, J. M., & Hansing, R. L. (1997). Nutrients, organic carbon and organic nitrogen in the upper water column of the Arctic Ocean: Implications for the sources of dissolved organic carbon. *Deep Sea Research Part II: Topical Studies in Oceanography, 44*(8), 1571–1592. https://doi.org/10.1016/s0967-0645(97)00051-9

Zhang, Y., Li, H., Xiao, K., Wang, X., Lu, X., Zhang, M., et al. (2017). Improving Estimation of Submarine Groundwater Discharge Using Radium and Radon Tracers: Application in Jiaozhou Bay, China. *Journal of Geophysical Research: Oceans, 122* (10), 8263-8277. https://doi.org/10.1002/2017JC013237

Zolkos, S., Krabbenhoft, D. P., Suslova, A., Tank, S. E., McClelland, J. W., Spencer, R. G. M., et al. (2020). Mercury Export from Arctic Great Rivers. *Environmental Science & Technology, 54* (7), 4140-4148. https://doi.org/10.1021/acs.est.9b07145

Chapter 2: Radium inputs into the Arctic Ocean from rivers: a basin-wide estimate

Emma J. Bullock[1], Lauren Kipp[2], Willard Moore[3], Kristina Brown[4], Paul J. Mann[5], Jorien E. Vonk[6], Nikita Zimov[7], and Matthew A. Charette[8]

[1]MIT-WHOI Joint Program in Oceanography/Applied Ocean Science & Engineering, Cambridge and Woods Hole, MA; [2]Department for Environmental Sciences, Rowan University, Glassboro, NJ; [3]Earth, Ocean, and Environment College of Arts and Sciences, University of South Carolina, SC; [4]Department of Fisheries and Oceans, Institute of Ocean Sciences, Sidney, BC, Canada; [5]Department of Geography and Environmental Sciences, Northumbria University, Newcastle upon Tyne, United Kingdom; [6]Faculty of Science, Earth, and Climate, Vrije Universiteit Amsterdam, Amsterdam, Netherlands; [7]North-East Scientific Station, Pacific Institute for Geography, Far-East Branch, Russian Academy of Sciences, Cherskiy, Russia; [8]Department of Marine Chemistry and Geochemistry, Woods Hole Oceanographic Institution, Woods Hole, MA

Originally published in 2022 in Journal of Geophysical Research: Oceans. Reproduced here with permission.

Bullock, E. J., Kipp, L., Moore, W., Brown, K., Mann, P. J., Vonk, J. E., Zimov, N., Charette, M. A. (2022). Radium Inputs into the Arctic Ocean from Rivers: A Basin-Wide Estimate. *Journal of Geophysical Research: Oceans, 127* (9), e2022JC018964.
https://doi.org/10.1029/2022JC018964

Abstract

Radium isotopes have been used to trace nutrient, carbon, and trace metal fluxes inputs from ocean margins. However, these approaches require a full accounting of radium sources to the coastal ocean including rivers. Here, we aim to quantify river radium inputs into the Arctic Ocean for the first time for ^{226}Ra and to refine the estimates for ^{228}Ra. Using new and existing data, we find that the estimated combined (dissolved plus desorbed) annual ^{226}Ra and ^{228}Ra fluxes to the Arctic Ocean are [7.0 – 9.4] x 10^{14} dpm y^{-1} and [15-18] x 10^{14} dpm y^{-1}, respectively. Of these totals, 44% and 60% of the river ^{226}Ra and ^{228}Ra, respectively are from suspended sediment desorption, which were estimated from laboratory incubation experiments. Using Ra isotope data from 20 major rivers around the world, we derived global annual ^{226}Ra and ^{228}Ra fluxes of [7.4 – 17] x 10^{15} and [15 – 27] x 10^{15} dpm y^{-1}, respectively. As climate change spurs rapid Arctic warming, hydrological cycles are intensifying and coastal ice cover and permafrost are diminishing. These river radium inputs to the Arctic Ocean will serve as a valuable baseline as we attempt to understand the changes that warming temperatures are having on fluxes of biogeochemically important elements to the Arctic coastal zone.

1. Introduction

Radium (Ra) isotopes have been used for decades to track sediment-water interactions, and provide a method to differentiate nutrient and trace metal inputs from shelves, rivers, and groundwater (eg. Moore & Krest, 2004; Peterson et al. 2013; Tomasky-Holmes et al. 2013). While they themselves are soluble in seawater, ^{226}Ra and ^{228}Ra are supplied by the radioactive decay of their sediment-bound parent isotopes, ^{230}Th and ^{232}Th respectively (Moore & Edmund, 1984). With half lives of 5.8 years for ^{228}Ra and 1600 years for ^{226}Ra, the distribution of these isotopes in the marine environment is controlled by different factors (Elsinger & Moore, 1980; Webster et al., 1995; Rutgers van der Loeff et al. 2003). The half life of ^{226}Ra is on the same order of magnitude as the global ocean overturning circulation, causing the distribution of ^{226}Ra in the ocean to be primarily controlled by slow removal from the surface ocean and release from marine sediments (Webster et al., 1995; Rutgers van der Loeff et al. 2003). With a considerably shorter half-life, the distribution of ^{228}Ra in the ocean is more restricted, the result being that ^{228}Ra has much higher relative activities close to the source of its release, such as over continental shelves, river mouths, or near submarine groundwater discharge (Moore et al., 1986; Moore & Shaw, 2008). As such, ^{228}Ra can be used to pinpoint solute sources from estuarine, fluvial, and shelf inputs to the open ocean (Moore et al. 1986; Moore & Todd, 1993; Rutgers van der Loeff et al. 1995; Moore & Krest, 2004).

Recent studies have found that the largest source of ^{228}Ra to the Arctic Ocean comes from continental shelves and that shelf inputs have increased substantially over the past decade (Kipp et al. 2018, 2019, 2020; Rutgers van der Loeff et al. 2018). However, rivers are also an important Ra source and it is currently unknown whether they are similarly sensitive to changing fluxes. Physical and biogeochemical processes in the Arctic Ocean are uniquely dependent on riverine inputs, due to the fact that despite having just 1% of the ocean's volume, the Arctic Ocean receives 10% of global river discharge (McClelland et al. 2012). Such a large influx of freshwater helps create a highly stratified surface layer in the Arctic Ocean, limiting upwelling and increasing the biogeochemical influence of riverine inputs on the upper water column (Klunder et al. 2012; Kipp et al. 2020). Along with Ra, rivers in the Arctic are known to contain high organic matter (OM) concentrations, accounting for 25% of the dissolved organic carbon supply to the central Arctic Ocean (Wheeler et al. 1997). They have also been shown to be a major source of trace metals to the Arctic Ocean, such as iron (Fe) and manganese (Mn) (Middag et al. 2011; Klunder et al. 2012; Charette et al. 2020).

Despite the potential for Ra to differentiate inputs from shelves, rivers, and groundwater, few studies have specifically investigated fluvial radium inputs to the Arctic Ocean. Radium can be both dissolved in rivers and released from suspended sediments in the estuarine mixing zone (Li et al. 1977; Rutgers van der Loeff et al. 2003). This desorption of Ra occurs along the salinity gradient as the fresh river water mixes with the ocean endmember, peaking at low to intermediate salinities (Li & Chan, 1979; Elsinger & Moore, 1980; Webster et al., 1995; Moore & Shaw, 2008). Rutgers van der Loeff et al. (2003) was one of the first studies to report dissolved radium measurements in major Arctic rivers (the Ob, Lena, and Yenisey rivers). Kipp et al. (2020) added North American river radium measurements (the Mackenzie and Yukon rivers). In another study, the authors used the weighted average of dissolved radium from three of these major rivers (Ob, Lena, and Mackenzie), as well as the experimentally determined Mackenzie River desorption values with the recorded sediment load to make a scaled-up estimation of total ^{228}Ra added to the Arctic Ocean due to fluvial inputs (Kipp et al. 2018). However, it's known that sediment loads and other indicators like dissolved and particulate organic carbon are considerably different in North American rivers as opposed to Eurasian rivers, largely due to their distinct drainage basin characteristics (Holmes et al. 2002, 2012; Amon et al. 2012). These differences could impact the desorption of Ra from suspended sediments and have not been investigated for Eurasian rivers.

Using a combination of new and historical data, this paper aims to refine ^{228}Ra riverine fluxes and present the first ^{226}Ra riverine flux estimate to the Arctic Ocean. These estimates will aid in the use of Ra isotopes as tracers of sediment-derived material fluxes into this high latitude basin. This paper also helps establish baseline values for riverine Ra fluxes in the Arctic. As the Arctic warms in response to climate change, freshwater fluxes from rivers have been increasing (Holmes et al. 2002; Rawlins et al. 2010; Haine et al. 2015; Déry et al. 2016), and are projected to increase over the next few decades (Andreson et al. 2020; Wang et al. 2021). Greater understanding of Ra transport is further necessary for understanding processes impacting Ra transport - such as increased permafrost thaw (Biskaborn et al., 2019; IPCC, 2021) and increased coastal erosion (Günther et al. 2013, Irrgang et al., 2022) - have also been documented. Finally, using data from major global rivers, we present a new global river Ra flux estimate which allows us to put our Arctic results into a broader context.

2. Materials and Methods

2.1 Dissolved Riverine Ra Concentrations

Radium samples were collected in the Ellice River in August and September 2017, the Kolyma River in June and September 2019, and the Buskin, Sustina, Matanuska, and Knik Rivers (hereafter referred to as Southern Alaska Rivers) in September 2019 (Figure 1). The Ellice River is located in Nunavut, Canada, on the mainland side of the Canadian Arctic Archipelago. The Kolyma River is a major river in Siberia, draining into the East Siberian Sea and represents the largest Arctic river basin underlain by continuous permafrost. The Buskin River is located on Kodiak Island, AK, while the Sustina, Matanuska, and Knik Rivers drain into Cook Inlet near Anchorage, AK. The samples were collected using either a bilge or well pump and the river water was passed through a 1 or 5 µm prefilter to remove suspended sediment before being filtered at <1 L/min onto Mn-coated acrylic fiber. The fiber was rinsed with Ra-free MilliQ water to remove any salts or sediment, then partially dried.

Samples with low activities (<0.4 dpm) were analyzed for ^{228}Ra via ^{228}Th ingrowth using a delayed coincidence counter (RaDeCC) (Moore, 2008), as described in Charette et al. (2015). Briefly, when ^{228}Ra is extracted onto the Mn fiber, ^{228}Th is extracted in parallel. Using the initial concentration of ^{228}Th and the concentration of ^{228}Th after 1 - 2 years, measured via RaDeCC, along with the decay constants of ^{228}Th and ^{228}Ra, the initial concentration of ^{228}Ra can be calculated. Low activity samples were analyzed for ^{226}Ra via ^{222}Rn emanation (Key et al. 1979), as described in Charette et al. (2015). Fibers were placed in a fiber holder that was then flushed with He for 5 minutes at 250 mL/min, sealed, and left for two weeks before analysis via ^{222}Rn ingrowth and scintillation counting. These two methods were used for low activity samples due to better method sensitivity than gamma counting (Charette et al., 2001), which was used for samples with high activities (>0.4 dpm per sample). For this method, the fibers were ashed (880 °C, 16 h), homogenized, capped with epoxy resin, and left for >3 weeks to obtain secular equilibrium between ^{226}Ra and its daughter radionuclides. The samples were then counted in a well-type gamma spectrometer for ^{228}Ra (via ^{228}Ac at 338 keV) and ^{226}Ra (via ^{214}Pb at 351.9 keV) (Charette et al., 2001).

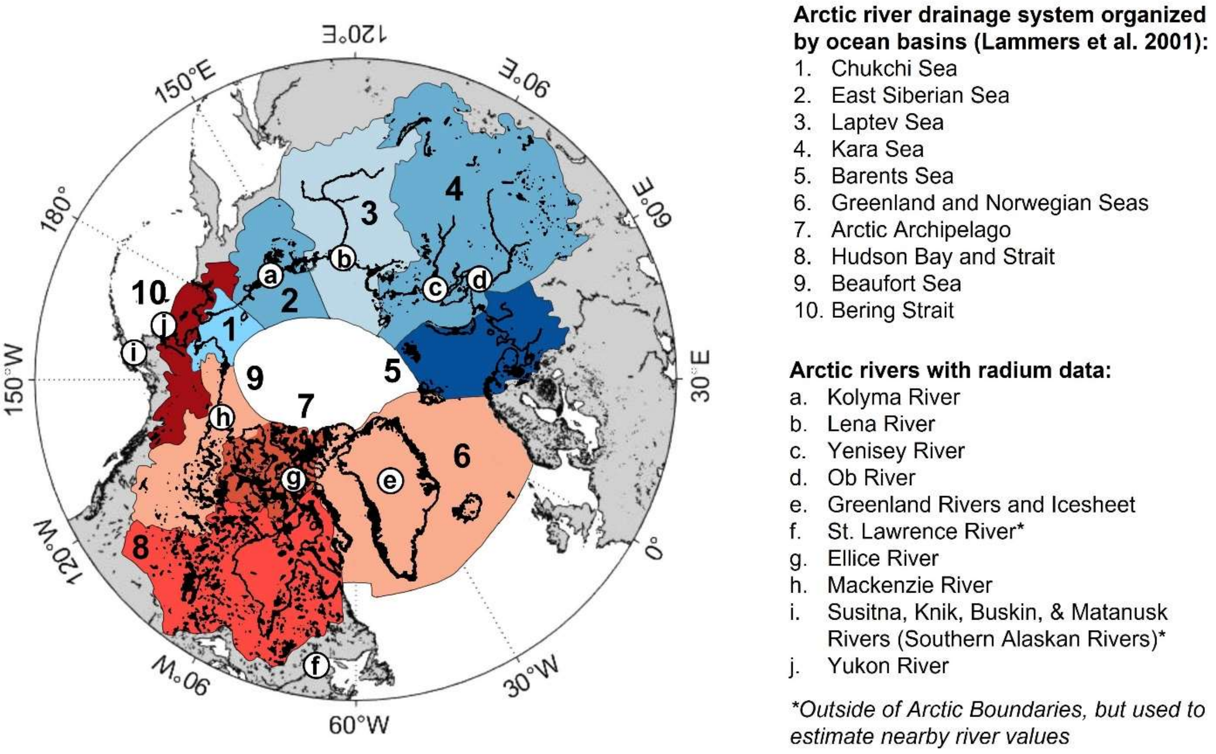

Figure 1. Map of Arctic with Arctic river drainage basins defined according to the methodology of Lammers et al. (2001) and labeled according to receiving marginal sea. North American drainage basins are represented in shades of red while Eurasian drainage basins are in blue. Arctic rivers with radium data are labeled at each river's mouth with white circles. Drainage basin and river names can be found in key.

2.2 Desorption Experiments

Suspended sediment from the Southern Alaskan Rivers was collected in September 2019 using a bilge pump to filter water through a 1 μm Hytrex filter. The filters were sealed in plastic bags and kept refrigerated until desorption experiments were performed. Bottom sediment from the Kolyma River was collected in summer 2018 from the Northeast Science Station in Cherskiy between July 23 to August 3. River bed sediment was sampled using a Van Veen grab-sampler and a stainless steel spoon, and stored in Whirl-Pak® bags. All samples represent recently deposited sediment rich in silt and clay in more quietly flowing locations of the river or delta. Within 12 hours after collection, sediments were frozen (-20°C) and remained so during transport. Sediment was thawed and dried before desorption experiments were performed in January and February 2022.

Desorption experiments were performed on suspended and recently deposited sediments from the Kolyma River and the Southern Alaskan Rivers. Two methods of desorption were performed based on the collection method of the suspended sediment. First, coastal seawater from Vineyard Sound was collected and filtered by the Environmental Systems Laboratory in Woods Hole, MA. The filtered seawater was then passed through manganese-oxide coated fibers (2 packed holders, 10 g each) at a flow rate of 0.5 L min^{-1} in order to remove Ra from the water. For each desorption experiment, 20 L of this filtered, Ra-free seawater was chilled to 4 - 6 °C. For samples collected on cartridge filters, the filter was removed from its plastic bag and placed in an appropriately sized cartridge filter holder. A peristaltic pump circulated the filtered seawater through the filter at a rate of 1.25 L min^{-1} for 6 hours. This flow rate and length of time was chosen following preliminary experiments (S5.2) which showed that more radium was desorbed after three hours, but no significant increases in radium desorption occurred in exposures lasting longer than six hours. After 6 hours, the cartridge holders were removed and the seawater was filtered through Mn-coated acrylic fiber at a flow-rate ≤ 0.5 L min^{-1} for 3 hours. The fibers were treated and analyzed for radium isotopes using the same methods as the dissolved fibers (see above). The cartridge filters were ashed (500 °C, 16 h) in order to obtain the sediment weight for each sample.

The second method was performed on loose, recently deposited sediment from the Kolyma River, collected in 2018. Prior to the experiment, the sediment was packed into gamma counting vials and capped with a plastic vial cap. The sediment was then gamma counted using the same method as above, in order to get the bulk sediment ^{226}Ra and ^{228}Ra totals. The loose sediment (10 - 11 g) was then added to the seawater and was shaken every 15 minutes for 6 hours. The water was then filtered through two acrylic fiber filters to remove sediment, followed by a Mn-coated acrylic fiber (≤ 0.5 L min^{-1}) to collect Ra. The fibers were treated and analyzed for radium isotopes using the same methods as the dissolved fibers (see above). The percentages of Ra desorbed were then calculated by dividing the desorbed Ra values by the bulk Ra activities.

3. Results and Discussion

3.1 Radium in Arctic Rivers

3.1.1 Dissolved Radium Activities

Measured freshwater Ra concentrations in Arctic rivers (Table 1) range from 1.48 - 27.3 dpm/100L (mean = 10.0 dpm/100L) for ^{226}Ra and 2.52 - 40.9 dpm/100L (mean = 16.9 dpm/100L) for ^{228}Ra. Averages for the Eurasian continent were 11.7 dpm/100L for ^{226}Ra and 19.3 dpm/100L for ^{228}Ra. These are higher than North American averages: 8.70 dpm/100L for ^{226}Ra and 11.7 dpm/100L for ^{228}Ra (Table 1). The range of Arctic dissolved Ra values we report are comparable to dissolved concentrations found in rivers worldwide (Table S5). In non-Arctic rivers, freshwater dissolved ^{226}Ra values range from 2.74 - 24.5 dpm/100L (global ^{226}Ra mean = 7.6 dpm/100L; including Arctic = 7.9 dpm/100L) and ^{228}Ra values range from 3.80 - 92.6 dpm/100L (global ^{228}Ra mean = 16.4 dpm/100L; including Arctic = 16.3 dpm/100L). Our Arctic averages are slightly higher than global average concentrations (Figure 2), however we cannot discount the potential that this is due to insufficient sampling of Arctic freshwaters over the entire annual cycle. Arctic river discharge during the long winter season is typically low, followed by significant high discharge events during spring and moderate runoff over summer. The spring freshet event accounts for ~50% of total annual discharge for the Kolyma and Yenisey rivers, and ~30% for the Ob and Mackenzie rivers (Holmes et al. 2012). Significant seasonal changes in radium concentrations can occur over the hydrologic year as evidenced by measurements in the Mackenzie and Yukon rivers by Kipp et al. (2020). The majority of Ra measurements from Arctic rivers have been conducted during mid- to late-summer due to access and logistics, preventing us from using a weighted average based on seasonal river flow changes, which could impact our flux estimates.

Table 1. Measured dissolved Ra concentrations and Ra desorption from suspended sediment in Arctic Rivers.

River	Dissolved (dpm/100L)		Desorbed (dpm/g)		Source
	^{226}Ra	^{228}Ra	^{226}Ra	^{228}Ra	
Yenisey (S)	3.25 ± 0.37	9.00 ± 1.34			Rutgers van der Loeff et al. 2003
Yenisey (W)	6.1 ± 0.7[a]	13.7 ± 2.1 [a]			
Lena (S)	7.02 ± 0.37[b]	16.32 ± 2.34[b]			Rutgers van der Loeff et al. 2003; Charkin et al. 2020
Lena (W)	13.1 ± 0.4	24.9 ± 0.9			
Ob (S)	2.48 ± 0.37[b]	4.66 ± 1.25[b]			Rutgers van der Loeff et al. 2003
Ob (W)	27.3 ± 0.61	40.9 ± 3.7			
Mackenzie	17.37 ± 0.28	17.03 ± 1.02	0.47 ± 0.06[c]	0.94 ± 0.25[c]	Kipp et al. 2020
Yukon	14.35 ± 0.42	19.51 ± 1.81			Kipp et al. 2020; This Study
Kolyma	3.08 ± 0.41	2.52 ± 0.89	0.26 ± 0.02[c]	0.34 ± 0.07[c]	This Study
Ellice	1.48 ± 0.30	7.70 ± 1.54			This Study
St. Lawrence	2.55 ± 0.26	5.11 ± 0.51	0.32 ± 0.03	0.98 ± 0.10	Sérodes and Roy, 1982
Southern Alaska Rivers (Avg)	2.94 ± 0.42	3.88 ± 1.65	0.12 ± 0.05[c]	0.08 ± 0.02[c]	This Study
Greenland River and Ice Sheet	2.00 ± 0.02	23.00 ± 1.20	0.10 ± 0.03	0.42 ± 0.08	Linhoff et al. 2020

(S) = Spring/Summer; (W) = Fall/Winter

a) estimated based on % flocculated in Lena river, which contains similar DOC values; b) effective riverine endmember (by this studies' authors) based on salinity gradient through estuary after initial flocculation; c) experimentally determined through laboratory desorption experiments

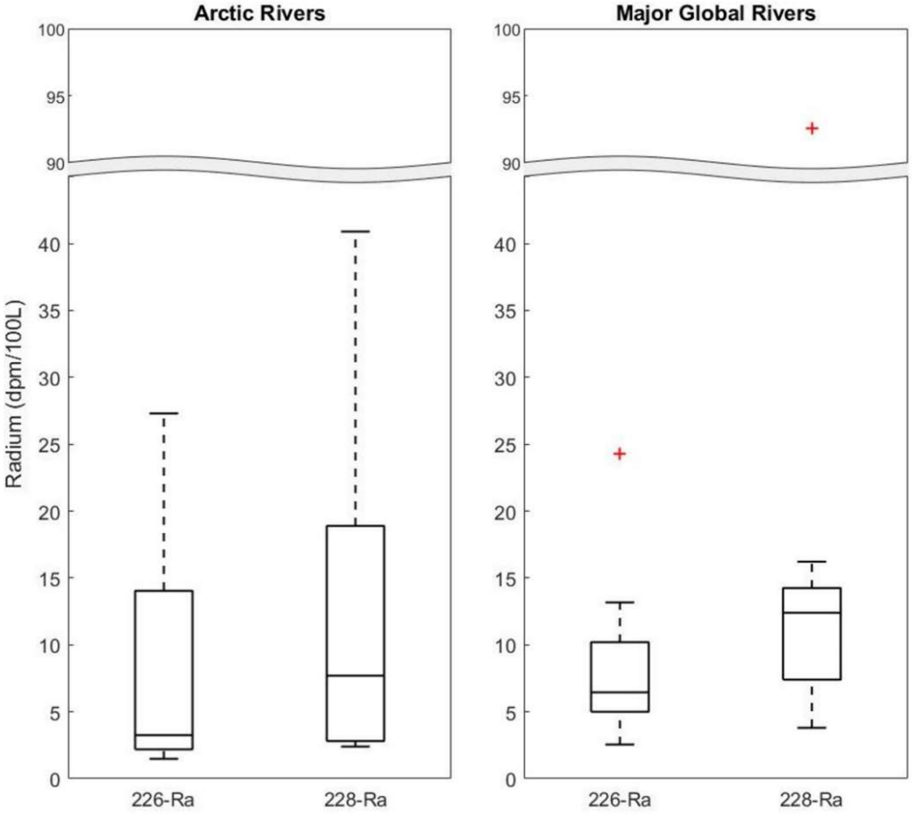

Figure 2. Box and whisker plot for Ra concentrations in fresh river water in Arctic rivers and major global rivers. It is important to note that the concentrations here reflect the actual freshwater concentrations, not the effective endmembers used in our input model for the Lena and Ob rivers. The outliers on the major global rivers plot are from the Parana and Uruguay river system.

3.1.2 Desorbed Radium from Suspended Sediments

To the best of our knowledge, this study presents the first radium desorption data for a Eurasian river. The total Ra present on the Kolyma sediments collected by this study were 1.6 ± 0.1 dpm/g for ^{226}Ra and 2.1 ± 0.5 dpm/g for ^{228}Ra. The amount desorbed was 0.33 ± 0.01 dpm/g for ^{226}Ra and 0.39 ± 0.05 dpm/g for ^{228}Ra. This results in a desorbable fraction of approximately 21% for ^{226}Ra and 19% for ^{228}Ra. The Mackenzie River has higher desorption rates for both isotopes: 0.46 ± 0.06 dpm/g for ^{226}Ra (14% desorbed) and 0.94 ± 0.25 dpm/g for ^{228}Ra (30% desorbed) (Kipp et al. 2018,. 2020). The Southern Alaskan Rivers had the lowest desorption rates: 0.12 ± 0.05 dpm/g for ^{226}Ra (14% desorbed) and 0.08 ± 0.02 dpm/g for ^{228}Ra (10% desorbed). Sediment grain size and mineralogy are key factors controlling differences in radium desorption behavior between rivers. Given the contrasting characteristics of Eurasian and North American river basins, it is unsurprising that the Kolyma desorption values are notably different from those reported for the Mackenzie River. Eurasian rivers, such as the Kolyma, drain large areas of low-relief tundra and wetlands, resulting in low suspended particulate loads but high dissolved organic carbon concentrations (Amon et al. 2012). Rivers in North America, by contrast, often drain mountainous regions and forests, where bedrock composition differs and high erosion rates result in considerable inorganic material fluxes to the Arctic Ocean (Amon et al. 2012). These high inorganic fluxes support higher desorption rates for North America compared to Eurasia. However, more data is needed to determine if the contrasting desorption rates are representative of their respective continents.

3.1.3 Flocculation in Eurasian Rivers

Numerous studies in temperate river estuaries have shown non-conservative addition at low- to mid-salinities (e.g., Li & Chen, 1979; Key et al. 1985). Values within the salinity mixing zone of the estuary that fall above the conservative mixing line have been attributed to radium desorption from suspended sediment (Elsinger & Moore, 1984; Krest et al. 1999). More recently, it has been learned that some of this non-conservative addition could be due to groundwater inputs or sediment resuspension (Moore & Shaw, 2008). However, Ra desorption from suspended sediments is still considered to be the major contributor of river-derived Ra to the coastal ocean (Kwon et al. 2014; Le Gland et al. 2017; Cho et al. 2018); this includes the Mackenzie River estuary (Kipp et al. 2020; Figure 3A).

However, a study of the Ob and Lena Rivers showed the opposite trend: a 50% and over 90% decrease in the freshwater Ra isotope activities at low salinities in the Lena and Ob Rivers, respectively (Rutgers van der Loeff et al., 2003). No apparent addition or removal of Ra isotopes was observed within the estuaries following this initial decrease (Figure 3B). This study attributed the rapid removal of Ra in these estuaries to the high concentrations of dissolved organic carbon (DOC) present in these large Eurasian river systems, which have been shown to flocculate out of solution in the estuarine mixing zone (Rutgers van der Loeff et al. 2003).

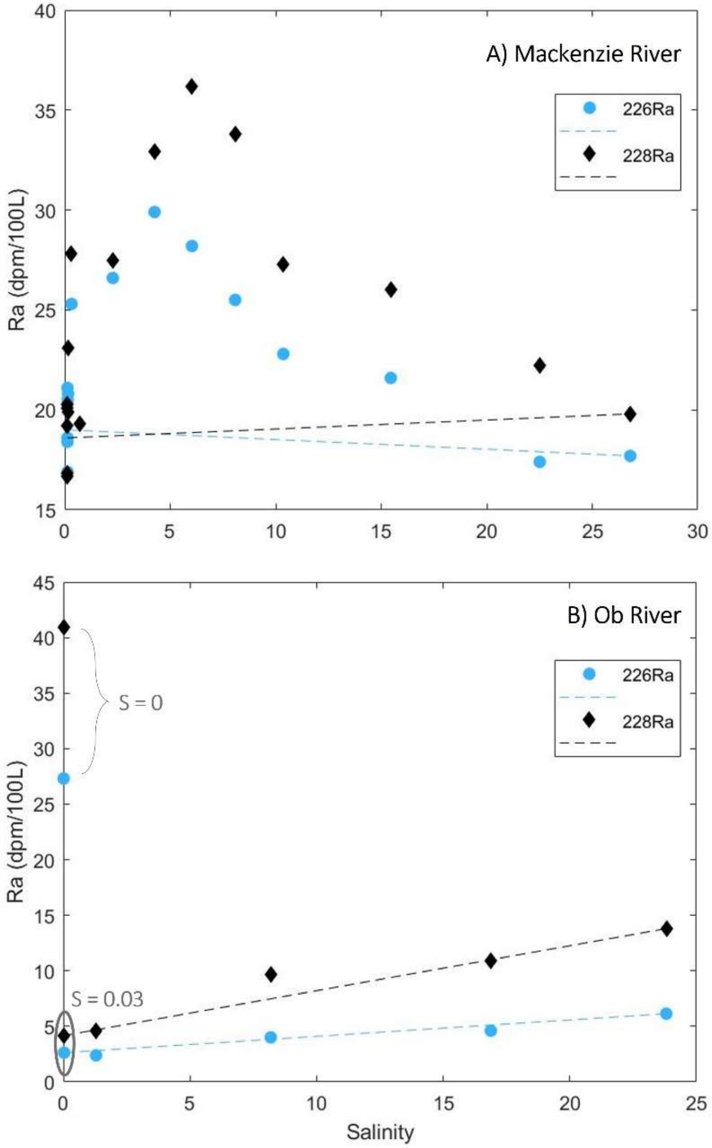

Figure 3. Ra concentrations and conservative mixing trends for two Arctic rivers. A) values from the Mackenzie River estuary (North America), published by Kipp et al. (2020). Values above the conservative mixing line indicate inputs from groundwater or sediment desorption; B) values from the Ob River estuary (Siberia), published by Rutgers van der Loeff et al. (2003). Intense flocculation removes most Ra from the Ob river at low salinities, requiring the use of a modified riverine end member that includes multiple processes (ie. flocculation & desorption).

Estuarine flocculation removal has also been reported for barium in the Ob and Yenisey Rivers (Ba; Guay & Falkner, 1998), which is known to behave similarly to Ra in riverine systems (Moore & Edmond, 1984; Moore & Shaw, 2008; Kipp et al., 2020). However, this process was observed only in samples collected during August, while samples collected in September showed no net removal. Due to the seasonality in removal, it was proposed that losses must be due to biological processes, or as a result of changing riverine organic matter composition between summer and fall (Guay & Falkner, 1998).

To gain a better understanding of this phenomenon, we examined two decades of seasonal measurements collected as part of the Arctic Great Rivers Observatory (Holmes et al. 2021; *https://arcticgreatrivers.org/data/*). We compared data for rivers previously reported to exhibit removal processes (Ob, Lena, & Yenisey) with those which have not (Kolyma, Yukon, & Mackenzie). We compared freshwater discharge, DOC, particulate organic carbon (POC), colored dissolved organic matter (CDOM), total suspended solids (TSS), particulate organic nitrogen (PON), nitrate (NO_3^-), ammonium (NH_4^+), temperature, alkalinity, and pH. Ice break up and thaw led to peaks in freshwater discharge, TSS, and DOC during June, with steady declines until winter baseline levels were reached in October or November across all rivers studied. Nutrients, such as organic nitrogen, followed opposing trends, likely due to uptake by microbes. DOC and CDOM concentrations were lower in our non-removal rivers (Kolyma, Yukon, and Mackenzie Rivers) relative to rivers where removal processes had been observed (Ob, Lena, and Yenisey), indicating that differences in organic matter concentrations and composition could be driving Ra removal processes in select Siberian rivers.

3.2 Calculations of Pan-Arctic Radium Flux Estimates

This paper uses the International Hydrographic Organization (IHO) definition of the Arctic (IHO, 2001), which also includes the Bering Strait and the Greenland and Norwegian Seas. River drainage basins are defined following the methodology of Lammers et al. (2001) and are referred to according to the receiving marginal sea (Fig. 1). River discharge and sediment load values are shown in Figure 4 for gauged rivers (water discharge and sediment load estimates are provided in S2: Table S1).

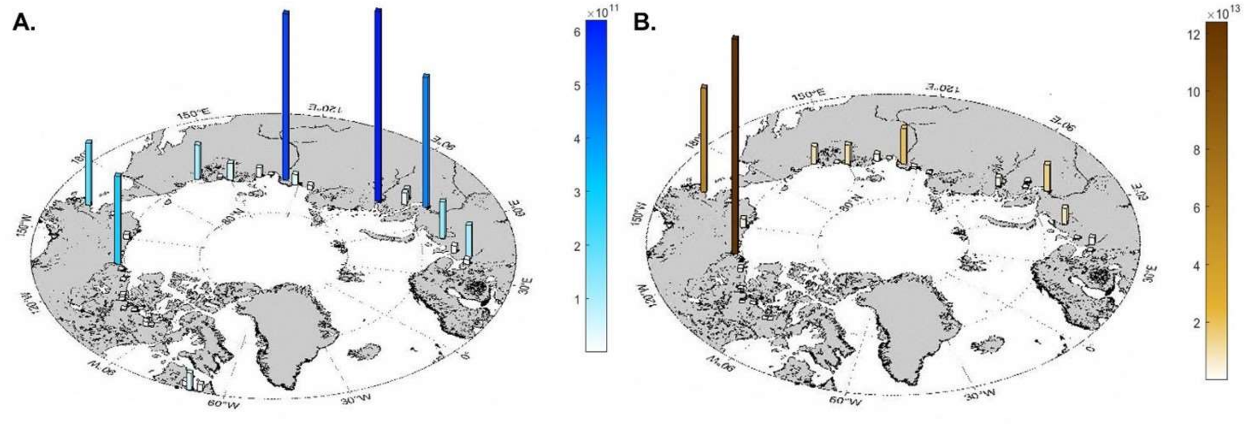

Figure 4. Maps of the Arctic showing A) river water discharge (m^3 y^{-1}) and B) sediment load (g y^{-1}) for Arctic rivers with available river gauging and sediment load data (Refs: Table S1). Greenland water discharge is omitted from these figures as it also includes ice sheet contributions.

Reported errors on Ra fluxes derived here represent those calculated for dissolved concentrations and desorption rates, and not for potential changes or variations in river discharge or sediment loads. Dissolved Ra concentrations have previously been determined for the Lena, Ob and Yenisey rivers on the Eurasian side of the Arctic, the Mackenzie, Yukon and St. Lawrence rivers on the North American side, and the Greenland ice sheet and rivers (Table

1). Here, we add dissolved data from the Kolyma River on the Eurasian continent, and data for the Ellice River and four Southern Alaska Rivers from North America. Radium desorbed from suspended sediment was calculated using suspended sediment loads and desorption values (dpm/g suspended sediment) based on the appropriate continent. The Mackenzie River desorption value was used for most of North America, with the following exceptions: the Bering Strait, where we used an average of the Mackenzie River's and Southern Alaska Rivers' desorption values, and Hudson Bay, which utilized estuarine data from the St. Lawrence River. The desorption value used for the Eurasian drainage basins was derived from our measurements from the Kolyma River.

In order to estimate total annual Ra fluxes from a river, the dissolved and desorbed inputs must be summed, as shown in Equation 1:

$$\boldsymbol{Ra_{Dis,i}} = \left(\boldsymbol{C_{fw,i}} \times \boldsymbol{D_i}\right) + \left(\boldsymbol{C_{d,i}} \times \boldsymbol{SS_i}\right) \qquad \text{(Equation 1)}$$

$Ra_{Dis,\,i}$ = total annual Ra inputs from river 'i' (dpm y^{-1})

$C_{fw,\,i}$ = dissolved freshwater Ra concentration in river 'i' (dpm m^{-3})

D_i = mean annual water discharge of river 'i' (m^3 y^{-1})

$C_{d,\,i}$ = Ra desorption from sediments in river 'i' (dpm g^{-1})

SS_i = mean annual sediment load of river 'i' (g y^{-1})

To quantify the total river Ra flux to the Arctic Basin, we compared several scaling approaches. The most basic approach utilized average Ra data and total estimated water and sediment discharges for North America and Eurasia (Lammers et al., 2001; Gordeev, 2006), Greenland (Overeem et al., 2017), and Hudson Bay (Kuzyk et al. 2009).This approach took an average dissolved Ra concentration for all North American rivers with Ra data and multiplied it by the total North American river water discharge into the Arctic Ocean to estimate the dissolved flux. Similarly, it took the average North American sediment Ra desorption rate multiplied by the estimated sediment load from all North American Arctic rivers to derive the desorbed flux. Adding these terms together produced an averaged North American Arctic river Ra flux. This approach was repeated for Eurasia and Greenland, with the sum of the three results producing a pan-Arctic Ra river flux estimate that could account for broad differences between landmasses. This method was repeated using the median dissolved Ra concentrations and median sediment desorption rates, in case outliers were distorting the average.

While this approach is the most straightforward, it obscures any finer scale geographical differences that might be present. As a result, we used another approach that separated rivers based on their receiving marginal seas and scaled up by these drainage basins. For rivers with radium data and simple desorption behavior, Equation 1 was used without modification. Monitored rivers without radium data were grouped based on proximity and watershed similarity to a major river that did have radium values (Table S2); for these groupings, Equation 1 was used with the assumption that the nearby major river Ra values were similar to those in the unsampled river. For all unaccounted for river discharge into each marginal sea, Equation 2 was used to scale up the Ra flux based on percent of water discharge remaining, following methods used in other flux studies (Wheeler et al. 1997; McClelland et al. 2016):

$$\boldsymbol{Ra_{MS}} = \textstyle\sum_i \boldsymbol{Ra_{Dis,i}} + \left[\boldsymbol{1} + \left(\frac{\boldsymbol{D_{Basin}} - \sum_i \boldsymbol{D_i}}{\boldsymbol{D_{Basin}}}\right)\right] \qquad \text{(Equation 2)}$$

Ra_{MS} = estimated total annual Ra inputs to select marginal sea (dpm y^{-1})

D_{Basin} = total estimated riverine flux for select river drainage basin (m^3 y^{-1})

For the Yenisey, Ob, and Lena Rivers, where flocculation has been observed during summer, different Ra values were employed for the fraction of water discharged in the summer vs the winter (Table 1). Based on the DOM data, we assumed that flocculation removal was restricted to June, July, and August. Using monthly discharge data between 2004 and 2020 (Holmes et al. 2021), we found that the average summer discharge accounts for 47% of the Yenisey River's annual discharge, 52% of the Ob's annual discharge, and 64% of the Lena's annual discharge. For this discharge we used the effective freshwater endmember Ra concentrations, after flocculation has led to some removal of Ra from the estuary, in order to calculate the summer Ra flux. For the remaining fall and winter discharge, we used Equation 1, with $C_{fw,\,i}$ equalling the pure freshwater/pre-removal Ra concentrations for the three rivers. The pre-removal concentration for the Yenisey River was estimated based on the percent removal that occurs in the Lena River, given its similar DOC and CDOM fluxes.

3.3 Total Riverine Radium Inputs to the Arctic Ocean

3.3.1 Total Riverine Flux of Radium to the Arctic Ocean

For the geographical separation method, the total dissolved flux is estimated at (5.10 ± 0.25) x 10^{14} dpm y^{-1} for ^{226}Ra and (9.9 ± 1.2) x 10^{14} dpm y^{-1} for ^{228}Ra (Table 2). The total desorbed flux from suspended sediments is estimated at (3.96 ± 1.50) x 10^{14} dpm y^{-1} for ^{226}Ra and (6.58 ± 2.87) x 10^{14} dpm y^{-1} for ^{228}Ra. The estimated total annual riverine ^{226}Ra and ^{228}Ra fluxes to the Arctic Ocean are (9.06 ± 1.37) x 10^{14} dpm y^{-1} and (16.5 ± 4.0) x 10^{14} dpm y^{-1}, respectively. The total inputs calculated by using the averaging and median methods are slightly less than those found using the geographical separation method (Table 2), and all ^{228}Ra estimates fall slightly above the best estimate published by Kipp et al. (2018) but within their error: 12.6 x 10^{14} dpm y^{-1} (range: 4.6 - 22.7 x 10^{14} dpm y^{-1}). Because of the good agreement between the methods, hereafter we will focus solely on the geographical separation method, since it allows us to better understand regional variations in Ra fluxes.

Despite Eurasian runoff delivering 1.4 times the freshwater to the Arctic Ocean as from North America, it contributed 2.2 times less ^{226}Ra and 2.0 times less ^{228}Ra per year (Table 2). This is driven by lower relative sediment loads and desorption rates as compared to the North American rivers. Eurasian rivers derive just 29% of their ^{226}Ra and ^{228}Ra fluxes from desorption, while this process accounts for roughly 49% and 44% of North American ^{226}Ra and ^{228}Ra inputs, respectively. These differences are likely due to a combination of higher organic to mineral ratios in suspended material in Eurasian rivers (Amon et al. 2012) and seasonal Ra removal within certain estuaries (Rutgers van der Loeff et al. 2003).

Table 2. Estimated annual riverine Ra flux to Arctic Ocean by Ocean Basin. Percent accounted for refers to how much annual discharge is accounted for based on our directly sampled rivers.

Arctic Marginal Sea	Annual Discharge (10^{11} m3/y)	Percent Accounted for	Estimated Ra Flux to Arctic Ocean (10^{12} dpm/y)					
			^{226}Ra	error	Des. %	^{228}Ra	error	Des. %
CAA	2.02	16%	4.06	0.94		17.7	3.9	
Barents Sea	4.46	60%	67.2	6.5		102	19	
Beaufort Sea	4.18	74%	156	46		239	120	
Bering Strait	3.12	72%	87.9	7.8		141	91	
Chukchi Sea [a]	1.20	0%	-	-		-	-	

East Siberian Sea	2.43	71%	15.3	1.6		16.4	18.9	
Hudson Bay	9.68	2%	28.9	5.0		80.5	23.4	
Kara Sea	12.3	91%	110	7		199	29	
Laptev Sea	7.63	82%	73.2	3.1		152	24	
Greenland	4.90		34.5	6.47		216	24	
N. America Total	19.6	30%	601	49	49%	946	285	44%
Eurasia Total	28.0	78%	271	14	29%	484	89	29%
Pan-Arctic Total	52.5	62%	906	137	44%	1650	400	60%
Averaging Pan-Arctic Total	52.5	NA	750	50	44%	1640	180	53%
Median Pan-Arctic Total	52.5	NA	820	280	51%	1240	450	45%
Des. = Desorption CAA = Canadian Arctic Archipelago a) Chukchi Sea had no rivers matching the criteria.								

3.3.2 Arctic Riverine Fluxes relative to Other Sources of Ra

Significant sources of Ra to the Arctic Ocean include advection through the Bering Strait and from the North Atlantic, diffusion from continental shelves, rivers, and ice-rafted sediment (Kadko & Muench, 2005; Kipp et al. 2018). Our ^{228}Ra river flux accounts for 5.5% of all ^{228}Ra inputs to the Arctic Ocean, with the largest input to the Arctic Ocean proper coming from continental shelves (92%; Kipp et al. 2018). Using the same methods as in Kipp et al. (2018) we estimate inputs for ^{226}Ra, with activities of ^{226}Ra isotopes that were measured on the 2015 U.S. GEOTRACES Arctic Transect (GN01) (for details, see Kipp et al. 2018). Briefly, Atlantic inflow was estimated to contain 6.3 Sv of water with a concentration of 7.43 dpm/100L (Besqcqynska-Moller et al 2012; Rudels et al. 2015), the Bering Strait was estimated to contribute 1.1 Sv with a concentration of 12.1 dpm/100L (Woodgate et al. 2012), giving us advective inputs of 1.90 x 10^{16} dpm y^{-1}. Shelf inputs were estimated using a shelf area of 7.94 x 10^{12} m^2 (Jakobsson, 2002) and an activity of 1070 dpm m^{-2} y^{-1}, for a total of 8.49 x 10^{15} dpm y^{-1}. Ice-rafted sediment activities were negligible. Consequently, rivers account for 3.2% of ^{226}Ra inputs to the Arctic Ocean proper, with shelves accounting for 29.8% and advection accounting for 67%.

Barium and Ba isotopes have previously been used to separate western vs. eastern riverine inputs within the Arctic Ocean, while Ra isotope activity ratios (AR) have been used to track water masses within the Arctic Ocean (Kadko & Muench, 2005; Kipp et al. 2018, 2019; Rutgers van der Loeff et al. 1995). North American rivers, including both dissolved and desorbed inputs, have a weighted ^{228}Ra/^{226}Ra AR of 1.56 while the Eurasian rivers have a weighted average of 1.84. These riverine ARs values are significantly lower than the AR ~ 3.9 observed over the Laptev Shelf (Rutgers van der Loeff et al., 2003) and the AR ~ 2.8 seen over the Chukchi shelf (Kipp et al., 2019; Vieira et al. 2018). This could allow differentiation between shelf and riverine Ra isotope inputs in certain regions of the Arctic Ocean, which has always been uncertain based on salinity alone (Kipp et al. 2019).

4. Arctic River Radium Fluxes in a Global Context

4.1 Total Riverine Flux of Radium to the Global Ocean

Ra data from 20 rivers were utilized, accounting for 50% of global riverine water discharge (Suzuki et al. 2018). Using the global median for riverine Ra concentrations and desorption rates (see SI:S4), as well as global estimates for water discharge and sediment inputs (Overeem et al. 2017), the estimated global river ^{226}Ra and ^{228}Ra inputs are (15 ± 2) x 10^{15} dpm y^{-1} and (19 ± 2) x 10^{15} dpm y^{-1}, respectively, while the globally averaged estimate is somewhat higher: (17 ± 13) x 10^{15} dpm y^{-1} and (27 ± 20) x 10^{15} dpm y^{-1} for ^{226}Ra and ^{228}Ra, respectively (Table 3). Using an ocean basin approach, the annual ^{226}Ra and ^{228}Ra fluxes to the global ocean are (7.4 ± 5.0) x 10^{15} dpm y^{-1} and (15.3 ± 3.8) x 10^{15} dpm y^{-1}, respectively (Table 3; SI:S4). For this approach, the Atlantic Ocean contributes the largest percentage of riverine radium inputs, followed by the Indian and Pacific Oceans. The Arctic Ocean receives 12% of global riverine ^{226}Ra inputs and 11% of ^{228}Ra inputs, similar percentages to global river discharge (McClelland et al. 2012). Considering the fact that the Arctic Ocean accounts for just 3% of the global ocean surface area, such high riverine Ra inputs result in rivers having a much larger impact on Arctic Ocean surface water Ra concentrations than would be observed in the Atlantic or Pacific Oceans.

The global estimates are in good agreement with literature estimates for ^{228}Ra (fluxes ranging from 12 - 37 x 10^{15} dpm $y^{-1;}$ (Cho et al. 2018; Kwon et al. 2014; Le Gland et al. 2017), and ^{226}Ra (estimate equalling 11.7 ± 5.3 x 10^{15} dpm y^{-1} (Xu et al. 2022)). The latter study utilized a Monte Carlo simulation with average ^{226}Ra concentrations from 13 rivers and average desorption values from 8 rivers to derive their riverine ^{226}Ra flux estimate. The discrepancy between our two approaches is much larger for the global estimates than it was for the Arctic estimates. The range in dissolved ^{226}Ra concentrations for the 30 rivers with available data was 1.48 - 24.3 dpm 100L^{-1}. For ^{228}Ra the range is even larger: 2.4 - 92.6 dpm 100L^{-1}. Thus, high outliers in these ranges drive up the global average and the median may not accurately capture this range. For the rest of our discussion, the globally averaged value is treated as an upper limit of potential riverine Ra inputs to the global ocean, while the ocean basin method is treated as a more realistic estimate.

Table 3. Estimated global annual riverine Ra flux to ocean. Data and methods can be found in supplementary information.

Ocean Basin	Annual Discharge (10^{12} m^3/y)	Percent Accounted for	Estimated Ra Flux to Global Ocean (10^{14} dpm/y)					
			^{226}Ra	error	Des. %	^{228}Ra	error	Des. %
Atlantic	17.3	67%	27.3	16.2		49.6	12.6	
Pacific	8.25	18%	17.5	11.6		46.3	8.0	
Indian	3.80	54%	17.8	20.8		38.4	13.1	
Arctic	5.25	62%	9.06	1.37		16.5	4.0	
Baltic Sea	0.46	2%	0.15	0.04		0.21	0.03	
Combined: Black Sea, Red Sea, and Mediterranean	1.09	5%	1.36	0.16		1.67	0.34	
Global Total	37.0	50%	73.2	50.2	79%	150	40	76%
Averaging Global Total	37.0	NA	170	130	83%	270	200	79%
Median Global Total	37.0	NA	150	20	85%	190	20	74%
Des. = Desorption								

4.2 Global Riverine Fluxes relative to Other Sources of Ra

To place our global radium river fluxes in context, we compare it to other major sources of radium to the global ocean (Figure 5). Estimates for ^{228}Ra from SGD range from (85 ± 7) x 10^{15} dpm y^{-1} (Le Gland et al. 2017) to approximately 130 x 10^{15} dpm y^{-1} (Kwon et al. 2014; Cho et al. 2018). SGD inputs of ^{228}Ra are thus 5 to 9 times higher than the ^{228}Ra flux from rivers. For continental shelf sediments, Le Gland et al. (2017) estimated that ^{228}Ra fluxes fall between (9.9 - 150) x 10^{15} dpm y^{-1}, while Kwon et al. (2014) estimated this flux at 55 x 10^{15} dpm y^{-1}. Depending on the estimate, ^{228}Ra inputs from the shelves could either be on par with riverine inputs or up to 10 times greater. Dust can be neglected as it contributes <1% of ^{228}Ra inputs to the ocean (Kwon et al. 2014; Le Gland et al. 2017). A conservative estimate therefore places ^{228}Ra inputs from rivers around 10% of the total ^{228}Ra inputs to the global surface ocean.

Most studies have assumed that <10% of ^{226}Ra inputs to the ocean are sourced from rivers based on the flux required to close the ocean mass balance for ^{226}Ra (Ku & Luo, 1994; Ku & Luo, 2008). For SGD, Xu et al. (2022) reported a ^{226}Ra flux of 24 ± 7 x 10^{15} dpm y^{-1}. Our estimate, which used the global median groundwater ^{228}Ra/^{226}Ra AR (2.28; Charette & Moore, 2022) applied to the previously discussed model-derived ^{228}Ra SGD inputs, results in a flux range for ^{226}Ra from SGD of 37 x 10^{15} - 57 x 10^{15} dpm y^{-1}. Using a continental shelf area of 2.73 x 10^{13} m^2, a ^{228}Ra flux from the shelves of (55 ± 50) x 10^{15} dpm y^{-1} (Kwon et al., 2014; Le Gland et al., 2017), and a continental shelf sediment AR of 1.5 (Moore and Shaw, 1998), we get a shelf ^{226}Ra flux of (37 ± 33) x 10^{15} dpm y^{-1}, in good agreement with the value of 42 x 10^{15} dpm y^{-1}, estimated by Xu et al. (2022). Deep sea sediment inputs have high errors, with diffusive fluxes ranging from 15 dpm m^{-2} y^{-1} to 2100 dpm m^{-2} y^{-1} (Costello, Smith, & Fraczek 2015). Using an intermediate diffusive flux estimate of 1057 dpm m^{-2} y^{-1} and a deep sea sediment area of 2.81 x 10^{14} m^2 (Cochran & Krishnaswami, 1980) we get a ^{226}Ra deep sea sediment flux of ~300 x 10^{15} dpm y^{-1}. Finally, hydrothermal vents are thought to supply ^{226}Ra to the ocean at a rate between 2 - 6 x 10^{15} dpm y^{-1} (Dymond et al. 1983; Kipp et al. 2018). Taken together, our estimate places ^{226}Ra inputs from rivers around 2% of the total ^{226}Ra inputs to the global ocean.

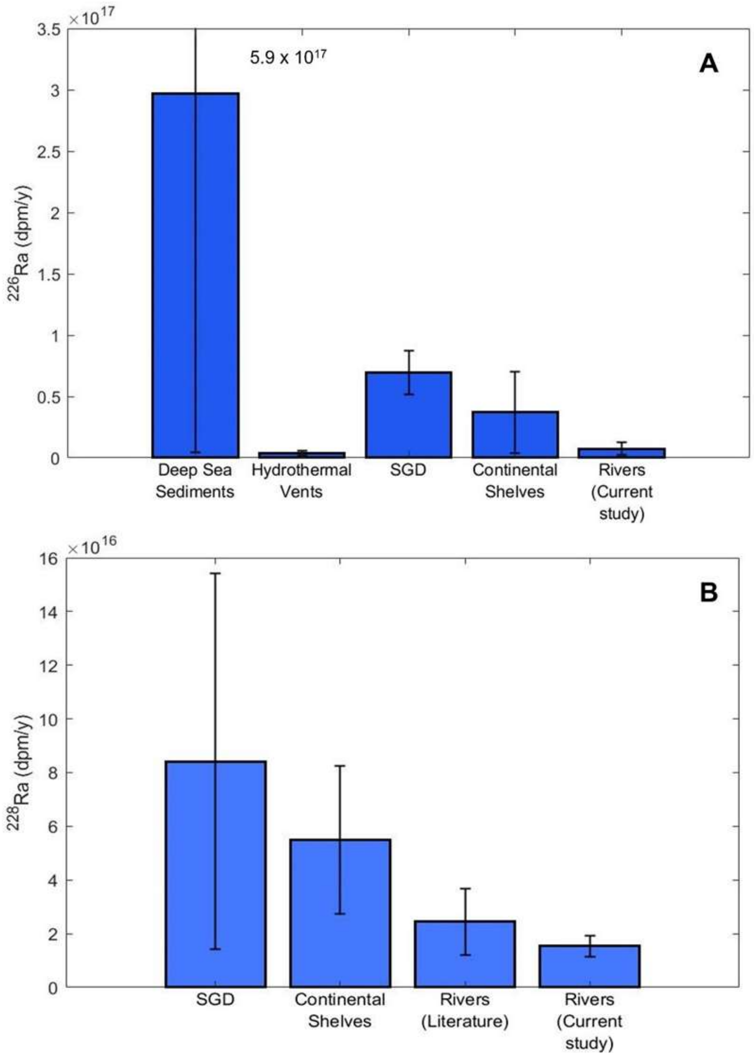

Figure 5. Boxplot of major Ra sources to the global ocean. A) annual ^{226}Ra inputs to the global ocean (dpm/y). B) annual ^{228}Ra inputs to the global ocean (dpm/y), omitting deep ocean inputs. SGD = Submarine Groundwater Discharge.

4.3 The Importance of Dissolved and Desorbed Inputs

Based on this study and other recent work, desorbed radium inputs dominate riverine radium fluxes to the global ocean (Kwon et al. 2014; Le Gland et al. 2017). This viewpoint was informed by early studies of radium desorption in rivers, where desorption was inferred from estuary mixing gradients (Li et al. 1977; Elsinger and Moore, 1980). It is now understood that submarine groundwater discharge can be a major source of radium to river estuaries (eg. Krest et al. 1999; Luek & Beck, 2014). This process likely resulted in overestimates of the desorption Ra source during the formative years of radium studies in rivers. During these early studies, a proposed estimate of 2 dpm ^{228}Ra /g for desorbable radium became popular and has since been used in numerous studies and models to estimate desorption inputs to the ocean (Moore et al. 2008; Kwon et al. 2014; Le Gland et al. 2017).

To date, few studies have attempted to directly quantify Ra isotope desorption from riverine suspended sediment (Table 1; Table S5). However, with few exceptions, these desorption studies reported values below both the 2.0 dpm/g estimate and the theoretical approach by Webster et al. (1995). For the 20 rivers utilized in our global calculation, the range of desorbable ^{226}Ra is 0.21 - 2.74 dpm/g (mean = 1.08 dpm/g) and the range for ^{228}Ra is 0.39 - 5.97 dpm/g (mean = 1.63 dpm/g) (Table S5). For rivers where desorption experiments were not performed, the upper limit theoretical values from Webster et al. (1995) were used (n = 3) or the desorption rate was calculated based on estuarine inputs (n = 5). Both of these methods are likely to overestimate actual desorption contributions, highlighting the importance of performing desorption experiments, rather than relying on an average value from the literature, or on current theoretical models which do not take differences in mineralogy into account.

While rivers with large amounts of suspended sediment do tend to have inputs dominated by desorption, the story is more complex. Whether a river contributes more dissolved or desorbed radium depends on several factors, including the dissolved concentration, the desorbable radium per gram, and importantly, the suspended sediment concentration. Our data synthesis suggests that sediment load is more important to total riverine radium inputs than discharge (Figure 6). For example, despite the Congo River having 1.4 dpm/g more desorbable ^{226}Ra than the Amazon, the Amazon has a greater proportion of ^{226}Ra inputs from desorption because its suspended sediment load is 27 times higher. In contrast, smaller rivers tend to contribute proportionally higher amounts of dissolved radium. Rivers in this study had a range of relative dissolved inputs: 14% - 99.9% with an average of 55% for ^{226}Ra and 11% - 99.9% with an average of 56% for ^{228}Ra. As a result, it is most important to consider these factors when looking at individual river and coastal systems, since the overall weighted dissolved inputs to the global ocean remain low at 21% and 24% for ^{226}Ra and ^{228}Ra, respectively.

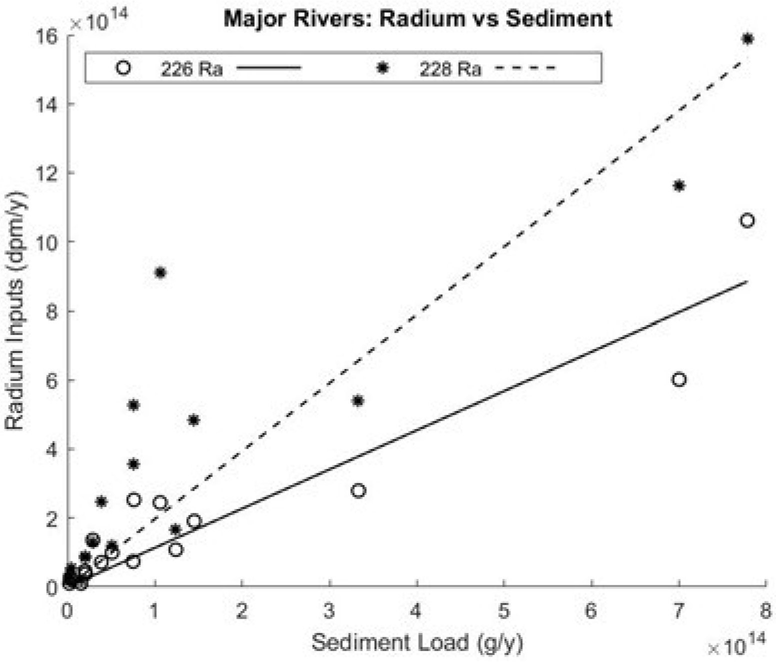

Figure 6. Total annual radium inputs compared to sediment load for major global rivers. The slopes are 1.1 (R^2 = 0.88) for ^{226}Ra and 2.0 (R^2 = 0.74) for ^{228}Ra.

5. Conclusions

This study quantified riverine ^{226}Ra and ^{228}Ra fluxes into the Arctic Ocean and provides the first Ra desorption data for Eurasian rivers. It was found that North America contributes the majority of Ra from riverine fluxes to the Arctic Ocean: 66% of ^{226}Ra and 57% of ^{228}Ra. This is due to larger suspended sediment inputs and higher desorption rates in North American rivers. Some Eurasian rivers' Ra inputs are also decreased due to organic matter flocculation in their estuaries, which can scavenge Ra before it reaches the coast. On a global scale, the Arctic

Ocean collects a proportionate amount of Ra compared to its riverine inputs of 11 - 12% the global total.

River and sediment inputs to the Arctic Ocean have increased over past decades due to warming temperatures and changing atmospheric moisture patterns, and are expected to increase in the future as warming continues (Andreson et al. 2020; Wang et al. 2021).. Higher temperatures have also led to declining summer sea ice cover (Grosfeld et al. 2015; Serreze et al. 2007), more extensive permafrost thaw (Biskaborn et al., 2019; IPCC, 2021), and faster rates of coastal erosion (Günther et al. 2013, Irrgang et al., 2022). There is also evidence of increasing pore water exchange rates from continental shelves, (Kipp et al. 2018; Rutgers van der Loeff et al. 2018), which may be linked to increased wave action and vertical mixing on shelves associated with the diminishing ice cover (Carmack & Chapman, 2003; Rainville & Woodgate, 2009; Williams & Carmack, 2015). Recently, groundwater has also been shown to be an important source of nutrients to the Arctic Ocean (Charkin et al. 2017; Connolly et al. 2020; Lecher et al. 2016). This source is also predicted to increase with warming temperatures (Neilson et al. 2018; Connolly et al. 2020). All of these changes are expected to increase Ra inputs to the Arctic Ocean, which would impact the relative contributions of Ra sources, including that for rivers.

Although this study provides a baseline estimate for Ra contributions from rivers, future work is needed to capture changes in Ra fluxes as climate-driven changes occur in hydrology, groundwater supply and changing OM supply to coastal systems. Seasonal variability in Ra concentrations need to be further constrained, particularly during the high flow spring freshet. More work is also needed to determine whether desorption rates are consistent throughout continents, or whether rivers vary significantly. Finally, a better understanding is needed of the removal processes in Eurasian rivers. This is particularly important in terms of climate change, as warming temperatures and changing watershed conditions are shifting OM properties and distributions across coastal interfaces.

Acknowledgments

The authors would like to thank Jessica Dabrowski, Juri Palmtag, Dirk Jong, Lisa Bröder, Kirsi Keskitalo, and the staff of the Northeast Science Station in Cherskiy for their assistance in sample collection in Alaska and Siberia. We would also like to thank Paul Henderson for his work in the field and for his help analyzing samples, and Heather H. Kim for her advice regarding statistical analyses. This study was a broad, collaborative effort that would not have been possible without contributions from numerous funding sources, including the National Science Foundation (NSF-0751525, NSF-1736277, NSF-1458305, NSF-1938873, NSF-2048067, NSF-2134865), the NERC-BMBF project CACOON [NE/R012806/1] (UKRI NERC) and BMBF-03F0806A, and an EU Starting Grant (THAWSOME-676982).

Open Research

Data from the Kolyma River, the Southern Alaskan Rivers, and previously unpublished submarine groundwater discharge data have been archived at the Biological and Chemical Oceanography Data Management Office (Biological and Chemical Oceanography Data Management Office (BCO-DMO). Dissolved radium data from these rivers can be found at *https://www.bco-dmo.org/dataset/878527* [See citation below: (Charette & Bullock, 2022a)]. Desorption data from these rivers can be found at *https://www.bco-dmo.org/dataset/878663* (Charette & Bullock, 2022b). The submarine groundwater global database can be found at *https://www.bco-dmo.org/dataset/878519* (Charette & Moore, 2022). These data are also available as supporting information.

References

Allison, M. A., Demas, C. R., Ebersole, B. A., Kleiss, B. A., Little, C. D., Meselhe, E. A., et al. (2012). A water and sediment budget for the lower Mississippi-Atchafalaya River in flood years 2008 - 2010: Implications for sediment discharge to the oceans and coastal restoration in Louisiana. *Journal of Hydrology, 432-433*, 84-97. *https://doi.org/10.1016/j.jhydrol.2012.02.020*

Amon, R. M. W., Rinehard, A. J., Duan, S., Louchouarn, P., Prokushkin, A., Guggenberger, G., et al. (2012). Dissolved organic matter sources in large Arctic rivers. *Geochimica et Cosmochimica Acta, 94*, 217-237. *http://doi.org/10.1016/j.gca.2012.07.015*

Beszczynska-Möller, A., Fahrbach, E., Schauer, U., & Hansen, E. (2012). Variability in Atlantic water temperature and transport at the entrance to the Arctic Ocean, 1997 - 2010. *ICES Journal of Marine Science, 69* (5), 852-863. *https://doi.org/10.1093/icesjms/fss056*

Biskaborn, B. K., Smith, S. L., Noetzli, J., Matthes, H., Vieira, G., Streletskiy, D. A., et al. (2019) Permafrost is warming at a global scale. *Nature Communications, 10,* 264. *https://doi.org/10.1038/s41467-018-08240-4*

Brabets, T. P., Nelson, G. L., Dorava, J. M., & Milner, A. M. (1999). Water-Quality Assessment of the Cook Inlet Basin, Alaska - Environmental Setting. In *Water-Resources Investigations Report 99-4025*, Snyder, E. F., Harris, L.-L., & Benson, S. L. (Eds). U.S. Geological Survey.

Breier, J. A., Breier, C. F., & Edmonds, H. N. (2005). Detecting submarine groundwater discharge with synoptic surveys of sediment resistivity, radium, and salinity. *Geophysical Research Letters, 32. https://doi.org/10.1029/2005GL024639*

Carmack, E., & Chapman, D. C. (2003). Wind-driven shelf/basin exchange on an Arctic shelf: The joint roles of ice cover extent and shelf-break bathymetry. *Geophysical Research Letters, 30*(14). *https://doi.org/10.1029/2003GL017526*

Carson, M. A., Jasper, J. N., & Conly, F. M. (1998). Magnitude and Sources of Sediment Input to the Mackenzie Delta, Northwest Territories, 1974-94. *Arctic, 51*(2), 116-124. *https://doi.org/10.14430/arctic1053*

Charette, M. A. (2007). Hydrologic forcing of submarine groundwater discharge: Insight from a seasonal study of radium isotopes in a groundwater-dominated salt marsh estuary. *Limnology and Oceanography, 52*(1), 230-239. *https://doi.org/10.4319/lo.2007.52.1.0230*

Charette, M. A., Buesseler, K. O., & Andrews, J. E. (2001). Utility of radium isotopes for evaluating the input and transport of groundwater-derived nitrogen to a Cape Cod estuary. *Limnology and Oceanography, 46*(2), 465-470. *https://doi.org/10.4319/lo.2001.46.2.0465*

Charette, M. A. & Buesseler, K. O. (2004). Submarine groundwater discharge of nutrients and copper to an urban subestuary of Chesapeake Bay (Elizabeth River). *Limnology and Oceanography, 49*(2), 376-385. *https://doi.org/10.4319/lo.2004.49.2.0376*

Charette, M. A., Bullock, E. J. (2022a) Dissolved Radium from Kolyma (Russia), Ellice (Canada), and Kodiak Island (USA) Rivers. Biological and Chemical Oceanography Data Management Office (BCO-DMO). (Version 1) Version Date 2022-08-16. doi:10.26008/1912/bco-dmo.878527.1 [August 18, 2022]

Charette, M. A., Bullock, E. J. (2022b) Desorbed Radium from Kolyma (Russia), Ellice (Canada), and Kodiak Island (USA) Rivers. Biological and Chemical Oceanography Data Management Office (BCO-DMO). (Version 1) Version Date 2022-08-16. doi:10.26008/1912/bco-dmo.878663.1 [August 18, 2022]

Charette, M. A., Henderson, P. B., Breier, C. F., & Liu, Q. (2013). Submarine groundwater discharge in a river-dominated Florida estuary. *Marine Chemistry*, *156*, 3-17. *https://doi.org/10.1016/j.marchem.2013.04.001*

Charette, M. A., Moore, W. S. (2022) Measurements of global dissolved submarine groundwater discharge (SGD) 226-Radium and 228-Radium. Biological and Chemical Oceanography Data Management Office (BCO-DMO). (Version 1) Version Date 2022-08-16. doi:10.26008/1912/bco-dmo.878519.1 [August 18, 2022]

Charette, M. A., Morris, P. J., Henderson, P. B., & Moore, W. S. (2015). Radium isotope distributions during the US GEOTRACES North Atlantic cruises. *Marine Chemistry, 177*(1), 184-195. *https://doi.org/10.1016/j.marchem.2015.01.001*

Charette, M. A., Kipp, L. E., Jensen, L. T., Dabrowski, J. S., Whitmore, L. M., Fitzsimmons, J. N., Williford, T., et al. (2020). The Transpolar Drift as a Source of Riverine and Shelf-Derived Trace Elements to the Central Arctic Ocean. *Journal of Geophysical Research: Oceans, 125*, e2019JC015920. *https://doi.org/10.1029/2019JC015920*

Charkin, A. N., Pipko, I. I., Pavlova, G. Y., Dudarev, O. V., Leusov, A. E., Barabanschikov, Y. A., et al. (2020). Hydrochemistry and isotopic signatures of subpermafrost groundwater discharge along the eastern slope of the Lena River Delta in the Laptev Sea. *Journal of Hydrology, 590,* 125515. *https://doi.org/10.1016/j.jhydrol.2020.125515*

Charkin, A. N., Rutgers van der Loeff, M., Shakhova, N. E., Gustafsson, Ö., Dudarev, O. V., Cherepnev, M. et al. (2017). Discovery and characterization of submarine groundwater discharge in the Siberian Arctic seas: a case study in the Buor-Khaya Gulf, Laptev Sea. *The Cryosphere, 11,* 2305-2327. *https://doi.org/10.5194/tc-11-2305-2017*

Chen, Z., Shen, H., & Zhanghua, W. (2001). Yangtze river of China: historical analysis of discharge variability and sediment flux. *Geomorphology, 41*, 77 - 91.

Cho, H.-M., Kim, G., Kwon, E. Y., Moosdorb, N., Garcia-Orellana, J., & Santos, I. R. (2018). Radium tracing nutrient inputs through submarine groundwater discharge in the global ocean. *Scientific Reports, 8,* 2439. *https://doi.org/10.1038/s41598-018-20806-2*

Cochran, J. K. & Krishnaswami, S. (1980). Radium, thorium, uranium, and Pb-210 in deep-sea sediments and sediment pore waters from the North Equatorial Pacific. *American Journal of Science*, *280*(9), 849–889.

Connolly, C., Cardenas, M. B., Burkart, G. A., Spencer, R. G. M., & McClelland, J. W. (2020). Groundwater as a major source of dissolved organic matter to Arctic coastal waters. *Nature Communications. 11,* 1479. *https://doi.org/10.1038/s41467-020-15250-8*

Costello, M. J., Smith, M., & Fraczek, W. (2015). Correction to Surface Area and the Seabed Area, Volume, Depth, Slope, and Topographic Variation for the World's Seas, Oceans, and Countries. *Environmental Science and Technology, 49*(11), 7071-2. *https://doi.org/10.1021/acs.est.5b01942*

Crotwell, A. M., & Moore, W. S. (2003). Nutrient and radium fluxes from submarine groundwater discharge to Port Royal Sound, South Carolina. *Aquatic Geochemistry, 9,* 191-208. *https://doi.org/10.1023/B:AQUA.0000022954.89019.c9*

Dai, G., Wang, G., Li, Q., Tan, E., & Dai, M. (2021). Submarine groundwater discharge on the western shelf of the northern south china sea influenced by the pearl river plume and upwelling. *Journal of Geophysical Research: Oceans*, *126*(4), e2020JC016859. *https://doi.org/10.1029/2020JC016859*

Déry, S. J., Stadnyk, T. A., MacDonald, M. K., & Gauli-Sharma, B. (2016) Recent trends in variability in river discharge across northern Canada. *Hydrological Earth System Science, 20,* 4801-4818. *https://doi.org/10.5194/hess-20-4801-2016*

Dymond, J., Cobler, R., Gordon, L., Biscaye, P., & Mathieu, G. (1983). 226Ra and 222Rn contents of Galapagos Rift hydrothermal waters - the importance of low-temperature interactions with crustal rocks. *Earth and Planetary Science Letters, 64,* 417-429.

Dulaiova, H., Burnett, W.C., Chanton, J.P., Moore, W.S., Bokuniewicz, H.J., Charette, M.A., & Sholkovitz, E. (2006). Assessment of groundwater discharges into West Neck Bay, New York, via natural tracers. *Continental Shelf Research, 26,* 1971-1983. *https://doi.org/10.1016/j.csr.2006.07.011*

Elsinger, R. J., & Moore, W. S. (1980). 226Ra behaviour in the Pee Dee River-Winyah Bay estuary. *Earth and Planetary Science Letters, 48*(2), 239-249. *https://doi.org/10.1016/0012-821X(80)90187-9*

Elsinger, R. J., & Moore, W. S. (1984). 226Ra and 228Ra in the Mixing Zones of the Pee Dee River-Winyah Bay, Yangtze River and Delaware Bay Estuaries. *Estuarine, Coastal, and Shelf Science, 18*(6)*,* 601-613. *https://doi.org/10.1016/0272-7714(84)90033-7*

Forbes, D. L. (1981) Babbage River Delta and Lagoon: Hydrology and Sedimentology of an Arctic Estuarine System. PhD Thesis, University of British Columbia.

Garcia-Solsona, E., Garcia-Orellana, J., Masqué, P., & Dulaiova, H. (2008). Uncertainties associated with 223Ra and 224Ra measurements in water via a delayed coincidence counter (RaDeCC). *Marine Chemistry*, *109* (3-4): 198-219.

Garzanti, E., Andó, S., France-Lanord, C., Censi, P., Vignola, P., Galy, V., & Lupker, M. (2011). Mineralogical and chemical variability of fluvial sediments 2. Suspended-load silt (Ganga-Brahmaputra, Bangladesh). *Earth and Planetary Science Letters, 302,* 107 - 120.

George, C., Moore, W. S., White, S. M., Smoak, E., Joye, S. B., Leier, A., & Wilson, A. M. (2020). A New Mechanism for Submarine Groundwater Discharge from Continental Shelves. *Water Resources Research, 56* (11), e2019WR026866. https://doi.org/10.1029/2019WR026866

Godoy, J. M., de Carvalho, Z. L., da Costa Fernandes, F., Danelon, O. M., Godoy, M. L. D. P., Ferreira, A. C. M., & Roldão, L. A. (2006). ^{228}Ra and ^{226}Ra in Coastal Seawater Samples from the Ubatuba Region - Brazilian Southwestern Coastal Region. *Journal of the Brazilian Chemical Society, 17*(4). *https://doi.org/10.1590/S0103-50532006000400014*

Gonneea, M. E., Mulligan, A. E. & Charette, M. A. (2013). Seasonal cycles in radium and barium within a subterranean estuary: Implications for groundwater derived chemical fluxes to surface waters. *Geochimica et Cosmochimica Acta, 119,* 164-177. *https://doi.org/10.1016/j.gca.2013.05.034*

Gordeev, V. V. (2006). Fluvial sediment flux to the Arctic Ocean. *Geomorphology, 80,* 94-104. *http://doi.org/10.1016/j.geomorph.2005.09.008*

Grosfeld, K., Treffeisen. R., Asseng, J., Bartsch, A., Bräuer, B., Fritzsch, B., et al. (2015). Online Sea-Ice Knowledge and Data Platform <*www.meereisportal.de*>. *Polarforschung, 85*(2), 143-155. *http://doi.org/10.2312/polfor.2016.011*

Gu, H., Moore, W. S., Zhang, L., Du, J., & Zhang, J. (2012). Using radium isotopes to estimate the residence time and the contribution of submarine groundwater discharge (SGD) in the Changjiang effluent plume, East China Sea. *Continental Shelf Research, 35,* 95-107. *https://doi.org/10.1016/j.csr.2012.01.002*

Guay, C. K., & Falkner, K. K. (1998). A survey of dissolved barium in the estuaries of major Arctic rivers and adjacent seas. *Continental Shelf Research, 18,* 859-882. *https://doi.org/10.1016/S0278-4343(98)00023-5*

Günther, F, Overduin, P. P., Sandakov, A. V., Grosse, G., & Grigoriev, M. N. (2013). Short- and long-term thermo-erosion of ice-rich permafrost coasts in the Laptev Sea region. *Biogeosciences, 10,* 4297-4318. *https://doi.org/10.5194/bg-10-4297-2013*

Haine, T. W. N., Curry, B., Gerdes, R., Hansen, E., Karcher, M., Lee, C., et al. (2015). Arctic freshwater export: Status, mechanisms, and prospects. *Global and Planetary Change, 125,* 13-35. *https://doi.org/10.1016/j.gloplacha.2014.11.013*.

Holmes, R. M., McClelland, J. W., Peterson, B. J., Shiklomanov, I. A., Shiklomanov, A. I., Zhulidov, A. V., et al. (2002). A circumpolar perspective on fluvial sediment flux to the Arctic Ocean. *Global Biogeochemical Cycles, 16*(4), 1098. *https://doi.org/10.1029/2001GB001849*

Holmes, R. M., McClelland, J. W., Peterson, B. J., Tank, S. E., Bulygina, E., Eglinton, T. L., et al. (2012). Seasonal and Annual Fluxes of Nutrients and Organic Matter from Large Rivers to the Arctic Ocean and Surrounding Seas. *Estuaries and Coasts, 35,* 369-382. *https://doi.org/10.1007/s12237-011-9386-6*

Holmes, R.M., McClelland, J.W., Tank, S.E., Spencer, R.G.M., & Shiklomanov, A.I. (2021). Arctic Great Rivers Observatory. Water Quality Dataset & Absorbance Dataset, Version 2022/04/05. https://www.arcticgreatrivers.org/data

International Hydrographic Organization (IHO), Limits of Ocean and Seas, rep. S-23, draft, 4th ed., Monaco, October 2001.

IPCC (2021). Climate Change 2021: The Physical Science Basis. In *Contribution of Working Group I to the Sixth Assessment Report of the Intergovernmental Panel on Climate Change*, Masson-Delmotte, V., et al. (Eds.). Cambridge University Press. In Press. Retrieved from *https://www.ipcc.ch/report/sixth-assessment-report-working-group-i/*

Irrgang, A. M., Bendixen, M., Farquharson, L. M., Baranskaya, A. V., Erikson, L. H., Gibbs, A. E., et al. (2022). Drivers, dynamics, and impacts of changing Arctic coasts. *Nature Reviews Earth & Environment, 3,* 39-54. *https://doi.org/10.1038/s43017-021-00232-1*

Isupova, M. V. & Mikhailov, V. N. (2018). Long-Term Variations of Water Runoff and Suspended Sediment Yield in the Parana and Uruguay Rivers. *Water Research, 45*(6), 846 - 860.

Jakobsson, M. (2002). Hypsometry and volume of the Arctic Ocean and its constituent seas. *Geochemistry, Geophysics, Geosystems, 3* (5), 1-18. *https://doi.org/10.1029/2001GC000302*

Jones, S. H., Madison, R. J., & Zenone, C. (1978). Water Resources of the Kodiak-Shelikof Subregion, South-Central Alaska, In *Hydrologic Investigations Atlas HA-612*. U.S. Geological Survey.

Kadko, D. & Muench, R. (2005). Evaluation of shelf-basin interaction in the western Arctic by use of short-lived radium isotopes: The importance of mesoscale processes. *Deep Sea Research Part II: Topical Studies in Oceanography, 52* (24-26), 3227-3244. *https://doi.org/10.1016/j.dsr2.2005.10.008*

Key, R. M., Brewer, R. L., Stockwell, J. H., Guinasso Jr., N. L., & Schink, D. R. (1979). Some improved techniques for measuring radon and radium in marine sediments and in seawater. *Marine Chemistry*, *7*(3), 251-264. *https://doi.org/10.1016/0304-4203(79)90042-2*

Key, R. M., Stallard, R. F., Moore, W. S., & Sarmiento, J. L. (1985). Distribution and Flux of Ra-226 in the Amazon River Estuary, *Journal of Geophysical Research, 90,* 6995-7004.

Kipp, L. E., Charette, M. A., Moore, W. S., Henderson, P. B., & Rigor, I. G. (2018). Increased fluxes of shelf-derived materials to the central Arctic Ocean. *Science Advances, 4*(1), eaao1302. *https://doi.org/10.1126/sciadv.aao1302*

Kipp, L. E., Henderson, P. B., Wang, Z. A., & Charette, M. A. (2020). Deltaic and Estuarine Controls on Mackenzie River Solute Fluxes to the Arctic Ocean. *Estuaries and Coasts, 43,* 1992-2014. *https://doi.org/10.1007/s12237-020-00739-8*

Kipp, L. E., Kadko, D. C., Pickart, R. S., Henderson, P. B., Moore, W. S., & Charette, M. A. (2019). Shelf-Basin Interactions and Water Mass Residence Times in the Western Arctic Ocean: Insights Provided by Radium Isotopes. *Journal of Geophysical Research: Oceans, 124*(5), 3279-3297. *https://doi.org/10.1029/2019JC014988*

Kipp, L. E., Sanial, V., Henderson, P. B., van Beek, P., Reyss, J.-L., Hammond, D. E., Moore, W. S., Charette, M. A. (2018). Radium isotopes as tracers of hydrothermal inputs and neutrally buoyant plume dynamics in the deep ocean. *Marine Chemistry, 201,* 51 - 65. *https://doi.org/10.1016/j.marchem.2017.06.011*

Klunder, M. B., Bauch, D., Laan, P., de Baar, H. J. W., van Heuven, & S., Ober, S. (2012). Dissolved iron in the Arctic shelf seas and surface waters of the central Arctic Ocean: Impact of Arctic river water and ice-melt. *Journal of Geophysical Research, 117,* C01027. *http://doi.org/10.1029/2011JC007133*

Knott, J. M.; Lipscomb, S. W.; Lewis, T. W. (1986). Sediment transport characteristics of selected streams in the Susitna River Basin, Alaska, October 1983 to September 1984. In *U.S. Geological Survey, Open-File Report 86 - 424W*. U.S. Geological Survey.

Krest, J. M., Moore, W. S., Gardner, L. R., & Morris, J. T. (2000). Marsh nutrient export supplied by groundwater discharge: Evidence from radium measurements. *Global Biogeochemistry Cycles, 14,* 167-176. *https://doi.org/10.1029/1999GB001197*

Krest, J. M., Moore, W. S., & Rama. (1999). 226Ra and 228Ra in the mixing zones of the Mississippi and Atchafalaya Rivers: indicators of groundwater input. *Marine Chemistry, 64*(3)*,* 129-152. *https://doi.org/10.1016/S0304-4203(98)00070-X*

Ku, T-L. & Luo, S. (1994). New appraisal of Radium 226 as a large-scale oceanic mixing tracer. *Journal of Geophysical Research, 99* (C5), 10255-10273. *https://doi.org/10.1029/94JC00089*

Ku, T-L. & Luo, S. (2008). Ocean circulation/mixing studies with decay-series isotopes. In S. Krishnaswami, J. Kirk Cochran (Eds.), *Radioactivity in the Environment* (Vol. 13, pp. 307-344). Amsterdam, NL: Elsevier. *https://doi.org/10.1016/S1569-4860(07)00009-5*

Kummu, M. & Varis, O. (2007). Sediment-related impacts due to upstream reservoir trapping, the Lower Mekong River. *Geomorphology, 85*, 275-293.

Kwon, E. Y., Kim, G., Primeau, F., Moore, W. S., Cho, H.-M., DeVries, T., et al. (2014). Global estimate of submarine groundwater discharge based on an observationally constrained radium isotope model. *Geophysical Research Letters, 41*(23), 8438-8444. *https://doi.org/10.1002/2014GL061574*

Lammers, R. B., Shiklomanov, A. I., Vörösmarty, C. J., Fekete, B. M., & Peterson, B. J. (2001). Assessment of contemporary Arctic river runoff based on observational discharge records. *Journal of Geophysical Research, 106*(D4)*,* 3321-3334. *https://doi.org/10.1029/2000JD900444*

Lamontagne, S., Taylor, A. R., Herpich, D., & Hancock, G. J. (2015). Submarine groundwater discharge from the South Australian Limestone Coast region estimated using radium and salinity. *Journal of Environmental Radioactivity, 140*, 30-41. https://doi.org/10.1016/j.jenvrad.2014.10.013

Laraque, A., Castellanos, B., Steiger, J., Lòpez, J. L., Pandi, A., Rodriguez, M., et al. (2013). A comparison of the suspended and dissolved matter dynamics of two large inter-tropical rivers draining into the Atlantic Ocean: the Congo and the Orinoco. *Hydrological Processes, 27*(15), 2153 - 2170.

Lecher, A. L., Kessler, J., Sparrow, K., Kodovska, F. G.-T., Dimova, N., Murray, J. et al. (2016). Methane transport through submarine groundwater discharge to the North Pacific and Arctic Ocean at two Alaskan sites. *Limnology and Oceanography, 61,* S344-S355. *https://doi.org/10.1002/lno.10118*

Lecher, A. L., Chien, C.-T., & Paytan, A. (2016). Submarine groundwater discharge as a source of nutrients to the North Pacific and Arctic coastal ocean. *Marine Chemistry, 186,* 167-177. *https://doi.org/10.1016/j.marchem.2016.09.008*

Le Gland, G., Mémery, L., Aumont, O., & Resplandy, L. (2017). Improving the inverse modeling of a trace isotope: how precisely can radium-228 fluxes toward the ocean and submarine groundwater discharge be estimated. *Biogeosciences, 14,* 3171-3189. *https://doi.org/10.5194/bg-14-3171-2017*

Legeleux, F. & Reyss, J.-L. (1996). ^{228}Ra/^{226}Ra activity ratio in oceanic settling particles: implications regarding the use of barium as a proxy for paleoproductivity reconstruction. *Deep Sea Research I, 43* (11-12), 1857-1863.

Li, Y.-H., Mathieu, G., Biscaye, P., & Simpson, H. J. (1977). The Flux of 226Ra from Estuarine and Continental Shelf Sediments. *Earth and Planetary Science Letters, 37,* 237-241. *https://doi.org/10.1016/0012-821X(77)90168-6*

Li, Y.-H. & Chan, L.-H. (1979). Desorption of Ba and 226Ra from River-Borne Sediments in the Hudson Estuary. *Earth and Planetary Science Letters, 43,* 343-350. *https://doi.org/10.1016/0012-821X(79)90089-X*

Li, Q., Qiao, S., Shi, X., Hu, L., Bai, Y., Zhu, A., & Cui, J. (2020). Sediment provenance of the East Siberian Arctic shelf: evidence from clay minerals and chemical elements. *EGU General Assembly 2020*, Online, EGU2020-8181. *https://doi.org/10.5194/egusphere-egu2020-8181*

Lima, J. E. F. W., Santos, P. M. C., Carvalho, N. O. & Silva, E. M. (2003). Diagnóstico do fluxo de sedimentos em suspensão na Bacia Araguaia-Tocantins. Embrapa Cerrados/ANEEL/ANA, Brasília, Brazil.

Linhoff, B., Charette, M., Wadham, J. (2020). Rapid mineral surface weathering beneath the Greenland Ice Sheet shown by radium and uranium isotopes. *Chemical Geology, 547*(5), 119663. *https://doi.org/10.1016/j.chemgeo.2020.119663*

Liu, Y., Jiao, J. J., Mao, R., Luo, X., Liang, W., & Robinson, C. (2019). Spatial Characteristics Reveal the Reactive Transport of Radium Isotopes (224Ra, 223Ra, and 228Ra) in an Intertidal Aquifer. *Water Resources Research, 55* (12), 10282-10302. *https://doi.org/10.1029/2019WR024849*

Luek, J. L. & Beck, A. J. (2014). Radium Budget of the York River estuary (VA, USA) dominated by submarine groundwater discharge with a seasonally variable groundwater end-member. *Marine Chemistry, 165,* 55-65. *https://doi.org/10.1016/j.marchem.2014.08.001*

Luo, X., Jiao, J. J., Liu, Y., Zhang, X., Liang, W., & Tang, D. (2018). Evaluation of Water Residence Time, Submarine Groundwater Discharge, and Maximum New Production Supported by Groundwater Borne Nutrients in a Coastal Upwelling Shelf System. *Journal of Geophysical Research: Oceans, 123* (1), 631-655. *https://doi.org/10.1002/2017JC013398*

Martinez, J. M., Guyot, J. L., Filizola, N., & Sondag, F. (2009). Increase in suspended sediment discharge of the Amazon River assessed by monitoring network and satellite data. *Catena, 79*, 257 - 264.

McClelland, J. W., Holmes, R. M., Dunton, K. H., & Macdonald, R. W. (2012). The Arctic Ocean Estuary. *Estuaries and Coasts, 35*, 353-368. *https://doi.org/10.1007/s12237-010-9357-3*

McClelland, J. W., Holmes, R. M., Peterson, B. J., Raymond, P. A., Striegl, R. G., Zhulidov, A. V. et al. (2016). Particulate organic carbon and nitrogen export from major Arctic rivers. *Global Biogeochemical Cycles, 30* (5), 629-643. *https://doi.org/10.1002/2015GB005351*

Meybeck, M., & Ragu, A. (2012). GEMS-GLORI world river discharge database. *Laboratoire de Géologie Appliquée, Université Pierre et Marie Curie, Paris, France, PANGAEA*. *https://doi.org/10.1594/PANGAEA.804574*

Middag, R., de Baar, H. J. W., Laan, P., & Klunder, M. B. (2011). Fluvial and hydrothermal input of manganese into the Arctic Ocean. *Geochimica et Cosmochimica Acta, 75,* 2393-2408. *http://doi.org/10.1016/j.gca.2011.02.011*

Moore, W. S. (2003). Sources and fluxes of submarine groundwater discharge delineated by radium isotopes. *Biogeochemistry, 66,* 75-93.

Moore, W. S. (2008). Fifteen years experience in measuring 224Ra and 223Ra by delayed-coincidence counting. *Marine Chemistry, 109*(3-4), 188-197. *https://doi.org/10.1016/j.marchem.2007.06.015*

Moore, W. S., Blanton, J. O., & Joye, S. (2006). Estimates of Flushing Times, Submarine Groundwater Discharge, and Nutrient Fluxes to Okatee River, South Carolina. *Journal of Geophysical Research: Oceans, 111. https://doi.org/10.1029/2005JC003041*

Moore, W. D. & de Oliveira, J. (2008). Determination of residence time and mixing processes of the Ubatuba, Brazil, inner shelf waters using natural Ra isotopes. *Estuarine, Coastal, and Shelf Science, 76* (3),512-521. *https://doi.org/10.1016/j.ecss.2007.07.042*

Moore, W. S., & Edmond, J. L. (1984). Radium and barium in the Amazon River system. *Journal of Geophysical Research, 89*(C2), 2061-2065. *https://doi.org/10.1029/JC089iC02p02061*

Moore, W. S., & Krest, J. (2004). Distribution of 223Ra and 224Ra in the plumes of the Mississippi and Atchafalaya rivers and the Gulf of Mexico. *Marine Chemistry*, *86*(3–4), 105–119. https://doi.org/10.1016/j.marchem.2003.10.001

Moore, W. S., Krest, J., Taylor, G., Roggenstein, E., Joye, S., & Lee, R. (2002). Thermal evidence of water exchange through a coastal aquifer: Implications for nutrient fluxes. *Geophysical Research Letters, 29. https://doi.org/10.1029/2002GL014923*

Moore, W. S., Sarmiento, J. L., & Key, R. M. (1986). Tracing the Amazon Component of Surface Atlantic Water Using 228Ra, Salinity and Silica. *Journal of Geophysical Research, 91*(C2)*,* 2574-2580. *https://doi.org/10.1029/JC091iC02p02574*

Moore, W. S., Sarmiento, J. L., & Key, R. M. (2008). Submarine groundwater discharge revealed by ^{228}Ra distribution in the upper Atlantic Ocean. *Nature Geoscience, 1*, 309-311. *https://doi.org/10.1038/ngeo183*

Moore, W. S. & Shaw, T. J. (1998). Chemical signals from submarine fluid advection onto continental shelf. *Journal of Geophysical Research: Oceans, 103*(C10), 21543-21552. *https://doi.org/10.1029/98JC02232*

Moore, W. & Shaw, T. (2008). Fluxes and Behavior of Radium Isotopes, Barium, and Uranium in Seven Southeastern US Rivers and Estuaries. *Marine Chemistry*, *108*(3–4), 236–254. *https://doi.org/10.1016/j.marchem.2007.03.004*

Moore, W. S., & Todd, J. F., (1993). Radium isotopes in the Orinoco estuary and eastern Caribbean Sea. *Journal of Geophysical Research: Oceans, 98*(C2), 2233-2244. *https://doi.org/10.1029/92JC02760*

Moore, W. S., & Wilson, A. M. (2005). Advective flow through the upper continental shelf driven by storms, buoyancy, and submarine groundwater discharge. *Earth and Planetary Sciences Letters, 235,* 564-576. *https://doi.org/10.1016/j.epsl.2005.04.043*

Moragoda, N., & Cohen, S. (2020). Climate-induced trends in global riverine water discharge and suspended sediment dynamics in the 21st century. *Global and Planetary Change, 191,* 103199. *https://doi.org/10.1016/j.gloplacha.2020.103199*

Nielson, B. T., Cardenas, M. B., O'Connor, M. T., Rasmussen, M. T., King, T. V., & Kling, G. W. (2018). Groundwater Flow and Exchange Across the Land Surface Explain Carbon Export Patterns in Continuous Permafrost Watersheds. *Geophysical Research Letters, 45*(15), 7596-7605. *https://doi.org/10.1029/2018GL078140*

Peterson, R. N., Burnett, W. C., Opsahl, S. P., Santos, I. R., Misra, S., & Froelich, P. N. (2013). Tracking suspended particle transport via radium isotopes (^{226}Ra and ^{228}Ra) through the Apalachicola-Chattahoochee-Flint River system. *Journal of Environmental Radioactivity, 116,* 65-75. *https://doi.org/10.1016/j.jenvrad.2012.09.001*

Purkl, S. & Eisenhauer, A. (2004). Determination of radium isotopes and Rn-222 in a groundwater affected coastal area of the Baltic Sea and the underlying sub-sea floor aquifer. *Marine Chemistry, 87,* 137-149. *https://doi.org/10.1016/j.marchem.2004.02.005*

Rainville, L., & Woodgate, R. A. (2009). Observations of internal wave generation in the seasonally ice-free Arctic. *Geophysical Research Letters, 36,* L23604. *https://doi.org/10.1029/2009GL041291*

Rama and Moore, W.S. (1996). Using the radium quartet for evaluating groundwater input and water exchange in salt marshes, *Geochimica et Cosmochimica Acta, 60*, 4645-4652.

Rawlins, M. A., Steele, M., Holland, M. M., Adam, J. C., Cherry, J. E., Francis, J. A., et al. (2010) Analysis of the Arctic System for Freshwater Cycle Intensification: Observations and Expectations. *Journal of Climate*, *23*(21), 5715-5737. *https://doi.org/10.1175/2010JCLI3421.1*

Robinson, R. A. J., Bird, M. I., Oo, N. W., Hoey, T. B., Aye, M. M., Higgitt, D. L., et al. (2007). The Irrawaddy River Sediment Flux to the Indian Ocean: The Original Nineteenth-Centry Data Revisited. *Journal of Geology, 115,* 629-640.

Rudels, B., Korhonen, M., Schauer, U., Pisarev, S., Rabe, B., Wisotzki, A. (2015). Circulation and transformation of Atlantic water in the Eurasian Basin and the contribution of the Fram Strait inflow branch to the Arctic Ocean heat budget. *Progress in Oceanography, 132,* 128-152. *https://doi.org/10.1016/j.pocean.2014.04.003*

Rutgers van der Loeff, M., Key, R. M., Scholten, J., Bauch, D., & Michel, A. (1995) 228Ra as a tracer for shelf water in the Arctic Ocean. *Deep Sea Research Part II: Topical Studies in Oceanography, 42*(6), 1533-1553. *https://doi.org/10.1016/0967-0645(95)00053-4*

Rutgers van der Loeff, M., Kühne, S., Wahsner, M., Höltzer, H., Frank, M., Ekwurzel, B., et al. (2003) 228Ra and 226Ra in the Kara and Laptev seas. *Continental Shelf Research, 23*(1)*,* 113-124. *https://doi.org/10.1016/S0278-4343(02)00169-3*

Rutgers van der Loeff, M., Kipp, L. E., Charette, M. A., Moore, W. S., Black, E., Ingrid, S., et al. (2018). Radium Isotopes Across the Arctic Ocean Show Time Scales of Water Mass Ventilation and Increasing Shelf Inputs. *Journal of Geophysical Research: Oceans, 12*3, 4853-4873. *https://doi.org/10.1029/2018JC013888*

Sanial, V., Moore, W. S., & Shiller, A. M. (2021). Does a bottom-up mechanism promote hypoxia in the Mississippi Bight? *Marine Chemistry, 235*, 104007. *https://doi.org/10.1016/j.marchem.2021.104007*

Sérodes, J.-B., & Roy, J.-C. (1983). Distribution of some radionuclides in the St. Lawrence estuary, Quebec, Canada. *Oceanologica Acta, 6*(2), 185-192.

Serreze, M. C., Barret, A. P., Slater, A. G., Woodgate, R. A., Aagaard, K., Lammers, R. B., et al. (2006). The large-scale freshwater cycle of the Arctic. *Journal of Geophysical Research, 111,* C11010. *https://doi.org/10.1029/2005JC003424*

Smith, J. N., Moran, S. B., & Macdonald, R. W. (2003). Shelf-basin interactions in the Arctic Ocean based on ^{210}Pb and Ra isotope tracer distributions. *Deep Sea Research Part 1: Oceanographic Research Papers, 50*(3), 397-416. *https://doi.org/10.1016/S0967-0637(02)00166-8*

Solin, G. L. (1996). Overview of Surface-Water Resources at the U.S. Coast Guard Support Center Kodiak, Alaska, 1987 - 1989. In *U.S. Geological Survey, Open-File Report 96-463*. U.S. Geological Survey.

Suzuki, T., Yamazaki, D., Tsujino, H., Komuro, Y., Nakano, H., & Urakawa, S. (2018). A dataset of continental river discharge based on JRA-55 for use in a global ocean circulation model. *Journal of Oceanography, 74,* 421-429. *https://doi.org/10.1007/s10872-017-0458-5*

Swarzenski, P. W., Orem, W. H., McPherson, B. F., Baskam, M., & Wan, Y. (2006). Biochemical transport in the Loxahatchee River estuary, Florida: The role of submarine groundwater discharge. *Marine Chemistry, 101,* 248-265. *https://doi.org/10.1016/j.marchem.2006.03.007*

Swarzenski, P. W., Reich, C. D., Kroeger, K. D., & Baskaran, M. (2007). Ra and Rn isotopes as natural tracers of submarine groundwater discharge in Tampa Bay, Florida. *Marine Chemistry, 104,* 64-84. *https://doi.org/10.1016/j.marchem.2006.08.001*

Syvitski, J. P. M. (2002). Sediment discharge variability in Arctic rivers: implications for a warmer future. *Polar Research, 21*(2), 323-330. *https://doi.org/10.3402/polar.v21i2.6494*

, J., Du, J., Moore, W. S., Zhang, G., Su, N., & Zhang, J. (2013). Nutrient inputs to a Lagoon through submarine groundwater discharge: The case of Laoye Lagoon, Hainan, China. *Journal of Marine Systems, 111-112*, 253-262. *https://doi.org/10.1016/j.jmarsys.2012.11.007*

Tomasky-Holmes, G., Valiela, I., & Charette, M. A. (2013). Determination of water mass ages using radium isotopes as tracers: Implications for phytoplankton dynamics in estuaries. *Marine Chemistry, 156,* 18-26. https://doi.org/10.1016/j.marchem.2013.02.002

U.S. Geological Survey, 2016, National Water Information System data Retrieved on July 17, 2020 from USGS Water Data for the Nation.
https://waterdata.usgs.gov/nwis/inventory/?site_no=15281000

https://waterdata.usgs.gov/nwis/uv?site_no=15284000

van Vliet, M. T. H., Wilberg, D., Leduc, S., & Riahi, K. (2013). Power-generation system vulnerability and adaptation to changes in climate and water resources. *Nature Climate Change Letters, 6,* 375-381. http://doi.org/10.1038/nclimate2903

Vieira, L. H., Achterberg, E. P., Scholten, J., Beck, A. J., Liebetrau, V., Mills, M. M., & Arrigo, K. R. (2019). Benthic fluxes of trace metals in the Chukchi Sea and their transport into the Arctic Ocean. *Marine Chemistry, 208,* 43-55. https://doi.org/10.1016/j.marchem.2018.11.001

Viscosi-Shirley, C., Mammone, K., Pisias, N., & Dymond, J. (2003). Clay mineralogy and multi-element chemistry of surface sediments on the Siberian-Arctic shelf: implications for sediment provenance and grain size sorting. *Continental Shelf Research, 23*(11-13). 1175-1200. https://doi.org/10.1016/S0278-4343(03)00091-8

Walling, D. E. (2008). The changing sediment load to the Mekong River. *AMBIO, 37,* 150-157.

Wang, X., Li, H., Jiao, J. J., Barry, D. A., Li, L., Luo, L. et al. (2015). Submarine fresh groundwater discharge into Laizhou Bay comparable to the Yellow River flux. *Scientific Reports, 5,* 8813. https://doi.org/10.1038/srep08814

Water Survey of Canada (2020). Back, Ellice, Hornaday, Firth, Omoloy, and Babbage River Records. Retrieved on July 17, 2020 from Environment and Climate Change Canada Historical Hydrometric Data web site. https://wateroffice.ec.gc.ca/mainmenu/historical_data_index_e.html

Webster, I. T., Hancock, G. J., & Murray, A. S. (1995). Modelling the effect of salinity on radium desorption from sediments. *Geochimica et Cosmochimica Acta, 59*(12)*,* 2469-2476. https://doi.org/10.1016/0016-7037(95)00141-7

Wheeler, P. A., Watkins, J. M., & Hansing, R. L. (1997) Nutrients, organic carbon and organic nitrogen in the upper water column of the Arctic Ocean: implications for the sources of dissolved organic carbon. *Deep Sea Research Part II Topical Studies in Oceanography, 44*(8), 1571-1592. https://doi.org/10.1016/s0967-0645(97)00051-9

Williams, W. J., & Carmack, E. C. (2015). The ‘interior’ shelves of the Arctic Ocean: Physical oceanographic setting, climatology and effects of sea-ice retreat on cross-shelf exchange. *Progress in Oceanography. 139,* 24-41. https://doi.org/10.1016/j.pocean.2015.07.008

Windham, H. L., Niencheski, L. F., Moore, W. S., & Jahnke, R. (2006). Submarine Groundwater Discharge: a Large, Previously Unrecognized Source of Dissolved Iron to the South Atlantic Ocean. *Marine Chemistry, 102,* 252-266. https://doi.org/10.1016/j.marchem.2006.06.016

Woodgate, R. A., Weingartner, T. J., & Lindsay, R. (2012). Observed increases in Bering Strait oceanic fluxes from the Pacific to the Arctic from 2001 to 2011 and their impacts on the Arctic

Ocean water column. *Geophysical Research Letters, 39* (24). *https://doi.org/10.1029/2012GL054092*

Xu B., Li, S., Burnett, W. C., Zhao, S., Santos, I., Lian, E., Chen, X., Yu, Z. (2022). Radium-226 in the global ocean as a tracer of the thermohaline circulation: Synthesizing half a century of observations. *Earth Science Reviews, 226,* 103956. *https://doi.org/10.1016/j.earscirev.2022.103956*

Young, M. B., Gonneea, M. E., Fong, D. A., Moore, W. S., Herrera-Silveira, J., Paytan, A. Characterizing sources of groundwater to a tropical coastal lagoon in a karstic area using radium isotopes and water chemistry. *Marine Chemistry, 109* (3-4), 377-394. *https://doi.org/10.1016/j.marchem.2007.07.010*

Yunker, M. B., Backus, S. M., Pannatier, E. G., Jeffries, D. S., & Macdonald, R. W. (2002) Sources and Significance of Alkane and PAH Hydrocarbons in Canadian Arctic Rivers. *Estuarine, Coastal, and Shelf Science, 55*, 1-31. *https://doi.org/10.1006/ecss.2001.0880*

Supplementary Information for Chapter 2

Introduction

This supplementary information provides details on the literature background used to estimate river water and sediment discharges. It provides greater detail and numerical values for individual rivers where radium (Ra) fluxes were calculated. It also clarifies the calculations used for our global riverine Ra flux, since they were similar enough to our Arctic calculations and so that they were not included in the main body of the article. Elaboration on the methods used for the desorption experiments and they process by which they were determined are also included.

S1. Arctic Rivers Water Discharge

There has been a large body of work devoted to pan-Arctic river discharge. One of the most comprehensive summaries comes from Lammers et al. (2001), in which the authors used discharge data from the Regional, Electronic, Hydrographic Data Network For the Arctic Region (R-ArcticNET). This digital databank includes data between the mid-1900s and 1990 from 3754 Arctic gaging stations, covering 73% of its non-glaciated area (168 gages per 10^6 km). It is compiled from a variety of government monitoring sources, including the United States Geological Survey (USGS), HYDAT - Environment Canada, the former Department for River Runoff and Water Management Problems in the State Hydrological Institute in Russia, and the Global Water and Water Use Archive for the remaining Eurasian countries. However, there are discrepancies in the coverage of different drainage basins. For example, the Beaufort and Laptev Seas have almost 90% of their drainage basins covered, followed by the Barents and Kara Seas at 75%; conversely, the CAA and the Chukchi Sea are only 17% and 24% covered, respectively (Lammers et al. 2001). More recent studies include better coverage of the North American rivers: Déry et al. (2016) focused specifically on river discharge from Canada, utilizing the Water Survey of Canada data for 42 rivers. Their runoff values built on several other studies which reported similar mean discharge values (Benke and Cushing, 2005; Milliman and Farnsworth, 2011). Discharge values can be seen in Table S1.

Table S1. Annual Arctic rivers' water discharge and sediment loads.

River	Discharge (10^{10} m^3/y)	Sources	Sediment Load (tons/y)	Sources
Yenisey	62	Guay and Falkner, 1998; Syvitski, 2002; Holmes et al. 2012	4.70E+06	Holmes et al. 2002
Lena	54.4		2.07E+07	
Ob	42.5		1.55E+07	
Mackenzie	28.7		1.24E+08	Carson et al. 1998; Gordeev, 2006
Yukon	20.3		6.00E+07	Holmes et al. 2002
Pechora	12.0		9.40E+06	
Kolyma	11.2		1.01E+07	
Severnaya Dvina	10.8		4.10E+06	

Indigirka	5.51	Guay and Falkner, 1998; Syvitski, 2002; Holmes et al. 2012	1.11E+07	Holmes et al. 2002
Taz	3.86	Syvitski, 2002; Holmes et al. 2002	7.00E+05	Holmes et al. 2002
Olenek	3.37		1.10E+06	
Pur	3.12		7.00E+05	
Yana	3.04		4.00E+06	
Mezen	2.38		6.00E+05	
A la Baleine	1.82	Meybeck & Ragu, 2012	4.62E+05	Meybeck & Ragu, 2012
Colville	1.60	Syvitski, 2002; Holmes et al. 2002	4.95E+06	Holmes et al. 2002
Onega	1.57		3.00E+05	
Back	1.55	Déry et al. 2016; Water Survey of Canada	9.31E+04	Water Survey of Canada
Anabar	1.53	Syvitski, 2002; Holmes et al. 2002	4.00E+05	Holmes et al. 2002
Susitna	0.92	USGS	2.92E+07	Knott et al. 1986; Brabets et al. 1999
Coppermine	0.88	Déry et al. 2016	2.32E+05	Yunker et al. 2002
Knik	0.76	USGS	7.50E+06	Knott et al. 1986; Brabets et al. 1999
Alezeya	0.52	Syvitski, 2002; Holmes et al. 2002	1.00E+05	Holmes et al. 2002
Burnside	0.42	Déry et al. 2016	3.91E+03	Déry et al. 2016
Hayes	0.41	Yunker et al. 2002	3.77E+04	Yunker et al. 2002
Matanuska	0.35	USGS	6.60E+06	Knott et al. 1987; Brabets et al. 1999
Ellice	0.28	Déry et al. 2016; Water Survey of Canada	2.37E+04	Déry et al. 2016;
Hornaday	0.24	Water Survey of Canada	2.08E+06	Forbes, 1981
Firth	0.21	Déry et al. 2016; Water Survey of Canada	2.70E+04	Water Survey of Canada
Omoloy	0.11		4.00E+04	Holmes et al. 2002
Babbage	3.5E-2	Water Survey of Canada	3.00E+05	Forbes, 1981
Buskin	1.1E-2	Solin, 1996	4.47E+02	Jones et al. 1978

S2. Riverine Suspended Sediment

S2.1 Arctic Rivers: Overview

Before the early 2000s, there was significant confusion and discrepancies in reported fluvial sediment fluxes to the Arctic Ocean. These early studies were confounded by several factors, including watershed development between sampling, insufficient sampling to account for the large annual variability in sediment fluxes, incorrect reporting, and seasonality of inputs (Holmes et al. 2002). There were also several different organizations monitoring Arctic rivers: the Russian Federal Service for Hydrometeorology and Environmental Monitoring (Roshydromet), Environment Canada, the HYDAT database (Water Survey of Canada), and the WATSTORE database of the National Water Data Exchange (NAWDEX, USGS) (Milliman and

Syvitski, 1992; Gordeev et al. 1996; Syvitski et al. 2000; Syvitski 2001; Holmes et al. 2002; Gordeev and Rachold, 2003; Gordeev, 2006). All of these organizations had different methods and coverage in sampling Arctic river sediment concentrations (see section S2.2).

An effort was made in the late 1990s/early 2000s to consolidate these datasets and make them comparable to each other. Holmes et al. (2002) did this for 19 arctic rivers, with an emphasis on the largest 8 rivers. Another comprehensive review by Gordeev (2006) added on to this work by combining their data with studies of other rivers done in the late 90s (Gordeev et al. 1996). There was also the creation of the GEMS/WATER Global Register of River Inputs (GEMS-GLORI) in 1997 (Meybeck and Ragu, 1997) which consolidated disparate river discharge and input records for 555 major world rivers. Additionally, several groups began to utilize existing geological and environmental data to model sediment fluxes for regions or environmental conditions that have not been sampled (see section S2.3), increasing our understanding of how different factors impact a river's sediment load (Milliman and Syvitski, 1992; Syvitski et al. 2000; Syvitski, 2001; Morehead et al. 2003; Overeem and Syvitski, 2008; Moragoda and Cohen, 2020).

S2.2 Arctic Rivers: Historical Suspended Sediment Sampling

Numerous organizations have been responsible for monitoring sediment concentrations in Arctic rivers: the Russian Federal Service for Hydrometeorology and Environmental Monitoring (Roshydromet), Environment Canada, the HYDAT database (Water Survey of Canada), and the WATSTORE database of the National Water Data Exchange (NAWDEX, USGS) (Milliman and Syvitski, 1992; Gordeev et al. 1996; Syvitski et al. 2000; Syvitski 2001; Holmes et al. 2002; Gordeev and Rachold, 2003; Gordeev, 2006). These organizations employed varying methods for measuring sediment (Holmes et al. 2002; Gordeev, 2006). Rivers monitored by Roshydromet began recording data between 1935 and 1966. Samples were collected at a specific depth during low flow, with twice daily collection at high flow. When SS concentrations were less than 100 g/m^3 then two samples are combined and processed together. When SS concentrations were less than 50 g/m^3, single samples collected over 5-10 days are combined and processed together. If SS concentrations less than < 5 g/m^3 lasted for a longer period of time, sampling was stopped until water discharge increased. Environment Canada began measurements in the 1970s, reporting depth integrated values taken from a single vertical river cross section where flow and depth were maximum. Occasionally surface samples were also taken and usually matched the depth integrated samples within 20%. Rivers were sampled primarily between May and October, while winter values were recorded only once or twice annually due to ice coverage. The USGS used a similar methodology to Environment Canada, but recorded data much more sparsely (~70 measurements taken on Yukon river between 1975 and 1996).

S2.3 Arctic Rivers: Modeling Suspended Sediment

On top of the compilation of existing data, there were also several studies published which attempted to use models to predict sediment fluxes. These models used existing data to elucidate the relationships between geological and environmental factors and riverine discharge and sediment load (Milliman and Syvitski, 1992; Syvitski et al. 2000; Syvitski, 2001; Morehead et al. 2003; Overeem and Syvitski, 2008; Moragoda and Cohen, 2020). The models generally used large sets of previously reported data. Syvitski et al. (2000) especially tried to impose strict quality controls on the rivers used to develop their model, based on long-term averaged discharge values, SS load, flow duration and peakedness, temperature (average and mean), drainage area, and the basin relief. All models had similar parameters: basin area, maximum headwater elevation, measured sediment loads from different geographic regions, basin topographical relief (Milliman and Syvitski, 1992; Syvitski et al. 2000; Syvitski et al. 2001; Morehead et al. 2003 Overeem and Syvitski, 2008). Other parameters, such as percentage of underlying permafrost, drainage basin temperature, level of glaciation, and vegetation were used to a lesser extent. Precipitation was almost never used, due to the notorious lack of correlation between precipitation and sediment load (review: Walling and Webb, 1986; Milliman and Syvitski, 1992). All sediment load values can be seen in Table S1.

S3. Radium Inputs from Arctic Rivers

A breakdown of each river that was calculated as an individual river can be seen in Table S2. The major river with Ra data available is located in the leftmost column. Rivers whose Ra concentrations were assumed to be the same as a major river are located below the corresponding major river. The seasonal differences between the Ob, Lena, and Yenisey River inputs are shown in Table S3. In all cases, winter inputs are larger than summer inputs, when removal processes dominate.

Reported errors on scaled up fluxes are the result of analytical error and an estimated range assumed within basins for unaccounted for water and sediment Ra inputs. The assumed range within basins was calculated from two basins which had multiple rivers sampled for radium. For Eurasia, the Kara Sea discharge basin was used, containing the Yenisey and Ob rivers, with standard deviations of 15 dpm ^{226}Ra 100L^{-1}, 0.25 dpm ^{226}Ra g^{-1}, 19.2 dpm ^{228}Ra 100L^{-1}, and 0.61 dpm ^{226}Ra g^{-1}. For North America, the Bering Strait discharge basin was used, containing the Yukon and the Southern Alaskan rivers, with standard deviations of 8.1 dpm ^{226}Ra 100L^{-1}, 0.25 dpm ^{226}Ra g^{-1}, 11.1 dpm ^{228}Ra 100L^{-1}, and 0.61 dpm ^{226}Ra g^{-1}. All discharge from rivers not sampled for Ra had these additional errors added to account for natural variations within discharge basins.

Table S2. Estimated annual independent river Ra fluxes to Arctic Ocean.

River		Estimated Ra Flux to Arctic Ocean (10^{10} dpm/y)			
		^{226}Ra	error	^{228}Ra	error
Yenisey		3003	340	7219	1080
	Taz	193	22	457	69
Lena		5203	222	10812	1043
	Yana	317	14	639	65
	Olenek	321	14	668	64
	Anabar	145	6	302	29
	Omoloy	10.5	0.4	22	2
Ob		6311	219	9626	1083
	Pechora	1845	67	2800	323
	Severnaya Dvina	1606	56	2449	276
	Pur	458	16	700	78
	Mezen	350	12	535	60
	Onega	230	8	351	39
Kolyma		608	66	626	170

	Indigirka	458	45	516	127
	Alezeya	19	2	15	5
Mackenzie		10813	824	16544	3393
	Firth	38	1	38	3
	Hornaday	139	13	236	54
	Babbage	20	2	34	8
Yukon		5733	445	9601	1867
Yukon & Mackenzie					
	Colville	486	50	758	208
Ellice		5	1	24	5
	Coppermine	24	4	90	19
	Burnside	6	1	33	7
	Back	27	5	128	26
St. Lawrence					
	Hayes	12	1	25	2
Ellice & St. Lawrence					
	A la Baleine	55	10	161	42
Kodiak					
	Buskin	0.19	0.02	0.41	0.10
	Knik	167	24	93	12
	Matanuska	54	15	74	10
	Susitna	343	75	356	37

Table S3. Seasonal differences in Eurasian river inputs.

River		Estimated Ra Flux to Arctic Ocean (10^{10} dpm/y)			
		^{226}Ra	error	^{228}Ra	error
Yenisey Total:		3003	340	7219	1080
	Summer	947	108	2623	390
	Winter	2056	232	4596	690
Lena Total:		5203	222	10812	1043
	Summer	2444	129	5682	815
	Winter	2759	93	5130	228
Ob Total		6311	219	9626	1083
	Summer	548	82	1030	276
	Winter	5763	137	8597	807

S4. Radium Inputs from Global Rivers

Our global model was focused on the 13 largest rivers by discharge located outside the Arctic. We utilized Suzuki et al. (2018) for global riverine fluxes based on receiving ocean basin in order to scale up our estimates. In order to get coverage for as many basins as possible, three minor rivers were added to our model: the Kalix, the Rhone, and the Var, in order to obtain data points for the Baltic Sea and the Mediterranean Sea. Hudson Bay inputs are approximated from Ra values in the St. Lawrence River (Sérodes & Roy, 1983) and the Ellice River (this study). Where possible, discharge and sediment loads were obtained from recent studies (Table S4).

Table S4. Annual rivers' water discharge and sediment loads for rivers outside of Arctic with Ra data.

River	Discharge (10^{10} m^3/y)	Sources	Sediment Load (tons/y)	Sources
Amazon	676	Suzuki et al. 2018	7.78×10^8	Martinez et al. 2009
Congo	126		3.20×10^7	Laraque et al. 2013
Orinoco	116		7.60×10^7	Laraque et al. 2013
Brahmaputra and Ganges	105		1.08×10^9	Garzanti et al. 2011
Changjiang	93.0		4.77×10^8	Chen et al. 2001
Parana and Uruguay	91.4		1.06×10^8	Isupova and Mikhailov, 2018
Mississippi	65.8		5.10×10^7	Allison et al. 2012
Mekong	57.7		7.50×10^7	Kummu and Varis, 2007; Walling, 2008
Araguaia-Tocantins	48.7		3.06×10^6	Lima et al. 2003
Irrawaddy	41.0		3.33×10^8	Robinson et al. 2007
St. Lawrence	38.0		2.29×10^6	Rondeau et al. 2000
Amur	33.1		2.00×10^7	Chalov et al. 2018
Pearl (Zhujiang)	28.6		3.87×10^7	Lai et al. 2016
Non-Major Rivers				
Kalix	0.76	Porcelli et al. 2001	1.82×10^4	Pontér et al. 1992
Rhone	5.36	Ollivier et al. 2008	7.04×10^2	Ollivier et al. 2008
Var	0.16	Potot, C. 2011	6.63×10^5	Mulder et al. 1998

When data was available, freshwater dissolved Ra concentrations and discharge were used to calculate the annual Ra dissolved load and desorption values and sediment loads were used to calculate the annual Ra desorbed load. Several rivers had total Ra on suspended sediment reported, but no desorption rates. In these cases, the theoretical value from Webster et al. (1995) was used (Table S5). Two rivers did not have completely freshwater values reported: the Mekong and the Xijiang. The Ra contributions for these rivers were calculated as a sum of dissolved and desorbed inputs, since the two could not be separated. The Congo River has no reported dissolved Ra values in the literature; however, barium has been measured in the Congo. Using the global average river ratio between Ba: ^{226}Ra and Ba:^{228}Ra, we estimated the likely Ra concentrations in the Congo. Finally, there were three major rivers that have not been sampled, but have nearby rivers with Ra data available: the Araguaia-Tocantins, the Irrawaddy, and the Amur Rivers. Since their watersheds share similar geologies and characteristics to their nearby neighbors, the values of the nearby rivers were assumed to be close approximations to the major rivers' actual Ra concentrations.

Table S5. Dissolved Ra concentrations, desorbed Ra data, or estimated combined (dissolved + desorbed) total Ra inputs for rivers outside of the Arctic with radium data.

River	Dissolved (dpm/100L)		Desorbed (dpm/g)		Source
	^{226}Ra	^{228}Ra	^{226}Ra	^{228}Ra	
Major Rivers					
Amazon	5.00 ± 0.12	7.40 ± 0.53	0.93 ± 0.24	1.40 ± 0.36	Key et al. 1985
Congo [a]	5.4 ± 2.7	8.2 ± 6.0	2.36 ± 0.26	0.92 ± 0.12	Abitu et al. 2021; Bridgestock et al. 2021
Orinoco	3.81 ± 0.46	6.30 ± 0.76	2.74 ± 0.27	5.97 ± 0.60	Moore and Todd, 1993
Brahmaputra and Ganges [b]	8.0 ± 0.8	14.0 ± 1.4	0.74 ± 0.07	1.45 ± 0.15	Sarin et al. 1990
Changjiang [b]	7.4 ± 0.7	15.8 ± 1.6	0.89 ± 0.09	2.43 ± 0.24	Su et al. 2015
Parana and Uruguay [b]	24.3 ± 2.4	92.6 ± 9.3	0.21 ± 0.2	0.62 ± 0.6	Dias et al. 2016
Mississippi	10.2 ± 1.0	12.3 ± 1.2	0.64 ± 0.05	0.74 ± 0.06	Krest, Moore, and Rama, 1999
Mekong [c]	12.8 ± 1.1	61.5 ± 2.5	–	–	Chen et al. 2010
Araguaia-Tocantins [d1]	5.00 ± 0.12	7.40 ± 0.52	0.93 ± 0.24	1.40 ± 0.36	
Irrawaddy [d2]	8.0 ± 0.8	14.0 ± 1.4	0.74 ± 0.07	1.45 ± 0.15	
St. Lawrence [b]	2.55 ± 0.26	5.11 ± 0.51	0.32 ± 0.03	0.98 ± 0.10	Sérodes and Roy, 1983
Amur [d3]	5.50 ± 0.55	12.5 ± 1.2	1.44 ± 0.14	2.22 ± 0.22	Yang et al. 2002
Pearl (Zhujiang) [c]	25 ± 1	86 ± 3	–	–	Dai et al. 2021
Minor Rivers					
Kalix	2.74 ± 0.72	3.80 ± 0.48	1.80 ± 0.18	3.57 ± 0.36	Porcelli et al. 2001
Rhone	10.8 ± 1.0	14.2 ± 2.7	1.36 ± 0.34	0.84 ± 0.21	Ollivier et al. 2008
Var	13.2 ± 2.13	16.2 ± 4.66	1.36 ± 0.34	0.84 ± 0.21	Potot, 2011

a) The Congo River had no dissolved radium data. Estimated from Barium ratios; b) Reported sediment Ra values used to estimate desorption based on Webster et al. 1995 model; c) Complications in estuary require a combined dissolved and desorbed approach because we cannot distinguish between them; d) Nearby river(s) used to approximate values – *d1*. Amazon River; *d2*. Brahmaputra and Ganges; *d3*. Nakdong and Chanjiang Rivers.

Our global estimate followed the same procedure as our Arctic estimate (2.3.1; Equation 1 and Equation 2). We scaled up Ra fluxes based on receiving ocean basin. Because suspended sediment loads are currently in a state of rapid change, we did not mathematically separate desorbed versus dissolved inputs when we scaled up to the full basin. Instead, we calculated the total annual Ra fluxes for our global rivers, then scaled up to the full basin based on unaccounted discharge. This introduces the assumption that suspended sediment concentrations in unsampled rivers are similar to those in major rivers, which may not always be the case. However, because of large uncertainties in sediment discharge rates, we believe this simplification is justified.

$$\boldsymbol{Ra_{Dis,i}} = \left(\boldsymbol{C_{fw,i}} \times \boldsymbol{D_i}\right) + \left(\boldsymbol{C_{d,i}} \times \boldsymbol{SS_i}\right) \qquad \text{(Equation 1)}$$

$Ra_{Dis,\,i}$ = total Ra inputs from river ‘i’ (dpm y^{-1})

$C_{fw,\,i}$ = dissolved Ra concentration in river ‘i’ (dpm m^{-3})

D_i = water discharge of river ‘i’ (m^3 y^{-1})

$C_{d,\,i}$ = desorption rate of Ra in river ‘i’ (dpm g^{-1})

SS_i = sediment load of river ‘i’ (g y^{-1})

$$\boldsymbol{Ra_{MS}} = \sum_i \boldsymbol{Ra_{Dis,i}} + \left[\mathbf{1} + \left(\frac{\boldsymbol{D_{Basin}} - \sum_i \boldsymbol{D_i}}{\boldsymbol{D_{Basin}}}\right)\right] \qquad \text{(Equation 2)}$$

Ra_{Basin} = estimated total annual Ra inputs to select ocean basin (dpm y^{-1})

D_{Basin} = total estimated riverine flux for select ocean basin (m^3 y^{-1})

Reported errors on scaled up fluxes are the result of analytical error and an estimated range assumed within basins for unaccounted for water and sediment Ra inputs. The assumed range within basins was calculated from the rivers draining into the Atlantic Ocean, since this is the most represented basin in the literature. The standard deviations from rivers draining into the Atlantic Ocean are 7.6 dpm ^{226}Ra 100L^{-1}, 1.0 dpm ^{226}Ra g^{-1}, 32 dpm ^{228}Ra 100L^{-1}, and 1.9 dpm ^{226}Ra g^{-1}. All discharge from rivers not sampled for Ra had these additional errors added to account for natural variations within discharge basins.

S5. Methods

S5.1 Sample Collection for Desorption Experiments

Suspended sediment was collected using a bilge pump to filter water before use for radium analysis. A Teledyne IR-20E cartridge filter (pore size - 10 µm) was used for the Kolyma River while all Alaskan river samples were filtered through a 1 µm Hytrex filter. The filters were sealed in plastic bags and kept refrigerated until desorption experiments were performed. Seawater for the desorption experiments was collected from Vineyard Sound (S = 32) and filtered for particulate matter (pore size - 0.2 µm) and radium (2 in-line Mn fibers; < 0.5 L/min).

Bottom sediment from the Kolyma River was collected in summer 2018 from the Northeast Science Station in Cherskiy between July 23 to August 3. River bed sediment was sampled using a Van Veen grab-sampler and a stainless steel spoon, and stored in Whirl-Pak® bags. These samples represent recently deposited sediment (i.e. with a large fraction of silt and clay) in more quietly flowing locations of the river and delta. Within 12 hours after collection, sediments were frozen (-20°C) and remained so during transport. Sediment was thawed and dried before desorption experiments were performed in January and February 2022.

S5.2 Preliminary Desorption Experiments

Coastal seawater from Vineyard Sound was collected and filtered by the Environmental Systems Laboratory in Woods Hole, MA. The filtered seawater was then passed through manganese-oxide coated fibers (2 packed holders, 10 g each) at a flow rate of 0.5 L min^{-1} in order to remove Ra from the water. The filtered seawater (S = 32.5) was added to clean plastic cubitainers (20L each) and chilled to 4-6°C.

Bottom sediment from the southern Alaskan rivers was dried at 60°C. For each experiment, 10 g of dried sediment was weighed and added to a liter of Ra-free freshwater, then filtered onto a 1 µm cartridge filter, in order to replicate the suspended sediment samples. A peristaltic pump then circulated the filtered seawater through the sediment loaded cartridge filter at a rate of 1.25 L min^{-1} for the duration of the desorption. A flow rate lower than 1.25 L min^{-1} was insufficient to remove air pockets from the cartridge holder and a flow rate higher than 1.25 L min^{-1} was high enough where tubing joints risked popping off. Desorptions were conducted for 3 hours, 6 hours, 8 hours, and 18 hours. Following the desorption, the seawater was filtered through Mn-coated acrylic fiber at a flow-rate ≤ 0.5 L min^{-1} for 3 hours, which were then immediately rinsed and run on RaDeCC counters. No more Ra was detected in the 8 and 18 hours desorptions than in the 6 hours desorption. The 3 hour desorption had the least amount of Ra detected. This led us to choose 6 hour desorptions for our experiments, meaning that our desorptions were longer than those performed by Gu et al. (2012) for Changjiang River sediment desorptions (2 - 3 hours) and shorter than the 24 hour desorptions established by the protocol in Krest et al. (1999).

S6. Submarine Groundwater Discharge

All submarine groundwater discharge (SGD) sites used to estimate the global mean and median ^{228}Ra and ^{226}Ra values and activity ratios (AR) are listed in Table S6, along with the dissolved Ra mean and median concentrations. Data can be located in the BCO-DMO repository (Charette & Moore, 2022).

Table S6. Submarine Groundwater Discharge Ra concentrations

Ocean	Site	Mean Conc. (dpm/L)		^{228}Ra/^{226}Ra AR		Sources
		^{226}Ra	^{228}Ra	mean	median	
Atlantic	Waquoit Bay, MA	0.90	3.64	4.03	3.68	Charette et al. 2001
	West Neck Bay, NY	0.12	0.58	4.79	3.88	Dulaiova et al. 2006; Moore et al. 2008
	Great South Bay, NY	1.07	2.40	2.25	2.09	Dulaiova et al. 2006; Moore et al. 2008
	Elizabeth River, VA	0.81	0.81	1.00	1.15	Charette & Bueseler, 2004
	Duck, NC	0.40	1.41	3.52	2.83	This Study
	Sunset Beach, NC & Folly Beach, SC	0.97	2.00	2.07	1.99	George et al. 2020; Moore et al. 2002; Moore & Wilson, 2005
	Charleston, SC	4.31	3.25	0.75	1.38	Moore & Wilson, 2005
	Myrtle Beach, SC	3.90	4.47	1.15	1.03	Moore et al. 2008
	North Inlet, SC	5.69	8.42	1.48	2.53	Krest et al. 2000, Moore et al. 2008
	Port Royal Sound, SC	1.31	0.98	0.75	0.96	Crotwell & Moore, 2003
	Hilton Head, SC	0.59	0.64	1.09	1.11	Crotwell & Moore, 2003
	Okatee, SC	3.20	10.28	3.21	3.29	Moore et al. 2006
	Ossabow, GA	2.58	3.45	1.34	2.37	Moore et al. 2008
	Sapelo, GA	10.65	7.79	0.73	0.80	Moore et al. 2008
	Apalachee Bay, FL	26.13	13.21	0.51	0.85	Moore, 2003
	Key Largo, FL	4.16	0.53	0.13	0.13	Moore et al. 2008
	West Coast, FL	14.36	1.76	0.12	0.12	Swarzenski et al. 2006; Moore, 2003; Swarzenski et al. 2007
	Mississippi Bight, MI	0.22	1.02	4.56	3.71	Sanial et al. 2021
	Neuces, TX	0.47	1.97	4.23	4.56	Breier et al. 2005
	Puerto Rico	0.13	0.10	0.76	0.93	Moore et al. 2008
	Praia de Piratininga, Brazil	0.43	2.71	6.31	8.82	Moore et al. 2008
	Ubatuba, Brazil	1.07	13.63	12.69	13.00	Moore & de Oliveira, 2008
	Patos Lagoon, Brazil	0.54	1.27	2.36	2.28	Moore et al. 2008; Windham et al. 2006
	Eckernforder Bay, Germany	0.38	0.76	2.00	2.17	Purkl & Eisenhauer, 2004
	Wadden Sea, Germany	1.04	4.72	4.54	5.49	Moore et al. 2008
	Venice Lagoon, Italy	1.61	4.92	3.06	2.81	Garcia-Solsona et al. 2008
	Celestun Lagoon, Yucatan	25.62	1.00	0.04	0.04	Young et al. 2008

	Alcalfar Cove, Minorca Island, W. Med.	0.36	0.20	0.56	0.74	Garcia-Solsona et al. 2010
Pacific	East China Sea	1.03	5.27	5.12	6.61	Tan et al. 2018
	South China Sea	0.73	3.18	4.36	7.42	Tan et al. 2018
	Jiulong estuary, China	2.50	6.80	2.72	2.20	Wang et al. 2015
	Sanggou Bay, China	3.37	4.97	1.47	1.76	Wang et al. 2015
	Layoe Lagoon, China	1.39	3.25	2.35	2.46	Tao et al. 2013
	Pearl River Delta, China	3.45	5.01	1.45	1.19	Luo et al. 2018
	Australia Limestone Coast	0.49	0.37	0.76	1.41	Lamontagne et al. 2014
	Gulf St. Vincent, Australia	1.53	2.97	1.94	3.06	Lamontagne et al. 2014
	Elkhorn Slough, CA	0.22	1.44	6.59	3.67	Breier et al. 2019
	Los Angeles Basin, CA	0.61	0.26	0.42	0.37	Swarzenski et al. 2013
	Adriatic Sea, Croatia	0.16	0.26	1.58	1.41	Liu et al. 2019
	Isimangaliso Wetland Park, South Africa	0.28	1.90	6.90	5.64	Moore et al. 2020
	Chili	1.00	0.71	0.71	0.19	This Study
	Guam	1.17	0.08	0.07	0.07	This Study
	Hawaii	0.08	0.15	1.83	1.75	This Study
	Shinsei Maru, Japan	0.23	0.35	1.52	3.46	This Study
	Fukushima, Japan (2013)	0.21	1.21	5.72	3.49	This Study
	Fukushima, Japan (2015)	0.24	1.34	5.52	6.48	This Study
Total Atlantic AR				2.70	2.22	
Total Pacific AR				2.83	2.33	
Global AR				2.74	2.28	

Chapter 3: Seasonality of Submarine Groundwater Discharge to an Arctic Coastal Lagoon Assessed with Radium Isotopes

Emma J. Bullock[1] (*ebullock@whoi.edu*), Isabel V. Schaal[1] (*ischaal@whoi.edu*), M. Bayani Cardenas[2] (*cardenas@jsg.utexas.edu*), James W. McClelland[3] (*jmcclelland@mbl.edu*), Paul Henderson[4] (*phenderson@whoi.edu*), Matthew A. Charette[4] (*mcharette@whoi.edu*)

1. MIT - WHOI Joint Program in Oceanography/Applied Ocean Science & Engineering, Cambridge and Woods Hole, MA, USA

2. Department of Geological Sciences, Jackson School of Geosciences, University of Texas at Austin, Austin, TX, USA

3. The Ecosystems Center, Marine Biological Laboratory, Woods Hole, MA, USA

4. Department of Marine Chemistry and Geochemistry, Woods Hole Oceanographic Institution, Woods Hole, MA, USA

Originally Published in 2024 in Limnology and Oceanography. Reproduced with permission.

Bullock, E. J., Schaal, I. V., Cardenas, M. B., McClelland, J. W., Henderson, P. B., Charette, M. A. (2024). Seasonality of submarine groundwater discharge to an Arctic coastal lagoon. *Limnology and Oceanography, 69* (6), 1429-1438.https://doi.org/10.1002/lno.12585

Abstract

Supra-permafrost submarine groundwater discharge (SGD) in the Arctic is potentially important for coastal biogeochemistry and will likely increase over the coming decades due to climate change. Despite this, land-to-ocean material fluxes via SGD in Arctic environments have seldom been quantified. This study used radium (Ra) isotopes to quantify SGD fluxes to an Arctic coastal lagoon (Simpson Lagoon, Alaska) during 5 sampling periods between 2021-2023. Using a Ra mass balance model, we found that the SGD water flux was substantial and dependent on environmental conditions. No measurable SGD was detected during the spring sampling period (June 2022), when the lagoon was partially ice-covered. During ice-free periods, the main driver of SGD in this location is wind-driven lagoon water level changes, not tides, which control surface water recirculation through sediments along the lagoon boundary. A combination of wind strength and direction led to low SGD fluxes in July 2022, with an SGD flux of (6 ± 3) x 10^6 m^3 d^{-1}, moderate fluxes in August 2021 and July 2023, which had an average flux of (17 ± 9) x 10^6 m^3 d^{-1}, and high fluxes in October 2022, at (79 ± 16) x 10^6 m^3 d^{-1}. This work demonstrates how soil and environmental conditions in the Arctic impact Ra mobilization, laying a foundation for future SGD studies in the Arctic and shedding light on the major processes driving Ra fluxes in this important environment.

1. Introduction

Submarine groundwater discharge (SGD) is an important contributor of chemical species in many coastal settings (Moore 1996; Moore 2008), yet is understudied in the Arctic (Lecher, 2017). Two forms of SGD exist in the Arctic: sub-permafrost SGD and supra-permafrost SGD. Sub-permafrost SGD inputs onto Arctic shelves have been investigated using heat flow modeling (Deming et al. 1992; Frederick and Buffett, 2015) and radium (Ra) isotopes (Charkin et al. 2017). Supra-permafrost studies focus on the soil active layer, which seasonally thaws between spring and early autumn. Supra-permafrost SGD has recently been shown to be an important source of methane (Lecher et al. 2015), nutrients (Lecher et al. 2016), and dissolved organic matter (Connolly et al. 2020) to the coastal Arctic Ocean. Furthermore, it will become increasingly important in this region due to amplified Arctic warming (IPCC 2021; Rantanen et al. 2022), which is leading to permafrost degradation, deeper active layers, and groundwater generation from melting ice.

For this study, we define SGD as the mix of fresh, brackish, and saline water originating from coastal sediments and discharging into nearby waters. Fluxes of SGD are often estimated using the four Ra isotopes (Moore 1996; Moore 2008; Garcia - Orellana et al. 2021): ^{223}Ra ($t_{1/2}$ ~ 11.4 d), ^{224}Ra ($t_{1/2}$ ~ 3.6 d), ^{226}Ra ($t_{1/2}$ ~ 1600 y) and ^{228}Ra ($t_{1/2}$ ~ 5.75 y). Since Ra isotopes are part of the U/Th decay series, they are sourced from crustal materials including rock and sediment. Radium sorbs strongly onto these materials under typical fresh groundwater conditions; however, upon encountering solutions of high ionic strength, Ra is released from sediment particles into the dissolved phase. This leads to brackish or saline SGD being enriched in Ra compared to inputs from rivers or other sources (Moore and Krest 2004), making Ra a useful tracer for SGD in coastal systems.

Given the heterogeneity of Arctic coastlines, Ra isotopes provide a way to integrate SGD inputs to a coastal system regardless of the driving forces. These can include terrestrial hydraulic gradients, wave setup and tidal pumping, flow- and topography-induced pressure gradients, wave pumping, benthic exchange caused by bioirrigation or pressure differentials, and density-driven convection (Moore 2010; Santos et al. 2012). In Arctic systems with continuous permafrost and limited tidal range, wind-driven water level changes (Guimond et al. 2023) and the depth of the seasonally thawed active layer (Dimova et al. 2015) have been shown to be dominating forces controlling SGD fluxes. Of the few Arctic supra-permafrost SGD studies published to date, all took place during summer months and only one utilized Ra isotopes (Lecher et al. 2015). The complex physics and chemistry associated with this environment means that questions remain regarding the magnitude of Arctic SGD. To fill this knowledge gap, this study has three goals: (1) to characterize the sources and sinks of Ra isotopes in an Arctic lagoon system, (2) to estimate SGD fluxes to an Arctic coastal lagoon, and (3) to explore seasonal and interannual differences in Ra isotope distributions and SGD fluxes that result from the unique seasonality in the Arctic.

2. Methods

2.1 Field Site and Sample Collection

The study was conducted in Simpson Lagoon (Fig. 1), an ~245 km^2 estuary with minimal tidal influence (<15 cm tidal range) located on the Alaskan Beaufort Sea coastline, which is fringed by similar lagoons covering over half of its length. Simpson Lagoon's coastline is 89 km long, including the barrier island shorelines that face the interior of the lagoon. The lagoon is shallow (average depth ~2 m) with annual shorefast ice cover lasting 8 - 9 months per year (Hanna et al. 2018). The mainland coastline of the lagoon is characterized by a narrow sandy beach backed by peat-rich polygon tundra bluffs (1 m high) and underlain by continuous permafrost (Hanna et al. 2018).

The average summer active layer depth ranges from 25-100 cm with the top ~20 cm consisting of organic peat and mineral soils found at deeper depths (Déry et al. 2005). Annual precipitation is approximately 22.5 cm y^{-1} (USDA[a] 2021; USDA[b] 2022). Major river inputs come from the Kuparuk River at the lagoon's easternmost end, various small streams along the coastline, and the Colville River at the lagoon's westernmost end. Narrow passages between barrier islands facilitate ocean-lagoon exchange, creating a semi-enclosed system.

Field campaigns and sampling were conducted during five different periods: spring (June 2022), summer (August 2021, July 2022, & July 2023), and autumn (September/October 2022). For all summer and autumn time periods, except for July 2023, lagoon surface samples were collected from a small boat in a shore-perpendicular transect (0.4 km, 0.8 km, 1.2 km, 1.6 km, 3.2 km, & 4.8 km from the mainland) at a depth of 0.5 m, with near-bottom samples collected at the three stations closest to shore and occasional extra stations sampled parallel to the shoreline. In July 2023, a full boat survey was conducted along the axis of the lagoon and in the surrounding Beaufort Sea (see Supplemental Materials: S2) using the R/V Proteus. Samples were occasionally collected by hand (grab sampling) in the intertidal zone. Lagoon surface water Ra samples had a volume of ~60 L, collected via bilge pump and filtered through two in-line Hytrex cartridge filters (10 µm, 1 µm). Samples collected from the R/V Proteus had volumes of ~70 L. The samples were weighed and filtered through a manganese coated acrylic fiber at a rate <1 L per minute. Salinity (S), dissolved oxygen (DO), temperature, turbidity, ORP, and pH were also measured with an AquaTROLL Multiparameter Sonde. Three rivers entering the lagoon were also sampled using the same hand collection technique: the Kuparuk River, the Putuligayuk River, and No Point Creek (see Supplemental Materials: S3).

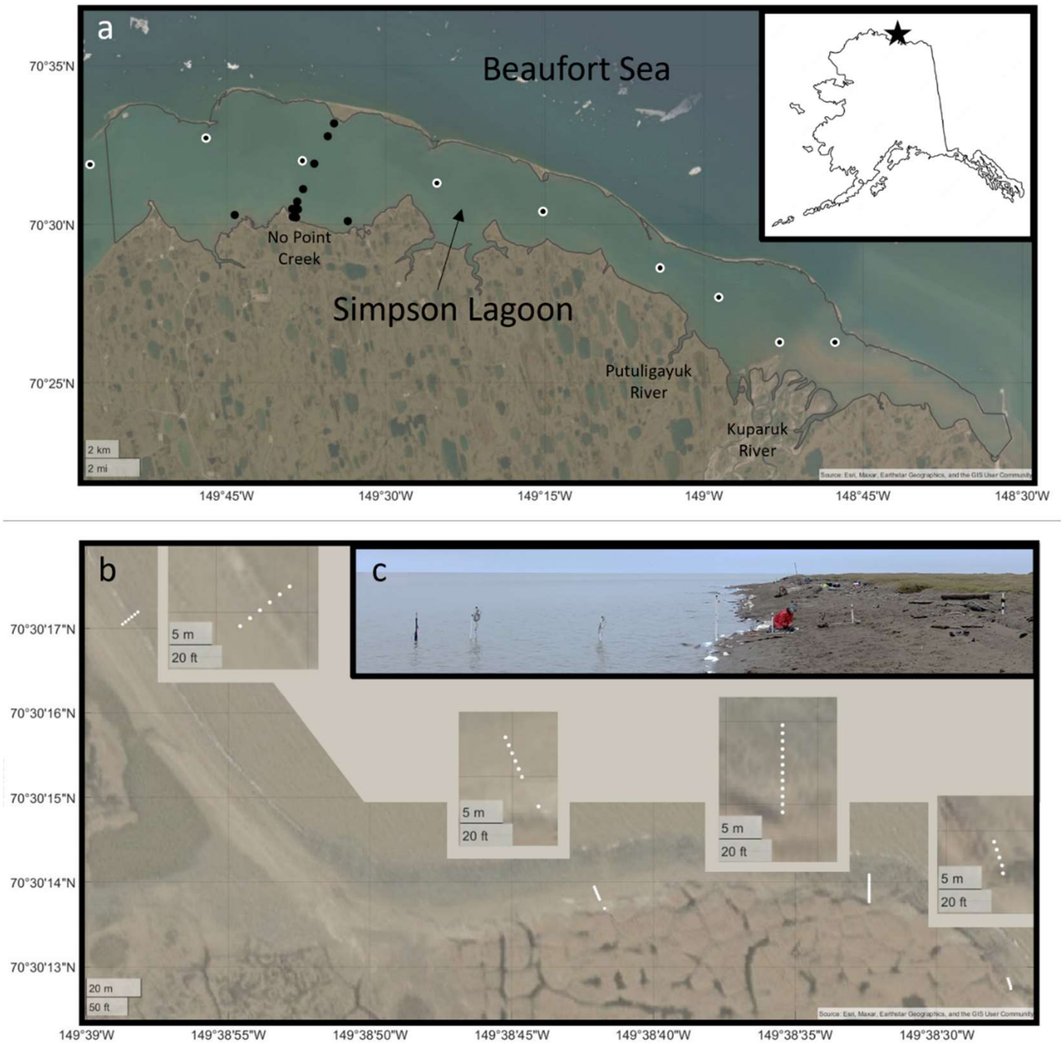

Figure 1. Map of Simpson Lagoon. (a) Full lagoon with location along the Alaskan Beaufort coastline shown in insert and repeated surface water sampling stations shown in black dots. July 2023 interior lagoon sampling stations shown in black dots with white outline. See Supplemental Materials for stations outside of lagoon. (b) Locations of shoreline piezometer transects. (c) Photograph depiction of a transect.

Groundwater sampling was designed to capture the heterogeneity of the field site, which included sandy beaches backed by either tundra bluffs or flat sand, tundra polygon wedges whose surrounding troughs create flow paths for fresh groundwater exiting the tundra, and subtidal areas with eroded peat interspersed with sandy sediment. Several shore-perpendicular transects of piezometers (4-12 stainless steel or PVC piezometers with six-inch-long screened intervals) were installed during each trip (Fig. 1), though not all piezometers were sampled for Ra each time. Transects were designed to traverse the subterranean estuary salinity gradient in all locations. Groundwater samples (0.5-30 L) for Ra isotopes were pumped from the piezometers directly through the Mn fiber column, which included a plug of uncoated acrylic fiber as a filter.

2.2 Sample Analysis

Ra isotopes (^{224}Ra, ^{223}Ra, ^{226}Ra, & ^{228}Ra) were measured via the following set of procedures. After collection, fibers were rinsed with Ra-free deionized water to remove any particles or salt residue, then partially dried so no water could be squeezed from the fiber. The short-lived isotopes ^{224}Ra and ^{223}Ra were measured within two days of sampling using RaDeCC delayed coincidence alpha detectors (Moore 2008). Supported ^{224}Ra and ^{223}Ra activities were determined by re-analyzing the fibers at three weeks and two months, respectively. Method efficiencies were determined using fiber standards spiked with known activities of ^{227}Ac, ^{232}Th, and ^{226}Ra and analyzed using the same method as the samples (Scholten et al. 2010).

The long-lived isotopes were measured as follows: ^{226}Ra was determined via the alpha scintillation technique described by Key et al. (1979). Briefly, fibers were placed in PVC housings, purged with helium, then sealed for three weeks to ensure equilibrium between ^{226}Ra and its daughter ^{222}Rn. The ^{222}Rn gas was collected by purging and cryo-trapping, then transferred to an alpha scintillation (Lucas) cell. The cells were analyzed on a radon counting system (Model AC/DC-DRC-MK 10-2). Method efficiencies were determined using fiber standards spiked with a known activity of ^{226}Ra (NIST SRM#4967A) and analyzed using the same method as the samples.

Finally, the fibers were combusted at 820°C for eight hours. The resultant ash was transferred to a polystyrene test tube and capped with epoxy before analysis for ^{228}Ra on high-purity well-type germanium detectors using peaks for ^{228}Ac (338 and 911 keV). In instances where ^{228}Ra activities were too low to be counted using ^{228}Ac, samples were allowed to age for 6 -12 months and ^{228}Ra was then determined via ^{228}Th ingrowth (238 keV). Select samples were also analyzed for ^{226}Ra using this technique via ^{214}Pb (352 keV). Detector efficiencies were determined using fiber standards that had been spiked with ^{226}Ra and ^{232}Th and then prepared in the same way as the samples.

3. Results

3.1 Surface Water Radium Activities

Surface water Ra activities are shown in Figure 2, with averages and ranges given in Table 1. At the time of the June sampling there were still 0.5–1.5 m of ice covering much of the lagoon. The sampled water, collected from the surface and through auger holes in the ice, was dominated by fresh meltwater. For a given sampling event, there was no notable surface water salinity gradient in the lagoon, though salinity varied dramatically seasonally and interannually.

Temperature and salinity measurements indicate that the lagoon was stratified during August 2021 and July 2022, with a fresher layer (0-1.7 m) overlying a saltier, colder bottom layer (>1.7 m, approx. bottom depth ~ 2 m). Salinity profiles were taken at all surface water stations, with the range of salinity values shown in Table 1. The bottom layer had higher Ra activities, with all isotope activities being 40-70% higher than the top layer activities. These higher values can be explained by diffusion inputs into the bottom layer from Simpson Lagoon sediments (see Supplemental Materials: S4). The Ra activities in the top layer of the lagoon for August 2021 and July 2022 were lower than those observed in the non-stratified periods of July 2023 or October 2022 (Table 1).

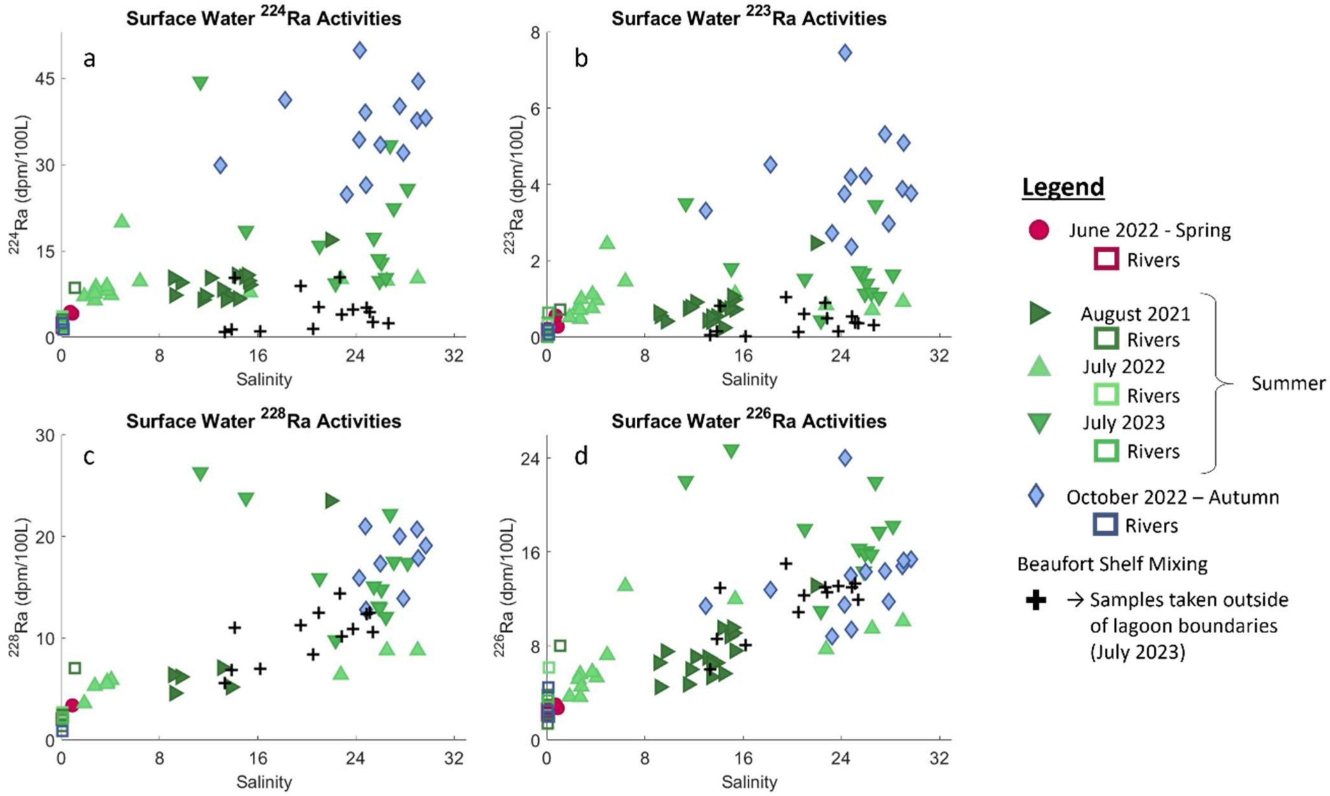

Figure 2. Lagoon surface, river, and ocean Ra activities across seasons for (a) ^{224}Ra, (b) ^{223}Ra, (c) ^{228}Ra, and (d) ^{226}Ra.

Table 1. Isotope activities (dpm/100L) and salinities (PSU) across sampling periods.

Sample Type	Sampling period	Salinity	^{224}Ra		^{223}Ra		^{228}Ra		^{226}Ra	
			avg	range	avg	range	avg	range	avg	range
Groundwater	June	0.1 - 62	42.3	3.3 –189	3.5	0.08 – 19	17.7	8.3 -35.3	7.0	0.52 -38
	August 2021	0.6 – 18	8.6	0.4 – 72	0.5	0.0 – 4.8	10.8	2.7 – 24.3	2.9	0.4 – 22.9
	July 2022	0.3 - 29	16.7	1.0 –125	1.4	0.0 – 11.0	–	–	2.6	0.7 – 9.6
	July 2023	0.6 – 20	19.8	1.6 –155	1.1	0.0 – 7.6	12.0	1.1 – 105	15.3	3.4 – 130
	October 2022	0.5 -36	13.9	0.7 - 72	1.1	0.03 - 6.4	10.8	7 -15.6	4.9	0.9 -13.6
Lagoon Surface Water	June	2.6	4.1	3.9 - 4.4	0.36	0.22 - 0.57	–	–	2.87	2.71 -3.02
	August 2021	9 – 22	9.1	6.5 - 16.9	0.77	0.25 – 2.47	8.8	4.6 – 23.5	7.4	4.5 – 13.1
	July 2022	2 – 29	9.2	6.4 – 19.9	0.99	0.48 – 2.44	6.2	3.6 – 8.8	7.1	3.6 – 13.1
	July 2023	11 – 28	19.4	9.4 – 44.4	1.71	0.44 – 3.51	16.8	9.8 – 26.3	17.7	11.0 – 24.7
	October 2022	13 - 30	36.2	24.8 - 44.4	4.10	2.37 - 7.45	18.2	13.9 - 20.7	13.7	9.4 -15.4
Rivers	All periods	>0.1	2.3	1.3 – 3.5	0.21	0.01 – 0.64	1.9	0.9 – 2.5	2.8	1.4 – 6.2
Runoff	All periods	0.1	3.7	1.6 – 8.6	0.25	0 – 0.70	4.9	2.7 – 7.0	4.2	2.3 – 8.0
Surface Water from Outside the Lagoon	July 2023	13 – 24	4.8	0.9 – 10.4	0.44	0.03 – 1.05	9.8	5.6 – 14.4	11.3	6.0 – 15.0
		25 - 31	3.6	2.4 – 5.1	0.40	0.31 – 0.54	11.8	10.6 – 12.5	12.7	11.9 – 13.3

3.2 Groundwater Radium Activities

Groundwater activities for each season are shown in Figure 3 and in Table 1. All sampling periods exhibited strong heterogeneity in Ra activities, with outliers that were two to three standard deviations higher than the mean. The spring period had substantially higher Ra averages than the other periods, which had comparable activities (Table 1).

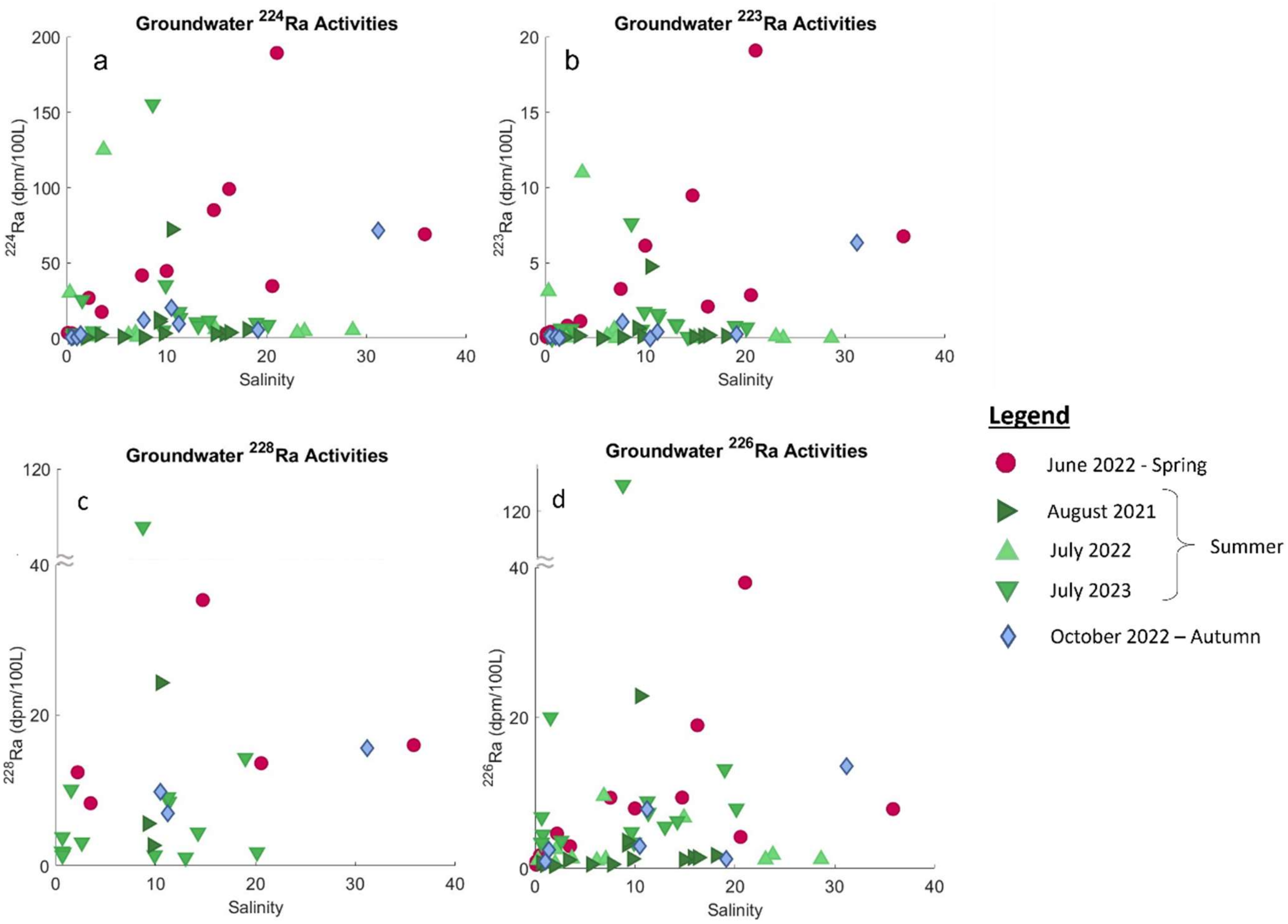

Figure 3. Groundwater Ra activities across seasons for (a) ^{224}Ra, (b) ^{223}Ra, (c) ^{228}Ra, and (d) ^{226}Ra.

3.3 River Radium Activities

Rivers can transport Ra to coastal waters in two ways: dissolved in river water and carried on suspended particles. The dissolved Ra activities in the Kuparuk River and Putuligayuk River were similar, with No Point Creek (reported as runoff) having slightly higher values (Table 1). Most Arctic rivers have not been sampled for short-lived isotopes; however, ^{226}Ra activities measured in this study ranged between 1.4 -3.9 dpm 100L^{-1}, which are lower than those seen in large Arctic rivers such as the Yenisey and Lena Rivers in Siberia (Rutgers van der Loeff et al. 2003), or the Mackenzie and Yukon Rivers in North America (Kipp et al. 2020), but are comparable to activities seen in similarly-sized Arctic rivers such as the Ellice River, rivers near Anchorage, AK (Bullock et al. 2022), and rivers in Greenland (Linhoff et al. 2020).

Riverine suspended sediments are also important, as ion-exchange-driven desorption can dominate riverine Ra inputs to coastal systems (Key et al. 1985). The desorption of Ra isotopes from Kuparuk River sediments was 0.09 ± 0.01 dpm g^{-1}, 0.006 ± 0.002 dpm g^{-1}, 0.07 ± 0.01 dpm g^{-1}, and 0.08 ± 0.004 dpm g^{-1} for ^{224}Ra, ^{223}Ra, ^{228}Ra, and ^{226}Ra, respectively. Desorption experiments on Putuligayuk River sediment was not possible due to loss of sample during transport. Discussion of desorption in a greater context can be found in the supplemental materials (S3).

4. Discussion

4.1 Impact of Wind Direction on Lagoon Flushing

The lagoon water level varied by over 75 cm during our five sampling periods despite predicted tidal amplitudes of <15 cm (Guimond et al. 2023). Guimond et al. (2023) show that this variability is due to changing wind direction, with sustained winds from the east causing set-down periods of low water level. Such wind patterns increase wave action and cause the lagoon to oscillate between low and high-water levels (Guimond et al. 2023), allowing for increased benthic advective flow, the drainage of previously saturated, elevated sediments, and increased, wind- and wave-driven recirculation through lagoon sediments. Our data, as discussed in the following sections, support this conclusion and indicate that strong easterly winds increase mixing between the lagoon and the Beaufort Sea, as well as SGD-derived Ra within the lagoon.

Lagoon water Ra values are higher following wind-driven set-down periods, as seen in July 2023 and October 2022 (see wind visualization: Supplemental .Fig 5). The highest values, seen during October 2022, were sampled immediately following a set-down period (Guimond et al. 2023). The lower Ra values from July 2023 were sampled several days after a set-down period (NOAA, 2023), allowing the water level to begin rising back to its median value in the interim, which reduced the observed impact of the set-down period on the lagoon inventory. The salinities during these periods reflect higher mixing rates with the Beaufort Sea (Table 1; Supplemental Table 3). In contrast, the sampling periods with stratification (August 2021 & July 2022) had lower surface salinities (Table 1) and lower percentages of wind coming from the east in the days leading up to sampling (see Supplemental Fig. 5; NOAA, 2023), although August 2021 still had higher wind speeds than those seen in July 2022 during surface water sampling. Winds from directions other than east therefore seem to allow the formation of a surface layer on the lagoon dominated by riverine inputs, while higher wind speeds still influence mixing between layers.

Since the activity ratios (AR) of ^{224}Ra:^{226}Ra are 1.4 ± 0.6 during August 2021 (S~12.5), July 2022 (S~3.6), and July 2023 (S~24.7) despite dramatically different salinities, it is unlikely that the ocean endmember is controlling Ra isotopes in the lagoon. In fact, the highest AR we observed was during the October 2022 sampling period (S~27), when the ^{224}Ra:^{226}Ra AR was 2.7 ± 0.3. Due to the short half-life of ^{224}Ra, it tends to be depleted in deeper ocean waters compared to shallow coastal systems (Moore 1998), as seen in the stations we sampled immediately outside of the lagoon (AR~0.4 ± 0.2). Instead, the higher AR speaks to an increase in short term processes, such as wave pumping and advective flow through sediments, which are not long enough to allow ingrowth of the long-lived isotopes (Michael et al. 2011). This points to SGD as driving high lagoon Ra inventories during periods of set-down.

4.2 Processes driving Groundwater Ra Variations

During the spring sampling period, the ground was still mostly frozen, with landfast ice along the shore. Groundwater had thus been in contact with the surrounding soil since the autumn period of the previous year. This longer residence time likely enriched the groundwater in Ra (Michael et al. 2011).

For all periods sampled, Ra activities showed minimal dependence on salinity, which is unusual given Ra has been shown to be enriched in brackish and saline groundwater due to competing cations interfering with Ra^{2+} adsorption onto solids (Webster et al. 1995; Gonneea et al. 2008; Beck and Cochran 2013). No associations with other measured parameters (pH, DO, ORP, temperature) were found that might explain these deviations; however, field observations and hydrological measurements revealed strong heterogeneity within the coastal sediments, with erosion and storm overtopping intermittently burying large, intact chunks of peat. Preferential flow paths and pooling were observed, potentially causing varied groundwater residence times within several square meters. Samples with different residence times but the same salinity will presumably have different Ra activities (Michael et al. 2011).

The ice-free season (summer and autumn) Ra activities in Simpson Lagoon groundwater exhibit lower averages compared to other, more temperate sites (Charette, Buesseler, & Andrews, 2001), likely due to factors impacting the solid/solution partitioning coefficient (K_d) of Ra. In a comparable site along the Beaufort Sea coastline, the carbon content of tundra soils averaged 12% (Bristol et al. 2021) – sediments with high organic matter content have a large adsorptive capacity for Ra and are capable of adsorbing up to ten times more Ra than clay (Simon and Ibrahim, 1990). Fe- and Mn-oxides (Gonneea et al. 2008; Beck and Cochran 2013) also increase the K_d for Ra isotopes. Indeed, the intertidal sediments in Simpson Lagoon have high Fe content based on visual observations and sediment core analyses (Schaal, 2023). Finally, since K_d is inversely related to temperature (Rama and Moore 1996; Gonneea et al. 2008), colder temperatures may be contributing to the low groundwater Ra activities compared to more temperate sites.

4.3 Submarine Groundwater Discharge Inputs into Simpson Lagoon

We employed the Ra isotope mass balance box model approach to quantify SGD (Moore 1996; Moore and Krest 2004; Garcia-Orellanas et al. 2021), using the short-lived isotopes (^{224}Ra & ^{223}Ra) only due to high background activities for the long-lived isotopes in the Beaufort waters immediately outside the lagoon (Fig. 2, Supplemental Fig. 1). The relative fraction of daily inputs of ^{224}Ra and ^{223}Ra for all sampling periods are shown in Figure 4. Detailed discussion of the model and all parameters used can be found in the supplemental materials.

Conversion of SGD in dpm d^{-1} to a water flux ($m^3\ d^{-1}$) requires a groundwater Ra endmember value in dpm m^{-3}. The choice of the Ra endmember value has been extensively debated in the literature (Michael et al. 2011; Cho and Kim, 2016; Cerdà-Domènech et al. 2017). The maximum Ra values are used to provide conservative, lower-limit SGD estimates in numerous studies (e.g. Moore 1996; Null et al. 2019); however, we chose to use the 90th percentile Ra activities from each sampling period to lower the impact of extreme outliers.

The SGD rates determined by ^{224}Ra and ^{223}Ra were averaged for each period with the standard deviation taken as the error. Inputs of Ra due to SGD could not be resolved for June 2022. The two periods with minimal easterly wind input had estimated SGD fluxes of $(22 \pm 8) \times 10^6\ m^3\ d^{-1}$ for August 2021 and $(6 \pm 3) \times 10^6\ m^3\ d^{-1}$ for July 2022. The impact of higher wind speeds during lagoon sampling can be seen in the higher flux from August 2021 (Supplemental Fig. 5). July 2023 had a high Ra inventory in the lagoon due to a recent set-down period, but an SGD flux similar to August 2021 and July 2022 at $(12 \pm 4) \times 10^6\ m^3\ d^{-1}$, presumably due to the fact that water levels had begun rising at the time of sampling. Finally, October 2022 was sampled directly following a set-down period, before water levels returned to normal. This resulted in not only a high Ra inventory in the lagoon, but also high SGD fluxes coming in at an estimated $(79 \pm 16) \times 10^6\ m^3\ d^{-1}$.

The SGD fluxes, which average $(160 \pm 90)\ m^3\ d^{-1}\ m^{-1}$ of shoreline during the non-easterly wind periods and $(890 \pm 200)\ m^3\ d^{-1}\ m^{-1}$ during the easterly wind period, are on the high range of the few supra-permafrost SGD fluxes reported for the Arctic. Two other sites along the Beaufort Coast reported fluxes of 1.0, 12, and 43 $m^3\ d^{-1}\ m^{-1}$ of shoreline during summer months (Dimova et al. 2015, Lecher et al. 2015, Connolly et al. 2020). Our SGD estimates are more in line with SGD fluxes reported for southern Alaska, including those seen at Kasitsna Bay

(125 m^3 d^{-1} m^{-1}) and Seldovia Slough ((170 ± 240) m^3 d^{-1} m^{-1}) (Dimova et al. 2015; Lecher et al. 2015). However, unlike these other sites, the SGD in Simpson Lagoon does not seem to be isolated to margin sediments, as indicated by the high Ra activities observed throughout the lagoon (Supplemental Fig. 1). Benthic exchange was estimated using a wave-pumping model developed by Sawyer et al. (2013). This simplified model shows that the shallow nature of the lagoon and hydraulic conductivities could allow SGD to occur over the full lagoon area (see Supplemental Materials: S7). In this case, SGD rates would be (0.06 ± 0.04) m^3 m^{-2} d^{-1} for the non-easterly wind periods, and (0.3 ± 0.1) m^3 m^{-2} d^{-1} for the easterly wind period.

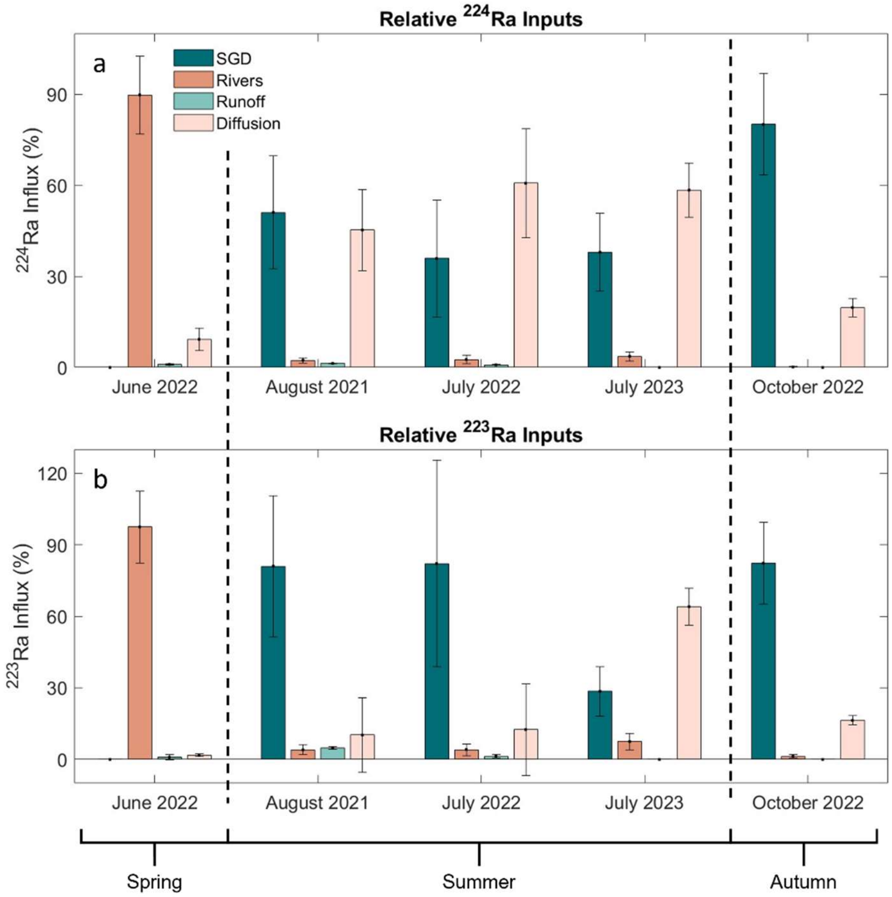

Figure 4. Relative daily inputs of Ra isotopes by source and season for (a) ^{224}Ra and (b) ^{223}Ra.

Demir et al. (submitted) used numerical models and in situ hydrological techniques to derive a freshwater SGD flux into Simpson Lagoon for August 2021 of (0.12-0.14) x 10^6 m^3 d^{-1}; this is equivalent to ~1% of the total SGD flux for that period, which is in the lower range seen at more temperate sites (Tamborski et al. 2015; Cho et al. 2018). This low percentage is likely due to the inclusion of lagoon water advection through bottom sediments as a component of SGD in our box model, as well as the limited capacity for a terrestrial water table to form, due to the shallow active layer depth and minimal topographical gradient

The observations in this study and those reported by Guimond et al. (2023) indicate that wind direction and speed are the dominating drivers of SGD in Simpson Lagoon during ice-free periods, with easterly winds driving higher SGD fluxes. Based on wind direction and strength in late-June through October of 2021, 2022, and 2023 (NOAA 2023), easterly winds that are sustained for a day or more occur 17 - 20% of the time. Given that ice and snow cover the land for roughly two-thirds of the year (McClelland et al. 2014), that leaves ~120 days (4 months) where SGD can occur. Based on set-down periods occurring 20% of the time and a 4-month ice-free season, our weighted annual SGD flux into Simpson Lagoon is (3.2 ± 1.2) x 10^9 m^3 y^{-1}, which is comparable to the annual flux of the Kuparuk River.

5. Conclusion

Since Arctic groundwater has been shown to be an important source of carbon and nutrients to an Arctic coastal zone (Connolly et al. 2020), understanding seasonal variability and driving processes are important for tracing its impact on these sensitive coastal systems. This study used the four Ra isotopes to characterize seasonal SGD inputs to an Arctic coastal lagoon and to investigate Ra dynamics within an Arctic estuarine system. The results showed that SGD is seasonally variable in the Arctic, with limited inputs during spring and inputs dependent on wind conditions during ice-free seasons. However, more research needs to be done to better understand the factors influencing Ra cycling in the Arctic. The interplay between Simpson Lagoon's soil/sediment characteristics, groundwater residence times, and seasonally changing salinity create unique Ra dynamics that appear to be dominated by short-term processes such as temporary water level changes and wind-driven wave pumping; however, this may not hold true along other Arctic coastlines with different topography and sediment properties. As the ice-free season grows longer and weather patterns change due to Arctic warming, understanding the processes controlling SGD in this environment will become increasingly important.

Acknowledgements

This project was funded by the National Science Foundation's Office of Polar Programs through grants 1938873 (Charette), 1938820 (Cardenas and McClelland), and 1656026 (McClelland). Assistance with fieldwork and data interpretation was provided by Cansu Demir, Julia Guimond, and Emily Bristol. We thank Hillcorp Alaska for providing access to field sites and Battelle Arctic Research Operations (via Polar Field Services) for logistical support. We also thank the Beaufort Lagoon Ecosystems Long Term Ecological Research program for sharing lab and field resources.

References

Adyasari, D., N.T. Dimova, H. Dulai, B.S. Gilfedder, I. Cartwright, T. McKenzie, and P. Fulekey. 2023. Radon - 222 as a groundwater discharge tracer to surface waters. Earth Sci. Rev. **238**: 104321. doi:*10.1016/j.earscirev.2023.104321*

Beck, A.J. and M.A. Cochran. 2013. Controls on solid - solution partitioning of radium in saturated marine sands. Mar. Chem. **156:** 38 - 48. doi:10.1016/j.marchem.2013.01.008

Bristol, E.M., C.T. Connolly, T.D. Lorenson, B.M. Richmond, A.G. Ilgen, R.C. Choens, D.L. Bull, M. Kanevskiy, G. Iwahana, B.M. Jones, and J.W. McClelland. 2021. Geochemistry of coastal permafrost and erosion-driven organic matter fluxes to the Beaufort Sea near Drew Point, Alaska. Front. Earth Sci. **8**. doi: *https://doi.org/10.3389/feart.2020.598933*

Bullock, E.J., L. Kipp, W. Moore, K. Brown, P.J. Mann, J.E. Vonk, N. Zimov, and M.A. Charette. 2022. Radium Inputs into the Arctic Ocean from Rivers: A Basin-Wide Estimate. J. Geophys. Res. Oceans*,* **127**(9): e2022JC018964. doi:*10.1029/2022JC018964*

Cerdà - Domènech, M., V. Rodellas, A. Folch, and J. Garcia–Orellana. 2017. Constraining the temporal variations of Ra isotopes and Rn in the groundwater end - member: Implications for derived SGD estimates. Sci. Total Environ. **595:** 849 - 857. doi:10.1016/j.scitotenv.2017.03.005

Charkin, A. N., M. Rutgers van der Loeff, N. E. Shakhova, Ö. Gustafsson, O. V. Dudarev, M. S. Cherepnev, A. N. Salyuk, A. V. Koshurnikov, E. A. Spivak, A. Y. Gunar, A. S. Ruban, and I. P. Semiletov. 2017. Discovery and characterization of submarine groundwater discharge in the Siberian Arctic seas: a case study in the Buor - Khaya Gulf, Laptev Sea. Cryosphere **11:** 2305 - 2327. doi:10.5194/tc -11 - 2305 - 2017

Charette, M. A., K. O. Buesseler, and J. E. Andrews. 2001. Utility of radium isotopes for evaluating the input and transport of groundwater - derived nitrogen to a Cape Cod estuary. L&O **46**(2): 465 - 470. doi:10.4319/lo.2001.46.2.0465

Cho, H.-M. and G. Kim. 2016. Determining groundwater Ra endmember values for the estimation of the magnitude of submarine groundwater discharge using Ra isotope tracers. Geophys. Res. Lett. **1-7**. doi:10.1002/2016GL068805

Cho, H.-M., G. Kim, E.Y. Kwon, N. Moosdorf, J. Garcia-Orellana, and I.R. Santos. 2018. Radium tracing nutrient inputs through submarine groundwater discharge in the global ocean. Sci. Rep. **8**: 2439. doi:10.1038/s41598 - 018 - 20806 - 2

Connolly, C. T., M. B. Cardenas, G. A. Burkart, R. G. M. Spencer, and J. W. McClelland. (2020). Groundwater as a major source of dissolved organic matter to Arctic coastal waters. Nat. Comm. **11:** 1479. doi:10.1038/s41467-020-15250-8

Dasher, D., T. Lomax, A. Bethe, M. Hoberg, S. Naidu, and S. Jewett. 2016. Offshore Oil/Gas Wastewater Study: 2014 Assessment of Simpson Lagoon. Report. Juneau: Alaska Department of Environmental Conservation. URL:*https://dec.alaska.gov/media/16815/simpson - lagoon - 2016.pdf* (accessed 3/27/2023).

Deming, D., J. H. Sass, A. H. Lachenbruch, and R. F. De Rito. 1992. Heat flow and subsurface temperature as evidence for basin - scale ground - water flow, North Slope of Alaska. Geo. Soc. Am. Bull. **104:** 528 - 542.

Déry, S. J., M. Stieglitz, Å. K. Rennermalm, and E. F. Wood. 2005. The Water Budget of the Kuparuk River Basin, Alaska. J. Hydrometer.*,* **6:** 633 - 655.

Dimova, N. T., W. C. Burnett, J. P. Chanton, and J. E. Corbett. 2013. Application of radon - 222 to investigate groundwater discharge into small shallow lakes. J. Hydro. **486:** 112-122. doi:*10.1016/j.jhydrol.2013.01.043*

Dimova, N. T., A. Paytan, J. D. Kessler, K. J. Sparrow, F. G.-T. Kodovska, A. L. Lecher, J. Murray, S. M. Tulaczyk. 2015. Current magnitude and mechanisms of groundwater discharge in the Arctic: Case Study from Alaska. Environ. Sci. Tech. **49:** 12036 -12043. doi:*10.1021/acs.est.5b02215*

Frederick, J. M., and B. A. Buffett. 2015. Effects of submarine groundwater discharge on the present day extent of relict submarine permafrost and gas hydrate stability on the Beaufort Sea continental shelf. J. Geophys. Res. Earth Surf. **120:** 417 - 432. doi:*10.1002/2014JF003349*

Garcia-Orellana, J., V. Rodellas, J. Tamborski, M. Diego-Feliu, P. van Beek, Y. Weinstein, M. Charette, A. Alorda-Kleinglass, H. A. Michael, T. Stieglitz, J. Scholten. 2021. Radium isotopes as submarine groundwater discharge (SGD) tracers: Review and recommendations. Earth Sci. Rev. **220:** 103681. doi:10.1016/j.earscirev.2021.103681

Gonneea, M. E., P. J. Morris, H. Dulaiova, and M. A. Charette. 2008. New perspectives on radium behavior within a subterranean estuary. Mar. Chem. **109**(3-4): 250 - 267. doi:10.1016/j.marchem.2007.12.002

Guimond, J. A., C. Demir, B. L. Kurylyk, M. A. Walvoord, J. W. McClelland, and M. B. Cardenas. 2023. Wind-modulated groundwater discharge along a microtidal Arctic coastline. Environ. Res. Lett. **18**(9): 094042. doi:*10.1088/1748 - 9326/acf0d8*

Hanna, A. J. M., T. M. Shanahan, M. A. Allison, T. S. Bianchi, and K. M. Schreiner. 2018. A multi-proxy investigation of late-Holocene temperature change and climate-driven fluctuations in sediment sourcing: Simpson Lagoon, Alaska. The Holocene **28**(6): 984-997. doi:10.1177/0959683617752845

Hsu, F., C. Su, P. Wang, and I. Lin. 2020. Temporal Variations of Submarine Groundwater Discharge into a Tide-Dominated Coastal Wetland (Gaomei Wetland, Western Taiwan) Indicated by Radon and Radium Isotopes. Water **12**(6): 1806. doi:10.3390/w12061806

IPCC. 2021. Climate Change 2021: The Physical Science Basis. In *Contribution of Working Group I to the Sixth Assessment Report of the Intergovernmental Panel on Climate Change*, Masson - Delmotte, V., et al. (Eds.). Cambridge University Press. In Press. Retrieved from https://www.ipcc.ch/report/sixth - assessment - report - working - group - i/

Key, R. M., N. L. Guinasso, and D. R. Schink. 1979. Emanation of radon-222 from marine sediments. Mar. Chem. **7**: 221–250. doi:10.1016/0304 - 4203(79)90041 - 0

Key, R. M., R. F. Stallard, W. S. Moore, and J. L. Sarmiento. 1985. Distribution and Flux of ^{226}Ra and ^{228}Ra in the Amazon River. J. Geophys. Res. **90**(C4): 6995-7004.

Kipp, L. E., P. B. Henderson, Z. A. Wang, and M.A. Charette. 2020. Deltaic and Estuarine Controls on Mackenzie River Solute Fluxes to the Arctic Ocean. ESCO **43**: 1992-2014. doi:10.1007/s12237 - 020 - 00739 - 8

Lecher, A.L. 2017. Groundwater Discharge in the Arctic: A Review of Studies and Implications for Biogeochemistry. Hydrology, **4**(3): 41. doi:10.3390/hydrology4030041

Lecher, A. L., C.-T. Chien, A. Paytan. 2016. Submarine groundwater discharge as a source of nutrients to the North Pacific and Arctic coastal ocean. Mar. Chem. **186**: 167-177. doi:10.1016/j.marchem.2016.09.008

Lecher, A. L., J. Kessler, K. Sparrow, F. G.-T. Kodovska, N. Dimova, J. Murray, S. Tulaczyk, and A. Paytan. 2015. Methane transport through submarine groundwater discharge to the North Pacific and Arctic Ocean at two Alaskan sites. L&O **61**: S344 - S355. doi:*10.1002/lno.10118*

Linhoff, B. S., M. S. Charette, and J. Wadham. 2020. Rapid mineral surface weathering beneath the Greenland Ice Sheet shown by radium and uranium isotopes. Chem. Geo., **547**: 119663. doi:10.1016/j.chemgeo.2020.119663

Luek, J. L. and A. J. Beck. 2014. Radium budget of the York River estuary (VA, USA) dominated by submarine groundwater discharge with a seasonally variable groundwater end-member. Mar. Chem. **165**: 55-65. doi:*10.1016/j.marchem.2014.08.001*

McClelland, J. W., A. Townsend-Small, R. M. Holmes, F. Pan, M. Stieglitz, M. Khosh, and B. J. Peterson. 2014. River export of nutrients and organic matter from the North Slope of Alaska to the Beaufort Sea. Water Resour. Res. **50**(2): 1823 -1839. doi:*10.1002/2013WR014722*

Michael, H. A., M. A. Charette, and C. F. Harvey. 2011. Patterns and variability of groundwater flow and radium activity at the coast: A case study from Waquoit Bay. Mar. Chem. **127**(1-4): 100 -114. doi:10.1016/j.marchem.2011.08.001

Moore, W. S. 1996. Large groundwater inputs to coastal waters revealed by ^{226}Ra enrichments. Nature, **380**: 612 - 614. doi:10.1038/380612a0

Moore, W. S. 1998. Application of ^{226}Ra, ^{228}Ra, ^{223}Ra, and ^{224}Ra in coastal waters to assessing coastal mixing rates and groundwater discharge to oceans. Proc. Indian Natl. Sci. Acad. **107** (4): 343 -349.

Moore, W. S. 2007. Seasonal distribution and flux of radium isotopes on the southeastern U.S. continental shelf. Jour. Geophys. Res. **112**: C10013. doi:*10.1029/2007JC004199*

Moore, W. S. 2008. Fifteen years experience in measuring 224Ra and 223Ra by delayed - coincidence counting. Mar. Chem. **109**: 188 -197.

Moore, W.S. 2010. The Effect of Submarine Groundwater Discharge on the Ocean. Ann. Rev. Mar. Sci. **2**: 59-88. doi:*10.1146/annurev - marine -120308 - 081019*

Moore, W. S. and R. Arnold. 1996. Measurement of ^{223}Ra and ^{224}Ra in coastal waters using a delayed coincidence counter. J. Geophys. Res., **108**(C1): 1321-1329.

Moore, W. S. and J. Krest. 2004. Distribution of ^{223}Ra and ^{224}Ra in the plumes of the Mississippi and Atchafalaya Rivers and the Gulf of Mexico. Mar. Chem. **86**: 105-119.

NOAA: Station PRDA2-9497645-Prudhoe Bay, AK, 2023, National Data Buoy Center, accessed [Jan 12, 2024] at URL [https://www.ndbc.noaa.gov/station_page.php?station=prda2].

Null, K. A., D. R. Corbett, J. Crenshaw, R. N. Peterson, L. E. Peterson, and W. B. Lyons. 2019. Groundwater discharge to the western Antarctic coastal ocean. Polar Res., **38**. doi:10.33265/polar.v38.3497

Rama and Moore, W.S. 1996. Using the radium quartet for evaluating groundwater input and water exchange in salt marshes. Geo. Cosmo. Acta **60**(23): 4645-4652.

Rantanen, M., A. Y. Karpechko, A. Lipponen, K. Nordling, O. Hyvärinen, K. Ruosteenoja, T. Vihma, and A. Laaksonen. 2022. The Arctic has warmed nearly four times faster than the globe since 1979. Comm. Earth Environ. **3**: 168. doi:10.1038/s43247 - 022 - 00498 -3

Rutgers van der Loeff, M., S. Kühne, M. Wahsner, H. Höltzen, M. Frank, B. Ekwurzel, M. Mensch, and V. Rachold. 2003. ^{228}Ra and ^{226}Ra in the Kara and Laptev Seas. Cont. Shelf Res. **23**(1): 113-124. doi:10.1016/S0278 - 4343(02)00169 -3

Santos, I. R., B. D. Eyre, M. Huettel. 2012. The driving forces of porewater and groundwater flow in permeable coastal sediments: A review. Est. Coast. Shelf Sci. **98**: 1-15. doi:*10.1016/j.ecss.2011.10.024*

Sawyer, A. H., F. Shi, J. T. Kirby, and H. A. Michael. 2013. Dynamic response of surface water-groundwater exchange to currents, tides, and waves in a shallow estuary. J. Geophys. Res. Oc. **118**: 1749-1758. doi:10.1002/jgrc.20154

Schaal, I. V. 2023. Distribution and behavior of trace metals in the subterranean estuary of an Arctic coastal lagoon. Master’s Thesis. Massachusetts Institute of Technology.

Scholten, J. C., M. K. Pham, O. Blinova, M. A. Charette, H. Dulaiova, and M. Eriksson. 2010. Preparation of Mn-fiber standards for the efficiency calibration of the delayed coincidence counting system (RaDeCC). Mar. Chem. **121**(1- 4): 206-214. doi:10.1016/j.marchem.2010.04.009

Simon, S. L. and S. A. Ibrahim. 1990. Biological uptake of radium by terrestrial plants. In: The Environmental Behaviour of Radium, vol. 1, IAEA. Technical Report Series, No. 310., pp. 545–599.

USDA[a], 2021. Precipitation, Accumulated, Prudhoe Bay, AK. Natural Resources Conservation Service and National Water and Climate Center, accessed (April 6, 2023) at URL [https://wcc.sc.egov.usda.gov/nwcc/site?sitenum=1177]

USDA[b], 2022. Precipitation, Accumulated, Prudhoe Bay, AK. Natural Resources Conservation Service and National Water and Climate Center, accessed (April 6, 2023) at URL [https://wcc.sc.egov.usda.gov/nwcc/site?sitenum=1177]

USGS[a]:15875000 COLVILLE R AT UMIAT AK, 2023, National Water Information System Data (USGS Water Data for the Nation), accessed [January 12, 2024], at URL [*https://waterdata.usgs.gov/monitoring-location/15875000/#parameterCode=00065&period=P7D*].

USGS[b]: KUPARUK R NR DEADHORSE AK, 2023, National Water Information System Data (USGS Water Data for the Nation), accessed [March 22, 2023], at URL [https://waterdata.usgs.gov/nwis/inventory/?site_no=15896000].

Webster, I. T., G. J. Hancock, and A. S. Murray. 1995. Modeling the effect of salinity on radium desorption from sediments. Geo. Cosmo. Acta **59**(12): 2469 – 2476.

Supplementary Information for Chapter 3

S1. Radium Isotope Box Model Terms

We used a mass balance box model approach to quantify SGD using radium (Ra) isotopes (Moore 1996; Moore 2008; Garcia-Orellanas et al. 2021), as shown in Supp. Equation 1. The left side of the equation consists of fluxes of Ra into the lagoon (dpm d^{-1}), while the right side are the fluxes out of the lagoon. For the summer periods, where stratification was observed, we consider a surface and bottom layer individually. The same model was used for the two short lived Ra isotopes, ^{224}Ra and ^{223}Ra.

$$J_{riv} + J_{diff} + J_{resp} + J_{SGD} = J_{mi} + J_{decay} \qquad \text{(Supplemental Equation 1)}$$

Potential sources of Ra isotopes to the lagoon include rivers (dissolved + desorbed; J_{riv}), diffusion from bottom sediments (J_{diff}), resuspension of lagoon bottom sediments (J_{resp}), and SGD (J_{SGD}) (S.Eq. 1). Rivers transport Ra in the dissolved phase, as well as on suspended sediments that can release Ra via ion exchange upon encountering higher salinities within an estuary (Rama and Moore 1996). Diffusive fluxes of Ra from lagoon bottom sediments occur due to the equilibrium between the sediment-bound Ra and porewater (Beck et al. 2007). This is particularly important for short-lived Ra isotopes, as the surface bound Ra lost via diffusion is replenished on a time scale of days to weeks (Cai et al. 2014; Rodellas et al. 2017). Resuspension of bottom sediments is dependent on wind and wave conditions, which increase orbital velocity at the bottom of the water column (Precht and Huettel 2003; Meselhe et al. 2013; McCorquodale et al. 2017).

Outputs of Ra in this system include loss via mixing with the Beaufort Sea (J_{mix}) and loss by radioactive decay (J_{decay}). Loss by decay is the product of the decay rate of each isotope and its inventory in the lagoon. Loss by mixing depends on calculating the lagoon residence time and Beaufort Sea endmember, in order to determine how mixing will dilute the lagoon's Ra inventories (Tamborski et al. 2020).

Constraining these inputs and outputs allows us to solve for J_{SGD} and determine SGD inputs to the lagoon in dpm d^{-1}, which can then be converted to a water flux. Each term in Supp. Equation 1 is discussed in the following sections.

S2. Survey of Lagoon and Surrounding Waters

In earlier sampling campaigns, the study was limited by boat capabilities and could only access a small region of the lagoon. However, in July 2023, samples were collected along the full horizontal axis of Simpson Lagoon and in the immediate outside waters at the easternmost and westernmost ends, where most mixing with the Beaufort Sea occurs. Sampling occurred from the R/V Proteus, with ~70L filtered seawater collected per sample. Station maps showing salinity, temperature, and the Ra isotopes can be seen in Supp. Figure 1.

In general, samples from the outer, eastern stations were colder and fresher, likely due to high inputs from ice meltwater (ice floes observed during sampling). However, in both these stations and the northern outer, western stations, which also have S and T values indicative of meltwater input, stratification was observed in the water column. Salinity profiles show stratification at these stations, with S increasing between 1.5 and 2.5 m in depth (Supp. Fig. 2). Radium activities are especially low at these stations due to dilution from sea ice meltwater.

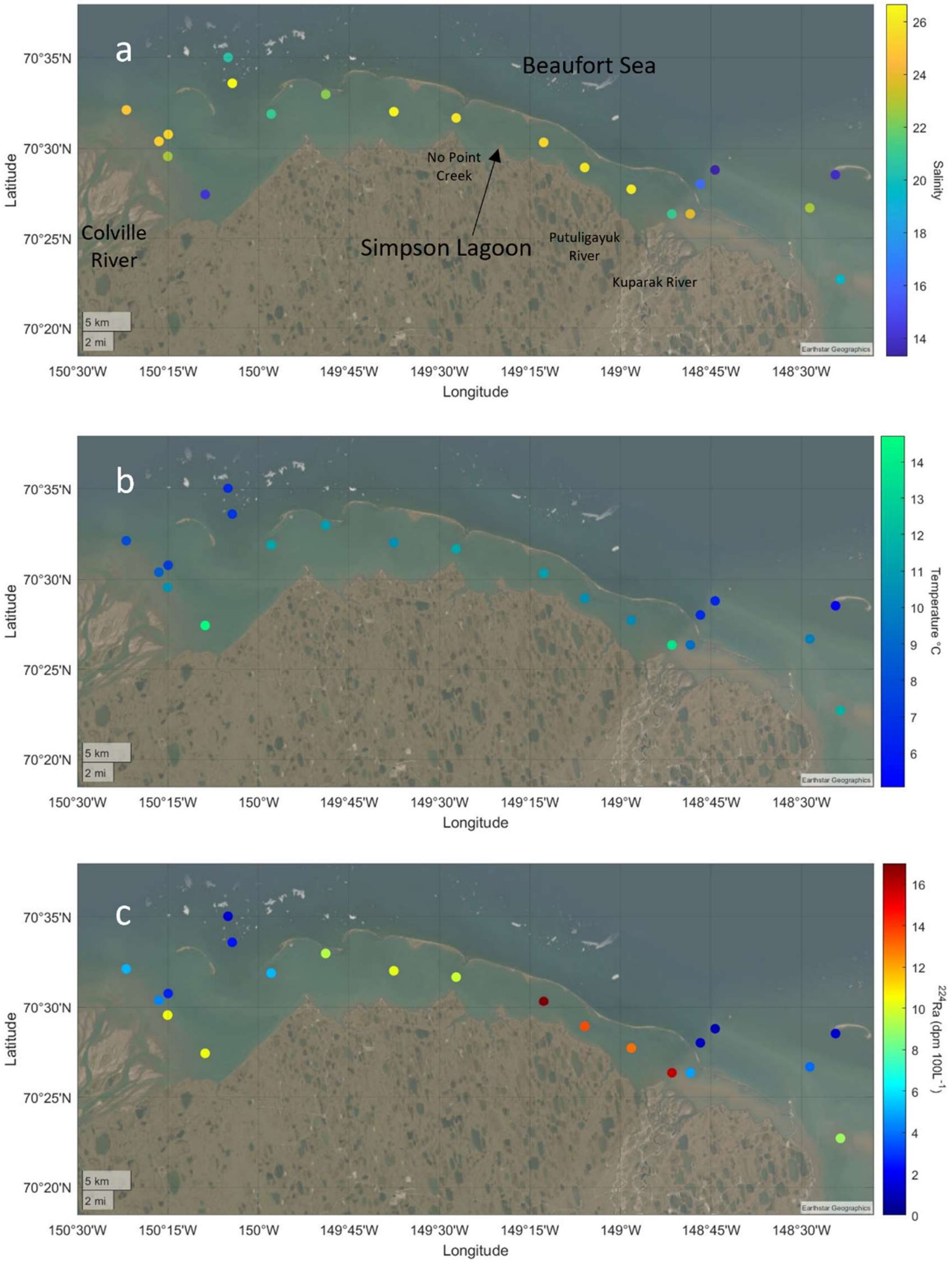

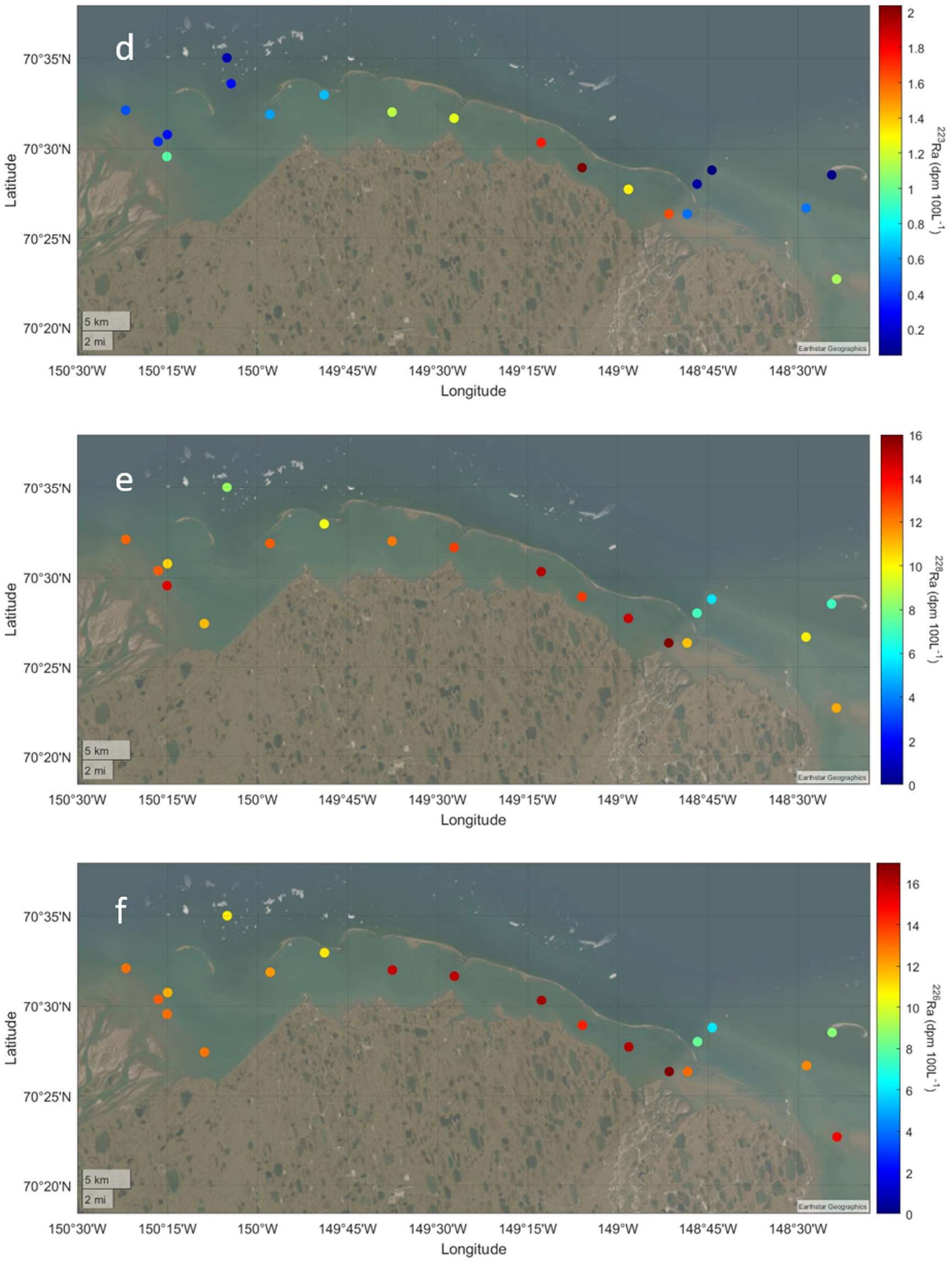

Supplemental Figure 1. Lagoon survey results for (a) salinity, (b) temperature, (c) ^{224}Ra, (d) ^{223}Ra, (e) ^{228}Ra, and (f) ^{226}Ra.

Near the mouth of the Colville River the depth decreases dramatically, which appears to force mixing between the layers of stratified ocean water, resulting in the highest salinities observed outside of the lagoon in the surface water. As most of the mixing between the lagoon and the Beaufort occurs at this wide western opening, and the fact that the salinities within the lagoon are higher than the surface water ocean samples taken, it is likely that these shallow, high salinity (S≥25) stations are the best representation of the ocean mixing endmember for this site, despite likely inputs from bottom sediment diffusion.

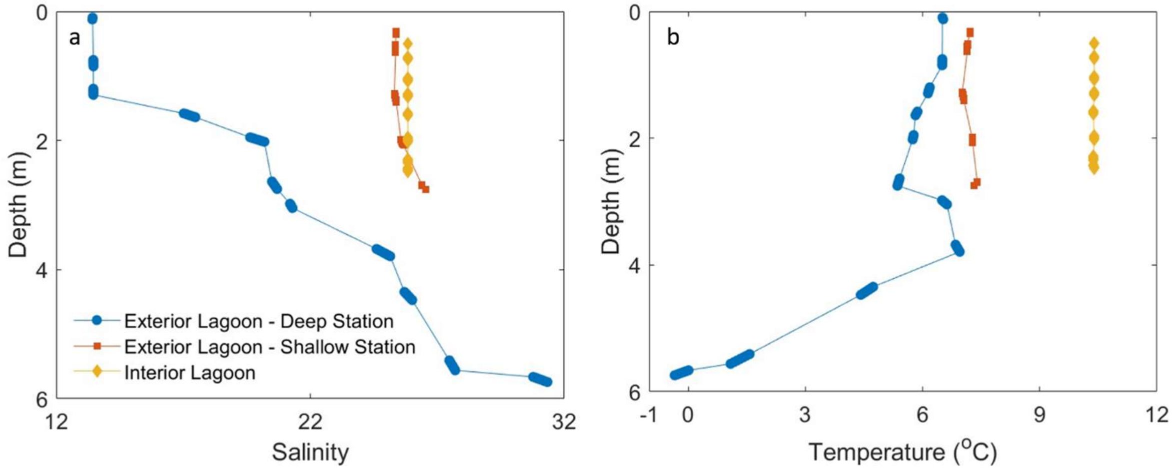

Supplemental Figure 2. Representative (a) salinity and (b) temperature plots acquired from CTD casts during the lagoon survey. Casts that were representative of most stations outside of the lagoon with deep water, outside of the lagoon with shallow water, and inside the lagoon are plotted here.

As a result, we averaged the activities from these stations [SLS20, 21, 24, 25: see data repository (Bullock et al. 2023)] to get the mixing endmember values we employed for ^{224}Ra, ^{223}Ra, ^{228}Ra, and ^{226}Ra, which were 3.64 ± 1.21 dpm 100L^{-1}, 0.37 ± 0.36 dpm 100L^{-1}, 11.8 ± 2.1 dpm 100L^{-1}, and 12.75 ± 0.35 dpm 100L^{-1}, respectively. These are comparable to Beaufort Shelf Ra samples for the short-lived isotopes, but considerably higher than reported long-lived isotopes: 4.8 ± 1.6 dpm 100L^{-1} for ^{224}Ra, 0.11 ± 0.22 dpm 100L^{-1} for ^{223}Ra, 5.5 ± 2.2 dpm 100L^{-1} for ^{228}Ra, and 6.8 ± 2.0 dpm 100L^{-1} for ^{226}Ra. The Beaufort Shelf samples were taken at a depth <50 m, compiled from historical datasets (Smith et al. 2003; Trimble et al. 2004; Kadko and Muench, 2005; Kadko et al. 2008; Kipp et al. 2019; Dabrowski et al. 2022). The higher long-lived isotope values closer to the coast likely result from higher inputs from coastal bottom sediments and/or direct SGD inputs to the Beaufort Shelf. Because of the similar activities between the exterior and interior lagoon for the long-lived isotopes, ^{226}Ra and ^{228}Ra could not be used to constrain SGD in our box models.

S3. Rivers

Three rivers were sampled during each sampling period of this study: the Kuparuk River, the Putuligayuk River, and No Point Creek. A single sample from the Sagavanirktok River was also taken during July 2022. The three waterways sampled each period are underlain with continuous permafrost with an annual thaw depth between 0.3 - 0.9 m (Stuefer et al. 2017). The Kuparuk River is a clear water tundra river that drains an area of 8,421 km^2 on the North Slope (Kreit et al. 1992; Déry et al. 2005). Over the past two decades, the Kuparuk has had an average annual discharge of 1.52 billion m^3, with roughly 60% of this discharge occurring during the spring freshet in late May/early June (McClelland et al. 2014; USGS: Kuparuk 2023). The Putuligayuk River is smaller, draining an area of 471 km^2 and discharging an average of 0.11 billion m^3 y^{-1} between 1999 and 2017 with 60 - 70% of this discharge occurring during the spring freshet (Arp et al. 2017; Stuefer et al. 2017). No Point Creek is a small, ungauged stream that is within several hundred meters of our main field site. Lagoon influence was observed at our sampling station there, with salinities higher than 2 being observed in the stream up to a quarter mile inland during high water level sampling visits, while salinities farther upstream were ~0.1. River samples were taken from rapidly-moving water close to the center of the streams using the same sampling methods as for the lagoon surface water.

S3.1 River Discharge and Caveats

Because there were no significant differences between dissolved Ra activities in different rivers or across seasons, river discharge was the most important factor governing dissolved Ra inputs to Simpson Lagoon. No current gauging station exists for the Putuligayuk River, so historical data from 1999 – 2017 were used (Arp et al. 2017). Discharge values for the Kuparuk and Colville Rivers were determined from USGS gauging stations (USGS[a] 2023; USGS[b] 2023) for the week leading up to the sampling period, as shown in Supp. Table 1. Because the Colville River gauge does not capture all discharge, the values were corrected using the modeled total discharge (McClelland et al. 2014) and accounting for the percentage missed by the gauge. Additionally, most Colville discharge bypasses the lagoon inlet. Based on sedimentation rates in Simpson Lagoon, it is unlikely that more than ~15% of annual Colville discharge enters the lagoon (Schreiner et al. 2013). Since this value is loosely constrained, we consider 5 – 15% of Colville River discharge as potentially entering the lagoon, as represented in the river discharge reported errors. The Ra activities applied to the Colville River discharge were the average between the Kuparuk and Putuligayuk Rivers. No Point Creek Ra activities were applied to all ungauged runoff.

S3.2 Ra desorption from riverine suspended sediments

Freshly deposited sediment from the edge of the freshwater reaches of the Kuparuk River was collected in glass jars during the summer sampling periods. The samples were dried at 40°C and a dry weight of ~30 g sediment was used for each desorption experiment. Coastal seawater (S~33) from Vineyard Sound was collected and filtered in the same way as in Section 2.3. A salinity of 33 was chosen to simulate maximum desorption and is similar to the salinities observed in the lagoon during the autumn sampling period. Although the salinities during the summer periods were closer to 15, most desorption occurs before this salinity is reached (Moore et al. 1995; Krest et al. 1999). Prior to the desorption experiment, the water was stored in a 20 L plastic cubitainer and cooled to 4 – 6°C to mimic summer period temperatures for the Kuparuk River.

Once cooled, 30 g of dry sediment were added to the cubitainer. A peristaltic pump was used to circulate water through the container to ensure sufficient agitation of the sediment. After six hours, the water was filtered through a Mn-oxide fiber at a rate <1 L min^{-1} to scavenge the desorbed Ra. A plug of plain acrylic fiber was used to filter out any sediment. The Mn-oxide fiber was then rinsed and analyzed in the same way described in Section 2.2 of the main paper.

To determine the percentage of desorbed ^{228}Ra and ^{226}Ra, Kuparuk River sediment was packed into plastic counting vials and capped with a plastic vial cap. The sediment was then counted using the same method as above to get the bulk sediment ^{226}Ra and ^{228}Ra totals. The percentages of Ra desorbed were calculated by dividing the desorbed Ra values by the bulk (^{226}Ra, ^{228}Ra) or surface Ra activities (^{223}Ra, ^{224}Ra), which were determined by emanation experiments.

S3.3 Emanation Experiments

Diffusion of Ra from bottom sediments and desorption from suspended riverine sediments are in part controlled by surface bound Ra, which we quantified via ^{224}Ra and ^{223}Ra emanation experiments on Simpson Lagoon bottom sediments and Kuparuk River suspended sediments. Our method was modified from Cai et al. (2012). Briefly, wet sediment was weighed, then dried at 60°C and weighed again. Between 20 - 25 g of sediment and 150 mL MilliQ water were added to a Teflon beaker to form a slurry. The slurry was ultrasonicated for 5 minutes. Next, 6 drops of concentrated $NH_3 \cdot H_2O$ were added to adjust the pH to between 8 - 9. Once the pH was corrected, 1.0 mL $KMnO_4$ (3.0 g L^{-1}) and 1.0 mL of $MnCl_2$ (8.0 g $MnCl_2 \cdot 4H_2O$ L^{-1}) were added and the mixture was stirred. This step creates a suspension of MnO_2, adsorbing the freed Ra in the slurry. The slurry was filtered through a 142 mm diameter, 0.7 µm pore size, GF filter. Vigorous stirring while filtering ensured even distribution of sediment on the filter. Vacuum filtration continued until no more water droplets could be pulled from the filter.

The filters and sediment were weighed to ensure the water to sediment ratio was ~0.4, as this can impact the efficiency of the measurement. The filters were placed in special chambers designed by Cai et al. (2012) and analyzed on RaDeCC delayed coincidence alpha detectors to determine the ^{224}Ra and ^{223}Ra emanating from the sediments. Method efficiencies were determined using fiber standards spiked with known activities of ^{227}Ac, ^{232}Th, and ^{226}Ra and analyzed using the same method as the samples (Scholten, 2010).

Supplemental Table 1. Water and sediment values used in the Ra box models.

Parameter	Units	Spring		-----------------------Summer-----------------------						Autumn	
		Jun - 22	±	Aug - 21	±	Jul - 22	±	Jul - 23	±	Oct - 22	±
River Discharge	x 10^6 m^3/day	35	28	11	3	9.4	0.5	28	9	4.8	0.2
Suspended Sediment Load	x 10^9 g/day	15	7	1.6	0.8	1.3	0.6	2.1	1.0	0.3	0.1
Runoff	x 10^6 m^3/day	20		2.9		4.4		0		0	
Sediment Resuspension	x 10^5 kg/day	NA		NA		NA		NA		1.4	6.0
Advective Flow (Bottom Sediments)	x 10^6 m^3/day	NA		16	3	18	3	17	3	26	4.3
Residence Time in Lagoon	days	1.4	0.2	9.4	4.2	26.5	7.1	5.0	3.1	3.9	4.5
Ocean Mixing	x 10^6 m^3/day	NA		52	16	18	4	100	40	130	70

S3.4 Results: radium inputs from riverine sediment

Desorption experiments and emanation experiments were performed, as detailed above. The desorbed activities account for ~60% of the total surface bound ^{224}Ra and ^{223}Ra on the Kuparuk River sediment, which come to 0.16 ± 0.01 dpm g^{-1} and 0.01 ± 0.001 dpm g^{-1} for ^{224}Ra and ^{223}Ra, respectively. This places the surface available Ra on river sediment between the values obtained for the silty fraction of Simpson Lagoon sediment (^{224}Ra: 0.35 ± 0.03 dpm g^{-1}; ^{223}Ra: 0.023 ± 0.007 dpm g^{-1}) and the sandy fraction (^{224}Ra: 0.10 ± 0.01 dpm g^{-1}; ^{223}Ra: 0.007 ± 0.002 dpm g^{-1}). The long-lived isotopes were checked using the bulk Ra activity of the river sediments. For the Kuparuk River, the ^{228}Ra activity was 0.7 ± 0.1 dpm g^{-1} and the ^{226}Ra activity was 1.14 ± 0.02 dpm g^{-1}. The Putuligayuk River activities were 1.0 ± 0.1 dpm g^{-1} and 1.45 ± 0.03 dpm g^{-1} for ^{228}Ra and ^{226}Ra, respectively. The desorption activities come to 9.5% of the total ^{228}Ra and 7.2% of the total ^{226}Ra activity. These percentages are lower than those seen in the Mackenzie River, which had desorption percentages of 30% for ^{228}Ra and 14% for ^{226}Ra

(Kipp et al. 2020) but are similar to those observed in rivers closer to Anchorage, AK (Bullock et al. 2022). If the desorption inputs from the Colville have the high desorption values seen in the Mackenzie (30% of total for ^{228}Ra and ^{226}Ra) instead of the lower values of the Kuparuk, the final SGD estimate would decrease by ~15%.

The desorption values are on the lower side, but still within the range of reported desorption values in the literature, which range from 7% (Luo et al. 2019) to greater than 50% (Moore and Scott 1986). In the same way that Ra K_d values appear to be impacting groundwater Ra activities, similar factors are likely preventing higher rates of desorption from riverine suspended sediments. Tundra rivers have high quantities of organic matter (Rawlins et al. 2021), which can block exchange sites where Ra could desorb when salinity increases (Rama and Moore 1996). Another factor that is known to strongly sorb Ra and therefore impact its partitioning coefficient is Fe-oxide (Gonneea et al. 2008; Beck and Cochran 2013). Suspended sediments for the Kuparuk and Colville rivers have been shown to be enriched in iron, particularly during periods of low flow where Fe averages 3.7% dry weight of Kuparuk suspended sediments (Trefry et al. 2004). Together, these factors may decrease the amount of Ra available for exchange upon entering the salinity mixing zone of the estuary, shedding light on the low percentage of Ra that is released during the desorption process in these rivers.

S4. Diffusion

S4.1 Diffusion Experiments

Two types of experiments were performed to quantify sediment diffusion as a potential source of Ra isotopes to the lagoon. Both experiments were conducted at 4 - 6°C to mimic Simpson Lagoon summer temperatures and were based on the method of Beck et al. (2007). In order to control the salinity of our experiments we used a mix of MilliQ water and seawater to achieve our target salinity. Water used for the first experiment was a mix of MilliQ water and coastal seawater, collected from Vineyard Sound and filtered by the Environmental Systems Laboratory in Woods Hole, MA. The second experiment utilized filtered Simpson Lagoon water with a salinity of ~15, to determine whether the high organic carbon content in Simpson Lagoon surface water might impact Ra diffusive fluxes. Ra was removed from both types of seawater by passing it through Mn-oxide coated fibers (2 packed cartridges, 10 g each) at a flow rate of 0.5 L min^{-1}.

Sampling conditions in 2021 (ie. choppy waters) made it difficult to take undisturbed cores from lagoon bottom sediment. Therefore, the first experiment used grab-sampled bottom sediment from 1.6 km offshore that was stored frozen after collection, thawed, and placed in 2 L plastic jars as a 4 cm thick layer (surface area = 0.0175 m^2) over which ~1 L of Ra-free water was added. Two concurrent incubations were run at salinities of 15 and 33, respectively. The experiment was sampled nine times, with the longest incubation lasting 22 days, to reach approximate equilibrium with the ^{224}Ra isotope and cover at least two half-lives for ^{223}Ra. During sampling, the overlaying water was removed, and all diffused Ra was scavenged onto Mn-oxide fibers. New Ra-free water was added to the incubations and the incubation time was reset.

The second experiment used two sediment cores, taken in July 2022, 0.4 km away from the mainland, that were overlain with 1 L of Ra-free seawater. Two incubations of 7 and 33 days were performed, after which the overlying water was filtered through a Mn-oxide fiber to scavenge the diffused Ra. For both experiments, the sample fibers were analyzed for all four Ra isotopes using the methods described in section 2.2 of the main paper.

S4.2 Diffusion from Bottom Sediments

Diffusion was calculated using the model from Beck et al. (2007):

$$I_t = \left(\frac{J_{diff}A}{\lambda}\right)\left(1 - e^{-\lambda t}\right) \qquad \text{(Supplemental Equation 2)}$$

where I_t is the Ra inventory at time t, J_{diff} is the Ra diffusive flux, A is the area of the sediment surface, and λ is the decay constant for the Ra isotope being measured. This model assumes the Ra flux is driven purely by diffusion. The short-lived isotope diffusion models are provided in Supp. Figure 3, with all diffusive flux rates located in Supplemental Table 2. These rates are on the lower end, but still well within the range of diffusive fluxes in the literature where they have been measured directly. These ranges are 1.2 -313 dpm m^{-2} d^{-1}, 1.13 - 4.9 dpm m^{-2} d^{-1}, 0.14 - 11.7 dpm m^{-2} d^{-1}, and 0.005 -11.0 dpm m^{-2} d^{-1} for ^{224}Ra, ^{223}Ra, ^{228}Ra, and ^{226}Ra, respectively (Beck et al. 2007; Rodellas et al. 2012; Garcia-Orellana et al. 2014; Rodellas et al. 2015; Rodellas et al. 2017).

For all isotopes, saline incubations had consistently higher Ra inventories than the brackish incubations, showing that Ra release via diffusion has a strong dependence on salinity in this environment. The rate increase between the brackish and saline incubations was substantial, with the isotopes increasing by factors of 3.9, 2.0, and 1.9 for ^{224}Ra, ^{228}Ra, and ^{226}Ra, respectively. The rate increase for ^{223}Ra was a factor of 27, which is likely not real and more reflective of detection limitations during the brackish incubations, rather than a high flux during the saline incubations. Both experimental designs produced similar results, increasing confidence in our diffusive flux estimates. For ^{224}Ra the saline jar incubations resulted in a flux of 62 ± 14 dpm m^{-2} d^{-1} (n = 10) while the saline core incubations were 24 ± 5 dpm m^{-2} d^{-1} (n = 3). These results were averaged to get a final flux of 43.4 dpm m^{-2} d^{-1}. The results for ^{223}Ra were even closer, with the jar incubation diffusive flux equaling 1.37 ± 0.34 dpm m^{-2} d^{-1} and the core incubations equaling 1.42 ± 0.31 dpm m^{-2} d^{-1}.

Supplemental Table 2. Ra inputs from sediment sources.

Source	Unit	^{224}Ra	±	^{223}Ra	±	^{228}Ra	±	^{226}Ra	±
River Desorption	dpm/g	0.09	0.01	0.006	0.002	0.07	0.01	0.08	0.004
Brackish Diffusion Rate	dpm/m^2/day	13.9	5.6	0.14	0.05	4.1	10.6	0.95	0.48
Saline Diffusion Rate	dpm/m^2/day	43.5	8.3	3.84	0.47	8.2	19.7	1.77	0.62

Previous studies that have utilized laboratory experiments to derive diffusive fluxes of Ra isotopes have incubated sediments either with water sourced from the overlying column of water or with seawater diluted to the maximum salinity observed during sampling (Beck et al. 2007; Rodellas et al. 2012; Rodellas et al. 2015). This study shows that seasonal variations in salinity can have important effects on diffusive inputs of Ra, with higher salinities during autumn driving up the diffusive flux of Ra from the sediments. This matches our understanding of Ra partitioning, since higher salinity solutions result in lower Kd values (Webster et al. 1995; Gonneea et al. 2008), resulting in a higher proportion of surface exchangeable Ra partitioning into the liquid phase due to cation exchange processes. As a result, we use the diffusive flux values that best correspond to the salinity measured each season: the brackish value for the spring period, an intermediate value between the brackish and saline fluxes for the August 2021 and July 2022 periods, and the saline value for the October 2022 and July 2023 periods.

Caveats for our diffusion fluxes include the fact that several samples during early incubations were impacted by sediment resuspension, where large amounts of sediment were resuspended when the overlying water was added and had not fully settled before the end of the incubation. Even if it had fully settled, resuspension could have increased activities via other means such as heighted porewater overturning. As a result, these data were omitted from our model but can still be seen in S. Fig. 3. Following this observation, care was taken when adding new overlaying water for all incubations to avoid significant resuspension effects. Additionally, the model we chose neglects the effects of bioirrigation, since previous studies have seen minimal to no evidence of this process occurring in Simpson Lagoon sediments (Hanna et al. 2014; Hanna et al. 2018). If we use the average diffusion rates estimated by Moore (2007), where intense bioirrigation was observed at the four sites under consideration, we get a 25% decrease in the SGD estimate from the easterly wind period. However, even if bioirrigation is occurring, it is unlikely to have rates as high as those observed in the locations looked at by Moore (2007).

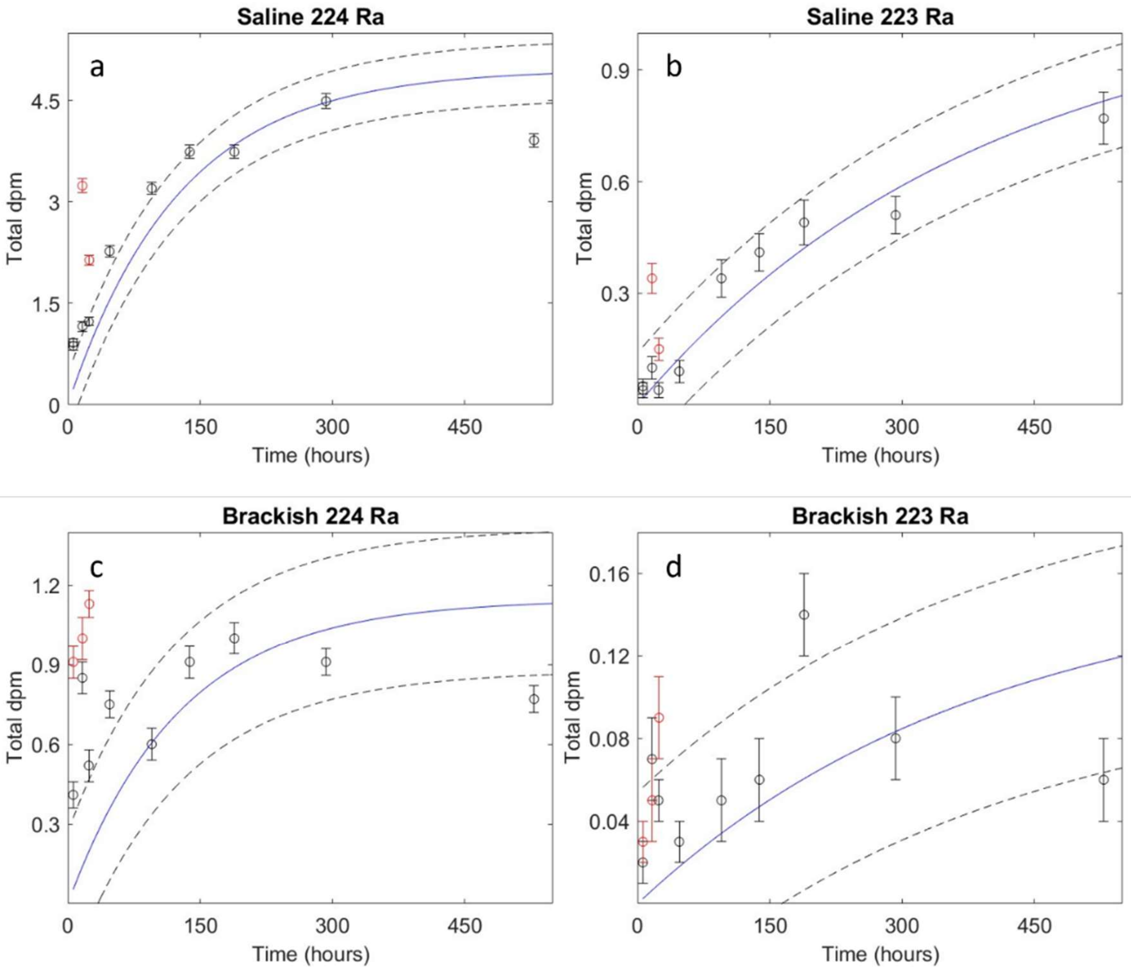

Supplemental Figure 3. Diffusion inventories over time in incubations with S~33 for ^{224}Ra (A) and ^{223}Ra (B). Diffusion inventories over time in incubations with S~15 for ^{224}Ra (C) and ^{223}Ra (D). Samples in red were early incubations where large amounts of sediment were resuspended and had not fully settled before the end of the incubation. These were omitted from the trend analysis and more care was taken to reduce resuspension for following samples.

S5. Runoff

The total watershed of Simpson Lagoon is approximately 70,000 km^2, according to satellite data analyzed in ArcGIS (ESRI 2021). The Colville watershed makes up 53,000 km^2 of this area (Walker & Hudson, 2003), the Kuparuk watershed accounts for 8,421 km^2 (Déry et al. 2005), and the Putuligayuk watershed consists of 474 km^2 (Stuefer et al. 2017). This leaves 8,100 km^2 that could facilitate runoff to the lagoon via ungauged streams.

To account for Ra inputs that may come from ungauged runoff, a runoff model for the Kuparuk River basin from Déry et al. (2005) was adopted:

$$P = R + E + \Delta S \qquad \text{(Supplemental Equation 3)}$$

In this model, P is the precipitation, R is the runoff, E is evapotranspiration, and ΔS is the change in soil moisture. Precipitation and soil moisture values were obtained from the Prudhoe Bay SNOTEL site (USDA^a, 2021; USDA^b, 2022). The evapotranspiration rate was assumed to be similar between the Kuparuk River basin and other areas of the Simpson Lagoon watershed, allowing the value of 46% of the total precipitation found by Déry et al. (2005) to be used.

Runoff was neglected for the thaw period, since it consisted largely of meltwater that had never come in contact with sediments and therefore would have little to no Ra present. Runoff was calculated for the ungauged regions for August 2021, July 2022, September/October 2022, and July 2023 using the SNOTEL site data (S. Table 1).

S6. Sediment Resuspension

A simplified sediment resuspension model was used, based on the model developed in the 2012 Louisiana Coastal Master Plan and refined in the 2017 plan (McCorquodale et al. 2017; Meselhe et al. 2013). The bottom sediment in Simpson Lagoon is largely silt and clay from the Colville and Kuparuk Rivers (Hanna et al. 2014, Hanna et al. 2018). These fine particle inputs give the lagoon a muddy appearance, as much of the river-sourced suspended sediments remain in the water column until ice reduces turbulence during the early winter (Weiss & Naidu, 1986). Ra inputs from these particles are considered part of the riverine inputs in our model, with resuspension calculated separately.

The equation for the resuspension of settled silt and clay is:

$$E_{res} = A\left(\frac{\tau_{bed}}{\tau_{cr}} - 1\right)^{n} \qquad \text{(Supplemental Equation 4)}$$

where A and n are calibration constants, $\boldsymbol{\tau}_{bed}$ is the bed shear stress, and $\boldsymbol{\tau}_{cr}$ is the critical shear stress required for resuspension of sediment particles. Given that the bottom sediment in Simpson Lagoon is largely derived from river deposition and is predominantly comprised of fine silt (Hanna et al. 2014), a critical shear stress ($\boldsymbol{\tau}_{cr}$) of 0.1 N m^{-2} was used, since this value has been shown to be most relevant for weakly consolidated, fine sediments (van Rijn, 2007). A maximum suspended sediment estimate was derived using a $\boldsymbol{\tau}_{cr}$ of 0.05 N m^{-2} for recently deposited, unconsolidated muddy sediments (van Rijn, 2007). For the calibration constants, we use the assumption often made in the literature of n = 1 and use the default value of 0.0001 for A (McCorquodale et al. 2017; Meselhe et al. 2013).

The bed shear stress is calculated using a friction coefficient [C_f = 0.0025 (McCorquodale et al. 2017)], the viscosity of the water (ρ_w), and the near-bed velocity (U_{bed}). The near-bed velocity is itself dependent on the wind driven current (U_w) and the bottom orbital velocity due to waves. We are neglecting the velocity effects of tides since Simpson Lagoon is a wind dominated estuary.

$$\tau_{bed} = C_f \cdot \rho_w \cdot (U_{bed})^2$$ (Supplemental Equation 5)

$$U_{bed} \approx U_c + U_{orb}$$ (Supplemental Equation 6)

The wind driven current is estimated from local wind speeds from Prudhoe Bay (NOAA, 2023) and a wind/current model for Simpson Lagoon discussed in Dasher et al. (2016) with wind speed (W_s) in m s^{-1} for the summer periods (August 2021: 4.2 m s^{-1}; July 2022: 3.9 m s^{-1}; July 2023: 4.4 m s^{-1}) and the autumn period (October 2022: 5.5 m s^{-1}) (NOAA 2023).

$$U_c = (10.1 + 1.74 \cdot W_s) \cdot 0.01$$ (Supplemental Equation 7)

The bottom orbital velocity is based on the method of Wiberg and Sherwood (2008):

$$U_{orb} = \frac{H_S \pi}{T \sin\left(\frac{2\pi d}{L}\right)}$$ (Supplemental Equation 8)

where H_s = significant wave height (m)

T = wave period (s)

L = wavelength (m)

d = water depth (m)

An average significant wave height was calculated using wind speed, water depth, and distance from shore in the windward direction (fetch) using the method of Sawyer et al. (2013) for a similarly shallow estuary:

$$H_S = \left(\frac{0.241 W_S{}^2}{g}\right)\left(\tanh(0.493\delta^{0.75})\tanh\left[\frac{0.00313\chi^{0.57}}{\tanh(0.493\delta^{0.75})}\right]\right)^{0.87}$$ (Supplemental Equation 9)

where χ = distance from shore in the windward direction = fetch (m)

δ = dimensionless water depth ($dg/W_s{}^2$)

The average wave period and wavelength were also calculated using the method from Sawyer et al. (2013):

$$T = \left(\frac{7.52 \quad s}{g}\right)\left(tanh(0.331\delta^{1.01})tanh\left[\frac{0.0005215\chi^{0.73}}{tanh(0.331 \quad ^{1.01})}\right]\right)^{0.37} \qquad \text{(Supplemental Equation 10)}$$

$$\left(\frac{2\pi}{T}\right)^2 \approx g\frac{2\pi}{L}tanh\left(\frac{2\pi}{L}d\right) \qquad \text{(Supplemental Equation 11)}$$

Once all parameters required for the calculation of E_{res} had been obtained, a simplified, tiered model of the lagoon bottom was used to estimate resuspension for the depths of 0 - 2.5 m (Supplemental Figure 4), where 1.5 m depth was estimated to be achieved by 1 km away from shore and ≥2 m depth was assumed greater than 2 km away from shore. The summer period models produced zero re-suspension of Ra containing sediments, based on wind speeds measured during the sampling periods and assuming weak consolidation of the bottom sediments. Sediments with less consolidation may be resuspended and river sediment that has not already settled may remain in the water column; however, in the case of river sediments we account for Ra inputs via desorption upon their entrance to the lagoon. The freeze up period model produced a resuspension of 1.0 – 9.1 x 10^5 kg d^{-1}. This is equivalent to 0.4 - 3.7 g m^{-2} d^{-1}, which is on the lower end of sediment resuspension rates but still within the range of those reported for another northern coastal lagoon (Lund-Hansen et al. 1999). Even assuming maximum desorption based on the exchangeable surface Ra, the inputs from resuspension during the autumn period come to <0.05% of total Ra inputs for both short-lived isotopes and <2% for both long-lived isotopes. During storms or extreme high wind events the inputs from resuspension are likely much higher.

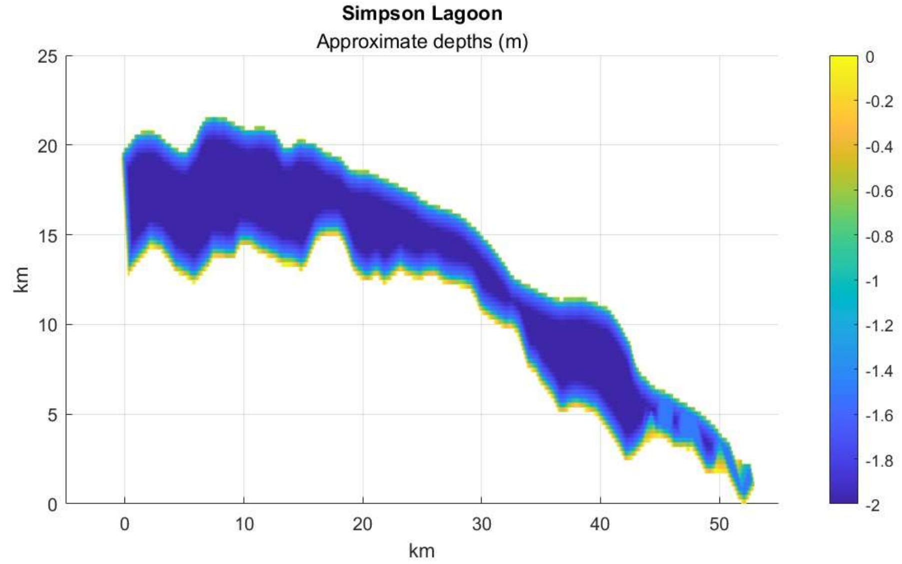

Supplemental Figure 4. Simplified depth model for Simpson Lagoon.

S7. Wind driven advective flow through bottom sediments

Benthic exchange was estimated using the wave-pumping model developed by Sawyer et al. (2013) for a similarly sized and shallow estuary in Delaware, USA. We neglect the impact of tides, since Simpson Lagoon is a wind dominated estuary. We also neglect the impact of bedforms, given no visual evidence of bedforms at our study site. Bedforms may be present elsewhere in the lagoon, so the results from this model are considered conservative.

The wave-pumping rate for a flat (no bedforms) bottom is given by

$$q_w = \frac{KH_S}{L\,cosh\left(\frac{2\pi}{L}d\right)} \qquad \text{(Supplemental Equation 12)}$$

Where K is the hydraulic conductivity. Three hydraulic conductivities (6.5 x 10^{-9} m s^{-1}, 9.5 x 10^{-5} m s^{-1}, and 1.1 x 10^{-4} m s^{-1}) were measured in Simpson Lagoon sediment (Guimond et al. 2023). The median hydraulic conductivity of 9.5 x 10^{-5} m s^{-1} was used in our best estimate model, though this is likely an overestimate as much of the lagoon bottom sediment is a small grain/clay-like material.

A simple depth model of the lagoon floor was created in MATLAB, based on our transect across the lagoon (S. Fig. 4). The lagoon model was split into a 100 x 1000 grid with fetch, wave height, wave period, wavelength, and finally the wave-pumping rate calculated for each grid space. The volume of water pumped through the bottom sediments was finally obtained by integrating the pumping rate over the bottom area of the lagoon and the course of a day.

Due to the presence of ice, advective flow driven by wind was assumed to be negligible during the thaw period. During the open water periods, the calculated advective flow based on the median K was similar across both years, with August 2021 equaling 1.6 ± 0.3 x 10^7 m^3 d^{-1}, July 2022 equaling 1.8 ± 0.3 x 10^7 m^3 d^{-1}, and July 2023 equaling 1.7 ± 0.3 x 10^7 m^3 d^{-1}. The increase of wind speeds during the freeze up period caused a predictable increase in advective flow, coming to 2.6 ± 0.4 x 10^7 m^3 d^{-1}.

S8. Ocean Mixing

S8.1 Lagoon Residence Time

Determining residence time is notoriously difficult, as different methods have different caveats and may not always be applicable to all systems. For example, tidal prism models are often used to calculate residence time (Sanford et al. 1992); however, in systems like Simpson Lagoon where wind-driven water level changes are greater than tidal influence, tidal prism models will not produce reliable results (Sanford et al. 1992). To obtain a maximum residence time estimate, we used a freshwater flushing calculation (Supp. Table 3). Given the river discharge during each sampling period, this estimate is based on how long it would take to fully replace the water in Simpson Lagoon using only river discharge. To maintain a similar volume within the lagoon, the water needs to leave the lagoon at a rate at least fast enough to keep up with the accumulation of river water. This estimate does not take ocean mixing into account.

Another method that can be used is a salt balance model:

$$T_w \;=\; V \div \left[\frac{(S_r*Q_r)-(S_L*Q_r)}{(S_r-S_{oc})} + Q_r\right] \qquad \text{(Supplemental Equation 13)}$$

where T_w = residence time in days

Q_r = flux from rivers and runoff (m^3 d^{-1})

S_r = salinity in rivers

S_L = average salinity in lagoon (seasonally dependent)

S_{oc} = salinity in the ocean (Beaufort Shelf)

A variation of this model was employed for the stratified periods, in order to account for mixing between layers and the different volumes of water at different salinities. Errors for all time points are based on uncertain inputs from the Colville River, with the minimum bound equaling 5% of Colville River discharge and the maximum bound equaling 15%. During the July 2023 lagoon survey, we observed that the water outside of the lagoon was ~2 higher than the highest salinities observed within the lagoon. For the stratified periods, we took the ocean endmember salinity as being 2 higher than the deep, salty layer of the lagoon, while the non-stratified period without exterior lagoon data (ie. October 2022) had an ocean salinity ~2 higher than the highest observed salinity measured in the lagoon. The ocean endmember salinity here is unlikely to be 30 or higher, due to inputs from major rivers that enter nearby coastal waters.

Based on our salt-balance calculations, July 2022 has the longest residence time of 31 ± 11 days, August 2022 has an intermediate time of 14 ± 3 days, and October 2022 and July 2023 have the shortest residence times of 9 ± 4 days and 2 ± 0.5 days, respectively. Despite their wide range, these residence times are consistent with the freshwater flushing times (Supp. Table 3) and the relative amount of freshwater present in the lagoon. We also observed the salinity in the lagoon increase from 11.3 to 26.8 in a 48-hour time period during our July 2023 field campaign, providing further evidence that mixing between the lagoon and the Beaufort Sea can occur on very short time scales.

We were also able to utilize our Ra data to estimate residence time by employing the continuous-input radium age model, which was developed by Moore et al. (2006) and estimates the apparent water age (τ) of a parcel in the estuary using the AR (short lived Ra isotope: long lived Ra isotope) of the main flux into the system (F) and the inventory AR in the estuary (I). F(^{224}Ra/^{226}Ra) and F(^{223}Ra/^{226}Ra) were both utilized and were based on the average activity ratios in groundwater samples for each sampling period. The decay constant of the short-lived isotope is represented by λ (λ_{224} ~ 0.19 d^{-1}; λ_{223} ~ 0.0608 d^{-1}).

$$\tau = \frac{F\left(\frac{224Ra}{226Ra}\right) - I\left(\frac{224Ra}{226Ra}\right)}{I\left(\frac{224Ra}{226Ra}\right)\lambda_{224}} \qquad \text{(Supplemental Equation 14)}$$

Our Ra - derived residence times are shown in Supp. Table 3. Estimates for June 2022 were not included as salinity data indicated that most water in the lagoon was from ice melt and rivers.

The July 2023 lagoon survey also allowed us to see variations in Ra activities across the full horizontal axis of the lagoon. As expected, higher activities were seen for the short-lived isotopes in the shallow eastern end of the lagoon (Supp. Fig. 1), where sediment discharge from the Kuparuk River keeps most of the area to depths under 2 m. The lowest activities are seen at the broad western mouth of the lagoon, where most exchange with Beaufort seawater occurs. Though fewer stations exhibit these low values, this is the deepest part of the lagoon. Intermediate activities are seen in the region where the three previous field campaigns sampled, where depths average 2 m. This indicates that the intermediate values in our main sampling area are likely a good indication of the overall inventory of the lagoon, solidifying our inventory estimates for August 2021, July 2022, and October 2022. Although the full lagoon average Ra activities and the activities from the main sampling area were relatively close (± 2 dpm/100L for

^{224}Ra and ± 0.3 dpm/100L for ^{223}Ra), we used the average values from this region to estimate the inventory of July 2023, in order to avoid the overestimation of SGD caused by the over-weighting of high Ra values from shallow regions.

As with our salt-balance results, we see July 2022 having the longest residence time of 18 ± 4 days (^{224}Ra:^{226}Ra) and 30 ± 13 days (^{223}Ra:^{226}Ra), and October 2022 having the shortest residence times of 2.3 ± 0.1 days (^{224}Ra:^{226}Ra) and 0.3 ± 0.2 days (^{223}Ra:^{226}Ra). However, both August 2021 and July 2023 have intermediate times of 6 ± 2 days (^{224}Ra:^{226}Ra) and 8 ± 1 days (^{223}Ra:^{226}Ra) for August 2021 and 6 ± 2 days (^{224}Ra:^{226}Ra) and 8 ± 10 days (^{223}Ra:^{226}Ra) for July 2023. Because of the inherent uncertainties within all of these models, we decided to average the salt-balance model and the two Ra isotope model results to determine our residence times for each sampling period (Supp. Table 3).

Supplementary Table 3. Comparison between residence times in Simpson Lagoon based on season and method of determination.

Method	August 2021	July 2022	October 2022	July 2023
Salt Balance^{a}	14 ± 3	31 ± 11	9.0 ± 4.4	1.6 ± 0.5
Freshwater Flushing^{b}	29 - 44	26 - 53	67 - 193	13 - 26
^{224}Ra/^{226}Ra^{c}	5.8 ± 2.0	18 ± 3.5	2.3 ± 0.1	5.8 ± 2.2
^{223}Ra/^{226}Ra^{d}	8.3 ± 1.2	30 ± 13	0.3 ± 0.2	7.5 ± 9.7
Average[1]	9.4 ± 4.2	26.5 ± 7.1	3.9 ± 4.5	5.0 ± 3.1

[1] Average of a, c, and d.

S8.2 Mixing with the Beaufort Sea

Mixing losses (dpm d^{-1}) are determined using a mixing equation that utilizes residence time (T_w), lagoon volume (V = 4.9 x 10^{8} m^{3}), activities of specific isotopes within the lagoon (A_{lag}), and the activity of the corresponding isotopes in the ocean endmember (A_{oc}) (Supplemental Equation 15):

$$J_{mix} = \frac{V(A_{lag}-A_{oc})}{T_w} \quad \text{(Supplemental Equation 15)}$$

For the summer periods, the ocean influx per layer was calculated based on the salinity balance, the inputs/losses from ocean mixing were then determined separately for the top and bottom layers, with the final value being the sum of the two layers.

The ocean endmembers used are the high salinity stations from the July 2023 lagoon survey (see section S2). It is possible that there are seasonal changes to the ocean endmembers, as seen in Kipp et al. (2019). If the ocean endmembers were higher at any point during the year, then this would serve to lower our SGD estimates. However, short-lived isotopes will be impacted to a lesser degree than long-lived isotopes. This was shown in an error test where we altered the potential ocean endmember in our model. The impact of a 10% increase in the ocean endmember has a negligible impact on the short-lived isotope box model SGD estimates (≤ 2% change).

S9. SGD Radium Inputs

Once all terms in our box model (Supplemental Equation 1) have been estimated apart from SGD inputs (J_{SGD}), we can solve for the SGD flux of Ra. Based on these box model results, SGD inputs of Ra are highest during the autumn sampling period. No evidence for SGD is present during spring, when shorefast ice limits the movement of groundwater and no Ra excess is detected in the lagoon. This does not exclude the possibility of some fresh or brackish groundwater entering the lagoon, but the Ra signal is low enough to be masked by the large riverine and diffusive Ra inputs. Intermediate SGD inputs are observed during the summer period, with Ra inputs from SGD being in the same order of magnitude as summer river fluxes. Finally, the large increase in Ra activities during the autumn period can only come from SGD inputs. Please see the main paper for further discussion.

S10. Wind Data

As discussed in the main paper, wind-driven changes to the lagoon water level are likely the driving force behind SGD fluxes in this system. Here we present the wind direction and speed in the days leading up to, and during, our lagoon sampling for each field campaign (S.Fig. 5). It is easy to see the sustained easterly winds in October 2022 and July 2023, which lead to set-down of the lagoon water level (Guimond et al. 2023).

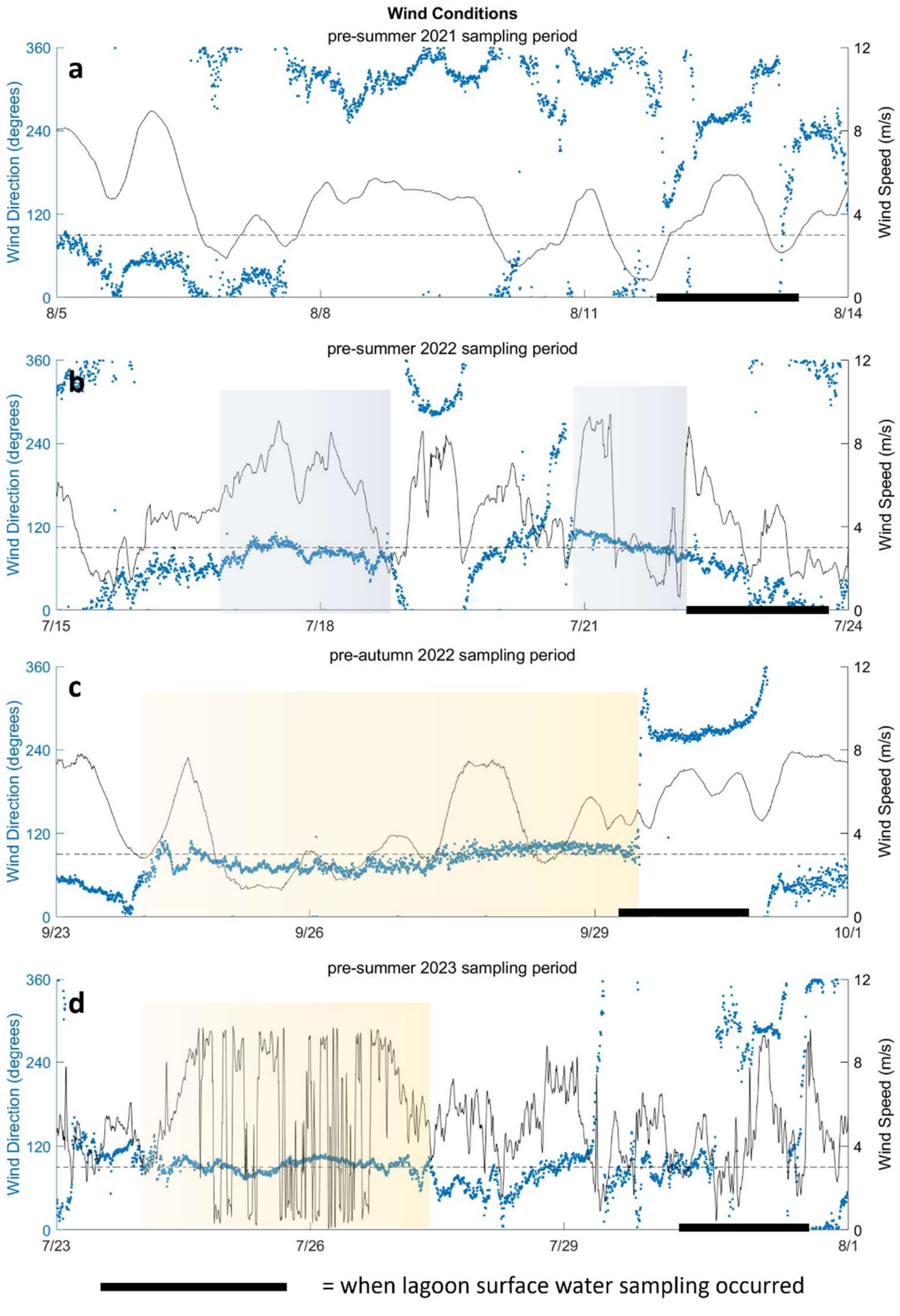

Supplemental Figure 5. Wind direction and speed for the days leading up to our lagoon sampling period for (a) August 2021, (b) July 2022, (c) October 2022, and (d) July 2023. Easterly winds occur at 90 degrees, as represented by the dotted black line. Periods with easterly winds sustained for long enough to induce set-down are highlighted in yellow, while periods with easterly winds but not enough time to induce set down are in grey.

References

Arp, C., D. Kane, S. Stuefer, and L. Hinzman. 2017. Hydrographic Data, Putuligayuk River Watershed, Alaska, 1999-2017. Arctic Data Center. doi:10.18739/A2FF3M05P

Beck, A. J. and M. A. Cochran. 2013. Controls on solid-solution partitioning of radium in saturated marine sands. Mar. Chem. **156**: 38-48. doi:10.1016/j.marchem.2013.01.008

Beck, A. J., J. P. Rapaglia, J. K. Cochran, and H. J. Bokuniewicz. 2007. Radium mass - balance in Jamaica Bay, NY: Evidence for a substantial flux of submarine groundwater. Mar. Chem. **106**(3-4): 419-441. doi:10.1016/j.marchem.2007.03.008

Bullock, E. J., M. A. Charette, P. Henderson, M. B. Cardenas, and J. McClelland. 2023. Radium in surface and ground water, Simpson Lagoon, Alaska, 2021-2022. Arctic Data Center. doi:*10.18739/A23B5W945*

Bullock, E. J., L. Kipp, W. Moore, K. Brown, P. J. Mann, J. E. Vonk, N. Zimov, and M. A. Charette. 2022. Radium Inputs Into the Arctic Ocean from Rivers: A Basin-Wide Estimate. J. Geophys. Res. Oc. **127**: e2022JC018964. doi:*10.1029/2022JC018964*

Cai, P., X. Shi, W. Moore, and M. Dai. 2012. Measurement of ^{224}Ra:^{228}Th disequilibrium in coastal sediments using a delayed coincidence counter. Mar. Chem. **138-139**: 1-6. doi:10.1016/j.marchem.2012.05.004

Cai, P., X. Shi, W. S. Moore, S. Peng, G. Wang, and M. Dai. 2014. ^{224}Ra:^{228}Th disequilibrium in coastal sediments: Implications for solute transfer across the sediment-water interface. Geo. Cosmo. Acta **125**: 68-84. https://doi.org/10.1016/j.gca.2013.09.029

Dabrowski, J. S., R. S. Pickart, D. A. Stockwell, P. Lin, and M. A. Charette. 2022. Physical drivers of sediment-water interaction on the Beaufort Sea shelf. Deep Sea Res. Part I: Oc. Res. Papers **181**: 103700. doi:10.1016/j.dsr.2022.103700

Dasher, D., T. Lomax, A. Bethe, M. Hoberg, S. Naidu, and S. Jewett. 2016. Offshore Oil/Gas Wastewater Study: 2014 Assessment of Simpson Lagoon. Report. Juneau: Alaska Department of Environmental Conservation. URL: https://dec.alaska.gov/media/16815/simpson - lagoon - 2016.pdf (accessed 3/27/2023).

Déry, S. J., M. Stieglitz, Å. K. Rennermalm, and E. F. Wood. 2005. The Water Budget of the Kuparuk River Basin, Alaska. J. Hydromet. **6**: 633-655.

ESRI 2021. ArcGIS Desktop: Release 10.8.2. Redlands, CA: Environmental Systems Research Institute.

Garcia-Orellana, J., V. Rodellas, J. Tamborski, M. Diego-Feliu, P. van Beek, Y. Weinstein, M. Charette, A. Alorda-Kleinglass, H. A. Michael, T. Stieglitz, and J. Scholten. 2021. Radium isotopes as submarine groundwater discharge (SGD) tracers: Review and recommendations. Earth Sci. Rev. **220**: 103681. doi:10.1016/j.earscirev.2021.103681

Gonneea, M. E., P. J. Morris, H. Dulaiova, and M. A. Charette. 2008. New perspectives on radium behavior within a subterranean estuary. Mar. Chem. **109**(3-4): 250-267. doi:*10.1016/j.marchem.2007.12.002*

Guimond, J. A., C. Demir, B. L. Kurylyk, M. A. Walvoord, J. W. McClelland, and M. B. Cardenas. 2023. Wind-modulated groundwater discharge along a microtidal Arctic coastline. Environ. Res. Lett. **18**(9): 094042. doi:*10.1088/1748 - 9326/acf0d8*

Hanna, A. J. M., M. A. Allison, T. S. Bianchi, F. Marcantonio, and J. A. Goff. 2014. Late Holocene sedimentation in a high Arctic coastal setting: Simpson Lagoon and Colville Delta, Alaska. Cont. Shelf Res. **74**: 11-24. doi:10.1016/j.csr.2013.11.026

Hanna, A. J. M., T. M. Shanahan, M. A. Allison, T. S. Bianchi, and K. M. Schreiner. 2018. A multi-proxy investigation of late-Holocene temperature change and climate-driven fluctuations in sediment sourcing: Simpson Lagoon, Alaska. The Holocene **28**(6): 984-997. doi:*10.1177/0959683617752845*

Kadko, D. and R. Muench. 2005. Evaluation of shelf-basin interaction in the western Arctic by use of short-lived radium isotopes: the importance of mesoscale processes. Deep-Sea Res. Part II: Topical Studies in Oceanography **52**(24-26): 3227-3244. doi:10.1016/j.dsr2.2005.10.008

Kadko, D., R. S. Pickart, and J. Mathis. 2008. Age characteristics of a shelf-break eddy in the western Arctic and implications for shelf-basin exchange. J. Geophys. Res. **113**: C02018. doi:10.1029/2007JC004429

Kipp, L. E., D. C. Kadko, R. S. Pickart, P. B. Henderson, W. S. Moore, and M. A. Charette. 2019. Shelf-Basin Interactions and Water Mass Residence Times in the Western Arctic Ocean: Insights Provided by Radium Isotopes. J. Geophys. Res. Oc. **124**: 3279 -3297. doi:10.1029/2019JC014988

Kipp, L. E., P. B. Henderson, Z. A. Wang, and M. A. Charette. 2020. Deltaic and Estuarine Controls on Mackenzie River Solute Fluxes to the Arctic Ocean. ESCO **43**: 1992-2014. doi:10.1007/s12237 - 020 - 00739 - 8

Kreit, K., B. J. Peterson, and T. L. Corliss. 1992. Water and sediment export of the upper Kuparuk River drainage of the North Slope of Alaska. Hydrobiologia **240**: 71-81.

Krest, J. M., W. S. Moore, and Rama. 1999. ^{226}Ra and ^{228}Ra in the mixing zones of the Mississippi and Atchafalaya Rivers: indicators of groundwater input. Mar. Chem. **64**: 129-152.

Lund-Hansen, L.C., M. Petersson, and W. Nurjaya. 1999. Vertical Sediment Fluxes and Wave-Induced Sediment Resuspension in a Shallow-water Coastal Lagoon. Estuaries **22**(1): 39-46.

Luo, H., J. Wang, , Q. Zhong, and J. Du. (2019). The desorption of radium isotopes in river sediments in Qinzhou Bay. Act. Oc. Sinica **41**(4), 27-41. doi:10.3969/j.issn.0253 - 4193.2019.04.003

McCorquodale, A., B. Couvillion, A. Dortch, M. Freeman, E. Meselhe, D. Reed, B. Roth, J. Shelden, G. Snedden, H. Wang, and E. White. 2017. 2017 Coastal Master Plan: Attachment C3 -1: Sediment Distribution. Version Final. Baton Rouge, Louisiana: Coastal Protection and Restoration Authority.

McClelland, J. W., A. Townsend-Small, R. M. Holmes, F. Pan, M. Stieglitz, M. Khosh, and B. J. Peterson. 2014. River export of nutrients and organic matter from the North Slope of Alaska to the Beaufort Sea. Water Res. Res., **50**(2): 1823-1839. doi:*10.1002/2013WR014722*

Meselhe, E., McCorquodale, J. A., Shelden, J., Dortch, M., Brown, T. S., Elkan, P., Rodrigue, M. D., Schindler, J. K., & Wang, Z. (2013). Ecohydrology Component of Louisiana’s 2012 Coastal Master Plan: Mass - Balance Compartment Model, J. Coast. Res. **67**: 16-28. doi:10.2112/SI_67_2.1

Moore, W. S. 1996. Large groundwater inputs to coastal waters revealed by ^{226}Ra enrichments. Nature, **380**: 612-614. doi:10.1038/380612a0

Moore, W. S. 2008. Fifteen years experience in measuring ^{224}Ra and ^{223}Ra by delayed - coincidence counting. Mar. Chem. **109**: 188-197.

Moore, W.S., H. Astwood, and C. Lindstrom. 1995. Radium isotopes in coastal waters on the Amazon shelf. Geo. Cosmo. Acta **59**(20): 4285- 4298.

Moore, W. S., J. O. Blanton, and S. B. Joye. 2006. Estimates of flushing times, submarine groundwater discharge, and nutrient fluxes to Okatee Estuary, South Carolina, J. Geophys. Res. Oc. **111**(C9). doi:10.1029/2005JC003041

Moore, D. G. and M. R. Scott. 1986. Behavior of ^{226}Ra in the Mississippi River Mixing Zone. J. Geophys. Res. **91**(C12): 14317-14329.

Precht, E. and M. Huettel. 2003. Advective pore-water exchange driven by surface gravity waves and its ecological implications. L&O **48**(4): 1674-1684. doi:10.4319/lo.2003.48.4.1674

Rama and W. S. Moore. 1996. Using the radium quartet for evaluating groundwater input and water exchange in salt marshes. Geo. Cosmo. Acta **60**(23): 4645- 4652.

Rawlins, M. A., C. T. Connolly, J. W. McClelland. 2021. Modeling Terrestrial Dissolved Organic Carbon Loading to Western Arctic Rivers. J. Geophys. Res. Biogeosci. **126**(10): e2021JG006420. doi:10.1029/2021JG006420

Rodellas, V., J. Garcia-Orellana, E. Garcia-Solsona, P. Masqué, J. A. Domínguez, B. J. Ballesteros, M. Mejías, and M. Zarroca. 2012. Quantifying groundwater discharge from different sources into a Mediterranean wetland by using ^{222}Rn and Ra isotopes. J. Hydro. **(466 – 467)**: 11- 22. doi:10.1016/j.jhydrol.2012.07.005

Rodellas, V., J. Garcia-Orellana, P. Masqué, and J. S. Font-Muñoz. 2015. The influence of sediment sources on radium-derived estimates of Submarine Groundwater Discharge. Mar. Chem. **171**: 107-117. doi:10.1016/j.marchem.2015.02.010

Rodellas, V., J. Garcia-Orellana, G. Trezzi, P. Masqué, T. C. Stieglitz, H. Bokuniewicz, J. K. Cochran, and E. Berdalet. 2017. Using the radium quartet to quantify submarine groundwater discharge and porewater exchange. Geo. Cosmo. Acta **196**: 58-73. doi:*10.1016/j.gca.2016.09.016*

Sanford, L. P., W. C. Boicourt, and S. R. Rives. 1992. Model for Estimating Tidal Flushing of Small Embayments, J. Waterw. Port Coast. Ocean Eng. **118**(6): 635 - 654.

Sawyer, A. H., F. Shi, J. T. Kirby, and H. A. Michael. 2013. Dynamic response of surface water-groundwater exchange to currents, tides, and waves in a shallow estuary. J. Geophys. Res. Oc. **118**: 1749-1758. doi:10.1002/jgrc.20154

Scholten, J. C., M. K. Pham, O. Blinova, M. A. Charette, H. Dulaiova, and M. Eriksson. 2010. Preparation of Mn-fiber standards for the efficiency calibration of the delayed coincidence counting system (RaDeCC). Mar. Chem. **121**(1 - 4): 206 - 214. doi:10.1016/j.marchem.2010.04.009

Schreiner, K. M., T. S. Bianchi, T. I. Eglinton, M. A. Allison, and A. J. M. Hanna. 2013. Sources of terrigenous inputs to surface sediments of the Colville River Delta and Simpson’s Lagoon, Beaufort Sea, Alaska. J. Geophys. Res. Biogeosci. **118**(2): 808-824. doi:*10.1002/jgrg.20065*

Smith, J. N., S. B. Moran, and R. W. Macdonald. 2003. Shelf-basin interactions in the Arctic Ocean based on ^{210}Pb and Ra isotope tracer distributions. Deep Sea Res. I, **50**: 397- 416. doi:10.1016/S0967-0637(02)00166-8

Stuefer, S. L., C. D. Arp, D. L. Kane, and A. K. Liljedahl. 2017. Recent extreme runoff observations from coastal arctic watersheds in Alaska. Water Resour. Res. **53**: 9145– 9163. https://doi.org/10.1002/2017WR020567

Tamborski, J., J. K. Cochran, H. Bokuniewicz, C. Heilbrun, J. Garcia-Orellana, V. Rodellas, and R. Wilson. 2020. Radium Mass Balance Sensitivity Analysis for Submarine Groundwater Discharge Estimation in Semi-Enclosed Basins: The Case Study of Long Island Sound. Front. Environ. Sci. **8**: 108. doi:10.3389/fenvs.2020.00108

Trimble, S. M., M. Baskaran, and D. Porcelli. 2004. Scavenging of thorium isotopes in the Canada Basin of the Arctic Ocean. Earth Planet. Sci. Lett. **222**: 915-932. doi:10.1016/j.epsl.2004.03.027

Trefry, J. H., R. D. Rember, R. P. Trocine, and M. Savoi. 2004. ANIMIDA TASK 5: Sources, Concentrations and Dispersion Pathways for Suspended Sediment in the Coastal Beaufort Sea. OCS Study MMS 2004 - 032. U.S. Department of Interior Minerals Management Service; Anchorage, AK. https://www.boem.gov/sites/default/files/boem -newsroom/Library/Publications/2004/2004_032.pdf

USDA[a], 2021. Precipitation, Accumulated, Prudhoe Bay, AK. Natural Resources Conservation Service and National Water and Climate Center, accessed (April 6, 2023) at URL [https://wcc.sc.egov.usda.gov/nwcc/site?sitenum=1177]

USDA[b], 2022. Precipitation, Accumulated, Prudhoe Bay, AK. Natural Resources Conservation Service and National Water and Climate Center, accessed (April 6, 2023) at URL [https://wcc.sc.egov.usda.gov/nwcc/site?sitenum=1177]

USGS[a]:15875000 COLVILLE R AT UMIAT AK, 2023, National Water Information System Data (USGS Water Data for the Nation), accessed [March 30, 2023], at URL [https://waterdata.usgs.gov/monitoring -location/15875000/#parameterCode=00065&period=P7D].

USGS[b]: KUPARUK R NR DEADHORSE AK, 2023, National Water Information System Data (USGS Water Data for the Nation), accessed [March 22, 2023], at URL [https://waterdata.usgs.gov/nwis/inventory/?site_no=15896000].

van Rijn, L. C. 2007. Unified View of Sediment Transport by Currents and Waves. I: Initiation of Motion, Bed Roughness, and Bed - Load Transport. J. Hydr. Eng. **133**(6): 649-667. doi:10.1061/ASCE0733-94292007133:6649

Walker, H. J. and P. F. Hudson. 2003. Hydrologic and geomorphic processes in the Colville River delta, Alaska. Geomorphology, **56**: 291-303.

Webster, I. T., G. J. Hancock, and A. S. Murray. 1995. Modelling the effect of salinity on radium desorption from sediments. Geo. Cosmo. Acta **59**(12): 2469-2476.

Weiss, H.V. and A. S. Naidu. 1986. ^{210}Pb flux in an Arctic Coastal Region. Arctic **39**(1): 59-64.

Wiberg, P. L. and C. R. Sherwood. 2008. Calculating wave-generated bottom orbital velocities from surface-wave parameters, Comput. and Geosci. **34**(10): 1243-1262. doi:10.1016/j.cageo.2008.02.010

Chapter 4: Methylmercury Inputs to the Arctic Ocean from Submarine Groundwater Discharge

Emma J. Bullock[1], Robert Mason[2], Emily M. Bristol[3], Hannah Inman[2], Wesley W. Huffman[2], M. Bayani Cardenas[4], James W. McClelland[5], Matthew A. Charette[6]

1. MIT-WHOI Joint Program in Oceanography/Applied Ocean Science & Engineering, Cambridge and Woods Hole, MA, USA

2. Department of Marine Sciences, University of Connecticut, Groton, CT, USA.

3. Marine Science Institute, University of Texas at Austin, Port Aransas, TX, USA.

4. Department of Geological Sciences, Jackson School of Geosciences, University of Texas at Austin, Austin, TX, USA

5. The Ecosystems Center, Marine Biological Laboratory, Woods Hole, MA, USA

6. Department of Marine Chemistry and Geochemistry, Woods Hole Oceanographic Institution, Woods Hole, MA, USA

Abstract: Supra-permafrost submarine groundwater discharge (SGD) is a potentially important, yet understudied, source of chemical species to the Arctic Ocean. Given that Arctic soils contain large quantities of mercury (Hg), some of which is present as the bioaccumulative neurotoxin methylmercury (MeHg), understanding the transport of Hg from these soils into coastal waters is essential for the people and wildlife of the region who rely on marine species for sustenance. Here, we conducted a multi-year seasonal study of total Hg (THg) and MeHg inputs to an Arctic coastal lagoon. Our analyses suggest that SGD inputs of THg during spring are negligible, while during summer and autumn they are 3.0 ± 1.7 mmol d^{-1} km^{-1} and 1.5 ± 0.6 mmol d^{-1} km^{-1} of lagoon shoreline, respectively, which are fluxes that are statistically similar to inputs from rivers. In contrast, SGD inputs of MeHg far exceed riverine and other inputs to the lagoon during ice-free periods, averaging 0.9 ± 0.6 mmol d^{-1} km^{-1} in summer and 0.10 ± 0.04 mmol d^{-1} km^{-1} in autumn, indicating that groundwater could be the dominant source of MeHg to the coastal Arctic Ocean during these times. As warming continues to thaw permafrost, the potential for groundwater mobilization and methylation of Hg in this region will likely increase. Consequently, this work challenges current assumptions regarding the dominant sources of MeHg to the Arctic Ocean and highlights a need to include SGD inputs in future high-latitude Hg budgets.

1. Introduction

Mercury (Hg) cycling in the Arctic is important due to the neurotoxic impacts of methylmercury (MeHg) on Arctic communities and ecosystems, primarily from the consumption of marine organisms (Dietz et al. 2013, AMAP, 2018, UN-Environment, 2019). Arctic soils contain high concentrations of Hg, largely due to the uptake of elemental Hg by vegetation and atmospheric circulation patterns that have caused enhanced Hg deposition in polar regions (Obrist et al. 2017, Dastoor et al. 2022). Furthermore, there is the potential for substantial Hg mobilization due to Arctic warming and release of Hg from permafrost (Mu et al., 2019, Chételat et al., 2022).

Despite these advances in our understanding of high-latitude Hg cycling, the transport of Hg through Arctic soils to the ocean has been largely overlooked. Recent mass balance studies on Arctic total Hg (THg) and MeHg acknowledged the potential importance of groundwater contributions, but lacked quantitative evidence due to the absence of data (Dastoor et al. 2022; Jonsson et al. 2022). Furthermore, Arctic MeHg budgets have significant uncertainties (Soerensen et al., 2016; Petrova et al., 2020; Jonsson et al., 2022), potentially leading to the overestimation of microbial water column production rates, as groundwater MeHg inputs were not included in these models. Understanding groundwater mobilization, methylation and transport of Hg to the Arctic Ocean is therefore critical for understanding current and future human and climate change impacts on Hg cycling and MeHg bioaccumulation in the Arctic.

Mass balance estimates of MeHg in the Arctic are complicated by its *in situ* formation and degradation through biological (Chiasson-Gould et al. 2014, Schartup et al. 2015, Soerensen et al. 2016, Mangal et al. 2019) and photochemical (Seller et al. 1996, Lehnherr et al. 2012, Klapstein et al. 2017, Klapstein & O'Driscoll, 2018) reactions. Despite prior estimates of low terrestrial fluxes of MeHg to estuarine systems, isotopic investigations show that most Hg in Arctic biota has near-zero Δ^{200}Hg values (Lim et al. 2024), which requires the oxidation of atmospheric Hg(0) to bioavailable Hg(II), rather than direct Hg(II) deposition (Zhou et al. 2021). One major oxidation pathway of Hg(0) in the Arctic is through terrestrial plants (Obrist et al. 2017), the impact of which can be seen in isotopic data from biota in the Mackenzie River delta (Lim et al. 2024).

However, apart from rivers, another potential source of Hg from terrestrial plants is submarine groundwater discharge (SGD), a well-known source of Hg into temperate coastal systems (Bone et al. 2007, Lee et al. 2011, Ganguli et al. 2014). SGD involves the discharge of fresh, brackish, or saline groundwater into coastal areas and is a known source of carbon and other species to the Arctic Ocean. SGD is a process that is expected to become increasingly important as warming drives thaw depths deeper in coastal Arctic regions (Connolly et al. 2020; Pedrazas et al., 2020). Hg is susceptible to release by SGD because recirculated saline water can mobilize Hg in sediments to a greater degree than fresh groundwater (Rahman et al. 2013, Spyropoulou et al. 2022). As aquatic microbial uptake is the foundation of biomagnification of MeHg into Arctic food webs and given evidence that suggests terrestrial inputs of MeHg may be more easily taken up compared to other sources (Jonsson et al. 2014, Jonsson et al. 2022), understanding the importance of SGD MeHg inputs compared to other external sources is vital for validating Hg ecosystem risk assessments.

This study investigated seasonal differences in dissolved MeHg and dissolved THg concentrations and fluxes from SGD into an Alaskan Arctic lagoon system using field measurements from five sampling campaigns across 3 years. Groundwater THg and MeHg concentrations were elevated compared to most non-polluted temperate regions (Laurier et al. 2007, Black[b] et al. 2009, Lee et al. 2011, Ganguli et al. 2012, Rahman et al. 2013, Szymczycha et al. 2013, Ganguli et al. 2014). Seasonal SGD-driven fluxes of THg and MeHg were found to depend on both the variations in dissolved constituent concentrations and changes in SGD water fluxes. During the ice-free season (post-freshet), MeHg inputs via SGD to Simpson Lagoon were found to exceed inputs from three nearby rivers. These results show that SGD is an important vector for Hg inputs to the Arctic Ocean that can no longer be overlooked in Arctic Hg models.

2. Study Location

Simpson Lagoon is a shallow semi-enclosed estuary (~245 km^2, average depth ~ 2m) situated along the Alaskan Beaufort Sea coast (Supplemental Fig. S1). The majority of this coastline is characterized by similar lagoons, which have minimal astronomical tidal influence (<15 cm), but experience large water level changes associated with wind direction and strength (Zimmerman et al. 2022, Guimond et al. 2023) and have shorefast ice from October to June (Reimnitz et al. 1978; Hanna et al. 2018). The shoreline consists of a narrow sandy beach that is backed by permafrost bluffs (~1 m), sections of which are experiencing degradation due to storm surge overtopping. Sand at this site is largely sourced from rivers, consisting of silicate minerals, such as quartz and feldspar, carried to the lagoon from the Brooks Range by the Colville River, as well as older silicate minerals and carbonates carried by Beaufort Shelf currents from the Mackenzie River (Schreiner et al. 2013). Some barrier islands have similar characteristics to the mainland, while others are thin sandbars with no tundra soils present. The site is underlain by continuous permafrost with an average summer active layer depth between 25-100 cm. Tundra soil at this site consists largely of peat and organic-rich soils near the surface with mineral soils found at deeper depths (Déry et al. 2005), while the beach is extremely heterogeneous in nature, consisting mostly of sand with intermittently buried blocks of peat. Lagoon sediments are fine-grained and largely sourced from deposition of river suspended sediments (Schreiner et al. 2013, Hanna et al. 2018). Temperatures range from winter lows of -40°C to summer highs of 10°C, with average annual precipitation of 22.5 cm y^{-1} (USDA, 2023). The lagoon receives freshwater inputs from multiple rivers and streams, with the largest rivers being the Kuparuk (discharge ~1.5 billion m^3 y^{-1}) (USGS: Kuparuk, 2023), the Putuligayuk (discharge ~0.11 billion m^3 y^{-1}; Arp et al. 2017; Stuefer et al. 2017), and the Colville (~13.3 billion m^3 y^{-1}; USGS: Colville, 2023) Rivers. The Kuparuk and Putiligayuk discharge directly into Simpson Lagoon, while the Colville sits at its westernmost end with most of its discharge (~90%) flowing directly into the ocean (Schreiner et al. 2013).

3. Dissolved Mercury Concentrations and Associations

Dissolved surface THg concentrations in Simpson Lagoon ranged from <0.2 - 8.6 pM (avg: 1.9 pM ± 1.6, median: 1.7, *n*=52) (Fig. 1a; Supplemental Table S1), while samples collected in July 2023 just outside the lagoon on the Beaufort Shelf had similar values (avg: 1.9 ± 0.7 pM, median: 1.6, *n*=11) (Supplemental Fig. S2). Groundwater THg concentrations were generally higher with a high degree of variability, ranging from <0.2 - 86.4 pM (avg: 15.3 ± 15.8 pM, median: 9.2, *n*=112). These concentrations put Simpson Lagoon on the lower end of reported uncontaminated coastal surface water THg concentrations in the Northern Hemisphere (1.01 - 256 pM, avg: 10.8 pM, median: 2.15 pM) and on the higher end for groundwater (1.39 - 262 pM, avg: 8.86 pM, median: 3.56 pM) (Bone et al. 2007, Laurier et al. 2007, Black[b] et al. 2009, Lee et al. 2011, Ganguli et al. 2012, Rahman et al. 2013, Szymczycha et al. 2013, Ganguli et al. 2014).

Due to the preservation technique of adding acid during sample collection, our MeHg concentrations are for the combined dissolved pools of dimethylmercury and monomethylmercury, since dimethylmercury is degraded under acidic conditions (Black[a] et al.

2009). The resulting lagoon MeHg concentrations ranged from <0.07 - 0.38 pM (avg: 0.08 ± 0.09 pM, median: BDL, *n*=47) (Fig. 1b) while almost all Beaufort Shelf samples fell below the limit of detection (<0.07 pM, *n*=9) (Supplemental Fig. S2). Groundwater MeHg concentrations ranged from <0.07 - 16.7 pM (avg: 3.3 ± 4.0 pM, median: 1.3, *n*=105). Again, this puts Simpson Lagoon on the low end for reported surface concentrations (0.03 - 0.6 pM, avg: 0.14 pM, median: 0.06 pM) and considerably higher than most reported coastal groundwater MeHg concentrations (<0.07 - 3.1 pM, avg: 0.65 pM, median: 0.33 pM) (Laurier et al. 2007, Black[b] et al. 2009, Lee et al. 2011, Ganguli et al. 2012).

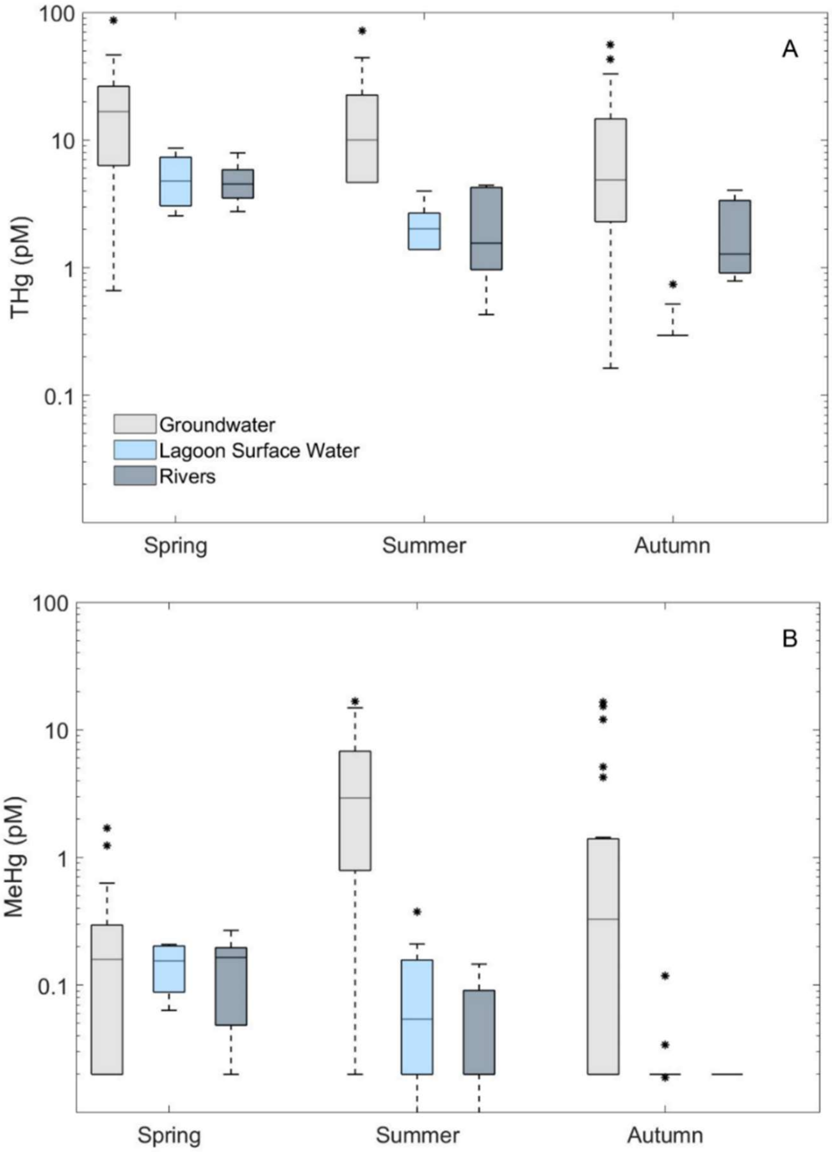

Figure 1. Seasonal concentrations for (A) dissolved THg and (B) dissolved MeHg in groundwater, lagoon surface water, and rivers on a log scale. Boxes contain values from the 0.25 to the 0.75 quartiles, with the central mark indicating the median. Whiskers extend to values less than 1.5 the interquartile range, with outliers indicated by asterisks. Summer concentrations include all three summer periods sampled (August 2021, July 2022, July 2023).

4. Seasonal Differences in THg and MeHg Concentrations

THg in Simpson Lagoon surface water shows strong seasonal differences, with THg concentrations decreasing dramatically between spring and autumn. This relationship is inverse to the lagoon salinity in 2022, which increased between June, July, and October 2022 due to a combination of decreasing river discharge and increased mixing with the Beaufort Sea. However, the salinity in July 2023 was similar to October 2022, while THg concentrations were still in line with the summer sampling periods from 2021 and 2022, indicating that river discharge and ocean mixing are not dominant controls on THg concentrations during the summer period. While atmospheric mercury depletion events occur in coastal environments during the spring (Toyota et al. 2014, Dastoor et al. 2022), lagoon ice and snow sampled during the spring field campaign indicate that local atmospheric deposition is not the cause of elevated THg concentrations during June (Supplemental Table S1). Instead, river inputs and runoff (non-gauged overland flow) appear to be the dominant control on lagoon THg during this period. Groundwater THg concentrations show no seasonally distinct trends (Fig. 1); however, THg does show a seasonally dependent positive correlation with dissolved organic carbon (DOC) (Supplemental Fig. S3). We also observed non-conservative removal of THg in the salinity mixing zone (Supplemental Materials S3), likely due to its interactions with DOC and its removal due to coagulation and aggregation within the organic- and Fe-rich sediments during salinity intrusion (Adyasari et al. 2023).

Unlike THg, dissolved MeHg in surface water does not show notable seasonal dependence, with photodegradation (lifetime < 10 days; Gårdfelt et al. 2001) (Seller et al. 1996, Lehnherr et al. 2012, Klapstein et al. 2017, Klapstein & O'Driscoll, 2018) and biological uptake (Chiasson-Gould et al. 2014, Schartup et al. 2015, Soerensen et al. 2016, Mangal et al. 2019) likely responsible for maintaining low surface water concentrations throughout the year. In the Kuparuk and Putiligayuk Rivers, concentrations and seasonal patterns of MeHg are similar to those observed in other Arctic rivers (Sonke et al. 2018), with the highest concentrations occurring during the spring freshet. Conversely, groundwater MeHg concentrations generally increase between the spring and summer periods, consistent with increased microbial activity at higher temperatures (Lehnherr et al. 2012, Yang et al. 2016, Jonsson et al. 2022), with median values declining in autumn (Fig. 1; Supplemental Table S1). Out of all ancillary parameters measured during the field campaigns (salinity, pH, dissolved oxygen, Fe & Mn (Schaal, 2024), oxidation reduction potential, DOC, & total dissolved nitrogen), MeHg showed no significant correlations.

5. Inputs of Hg to Simpson Lagoon

To calculate inputs of THg and MeHg to Simpson Lagoon (Table 1; Fig. 2), we utilized measured Hg concentrations and corresponding water fluxes (Table 1). The SGD flux to Simpson Lagoon, as reported in Bullock et al. (2024), is (27 ± 10) x 10^6 m^3 d^{-1}, which is for a 120-day ice-free period (summer/autumn) and takes seasonal and interannual variability into account. No SGD was measurable during the spring period. During the ice-free period, the SGD flux is dominated by recirculated lagoon water, as opposed to inflow from fresh groundwater. As a result, seasonal median THg and MeHg concentrations (Table 1) were used for groundwater endmember values to limit the impact of extreme freshwater outliers that may not be broadly representative of Hg concentrations in SGD.

Other Hg sources are shown in Figure 2, including diffusion from lagoon bottom sediments, as determined using sediment core incubations and theoretical calculations (Supplemental Materials S3). Wet deposition was estimated using THg concentrations in rain for the month of the sampling periods, collected at Toolik Field Station (NADP, 2023) and precipitation rates from Prudhoe Bay (Table 1) (USDA, 2023). MeHg wet deposition data was estimated based on THg concentrations in terrestrial Arctic rain containing 18% ± 12% MeHg (Zdanowicz et al. 2013, Soerensen et al. 2016).

Dissolved THg and MeHg river inputs were calculated using the average concentrations for each sampling period along with average river fluxes from the weeks leading up to and for the duration of the sampling periods (Table 1) (Arp et al. 2017, Stuefer et al. 2017, USGS: Kuparuk, 2023, USGS: Colville, 2023). Though about 50% of the THg in Arctic rivers is in the particulate phase (Sonke et al., 2018; Dastoor et al., 2022), up to 90% of suspended sediments are deposited within the freshwater reaches of river deltas (Emmerton et al. 2013, Zolkos et al. 2020). This would also limit THg exposure to high ionic-strength seawater, which can desorb Hg from sediments (Adyasari et al. 2023). For these reasons we have not included desorbed or riverine particulate Hg fluxes in our model; therefore, our riverine fluxes are lower limit estimates (Supplemental Materials S2).

In addition to rivers, we also calculate Hg fluxes from to runoff, which accounts for inputs from the non-gauged streams within the Simpson Lagoon watershed (Supplemental Materials S2). Diffusive fluxes of THg from lagoon bottom sediments were also considered, based on two laboratory-based sediment core incubation experiments (Supplemental Materials S3).

5.1 Seasonality of THg and MeHg Inputs

Rivers are the dominant source of dissolved THg to the lagoon during spring. As riverine inputs decrease during the seasonal transition to summer, SGD fluxes become the dominant source of dissolved THg, outstripping rivers by a factor of 10. As river fluxes continue to decline into the autumn period, SGD inputs of THg remain higher than river inputs, despite lower THg concentrations in SGD at that time (Table 1, Fig. 2).

Runoff contributions of THg to the lagoon are most important during spring, when concentrations are considerably higher than those of rivers due to the flushing of organic rich surface soils by snow meltwater (Zolkos et al. 2020). However, runoff fluxes decrease considerably following the spring melt and do not contribute to the THg budget substantially in the summer and autumn. Diffusion inputs from lagoon bottom sediments were determined to be 1.5 - 30 mmol THg d^{-1} (Supplemental Materials S3), with the caveat that periods of high turbulence may increase this flux. This makes diffusion fluxes relatively less important compared to rivers in the spring and SGD in the summer and autumn.

Similarly to THg, rivers and runoff are the most important inputs of MeHg during the spring. However, both river and runoff MeHg concentrations fall below the detection limit by the July sampling period, likely due to a combination of photochemical degradation and sorption to/settling of suspended organic matter (Varty et al. 2021). Meanwhile, SGD continues to supply MeHg to the lagoon during the summer and autumn at rates exceeding the maximum river inputs during the spring (Fig. 2, Table 1). The largest SGD rates are during the summer period, when groundwater MeHg concentrations are highest. MeHg diffusive fluxes were not measured; however, in other estuarine systems they tend to be 1-3 orders of magnitude lower than the THg flux, putting them between 0.01 - 3 mmol MeHg d^{-1} into Simpson Lagoon (Mason et al. 2006, Covelli et al. 2008) and therefore likely negligible compared to rivers in the spring and SGD in the summer and autumn.

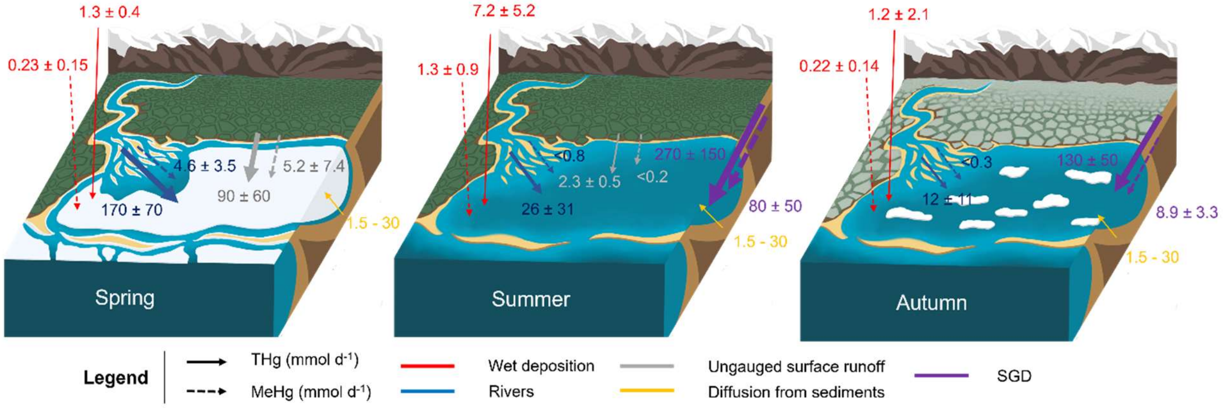

Figure 2. Simplified representation of major THg and MeHg inputs (mmol d^{-1}) to Simpson Lagoon across seasons, including wet deposition, rivers, ungauged surface runoff, diffusion from bottom lagoon sediments, and SGD. SGD values are based on median THg and MeHg groundwater concentrations and SGD water fluxes from Bullock et al. (2024).

Table 1. Major sources of THg and MeHg to Simpson Lagoon over the course of the year, with the water fluxes, THg concentrations, and MeHg concentrations used in flux calculations shown in Figure 2.

Season	**Source**	**Water flux (x 10^6 m^3 d^{-1})**	**THg (pM)**	**MeHg (pM)**
Spring	Rivers[a]	35 ± 28	4.8 ± 1.9	0.13 ± 0.10
	Runoff[b]	5.5 ± 4.4	16 ± 12	1.0 ± 1.3
	SGD[c]	0	15	0.16
	Wet Deposition[d]	0.02	63 ± 18	11.3 ± 7.6
Summer	Rivers [a]	11 ± 3	2.4 ± 2.8	BDL – 0.15
	Runoff[b]	2.4 ± 2.2	0.96 ± 0.20	BDL
	SGD[c]	27 ± 10	10.1 ± 5.5	2.9 ± 1.7
	Wet Deposition[d]	0.4	18 ± 13	3.2 ± 2.2
Autumn	Rivers [a]	4.8 ± 2.4	2.4 ± 2.3	BDL
	Runoff[b]	0	-	-
	SGD[c]	27 ± 10	4.9	0.33
	Wet Deposition[d]	0.08	15 ± 26	2.7 ± 1.8

- : Values were not measured or estimated for this parameter

BDL: Samples were below the detection limit (0.2 pM THg, 0.07 pM MeHg)

a: River discharge obtained from the following sources: Arp et al. (2017), Stuefer et al. (2017), USGS: Kuparuk (2023), USGS: Colville (2023). Final water fluxes entering Simpson Lagoon determined by Bullock et al. (2024).

b: Runoff water fluxes calculated in Bullock et al. (2024).

c: SGD water flux values obtained from Bullock et al. (2024). Median Hg concentrations are used for spring and

autumn. Averaged median concentrations across three sampling periods used for summer.
d: Precipitation data obtained from Prudhoe Bay weather station (USDA, 2023). Concentrations were obtained using wet deposition data for THg collected at Toolik Field Station and retrieved from the NADP database (NADP, 2024) and meteorological data from Toolik Field Station (Environmental Data Center Team, 2024). MeHg wet deposition concentrations were estimated based on THg concentrations in terrestrial Arctic rain containing 18% ± 12% MeHg (Zdanowicz et al. 2013, Soerensen et al. 2016).

5.2 Arctic SGD Hg Inputs in Context

The daily SGD fluxes shown in Figure 2 were normalized to the coastline of Simpson Lagoon (89 km, including the barrier islands) to enable comparison of our fluxes to other systems. The THg fluxes into Simpson Lagoon (summer: 3.0 ± 1.7 mmol d^{-1} km^{-1}; autumn: 1.5 ± 0.6 mmol d^{-1} km^{-1}), are higher than most temperate coastal sites where groundwater THg inputs have been reported. We restricted our comparison to studies where nearby point sources of pollution were not expected (i.e. heavy mining or other intensive mercury producing processes). These were mostly from the Northern Hemisphere and report fluxes ranging from 0.1 μmol d^{-1} km^{-1} in the Bay of Puck, near the Baltic Sea (Szymczycha et al. 2013) to 1.0 mmol d^{-1} km^{-1} in Pays de Caux, France (Laurier et al. 2007), with an average value around 0.26 mmol d^{-1} km^{-1} (Supplemental Materials S4) (Bone et al. 2007, Laurier et al. 2007, Black[b] et al. 2009, Lee et al. 2011, Ganguli et al. 2012, Szymczycha et al. 2013, Ganguli et al. 2014).

MeHg has been measured in fewer coastal groundwater studies of non-contaminated sites. Our coastline-normalized MeHg fluxes are 900 ± 600 μmol d^{-1} km^{-1} during the summer and 100 ± 40 μmol d^{-1} km^{-1} during the autumn. In comparison, reported MeHg fluxes from SGD for temperate coastal sites rarely exceed 10 μmol d^{-1} km^{-1} with an average 3.5 μmol d^{-1} km^{-1} (Laurier et al. 2007; Black[b] et al. 2009; Lee et al. 2011; Ganguli et al. 2012). The 2-7x higher MeHg inputs to Simpson Lagoon from SGD are likely due to the likelihood that water can recirculate through most of the lagoon's sediments (~2 x 10^8 m^2), due to its shallow nature. The high fluxes of MeHg may also be due to higher groundwater Hg concentrations than in temperate locations (Obrist et al. 2017) and the prevalence of strong microbial methylation of Hg in Arctic tundra soils (Podar et al. 2015, Yang et al. 2016), which may explain the high MeHg concentrations observed in Arctic watersheds and estuaries (Kirk and St. Louis, 2009).

Annual fluxes of Hg from SGD were calculated using the averaged median concentrations across the three summer periods (THg = 10.1 ± 6.5 pM; MeHg = 2.9 ± 1.7 pM), the median autumn sampling period values (THg = 4.9 pM; MeHg = 0.33 pM), the daily SGD flux of (27 ± 10) x 10^6 m^3 d^{-1} (Bullock et al. 2024) and Simpson Lagoon's coastline (89 km). Summer concentrations were used for ice-free days with average temperatures above freezing (72 days) and autumn concentrations were used for ice-free days with average temperatures below freezing (48 days) (USDA, 2023). Using these data, the annual fluxes were determined to be 290 ± 190 mmol THg y^{-1} km^{-1} and 70 ± 50 mmol MeHg y^{-1} km^{-1}. Annual riverine inputs of THg and MeHg to Simpson Lagoon come to 790 ± 290 mmol THg y^{-1} km^{-1} and 3 ± 1 mmol MeHg y^{-1} km^{-1}. This means that SGD inputs ~37% the amount of THg to the lagoon as rivers, but an order of magnitude more MeHg. If this relationship holds true across the Arctic, SGD may be a larger contributor of MeHg to the coastal Arctic Ocean than rivers, which are currently the main terrestrial source accounted for in Arctic MeHg box models (Jonsson et al. 2022).

6. Implications for Future Arctic Methylmercury Exposure

The findings suggest that SGD may be an important source of MeHg to the Arctic Ocean, with increasing potential to impact marine biota and influence human MeHg exposure as warming continues leading to further permafrost thawing and increased rates of Hg methylation in tundra soils. Our estimates of its magnitude and importance may help constrain the large uncertainties in current biogeochemical modeling of MeHg for the Arctic Ocean, since they reduce the amount of unaccounted for MeHg in the system, which is currently being attributed to *in situ* water column production despite valid questioning of this assumption (Semeniuk & Dastoor, 2017). Microbial production rates of MeHg in the Arctic water column, as determined by Lehnherr et al. (2011) from incubation studies, likely overestimate kinetic rates (Wang et al. 2020). This may be a function of the high Hg spikes used in the Lehnherr experiments (2-3 orders of magnitude above ambient). Recent models either use these rates directly or else compare their box model-derived estimates to these rates for validation (e.g. Soerensen et al. 2016; Semeniuk & Dastoor et al. 2017; Jonsson et al. 2022). Notably, Semeniuk & Dastoor (2017) discussed how the use of these rates in their model could not accurately reconstruct the observed MeHg concentrations in polar regions. Furthermore, Despins et al. (2023) found a strong correlation between Hg methylation and denitrification in the Arctic Ocean water column in association with the chlorophyll maximum at rates more than an order of magnitude lower than Lehnherr et al. (2011). Consequently, by using the higher rates to validate their mass balance, Jonsson et al. (2022)'s Arctic MeHg budget invoked higher *in situ* net methylation of Hg (5.1 Mg/yr) compared to terrestrial, riverine and atmospheric inputs (3.4 Mg/yr) to balance their budget, suggesting that external inputs were not the dominant source. However, this may not be the case if SGD MeHg inputs were included.

There is also the important consideration of spatial and temporal variability. While MeHg inputs from rivers are often localized to river mouths, with biological uptake and particle deposition acting to lower concentrations (Soerenson et al. 2016), the diffuse nature of MeHg inputs across the coastline may result in greater potential for exposure of microorganisms to the species. Arctic rivers also have strong seasonal variability, with most riverine Hg being supplied during the spring freshet (Zolkos et al. 2020). The presence of substantial, spatially distributed inputs of MeHg from SGD throughout the entire summer/autumn period could have important implications for our understanding of MeHg sources to the Arctic Ocean, as well as the subsequent impacts on communities who consume Arctic seafood and marine mammals.

However, considerably more research needs to be done before SGD can be definitively declared an important source of Hg to the Arctic Ocean. Not only does there need to be greater spatial sampling of SGD and groundwater concentrations of THg and MeHg in the Arctic, but the biological impact of SGD-derived Hg species must also be considered. For example, inputs of MeHg via SGD may have a greater potential to impact Arctic waters and be transported offshore due to high DOC concentrations, which combine to both stabilize dissolved MeHg and enhance biological uptake of Hg in heterotrophs (Soerensen et al. 2017; Schartup et al. 2018). Alternatively, MeHg associated with terrestrial DOM may be less likely to be taken up by marine plankton and bacteria (Schartup et al. 2015), which form the basis of the Arctic food web. This study exposes the potential for SGD to contribute Hg to the coastal Arctic Ocean, but in order to determine whether it contributes substantially to biological uptake into the Arctic food chain, MeHg fluxes from SGD need to be examined in future studies, better quantified, and included in future Arctic risk assessments and models.

7. Methods

7.1 Sample Collection

Samples were collected over three seasons: spring (June 2022), summer (August 2021, July 2022, & July 2023), and autumn (September/October 2022). A surface water transect from shore was sampled during the summer and autumn periods (Supplemental Fig. S1). Samples were taken from a small boat at a depth of 0.5 m (0.4 km, 0.8 km, 1.2 km, 1.6 km, 3.2 km, & 4.8 km from shore) with the first three stations also sampled ~0.2 m above the lagoon bottom sediment. During the July 2023 sampling period, surface water samples were collected from the *R/V Proteus* in a transect across the east-west axis of the lagoon, as well as in the Beaufort Sea surrounding the lagoon and near the mouth of the Colville River (Supplemental Figs. S1, S2).

Clean sampling techniques were used for collection of Hg samples. Samples were taken for surface water stations by lowering acid washed, Masterflex™ L/S™ High-Performance, C-FLEX™ tubing to the desired depth and filtering samples through a clean Geotech capsule filter (0.45 µm) via peristaltic pump. Hg samples were filtered into combusted and MQ rinsed 250 mL amber borosilicate bottles with PTFE lined caps that were pre-charged with 0.5 mL TM grade HCl for a final concentration of 0.2% sample volume. Care was taken to make sure samples were taken upwind of motor exhaust fumes and away from potential contamination from the boat. Surface water samples collected during June 2022 when the lagoon was still largely ice covered were obtained through auger-drilled holes in the sea-ice or from water flowing over the top of the ice. River samples and intertidal samples were collected using the same method as boat collection with the tubing being deployed by hand from shore. Salinity, dissolved oxygen (DO), temperature, turbidity, ORP, and pH were measured at each sampling point with an AquaTROLL Multiparameter Sonde or a Myron L Ultrameter™.

Groundwater samples were collected from stainless-steel or PVC piezometers using the same method as that for surface water samples. Blanks for Hg & TM samples were obtained by pumping Milli-Q® filtered water through each piezometer type, with no significant differences seen between the two. Several transects (4 - 8 piezometers, stainless steel or PVC with six-inch screens) were sampled during the campaigns, in order to test the heterogeneity of the site, with some transects returned to during multiple campaigns. Piezometers were driven down to the ice table, resulting in samples collected from ~6 cm above the ice/permafrost. For most piezometers installed in the intertidal and subtidal zones, an additional shallow piezometer was installed next to the primary one, so that samples could also be collected ~6 cm below the sediment/water interface. Transects were designed to traverse the sediment salinity mixing zone for all locations sampled. Several transects specifically followed tundra polygon troughs, as these may create preferential flow paths for groundwater leaving the tundra.

Snow and lagoon ice samples were collected during the June 2022, ~0.5 km from shore. Two snow samples separated by ~3 m were collected using clean plastic bags and acid-washed plastic scoops. Ice cores were collected from below the snow layer at each station using a SIPRE hand auger, with the edges of the ice cores scraped using a clean plastic trowel to remove any possible contamination from the core barrel, then stored in a clean plastic bag. As soon as the samples had mostly thawed, they were filtered, using the same Geotech filters, into the same acid-charged sample bottles as outlined above for long-term transport and storage. Clean and dirty snow and ice designations were based on visual observations of dust and sediment content in the samples.

Intertidal sediments were collected using clear PVC core barrels. The tundra active layer core was taken by cutting a rectangular core down to the ice interface with a bread knife. The permafrost core was taken using a SIPRE stainless steel drill powered corer. Cores were stored frozen at -20°C until they could be freeze dried, at which point they were stored in combusted amber glass jars.

7.2 Analysis of mercury

All mercury analyses were performed at the University of Connecticut and care was taken to ensure proper data quality assurance for Hg results (Supplemental Materials S5). THg was measured with a Tekran Series 2600 automated system with the dual gold pre-concentration/CVAFS method described by Bloom and Fitzgerald (1988). Prior to analysis, samples were digested with BrCl overnight. Following digestion, 12% $NH_2OH \cdot HCl$ was added to consume any remaining BrCl and then saturated $SnCl_2$ solution was used to convert all Hg^{II} to Hg^0. Standard curves were measured from THg certified reference materials (J.T. Baker, NIST) and the detection limit for this method was 0.2 pM, as determined by the standard deviation of the instrument blanks. Sample concentrations were corrected based on field and method blanks, which were 0.5 ± 0.2 pM (n = 7). Duplicate and triplicate samples differed by less than 10%. Every 10 to 15 samples analyzed was spiked with a known concentration of a certified THg reference material (J.T. Baker, NIST). Spike recoveries were 108% ± 13% the expected value. Samples are reported in their field blank- and spike-corrected form (field blank was subtracted from raw value and concentration was then normalized to spike recovery percentage).

THg in soil was measured on a Nippon MA-3000 Direct Mercury Analyzer (DMA) using thermal decomposition, amalgamation cold vapor atomic absorption spectroscopy (CVAAS). For each sample, ~200 mg of ball-milled sediment was placed in pre-combusted ceramic sample boats for analysis. Calibration was performed using liquid standard curves (THg; J.T. Baker, NIST). The standard reference material used was MESS-3 (marine sediment; National Research Council of Canada (NRC)), which yielded 0.085 ± 0.001 mg/kg. This is within the range of acceptable values for MESS-3 (0.091 ± 0.009 mg/kg). The detection limit for this method is 0.01 ng and the relative standard deviation (RSD) was 2%.

Given the high organic content in the groundwater, MeHg samples were pre-distilled to separate MeHg from the natural organics in solution after the addition of 50% H_2SO_4 and 20% KCl (Hammerschmidt and Fitzgerald, 2001, Balcom et al. 2015). Surface water and river samples were acidified with 9N H_2SO_4 at least 16 hours prior to analysis. Ascorbic acid (2.5%) was added just before MeHg analysis (Munson et al. 2014). All MeHg samples were derivatized with sodium tetraethylborate (NaTEB), then analyzed using a Tekran 2700 purge and trap gas chromatographic cold vapor atomic fluorescence spectrometry (CVAFS) automated instrument (Tseng et al. 2004). Calibration was performed using MeHg standard curves (Alfa Aesar, NIST) and sample concentrations were corrected based on average field and method blank values (avg: 0.09 pM, range: 0.00 – 0.21, n = 5). Duplicate and triplicate samples differed by less than 10%. Every 10 samples processed were spiked with a known concentration of a certified MeHg reference material (J.T. Baker, NIST). Spike recoveries were 71% ± 20%. The detection limit for this method is 0.07 pM based on Tseng et al. (2004) and modified slightly to match the utilized instrument. Samples are reported in their blank- and spike-corrected form (field blank subtracted from raw value and concentration normalized to spike recovery percentage).

7.3 Carbon Analysis

Groundwater DOC was obtained from 0.45 mm filtered samples, which were stored without preservatives and kept frozen until analysis. The samples were analyzed at the University of Texas Marine Science Institute using a Shimatzu TOC-V CSH analyzer. Due to flocculation of DOC that occurred after collection and/or freezing, groundwater samples were acidified to a pH of 2 with TM grade concentrated HCl and sonified prior to analysis to break up flocs. Additionally, the TOC analyzer was equipped to homogenize samples during analysis using magnetic stir bars, preventing any remaining flocs from settling out.

Tundra soils and intertidal sediments were prepared for soil organic carbon analysis in the same way as for THg (see above). The prepared samples were then analyzed for organic carbon via combustion at 900 - 1000°C, followed by column separation and measurement by thermal conductivity using an Elemental Microanalysis Flash EA 1112.

Acknowledgements

This project was funded by the National Science Foundation’s Office of Polar Programs through grants 2134865 (Bullock and Charette), 1938873 (Charette), 1938820 (Cardenas and McClelland), 1656026 (McClelland), and 1854454 (Mason). Assistance with fieldwork was provided by Cansu Demir, Isabel Schaal, Julia Guimond, and Paul Henderson. We thank Hillcorp Alaska for providing access to field sites and resources, as well as Battelle Arctic Research Operations (via Polar Field Services) for logistical support. We also thank the Beaufort Lagoon Ecosystems Long Term Ecological Research program, including the captain and crew of the *R/V Proteus*, for sharing lab and field resources.

Data Availability

The data used in this study are freely available in the Arctic Data Center (doi:10.18739/A2CF9J834).

References

Adyasari, D., Dimova, N., Waska, H., Chadhain, S. N. (2023). Dissolved organic matter and nutrient processing in organic-rich subterranean estuaries: Implications for future land use and climate scenarios. *Geochimica et Cosmochimica Acta, 362*, 65-76. https://doi.org/10.1016/j.gca.2023.10.025

AMAP. AMAP Assessment 2018: Biological Effects of Contaminants on Arctic Wildlife and Fish. Arctic Monitoring and Assessment Programme (AMAP), Oslo, Norway, 2018.

Arp, C., Kane, D., Stuefer, S., Hinzman, L. (2017). Hydrographic Data, Putuligayuk River Watershed, Alaska, 1999-2017. Arctic Data Center. https://doi.org/10.18739/A2FF3M05P

Balcom, P. H., Schartup, A. T., Mason, R. P., Chen, C. Y. (2015). Sources of water column methylmercury across multiple estuaries in the Northeast US. *Marine Chemistry, 177,* 721–730.

Black^a, F. J., Conaway, C. H., and Flegal, A. R. (2009). Stability of Dimethyl Mercury in Seawater and Its Conversion to Monomethyl Mercury. *Environmental Science & Technology, 43* (11), 4056-4062. https://doi.org/10.1021/es9001218

Black^b, F. J., Paytan, A., Knee, K. L., De Sieyes, N. R., Ganguli, P. M., Gray, E., Flegal, A. R. (2009). Submarine groundwater discharge of total mercury and monomethylmercury to central California coastal waters. *Environmental Science & Technology, 43* (15), 5652-9. https://doi.org/10.1021/es900539c

Bloom, N., Fitzgerald, W. F. (1988) Determination of volatile mercury species at the picogram level by low-temperature gas chromatography with cold-vapour atomic fluorescence detection. *Analytica Chimica Acta, 208*, 151–161.

Bone, S.E., Charette, M.A., Lamborg, C.H., Gonneea, M.E. (2007). Has Submarine Groundwater Discharge Been Overlooked as a Source of Mercury to Coastal Waters? *Environmental Science & Technology*, *41* (9), 3090 - 3095. https://doi.org/10.1021/es0622453

Bullock, E. J., Schaal, I. V., Cardenas, M. B., McClelland, J. W., Charette, M. A. (2024). Seasonality of submarine groundwater discharge to an Arctic coastal lagoon. *Limnology and Oceanography, 9999* (1-10). https://doi.org/10.1002/lno.12585

Chételat, J., McKinney, M. A., Amyot, M., Dastoor, A., Douglas, T. A., Heimbürger-Boavida, L.-E., Kirk, J., Kahilainen, K. K., Outridge, P. M., Pelletier, N., Skov, H., St. Pierre, K., Vuorenmaa, J., Wang, F. (2022). Climate change and mercury in the Arctic: Abiotic interactions. *Science of the Total Environment, 824,* 153715. https://doi.org/10.1016/j.scitotenv.2022.153715

Chiasson-Gould, S.A., Blais, J.M., & Poulain, A.J. (2014). Dissolved Organic Matter Kinetically Controls Mercury Bioavailability to Bacteria. *Environmental Science & Technology, 48*(6), 3153-3161. https://doi.org/10.1021/es4038484

Connolly, C. T., M. B. Cardenas, G. A. Burkart, R. G. M. Spencer, and J. W. McClelland. (2020). Groundwater as a major source of dissolved organic matter to Arctic coastal waters. Nature Communications, 11, 1479. https://doi.org/10.1038/s41467-020-15250-8

Covelli, S., Faganelli, J., De Vittor, C., Predonzani, S., Acquavita, A., Horvat, M. (2008). Benthic fluxes of mercury species in a lagoon environment (Grado Lagoon, Northern Adriatic Sea, Italy. *Applied Geochemistry, 23*(3), 529-546. https://doi.org/10.1016/j.apgeochem.2007.12.011

Dastoor, A., Angot, H., Bieser, J., Christensen, J. H., Douglas, T. A., Heimbürger-Boavida, L.-E., Jiskra, M., Mason, R., McLagan, D. S., Obrist, D., Outridge, P. M., Petrova, M. V., Ryjkov, A., St. Pierre, K. A., Schartup, A. T., Soerensen, A. L., Toyota, K., Travnikov, O., Wilson, S. J., Zdanowicz, C. (2022). Arctic mercury cycling. *Nature Reviews Earth & Environment, 3,* 270-286. https://doi.org/10.1038/s43017-022-00269-w

Déry, S. J., Stieglitz, M., Rennermalm, Å. K., & Wood, E. F. (2005). The Water Budget of the Kuparuk River Basin, Alaska. *Journal of Hydrometerology, 6*, 633 - 655.

Despins, M. C., Mason, R. P., Aguilar-Islas, Lamborg, C. H., Hammerschmidt, C. R., Newell, S. E. (2023). Linked mercury methylation and nitrification across the oxic sub-polar regions. *Frontiers in Environmental Chemistry, 4*, 1109537. https://doi.org/10.3389/fenvc.2023.1109537

Dietz, R., Sonne, C., Basu, N., Braune, B., O'Hara, T., Letcher, R. J., Scheuhammer, T., Andersen, M., Andreasen, C., Andriashek, D., Asmund, G., Aubail, A., Baagøe, H., Born, E. W., Chan, H. M., Derocher, A. E., Grandjean, P., Knott, K., Kirkegaard, M., Krey, A., Lunn, N., Messier, F., Obbard, M., Olsen, M. T., Ostertag, S., Peacock, E., Renzoni, A., Rigét, F. F., Skaare, J. U., Stern, G., Stirling, I., Taylor, M., Wiig, Ø., Wilson, S., Aars, J. (2013). What are the toxicological effects of mercury in Arctic biota? *Science of the Total Environment*, *443*, 775 - 790. https://doi.org/10.1016/j.scitotenv.2012.11.046

Emmerton, C. A., Graydon, J. A., Gareis, J. A., St. Louis, V. L., Lesack, L. F. W., Banack, J. K. A., Hicks, F., Nafziger, J. (2013). Mercury Export to the Arctic Ocean from the Mackenzie River, Canada. *Environmental Science & Technology, 47* (14), 7644-7654. https://doi.org/10.1021/es400715r

Environmental Data Center Team. 2024. Meteorological monitoring program at Toolik, Alaska. Toolik Field Station, Institute of Arctic Biology, University of Alaska Fairbanks, Fairbanks, AK 99775. https://www.uaf.edu/toolik/edc/monitoring/abiotic/met-data-query.php

Ganguli, P. M., Conaway, C. H., Swarzenski, P. W., Izbicki, J. A., Flegal, A. R. (2012). Mercury Speciation and Transport via Submarine Groundwater Discharge at a Southern California Coastal Lagoon System. *Environmental Science & Technology, 46* (3), 1480-1488. https://doi.org/10.1021/es202783u

Ganguli, P. M., Swarzenski, P. W., Dulaiova, H., Glenn, C. R., Flegal, A. R. (2014). Mercury dynamics in a coastal aquifer: Maunalua Bay, Oʻahu, Hawaiʻi. *Estuarine, Coastal and Shelf Science, 140,* 52-65. https://doi.org/10.1016/j.ecss.2014.01.012

Gårdfeldt, K., Sommar, J., Strömberg, D., Feng, X. (2001). Oxidation of atomic mercury by hydroxyl radicals and photoinduced decomposition of methylmercury in the aqueous phase. *Atmospheric Environment, 35* (17), 3039-3047. https://doi.org/10.1016/S1352-2310(01)00107-8

Guimond, J.A., Demir, C., Kurylyk, B.L., Walvoord, M.A., McClelland, J.W., Cardenas, M.B. (2023). Wind - modulated groundwater discharge along a microtidal Arctic coastline. *Environmental Research Letters, 18* (9), 094042. https://doi.org/10.1088/1748 - 9326/acf0d8

Hammerschmidt, C. R., Fitzgerald, W. F. (2001). Formation of artifact methylmercury during extraction from a sediment reference material. *Analytical Chemistry, 73*, 5930–5936.

Hanna, A.J.M., Shanahan, T.M., Allison, M.A., Bianchi, T.S., & Schreiner, K.M. (2018). A multi-proxy investigation of late-Holocene temperature change and climate-driven fluctuations in sediment sourcing: Simpson Lagoon, Alaska. *The Holocene, 28* (6), 984-997. https://doi.org/10.1177/0959683617752845

Jonsson, S., Skyllberg, U., Nilsson, M. B., Lundberg, E., Andersson, A., Björn, E. (2014). Differentiated availability of geochemical mercury pools controls methylmercury levels in estuarine sediment and biota. *Nature Communications, 5,* 4624. https://doi.org/10.1038/ncomms5624

Jonsson, S., Mastromonaco, M.N., Wang, F., Bravo, A.G., Cairns, W.R.L., Chételat, J., Douglas, T.A., Lescord, G., Ukonmaanaho, L., & Heimbürger-Boavida, L. (2022). Arctic methylmercury cycling. *Science of the Total Environment, 850,* 157445. https://doi.org/10.1016/j.scitotenv.2022.157445

Kirk, J. L., St. Louis, V. L. (2009). Multiyear total and methyl mercury exports from two major sub-Arctic rivers draining into Hudson Bay, Canada. *Environmental Science & Technology, 43* (7), 2254-2261. https://doi.org/10.1021/es803138z

Klapstein, S.J., O'Driscoll, N.J. (2018). Methylmercury Biogeochemistry in Freshwater Ecosystems: A Review Focusing on DOM and Photodemethylation. *Bulletin Environmental Contaminants and Toxicology, 100*, 14–25. https://doi.org/10.1007/s00128-017-2236-x

Klapstein, S.J., Ziegler, S.E., O'Driscoll, N.J. (2017). Methylmercury photodemethylation is inhibited in lakes with high dissolved organic matter. *Environmental Pollution, 232,* 392-401. https://doi.org/10.1016/j.envpol.2017.09.049

Lantuit, H., Overduin, P.P., Couture, N. Wetterich, S., Aré, F., Atkinson, D., Brown, J., Cherkashov, G., Drozdov, D., Forbes, D. L., Graves-Gaylord, A., Grigoriev, M., Hubberton, H.-W., Jordan, J., Jorgenson, T., Ødegård, R. S., Ogorodov, S., Pollard, W. H., Rachold, V., Sedenko, S., Solomon, S., Steenhuisen, F., Streletskaya, I., Vasiliev, A. (2012). The Arctic Coastal Dynamics Database: A New Classification Scheme and Statistics on Arctic Permafrost Coastlines. *Estuaries and Coasts, 35,* 383–400. https://doi.org/10.1007/s12237-010-9362-6

Laurier, F. J.G., Cossa, D., Beucher, C., Brévière, E. (2007). The impact of groundwater discharges on mercury partitioning, speciation and bioavailability to mussels in a coastal zone. *Marine Chemistry, 104* (3-4), 143-155. https://doi.org/10.1016/j.marchem.2007.06.007

Lee, Y., Rahman, M., Kim, G., Han, S. (2011). Mass Balance of Total Mercury and Monomethylmercury in Coastal Embayments of a Volcanic Island: Significance of Submarine Groundwater Discharge. *Environmental Science & Technology, 45* (23), 9891-9900. https://doi.org/10.1021/es202093z

Lehnherr, I., St. Louis, V. L., Hintelmann, H., Kirk, J. L. (2011). Methylation of inorganic mercury in polar marine waters. *Nature Geoscience, 4,* 298-302. https://doi.org/10.1038/ngeo1134

Lehnherr, I., St. Louis, V.L., Emmerton, C.A., Barker, J.D., Kirk, J.L. (2012). Methylmercury Cycling in High Arctic Wetland Ponds: Sources and Sinks. *Environmental Science & Technology, 46*(19), 10514-10522. https://doi.org/10.1021/es300576p

Lim, S. H., Kim, Y., Motta, L. C., Yang, E. J., Rhee, T. S., Hong, J. K., Han, S., Kwon, S. Y. (2024). Near surface oxidation of elemental mercury leads to mercury exposure in the Arctic Ocean biota. *Nature Communications, 15*, 7598. https://doi.org/10.1038/s41467-024-51852-2

Mangal, V., Stenzler, B.R., Poulain, A.J., & Guéguen, C. (2019). Aerobic and Anaerobic Bacterial Mercury Uptake is Driven by Algal Organic Matter Composition and Molecular Weight. *Environmental Science & Technology, 53*(1), 157-165. https://doi.org/10.1021/acs.est.8b04909

Mason, R.P., Kim, E.-H., Cornwell, J., Heyes, D. (2006). An examination of the factors influencing the flux of mercury, methylmercury, and other constituents from estuarine sediment. *Marine Chemistry, 102*(1-2), 96-110. https://doi.org/10.1016/j.marchem.2005.09.021

Mu, C., Zhang, F., Chen, X., Ge, S., Mu, M., Jia, L., Wu, Q., Zhang, T. (2019). Carbon and mercury export from the Arctic rivers and response to permafrost degradation. *Water Research, 161*, 54 - 60. https://doi.org/10.1016/j.watres.2019.05.082

Munson, K. M., Babi, D., Lamborg, C. H. (2014). Determination of monomethylmercury from seawater with ascorbic acid-assisted direct ethylation. *Limnology and Oceanography: Methods, 12* (1), 1-9. https://doi.org/10.4319/lom.2014.12.1

NADP: National Atmospheric Deposition Program (NRSP-3). 2023. NADP Program Office, Wisconsin State Laboratory of Hygiene, 465 Henry Mall, Madison, WI 53706.

Obrist, D., Agnan, Y., Jiskra, M., Olson, C. L., Colegrove, D. P., Hueber, J., Moore, C. W., Sonke, J. E., Helmig, D. (2017) Tundra uptake of atmospheric elemental mercury drives Arctic mercury pollution. *Nature, 547*, 201–204. https://doi.org/10.1038/nature22997

Pedrazas, M., Cardenas, M. B., Demir, C., Watson, J. A., Connolly, C. T., McClelland, J. W. (2020). Absence of ice-bonded permafrost beneath an Arctic lagoon revealed by electrical geophysics. *Science Advances, 6* (43). https://doi.org/10.1126/sciadv.abb5083

Petrova, M. V., Krisch, S., Lodeiro, P., Valk, O., Dufour, A., Rijkenberg, M., Achterberg, E. P., Rabe, B., Rutgers van der Loeff, M., Hamelin, B., Sonke, J. E., Garnier, C., Heimbürger-Boavida, L.-E. (2020). Mercury species export from the Arctic to the Atlantic Ocean. *Marine Chemistry, 225,* 103855. https://doi.org/10.1016/j.marchem.2020.103855

Podar, M., Gilmour, C. G., Brandt, C. C., Soren, A., Brown, S. D., Crable, B. R., Palumbo, A. V., Somenahally, A. C., Elias, D. A. (2015). Global prevalence and distribution of genes and microorganisms involved in mercury methylation. *Science Advances, 1* (9). https://doi.org/10.1126/sciadv.1500675

Rahman, M. M., Lee, Y. G., Kim, G., Lee, K., Han, S. (2013). Significance of submarine groundwater discharge in the coastal fluxes of mercury in Hampyeong Bay, Yellow Sea. *Chemosphere, 91* (3), 320-7. https://doi.org/10.1016/j.chemosphere.2012.11.052

Reimnitz, E., Toimil, L., & Barnes, P. (1978). Arctic continental shelf morphology related to sea-ice zonation, Beaufort Sea, Alaska. *Marine Geology, 28* (3-4), 179-181, 185-210. https://doi.org/10.1016/0025-3227(78)90018-X

Schaal, I. V. (2024). Distribution and behavior of trace metals in the subterranean estuary of an Arctic coastal lagoon. Master's Thesis, Massachusetts Institute of Technology and Woods Hole Oceanographic Institution. Print.

Schartup, A.T., Ndu, U., Balcom, P.H., Mason, R.P., Sunderland, E.M. (2015). Contrasting Effects of Marine and Terrestrially Derived Dissolved Organic Matter on Mercury Speciation and Bioavailability in Seawater. *Environmental Science & Technology, 49*(10), 5965-5972. https://doi.org/10.1021/es506274

Schartup, A. T., Ndu, U., Balcom, P. H., Mason, R. P., Sunderland, E. M. (2015). Contrasting Effects of Marine and Terrestrially Derived Dissolved Organic Matter on Mercury Speciation and Bioavailability in Seawater. *Environmental Science & Technology, 49* (10), 5965-5972. https://www.doi.org /10.1021/es506274

Schartup, A.T., Qureshi, A., Dassuncao, C., Thackray, C. P., Harding, G., Sunderland, E. M. (2018). A Model for Methylmercury Uptake and Trophic Transfer by Marine Plankton. *Environmental Science & Technology, 52* (2), 654-662. https://doi.org/10.1021/acs.est.7b03821

Schreiner, K. M., Bianchi, T. S., Eglinton, T. I., Allison, M. A., Hanna, A. (2013). Sources of terrigenous inputs to surface sediments of the Colville River Delta and Simpson Lagoon, Beaufort Sea, Alaska. *Journal of Geophysical Research: Biogeosciences, 118* (2), 808-824. https://doi.org/10.1002/jgrg.20065

Seller, P., Kelly, C.A., Rudd, J.W.M., MacHutchon, A.R. (1996). Photodegradation of methylmercury in lakes. *Nature, 380,* 694-697. https://doi.org/10.1038/380694a0

Semeniuk, K., Dastoor, A. (2017). Development of a global ocean mercury model with a methylation cycle: Outstanding issues. *Global Biogeochemical Cycles, 31* (2), 400-433. https://doi.org/10.1002/2016GB005452

Spyropoulou, A.E., Lazarou, Y.G., Sapalidis, A.A., Laspidou, C.S. (2022). Geochemical modeling of mercury in coastal groundwater. *Chemosphere, 286*(1), 131609. https://doi.org/10.1016/j.chemosphere.2021.131609

Soerensen[a], A. L., Jacob, D. J., Schartup, A. T., Fisher, J. A., Lehnherr, I., St. Louis, V. L., Heimbürger, L-E., Sonke, J. E., Krabbenhoft, D. P., Sunderland, E. M. (2016). A mass budget for mercury and methylmercury in the Arctic Ocean. *Global Biogeochemical Cycles*, *30* (4), 560 - 575.

Soerensen[b], A. L., Schartup, A. T., Gustafsson, E., Gustafsson, B. G., Undeman, E., Björn, E. (2016). Eutrophication Increases Phytoplankton Methylmercury Concentrations in a Coastal Sea—A Baltic Sea Case Study. *Environmental Science & Technology, 50*(21), 11787-11796. https://doi.org/10.1021/acs.est.6b02717

Soerensen, A. L., Schartup, A. T., Skrobonja, A., Björn, E. (2017). Organic matter drives high interannual variability in methylmercury concentrations in a subarctic coastal sea. *Environmental Pollution, 229,* 531-538. https://doi.org/10.1016/j.envpol.2017.06.008

Sonke, J. E., Teisserenc, R., Heimbürger-Boavida, L., Petrova, M. V., Marusczak, N., Le Dantec, T., Chupakov, A. V., Li, C., Thackray, C. P., Sunderland, E. M., Tananaev, N., Pokrovsky, O. S. (2018). Eurasian river spring flood observations support net Arctic Ocean mercury export to the atmosphere and Atlantic Ocean. *PNAS*, *115*(50), E11586-E11594. https://doi.org/10.1073/pnas.1811957115

Stuefer, S. L., Arp, C. D., Kane, D. L., & Liljedahl, A. K. (2017). Recent extreme runoff observations from coastal arctic watersheds in Alaska. *Water Resources Research, 53*, 9145–9163. https://doi.org/10.1002/2017WR020567

Szymczycha, B., Miotk, M., Pempkowiak, J. (2013). Submarine Groundwater Discharge as a Source of Mercury in the Bay of Puck, the Southern Baltic Sea. *Water, Air, & Soil Pollution, 224*, 1542. https://doi.org/10.1007/s11270-013-1542-0

Toyota, K., McConnell, J. C., Staebler, R. M. Dastoor, A. P. (2014). Air–snowpack exchange of bromine, ozone and mercury in the springtime Arctic simulated by the 1-D model PHANTAS - Part 1: In-snow bromine activation and its impact on ozone. *Atmospheric Chemistry and Physics, 14*, 4101–4133.

Tseng, C.-M., Hammerschmidt, C. R., Fitzgerald, W. F. (2004). Determination of methylmercury in environmental matrixes by on-line flow injection and atomic fluorescence spectrometry. *Analytical Chemistry, 76,* 7131–7136.

UN-Environment. Global Mercury Assessment 2018. UN-Environment Programme, Chemicals and Health Branch, Geneva, Switzerland, 2019.

USDA, 2023. Precipitation, Accumulated, Prudhoe Bay, AK. Natural Resources Conservation Service and National Water and Climate Center, accessed (March 28, 2024) at URL [https://wcc.sc.egov.usda.gov/nwcc/site?sitenum=1177]

USGS: KUPARUK R NR DEADHORSE AK, 2023, National Water Information System Data (USGS Water Data for the Nation), accessed [March 22, 2024], at URL [https://waterdata.usgs.gov/nwis/inventory/?site_no=15896000].

USGS: COLVILLE R AT UMIAT AK, 2023, National Water Information System Data (USGS Water Data for the Nation), accessed [March 22, 2024], at URL [https://waterdata.usgs.gov/monitoring-location/15875000/#parameterCode=00065&period=P7D].

Varty, S., Lehnherr, I., St. Pierre, K., Kirk, J., Wisniewski, V. (2021). Methylmercury Transport and Fate Shows Strong Seasonal and Spatial Variability along a High Arctic Freshwater Hydrologic Continuum. *Environmental Science & Technology, 55* (1), 331-340. https://doi.org/10.1021/acs.est.0c05051

Yang, Z., Fang, W., Lu, X., Sheng, G., Graham, D.E., Liang, L., Wullschleger, S.D., Gu, B. (2016). Warming increases methylmercury production in an Arctic soil. *Environmental Pollution, 214,* 504-509. https://doi.org/10.1016/j.envpol.2016.04.069

Zdanowicz, C., Krümmel, E. M., Lean, D., Poulain, A. J., Yumvihoze, E., Chen, J., Hintelmann, H. (2013). Accumulation, storage, and release of atmospheric mercury in a glaciated Arctic catchment, Baffin Island, Canada. *Geochimica et Cosmochimica Acta, 107,* 316-335. http://dx.doi.org/10.1016/j.gca.2012.11.028

Zimmerman, M., Erikson, L. H., Gibbs, A. E., Prescott, M. M., Escargzaga, S. M., Tweedie, C. E., Kasper, J. L., Duvoy, P. X. (2022). Nearshore bathymetric changes along the Alaska Beaufort Sea coast and possible physical drivers. *Continental Shelf Research, 242,* 104745, https://doi.org/10.1016/j.csr.2022.104745

Zolkos, S., Krabbenhoft, D. P., Suslova, A., Tank, S. E., McClelland, J. W., Spencer, R. G. M., Shiklomanov, A., Zhulidov, A. V., Gurtovaya, T., Zimov, N., Zimov, S., Mutter, E. A., Kutny, L., Amos, E., Holmes, R. M. (2020). Mercury Export from Arctic Great Rivers. *Environmental Science & Technology, 54* (7), 4140 - 4148. https://doi.org/10.1021/acs.est.9b07145

Zhou, J., Obrist, D., Dastoor, A., Jiskra, M., Ryjkov, A. (2021). Vegetation uptake of mercury and impacts on global cycling. *Nature Reviews Earth & Environment, 2,* 269-284. https://doi.org/10.1038/s43017-021-00146-y

Supplementary Information for Chapter 4

S1. Sampling Locations

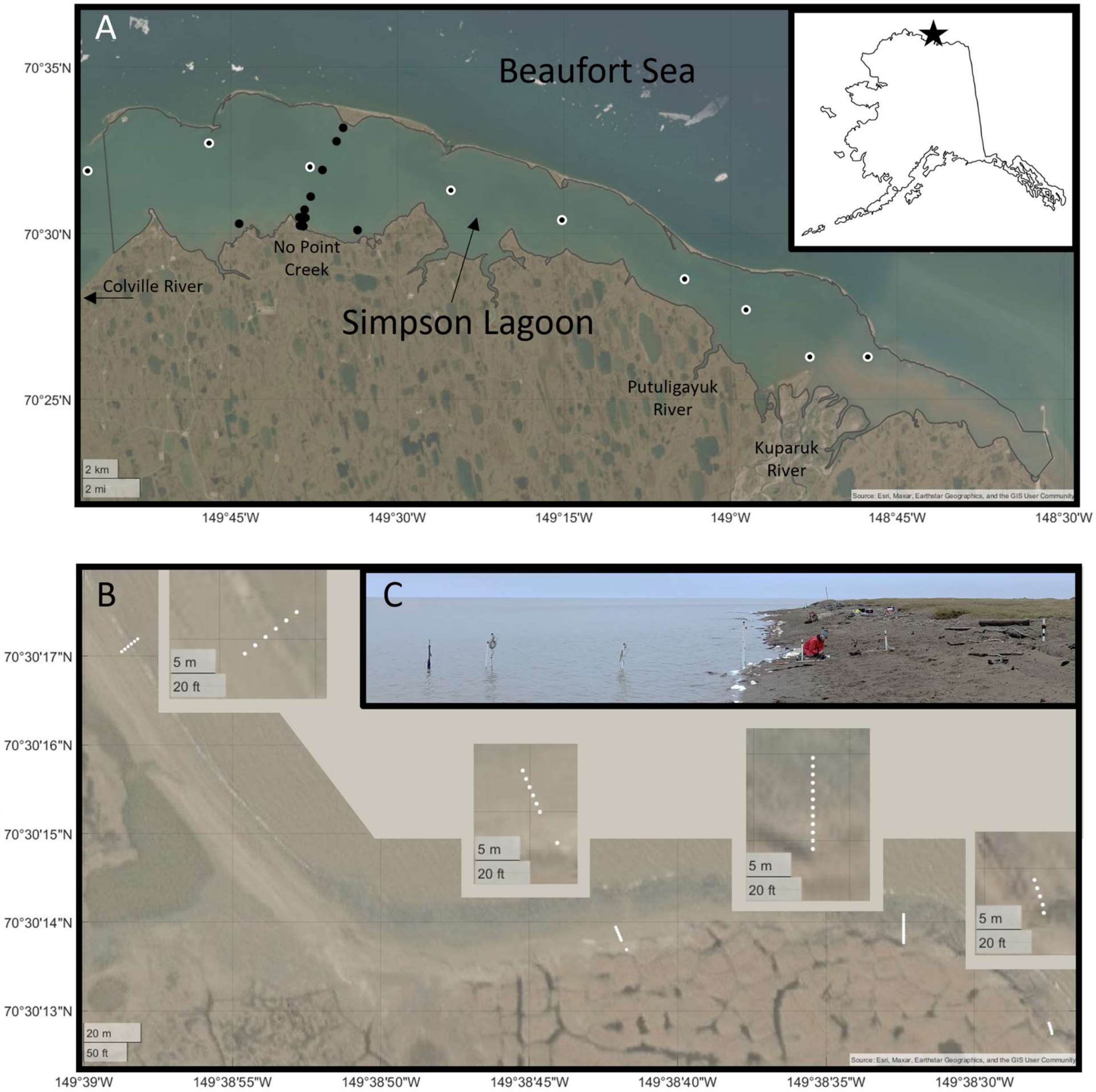

Supplemental Figure 1. Map of Simpson Lagoon, adapted from Bullock et al. (2024). (A) Full lagoon with location along the Alaskan Beaufort coastline shown in insert and repeated surface water sampling stations shown in black dots. July 2023 interior lagoon sampling stations shown in black dots with white outline. (B) Locations of shoreline piezometer transects. (C) Example of a piezometer transect.

S1.2 Lagoon Survey: July 2023

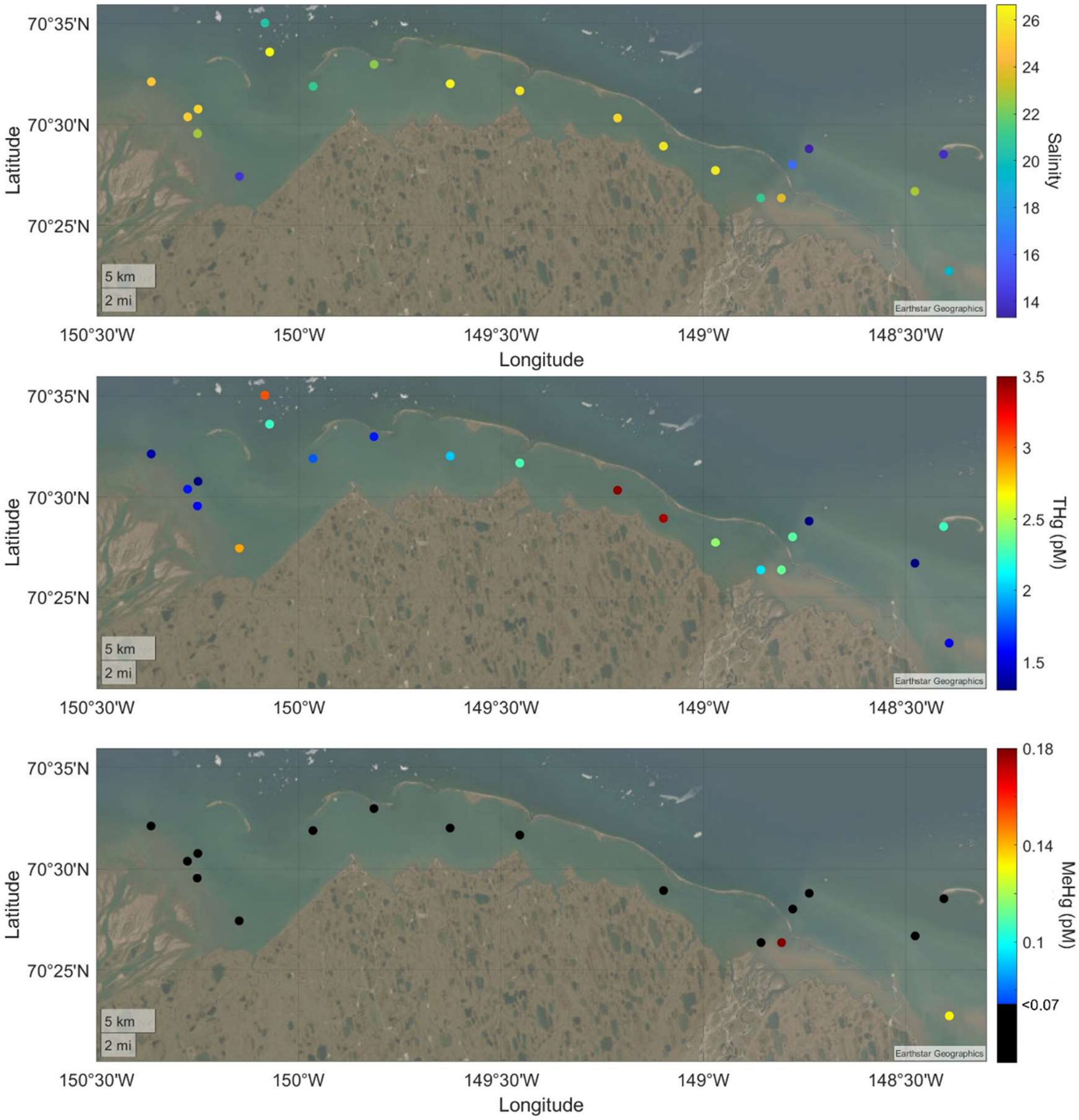

Supplemental Figure S2. Results from the July 2023 lagoon surface water survey for (A) salinity, (B) THg, and (C) MeHg. Symbols in black are below the detection limit, which is 0.2 pM for THg and 0.07 pM for MeHg.

S2. Riverine Inputs

Major rivers and ungauged runoff were estimated using the same method as Bullock et al. (2024). Ungauged runoff from various streams along the lagoon shore was estimated using a simplified equation from Pohl et al. (2007), utilizing precipitation (USDA, 2023), evaporation (Rawlins, 2021), and change in soil moisture (USDA, 2023) throughout the lagoon's watershed that did not feed into a major river (~8,100 km^2). Major river and runoff Hg contributions were estimated using different endmembers, as streams receive a larger relative input from groundwater and therefore tended to have slightly higher Hg concentrations (Supplemental Table 1).

THg inputs from riverine suspended particle desorption were estimated using freshly deposited sediment from the edge of the Kuparuk River. Samples were collected in acid cleaned, combusted amber glass jars during the summer sampling periods and frozen until use. Samples were freeze-dried and a dry weight of ~30 g sediment was used for each desorption experiment. Coastal seawater (S~33) from Vineyard Sound was collected and filtered by the Environmental Systems Laboratory in Woods Hole, MA. 20 L of water was cooled to 4 – 6°C in a cubitainer prior to use, in order to mimic in situ summer temperatures for the Kuparuk River estuary. The sediment was added to the cubitainer and the mixture was recirculated using a peristaltic pump with acid-cleaned tubing to maintain the sediment in solution. After six hours, a sample of the water was filtered and stored using the same techniques as field sampling.

Analysis of the water samples for THg, with the original concentration of the Vineyard Sound water subtracted, produced a THg desorption ratio of 20.8 ± 0.6 μg THg kg^{-1} sediment. This is the desorption rate at salinity 33, but may not be representative of desorption in Simpson Lagoon, given the fact that in spring the lagoon is dominated by freshwater and during other periods a fresh layer of water appears on the surface of the lagoon, likely causing the freshwater/saline interface in the river deltas to be past the point where much of the sediment is deposited. Because of these uncertainties, we do not include the desorption of THg in our lagoon sources table or graphic. If you apply this maximum desorption rate to the sediment fluxes from the rivers entering Simpson Lagoon, as calculated by Bullock et al. (2024) [using data from Kreit et al. (1992) and Walker and Hudson (2003)], you get a spring desorption flux of 1500 ± 800 mmol d^{-1} (from 14.6 ± 7.4 x 10^9 g sediment d^{-1}), a summer average desorption flux of 170 ± 150 mmol d^{-1} (from 1.7 ± 1.4 x 10^9 g sediment d^{-1}), and an autumn desorption flux of 80 ± 70 mmol d^{-1} (from 0.8 ± 0.6 x 10^9 g sediment d^{-1}). However, we reiterate that since up to 90% of riverine suspended sediments are thought to be deposited within the freshwater reaches of the rivers' deltas (Emmerton et al. 2013, Zolkos et al. 2020) and there are times when the lagoon itself is quite fresh, it is likely that these desorption flux calculations are considerably higher than the desorption actually occurring in the system due to ion exchange.

S3. Further Discussion of Hg Concentrations, Associations, and Diffusion Rates

S3.1 Associations of Groundwater THg and MeHg

Neither THg nor MeHg show statistically significant linear correlations with salinity, reflecting the heterogeneous nature of the soil and sediment at this field site, as well as variable Hg cycling along each groundwater flow path. Instead, non-conservative mixing of THg and MeHg along the groundwater salinity gradient occurs, with removal observed for THg and addition observed for MeHg between salinities 0.5 - 2.5. Cycling along this gradient is influenced by subsurface residence time, as well as the interplay and variability between salinity, dissolved organic carbon (DOC), sediment metal content (i.e. iron (Fe) & manganese (Mn)), and redox conditions (ie. ORP & dissolved oxygen (DO)) (Spyropoulou et al. 2022). Studies performed in temperate regions often show the release of THg within the salinity mixing zone of coastal aquifers due to the dissolution of Fe and Mn oxides (Bone et al. 2007, Spyropoulou et al. 2022), increased mobility due to associations with chloride ions (Bone et al. 2007, Rahman et al. 2013, Spyropoulou et al. 2022), and oxidative dissolution of HgS (Spyropoulou et al. 2022).

Supplemental Table S1. Groundwater values across seasons, including salinity, pH, THg, MeHg, Mn, Fe, and DOC. Unless otherwise indicated, reported values are the average and standard deviation for each parameter. Several sampling periods have missing categories (ie. rivers, ungauged runoff, or bottom layer of the lagoon), either due to sample loss or difficult sampling conditions. BDL indicates samples below the detection limit (0.2 pM for THg, 0.07 pM for MeHg).

Season	Sample Period	Sample type	Salinity	pH	THg (pM)	MeHg (pM)	DOC (µM)
Spring	Jun-22	Surface Water	1.9 ± 2.3	7.87 ± 0.28	5.0 ± 2.4	0.14 ± 0.06	330
		Groundwater (range)	0.1 - 35.8	6.38 - 9.50	0.7 - 86.4	BDL - 1.70	516 - 6550
		Groundwater (median)	2.19	8.0	15.4	0.16	1080
		Rivers	0.06 ± 0.02	7.48 ± 0.29	4.8 ± 1.9	0.13 ± 0.10	660 ± 110
		Runoff	0.12 ± 0.05		16.0 ± 11.6	0.95 ± 1.34	1370 ± 1130
		Clean Ice/Snow	0		0.14 ± 0.19	0.10 ± 0.05	
		Dirty Ice/Snow	0		1.10 ± 0.16	BDL	
Summer	Aug-21	Surface Water: Top Layer	12.0 ± 2.3	8.24 ± 0.08	1.4 ± 0.3	0.17 ± 0.03	
		Groundwater (range)	0.4 - 19.4	6.12 - 7.16	1.6 - 43.7	0.75 - 14.9	374 - 8140
		Groundwater (median)	5.1	6.74	9.0	4.35	4780
		Rivers	-	-	-	-	-
	Jul-22	Surface Water: Top Layer	3.4 ± 1.3	8.16 ± 0.25	2.5 ± 0.7	BDL	312 ± 89
		Surface Water: Bottom Layer	26.1 ± 3.2	8.06 ± 0.17	0.4 ± 0.5	BDL	125 ± 22
		Groundwater (range)	0.25 - 29.1	6.0 - 7.56	BDL - 44.1	BDL - 16.7	707 - 10800
		Groundwater (median)	11.9	7.06	5.3	1.04	3970
		Rivers	0.13 ± 0.05	8.05 ± 0.27	1.7 ± 1.7	BDL	530 ± 260
	Jul-23	Lagoon Interior Surface Water	23.1 ± 5.0	8.05 ± 0.08	2.75 ± 0.79	BDL - 0.38	204 ± 72
		Beaufort Shelf	21.2 ± 5.4	8.14 ± 0.02	1.89 ± 0.62	BDL	146 ± 54
		Groundwater (range)	0.6 - 20.2	6.50 - 7.61	1.1 - 71.6	0.2 – 10.9	206 - 11200

		Groundwater (median)	9.1	6.91	16.1	3.26	3184
		Rivers	0.12 ± 0.04	8.15 ± 0.05	3.1 ± 1.9	BDL	717 ± 133
Autumn	Oct-22	Surface Water	25.7 ± 3.2	7.95 ± 0.08	0.16 ± 0.25	0.01 ± 0.03	171 ± 81
		Groundwater (range)	0.5 - 36.1	6.33 - 7.33	0.2 - 55.8	0 - 16.5	358 - 14800
		Groundwater (median)	16.5	6.81	4.9	0.33	3710
		Rivers	0.12 ± 0.04	7.95 ± 0.87	2.0 ± 1.8	BDL	650 ± 110

Non-conservative removal of THg within the STE at this site may be driven by its association with flocculating organic material, which was visually observed in collected samples. Out of all ancillary parameters measured during the 2021 and 2022 field campaigns (salinity, pH, DO, Fe, Mn, ORP, DOC, & TDN), MeHg showed no significant correlations, while THg showed a seasonally dependent correlation with DOC. During spring, THg has a strong positive correlation with DOC ($R^2 = 0.8$, $p < 0.001$: Supplemental Fig. S2). This correlation also appears during the autumn ($R^2 = 0.7$, $p < 0.001$: Supplemental Fig. S2). However, the relationship between THg and DOC seems to be more complicated in summer, with July 2022 showing a moderate positive correlation ($R^2 = 0.5$, $p < 0.001$: Supplemental Figure 2), while August 2021 and July 2023 both show no statistically significant correlation between DOC and THg.

The ratio of DOC:THg in June groundwater (57 µmol C/pmol THg) is comparable to the ratio found in Simpson Lagoon soils and sediments (62 µmol DOC/pmol THg), indicating a reasonably steady-state environment between the solid and liquid partitioning of Hg species. This ratio increases to 129 µmol DOC/pmol THg in July 2022 and 215 µmol DOC/pmol THg in October, due to increasing DOC concentrations and a slight decrease in THg concentrations between spring, summer, and autumn. The decrease in groundwater THg concentrations over the course of the year could be due to multiple factors: reduction to Hg^0 and evasion to the atmosphere (Moore & Castro, 2012, Jiskra et al. 2015), microbial uptake and transformations (Barkay et al. 2011), leaching from soils (Schuster et al. 2011), and minor reductions from plant uptake (Obrist et al. 2017).

The disruption in the correlation between DOC and THg during the summer months may be due to microbial uptake and transformations of Hg. We see evidence of higher microbial activity during this time via higher MeHg concentrations in groundwater. Biological transformations of Hg^{II} to MeHg depend heavily on temperature and soil moisture (Barkay et al. 2011; Yang et al. 2016). Our data reflect this relationship, with average MeHg concentrations following soil temperature patterns (spring ~ 0.3 pM at -2.1°C, summer ~ 4.1 pM at 3.3°C, autumn ~ 2.6 pM at -0.5°C). These MeHg concentrations support the idea that processes impacting THg concentrations are most prominent during the warm summer months when microbial activity is highest.

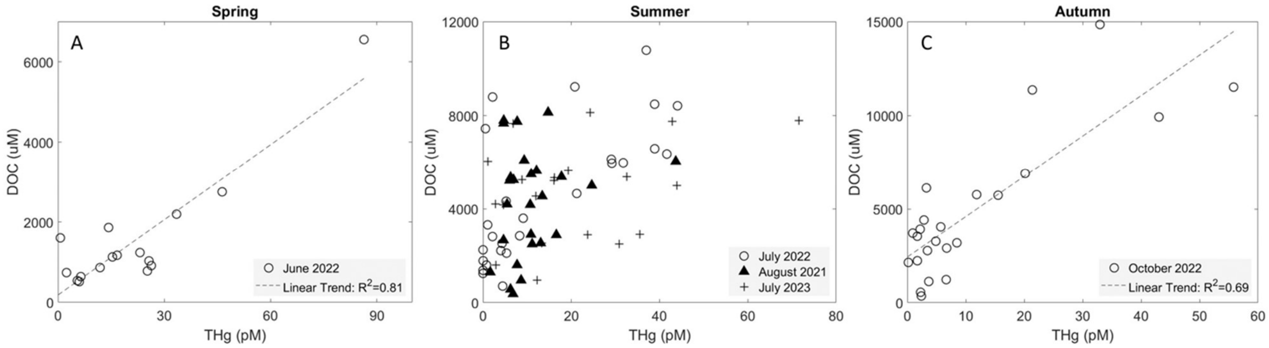

Supplemental Figure S3. Seasonal association of THg with DOC for (A) June 2022, (B) August 2021, July 2022, and July 2023 and (C) October 2022. Linear trends were calculated using the Pearson correlation method and have p-values <0.001.

S3.2 Diffusion Experiments

Diffusive fluxes from lagoon bottom sediments were determined by incubating two sediment cores according to a modified method from Koron and Faganeli (2012). Briefly, two sediment cores were taken from a boat using a Uwitec gravity corer at a distance of ~0.4 km from shore. The cores were capped and frozen until the experiment, at which time they were slowly thawed at a temperature of 4-6°C. Pre-filtered (1 µm) Simpson Lagoon water (1L) that had been collected at the time of sampling was used as the overlaying water in the experiment. The core was capped with a lid that allowed three, gas impermeable, acid washed Masterflex™ L/S™ High-Performance, C-FLEX™ tubes to extend into the chamber. One tube was fitted with a luer lock and was used to sample the overlying water. One tube was connected to an air pump and fitted with a bubbling stone to ensure the system remained oxygenated, as we saw no evidence of hypoxia in the lagoon bottom waters during any sampling period. The final tube allowed outflowing air to leave the system and prevent pressurization. Gold traps (Brooks Rand Instruments) were used in-line on each air tube to ensure no atmospheric contamination of Hg. Samples were collected at each time point via syringe. The volume of water withdrawn was compensated by adding the same amount of fresh Simpson Lagoon. Reported concentrations were corrected to account for these dilutions.

Diffusion rates across the whole lagoon were calculated using the surface area of the cores (0.00636 m^2) and the diffusion rates obtained from a logarithmic fit on the experimental data (pmol L^{-1} hr^{-1}) to get a flux in pmol m^{-2} d^{-1}. The fluxes were then scaled to Simpson Lagoon's surface area (2.45×10^8 m^2) and the molar mass of Hg to get the diffusion fluxes. Core 1 showed a diffusive flux of 100 ± 20 mmol d^{-1} while Core 2 showed little to no diffusion. The range of expected diffusion fluxes based on theoretical calculations using Hg(II) diffusion coefficients at 5°C [$D_{inorganic} = 4.86 \times 10^{-6}$ cm^2 s^{-1}; $D_{organic} = 5.29 \times 10^{-7}$ cm^2 s^{-1} (Pi et al. 2020)], subtidal porewater concentrations (THg: 1.92 ± 0.17 pM; DOC: 2231 ± 1121 µM), bottom water THg concentrations (BDL), a measured porosity of 0.26, and a range of diffusive boundary layer thicknesses ranging from 0.5 mm to 1 cm. The theoretical range was 1.5 – 30 mmol d^{-1}. The large range in diffusion fluxes based on these experiments may be the result of varying agitation from the bubblers used to ensure consistent oxygen concentrations. As a result, we report the range of theoretical values, with the understanding that periods with high turbulence may result in higher diffusive fluxes.

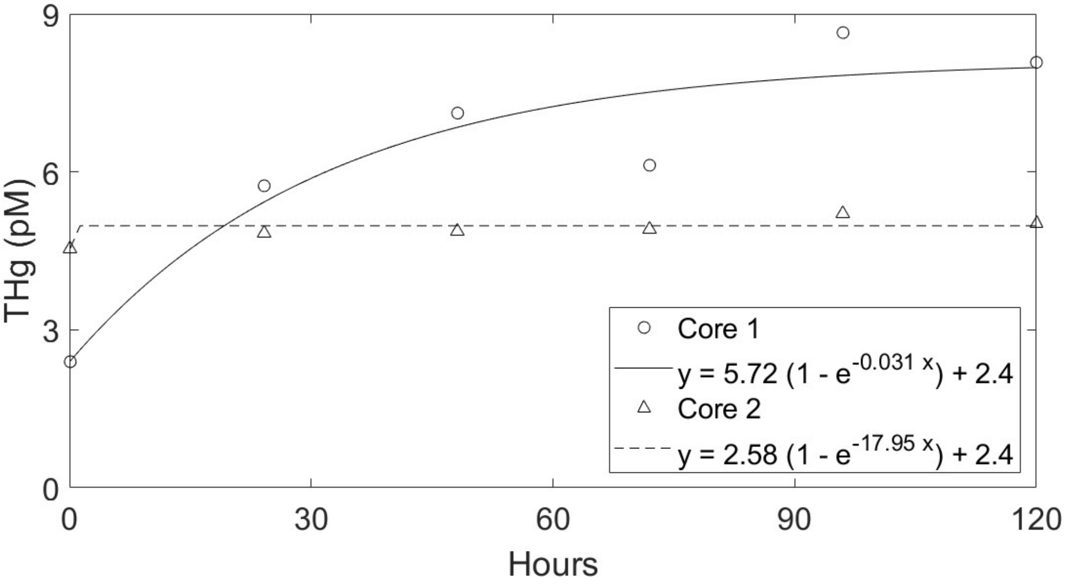

Supplemental Figure S4. Diffusion experiment results for two cores, taken from Simpson Lagoon bottom sediments. Core 1 showed evident diffusion of THg into the overlying water, while Core 2 showed minimal diffusion.

S4. Data Quality Assurance for Hg data

Care was taken to ensure the validity of the measured Hg values, including: using acid-washed, combusted glass vials with PTFE-lined lids for sampling, taking field and method blanks that were pre-acidified with the same acid as the samples, and leaving several MilliQ water blanks exposed to the open air overnight to check for atmospheric THg contamination. Based on the standard deviation of the instrument blanks run on the Tekran 2600, the detection limit was 0.2 pM THg (n = 18). Our method blanks, which were taken in the laboratory using the same equipment that was used in the field and substituting groundwater out for MilliQ water, were all 0.5 ± 0.1 pM THg (n = 5). Two field blanks were taken, using MilliQ water that was carried out to the field and the field sampling equipment. One of the two field blanks taken was below the detection limit and the other was 0.3 pM. Reported values have the method blank average (0.5 pM THg) subtracted from the raw values.

The two blanks that were left out in the laboratory overnight (16 hr) and showed slight atmospheric contamination (0.6 pM). For this reason, the diffusion experiments were fitted with gold-traps for all air being circulated, in order to remove potential contamination. All THg sample preparation for analysis occurred in a clean lab.

Based on the standard deviation of the instrument blanks run on the Tekran 2700, the detection limit for MeHg was 0.07 pM (n = 26). Our field blanks, consisting of MilliQ water pumped through both stainless steel and PVC piezometers, were below the detection limit (n = 2). . Our method blanks, taken in the laboratory using field equipment, were 0.09 pM (n = 2). Reported values have the method blank average (0.09 pM MeHg) subtracted from the raw values.

Standard curves were run every 36 hours during analysis. Instrument blanks, spiked samples, and operational recovery samples were run every 25-50 samples for THg (Tekran 2600) and every 12 samples for MeHg (Tekran 2700).

References

Barkay, T., Kroer, N., Poulain, A.J. (2011). Some like it cold: microbial transformations of mercury in polar regions. *Polar Research, 30,* 15469. https://doi.org/10.3402/polar.v30i0.15469

Bone, S.E., Charette, M.A., Lamborg, C.H., Gonneea, M.E. (2007). Has Submarine Groundwater Discharge Been Overlooked as a Source of Mercury to Coastal Waters? *Environmental Science & Technology*, *41* (9), 3090 - 3095. https://doi.org/10.1021/es0622453

Bullock, E. J., Schaal, I. V., Cardenas, M. B., McClelland, J. W., Charette, M. A. (2024). Seasonality of submarine groundwater discharge to an Arctic coastal lagoon. *Limnology and Oceanography, 9999* (1-10). https://doi.org/10.1002/lno.12585

Emmerton, C. A., Graydon, J. A., Gareis, J. A., St. Louis, V. L., Lesack, L. F. W., Banack, J. K. A., Hicks, F., Nafziger, J. (2013). Mercury Export to the Arctic Ocean from the Mackenzie River, Canada. *Environmental Science & Technology, 47* (14), 7644-7654. https://doi.org/10.1021/es400715r

Jiskra, M., Wiederhold, J. G., Skyllberg, U., Kronberg, R. M., Hajdas, I., Kretzschmar, R. (2015). Mercury deposition and re-emission pathways in boreal forest soils investigated with Hg isotope signatures. *Environmental Science & Technology, 49* (12), 7188– 7196. https://doi.org/10.1021/acs.est.5b00742

Koron, N., Faganeli, J. (2012) Benthic fluxes of mercury during redox changes in pristine coastal marine sediments from the Gulf of Trieste (northern Adriatic Sea). *Journal of Soils and Sediments*, *12*, 1604–1614. https://doi.org/10.1007/s11368-012-0602-1

Kriet, K., Peterson, B. J., Corliss, T. L (1992). Water and sediment export of the upper Kuparuk River drainage on the North Slope of Alaska. *Hydrobiologia, 240*, 71-81.

Moore, C. W., Castro, M. S. (2012). Investigation of factors affecting gaseous mercury concentrations in soils. *Science of the Total Environment, 419,* 136-143. https://doi.org/10.1016/j.scitotenv.2011.12.068

Obrist, D., Agnan, Y., Jiskra, M., Olson, C. L., Colegrove, D. P., Hueber, J., Moore, C. W., Sonke, J. E., Helmig, D. (2017) Tundra uptake of atmospheric elemental mercury drives Arctic mercury pollution. *Nature, 547*, 201–204. https://doi.org/10.1038/nature22997

Pedrazas, M., Cardenas, M. B., Demir, C., Watson, J. A., Connolly, C. T., McClelland, J. W. (2020). Absence of ice-bonded permafrost beneath an Arctic lagoon revealed by electrical geophysics. *Science Advances, 6* (43). https://doi.org/10.1126/sciadv.abb5083

Pi, K., Liu, J., Van Cappellen, P. (2020). Direct Measurement of Aqueous Mercury(II): Combining DNA-Based Sensing with Diffusive Gradients in Thin Films. *Environmental Science and Technology, 54* (21), 13680-13689. https://doi.org/10.1021/acs.est.0c03870

Pohl, S., Marsh, P., Bonsal, B. R. (2007). Modeling the Impact of Climate Change on Runoff and Annual Water Balance of an Arctic Headwater Basin. *Arctic, 60* (2), 173-186.

Rahman, M. M., Lee, Y. G., Kim, G., Lee, K., Han, S. (2013). Significance of submarine groundwater discharge in the coastal fluxes of mercury in Hampyeong Bay, Yellow Sea. *Chemosphere, 91* (3), 320-7. https://doi.org/10.1016/j.chemosphere.2012.11.052

Schuster, P.F., Strieg, R.G., Aiken, G.R., Krabbenhoft, D.P., Dewild, J.F., Butler, K., Kamark, B., Dornblaser, M. (2011). Mercury export from the Yukon River Basin and potential response to a changing climate. *Environmental Science & Technology, 45* (21), 9262–9267. https://doi.org/10.1021/es202068b

Spyropoulou, A.E., Lazarou, Y.G., Sapalidis, A.A., Laspidou, C.S. (2022). Geochemical modeling of mercury in coastal groundwater. *Chemosphere, 286*(1), 131609. https://doi.org/10.1016/j.chemosphere.2021.131609

USDA, 2023. Precipitation, Accumulated, Prudhoe Bay, AK. Natural Resources Conservation Service and National Water and Climate Center, accessed (March 28, 2024) at URL [https://wcc.sc.egov.usda.gov/nwcc/site?sitenum=1177]

Walker, H. J., Hudson, P. F. (2003). Hydrologic and geomorphic processes in the Colville River delta, Alaska. *Geomorphology, 56* (3-4), 291-303.

Yang, Z., Fang, W., Lu, X., Sheng, G., Graham, D.E., Liang, L., Wullschleger, S.D., Gu, B. (2016). Warming increases methylmercury production in an Arctic soil. *Environmental Pollution, 214*, 504-509. https://doi.org/10.1016/j.envpol.2016.04.069

Zolkos, S., Krabbenhoft, D. P., Suslova, A., Tank, S. E., McClelland, J. W., Spencer, R. G. M., Shiklomanov, A., Zhulidov, A. V., Gurtovaya, T., Zimov, N., Zimov, S., Mutter, E. A., Kutny, L., Amos, E., Holmes, R. M. (2020). Mercury Export from Arctic Great Rivers. *Environmental Science & Technology, 54* (7), 4140 - 4148. https://doi.org/10.1021/acs.est.9b07145

Chapter 5: Controls on Mercury Mobilization from Soils and Permafrost in Arctic Coastal Environments

Emma J. Bullock

Abstract

Mercury (Hg) is an element of concern for humans and wildlife, given its neurotoxic effects when in the form methylmercury (MeHg). With the Arctic warming up to four times faster than the rest of the globe, vast stores of currently sequestered Hg may become vulnerable to release from degrading permafrost soils. While factors controlling Hg methylation have received significant attention, factors influencing the fate of MeHg in the environment remain understudied, particularly in Arctic soils. This study examines groundwater samples taken during four sampling campaigns between 2021 and 2023 at Simpson Lagoon, Alaska, to explore the key species associated with total Hg (THg) and MeHg cycling in an Arctic coastal aquifer's salinity mixing zone. Selective leaching experiments were performed on tundra active layer, tundra permafrost, and intertidal sediments to understand how THg is complexed in the solid state as well. These data were then compared with results from sediment plug flow-through experiments on tundra and permafrost cores from three Arctic coastal locations (Elson Lagoon, Drew Point, and Simpson Lagoon) to identify controls on THg and MeHg mobilization under varying coastal groundwater conditions. Utilizing all of these data, we find that in Arctic soils of peat origin and high organic matter content, dissolved organic carbon (DOC) is the most significant control on MeHg mobilization from the soils. For THg in organic rich soils, relatively unprocessed DOC, such as from active layer soils, is more important for mobilization than overall DOC concentrations. In thawed permafrost of lacustrine origin and lower organic matter content, the effect of higher salinities driving the salting out of DOC, sulfate reduction, and metal oxide dissolution is more important for THg and MeHg mobilization from the soils. This study reveals the importance of considering salinity intrusion into coastal Arctic aquifers and the necessity of considering soil type when estimating groundwater fluxes of Hg species from degrading Arctic permafrost to the Arctic Ocean.

1. Introduction

Mercury (Hg) is a neurotoxic element that disproportionately impacts Arctic communities and wildlife (Fernández-Llamazares et al. 2020, Basu et al. 2022) in the bioaccumulative form methylmercury (MeHg). Due to atmospheric circulation patterns that drive Hg deposition in polar regions (Halbach et al. 2017, Dastoor et al. 2022), and given that 70% of Hg deposition into Arctic soils comes from plant uptake of atmospheric elemental Hg (Obrist et al. 2017, Jiskra et al. 2019), Arctic soils act as a major global sink for this volatile toxin (Jonsson et al. 2022). In active layer soils, the seasonally thawed layer that sits above the permafrost ice table, there is an estimated 212 Gg of sequestered Hg, with this value increasing to nearly 600 Gg if the top three meters, including permafrost, are included (Dastoor et al. 2022). With permafrost degrading and the seasonally thawed active layer growing deeper each year due to fast Arctic warming (Biskaborn et al. 2019, Smith et al. 2022), the potential mobilization of vast stores of Hg is becoming an urgent issue that needs to be addressed.

Groundwater is one pathway through which Hg could be transported from thawing Arctic soils into waterways and the Arctic Ocean, as is known to occur with dissolved organic carbon (DOC) released from thawing permafrost (Ward and Cory, 2015). In temperate regions, salt water intrusion into coastal aquifers has been shown to mobilize Hg (Bone et al. 2007, Rahman et al. 2013, Spyropoulou et al. 2022). This zone where saline and fresh groundwater mix – called the subterranean estuary – plays host to numerous biotic and abiotic reactions, such as ion exchange, dissolution/precipitation of minerals, and fluctuating metal concentrations due to rapid changes in redox conditions (Bone et al. 2007, Moore, 1999). Many of the species known to impact Hg(II) and MeHg movement in soils have strong gradients or experience dynamic production and removal in subterranean estuaries, including organic matter (OM) and DOC (Wallschläger et al. 1996, Hammerschmidt et al. 2004, Jonsson et al. 2012), sulfide species (Benoit et al. 1999, Johannesson and Neumann, 2013, Gong et al. 2023), metal oxides (Luther et al. 1992, Mehrohtra and Sedlak, 2005), and chloride ions (Kozin and Hansen, 2013, Spyropoulou et al. 2022).

While a vast amount of research has addressed controls on Hg(II) methylation in sediments (Benoit et al. 2003, Kerin et al. 2006, Mehrohtra and Sedlak 2005, Lambertsson and Nilsson, 2006, Kim et al. 2011, Graham et al. 2012, Jonsson et a. 2012, Chiasson-Gould et al. 2014, Schaefer et al. 2014, Mazrui et al. 2016, Ghimire et al. 2019), our understanding of MeHg's fate once produced remains limited, particularly in groundwater (Aleku et al. 2024). Given the negative health impacts of MeHg on Arctic communities and fauna, identifying controls on MeHg mobilization by groundwater in thawing Arctic soils is vital for future risk and exposure assessments. This study aims to address this knowledge gap by utilizing active layer and permafrost soil samples from three locations along the Beaufort Sea coastline in sediment plug flow-through experiments, in order to investigate the impact of saline groundwater intrusion on thawing Arctic soils. *In situ* groundwater samples from four sampling campaigns to an Arctic coastal lagoon were also analyzed, along with a time series that traversed the subterranean estuarine mixing zone during changing salinity conditions, in order to compare experimental findings to *in situ* groundwater associations. Together, these analyses help elucidate the major factors controlling total Hg (THg) and MeHg retention or mobilization in Arctic soils when exposed to varying groundwater conditions.

2. Methods

2.1 Study Locations

Permafrost and tundra core samples were taken from three locations along the Alaskan Beaufort Sea Coastline: Elson Lagoon, Drew Point, and Simpson Lagoon (Figure 1). The Beaufort Sea Coastline is characterized by shallow lagoons and substantial coastal erosion, with regions such as Drew Point approaching the fastest erosion rates worldwide of 22 m per year (Jones et al. 2018). There are substantial variations in soil types, carbon content, and topography throughout the coastline (Ping et al. 2011), with the three sites chosen for this study each having unique properties that allow for comparisons across different environments.

Figure 1. Location of field sites on the Beaufort Sea coastline of Northern Alaska, with a typical length of shoreline shown for A) Elson Lagoon, B) Drew Point, and C) Simpson Lagoon.

Elson Lagoon's active layer has been measured to depths of 30 cm (Brown et al. 2003), though recent models suggest it may now reach 50 cm below ground due to increased soil temperatures and rainfall (Rawlins, 2021). The active layer consists of tundra peat soils and reworked, fine-grained lake sediments from drained lake basins (Brown et al. 2003). At the coast, bluff elevations range from 1.8 - 4.4 m above sea level (Tweedie et al. 2012). The site is underlain by permafrost and expresses polygon tundra morphologies on the surface, with young, flat-topped polygons in some regions and older, high-centered polygons with deteriorating ice wedges in others (Brown et al. 2003). Ice content in permafrost at Elson Lagoon ranges from 40 - 70% (Brown et al. 2003).

Drew Point is the least protected site sampled, corresponding with the highest rates of coastal erosion (Gibbs and Richmond, 2015). The site is dominated by thermokarst lakes and drained lake basins (Jones and Arp, 2015), leading to an active layer consisting of reworked lake sediments and mineral soil permafrost that is largely of marine or lacustrine origin (Rawlinson, 1993, Bristol et al. 2021). The active layer sediments annually thaw to a depth of ~40 cm (Bristol et al. 2021). The ice content of the permafrost is the highest of the three sites, reaching up to 90% in some areas, and wedge ice is abundant (Kanevskiy et al. 2013). High rates of erosion have led to impressive bluff elevations, reaching 1.6 - 7.1 m above sea level (Jones et al. 2018).

Details on the Simpson Lagoon study location have been previously described in Bullock et al. (2024[a], 2024[b]). Briefly, the site is largely tundra, with an active layer that thaws to 25 - 100 cm and is dominated by peat soils (Déry et al. 2005). Some of the tundra expresses polygon and ice wedge morphology, with permafrost ice content between 50 - 80%, while other sections have been degraded, likely by storm surge overtopping. Simpson Lagoon has the lowest lying topography of all three sites, with bluffs of just ~1 m above sea level along most of the shoreline. Its low-lying topography and protection, in the form of barrier islands, means that Simpson Lagoon has the lowest rate of coastal erosion of the three sites (Schreiner et al. 2013). This has led to the presence of a narrow sandy beach between the lagoon and the bluffs, with sand consisting of silicate minerals carried to the lagoon from the Brooks Range by the Colville River and silicates and carbonates carried by Beaufort Shelf currents from the Mackenzie River (Schreiner et al. 2013).

2.2 Sample Collection

The permafrost core samples from Elson Lagoon were collected in July and August 2019. Various permafrost soil horizons were targeted by taking advantage of exposed bluff faces, with accurate location and elevation ensured via Differential Global Positioning System measurements taken at each site. For each core, the bluff face was cleared of debris and sediment cores were collected by drilling into the bluff face horizontally with a battery powered drill and SIPRE stainless steel drill powered core sampler. The permafrost core samples from Drew Point were collected in April 2018 using the same SIPRE coring system, as described by Bristol et al. (2021). The core utilized in this study was taken from a young drained thermokarst lake basin. For both Elson Lagoon and Drew Point, samples were kept frozen in the field using a cooler with Techni ice, and transported to the Barrow Arctic Research Center in Utqiaġvik, Alaska, to be stored in a -40°C freezer. Permafrost cores were sectioned using a circular table saw and shipped frozen in clean plastic bags to Woods Hole, MA, where they were stored at -20°C until use.

In situ groundwater sampling for Hg at Simpson Lagoon has been described in Bullock et al. (2024^{b}). Briefly, samples were collected from a ~1 km long section of shoreline that was characterized by a narrow sandy beach backed by 1 m high tundra polygon bluffs. Stainless steel or PVC piezometers were installed in transects traversing the subterranean salinity mixing gradient, with three transects (T1, T2, and T3) revisited on at least two field campaigns. T1 was sampled in August 2021, July 2022, October 2022, and July 2023. T2 was sampled in August 2021 and July 2022. T3 was sampled in July 2022 and October 2022. T1 traversed a narrow sandy beach, backed by 1 m high tundra bluffs. T3 was similar, but bordered a small stream that discharged following rainfall events. T2 was distinct in that it was located in a trough between two degrading tundra polygons bluffs and had the smallest sandy strip of all three.

Permafrost and active layer cores for Simpson Lagoon groundwater plug flow-through experiments were collected in October 2022 and July 2023, with preliminary cores from transect T1 used in the selective leaching experiments collected in August 2021. The T1 intertidal core was collected by pushing a clear PVC core barrel into the sandy sediment until the ice table was reached (35 cm). Minimal compression (<3 cm) was observed. The tundra active layer cores were collected by cutting a rectangular section out of the active layer down to the ice table using a bread knife (active layer depth ~ 22 cm). The permafrost cores were taken directly below the active layer cores, using the same SIPRE system as used in Elson Lagoon and Drew Point. Approximately 15 cm of the upper permafrost layer were lost due to complications with the sampling process, resulting in the first samples analyzed from the permafrost core being from 38 cm below the surface. Cores were stored in clean plastic bags or PVC pipes and transported in coolers back to the lab (<6hr) where they were frozen at -20°C. The cores were shipped intact and frozen to Woods Hole, MA, where they were stored at -20°C until use.

Clean sampling techniques were used for collection of dissolved *in situ* Hg samples. Samples were collected using a peristaltic pump with acid washed, Masterflex™ L/S™ High-Performance, C-280 FLEX™ tubing and filtering samples through a clean Geotech PES capsule filter (0.45 µm). Lagoon samples were taken by placing the same tubing into the water at the shoreline. Samples for Hg analysis were filtered into combusted and MQ rinsed 250 mL amber borosilicate bottles with PTFE lined caps that were pre-charged with 0.5 mL TM grade HCl for a final concentration of 0.2% sample volume. Trace metal (TM) samples were filtered into LDPE or HDPE bottles precharged with TM grade nitric acid for a final concentration of 1%. Samples for DOC were filtered, using the same tubing and filters, into clear plastic polypropylene vials and stored frozen until analysis. Blanks (Hg & TM) were taken from both types of piezometers utilized, with no significant differences seen between the stainless steel piezometer blanks and the PVC piezometer blanks. Salinity, dissolved oxygen (DO), temperature, turbidity, oxygen reduction potential (ORP), and pH were measured at each sampling point with an AquaTROLL Multiparameter Sonde or a Myron L Ultrameter^{TM}. Missing DO and ORP measurements are due to electrode malfunctions or severe drift in the field, which happened more frequently when conditions were near or below 0°C. Sulfide was measured during the July 2023 sampling campaign using a Mettler Toledo^{TM} Ion Selective Electrode (Ag^+/S^{2-}) using Thermo Scientific^{TM} Orion^{TM} reagents (Sulfide Anti-Oxidant Buffer) and were calibrated using a sodium sulfide nonahydrate (ACS) solution that was prepared daily.

2.3 Sediment Operational Leaching Experiments

To better understand the species associated with THg in the soils and intertidal sediments of transect T1, we utilized a sequential extraction method developed by Fernández-Martínez and Rucandio (2013). This method targets Hg associated with labile species in the first leach, humic and fulvic complexes in the second leach, crystalline oxides in the third leach, and sulfide species in the fourth leach. Briefly, for the first leach, 5 g of sediment were combined with 0.2 M HNO_3 in combusted 40 mL borosilicate glass centrifuge tubes with PTFE-lined caps. The tubes were then placed in a rotary shaker that was partially submerged in a 50°C ultrasonic bath and shaken for 2 hours at 35 rpm, with ultrasonic agitation applied for 15 minutes every half hour. The supernatant was collected via centrifugation and syringe filtration (0.45 µm Cytiva Whatman Uniflo Syringe PTFE filters) into acid-washed, combusted amber borosilicate glass vials with PTFE-lined caps (40 mL) that had been pre-charged with TM grade HCl for a final concentration of 0.2% sample volume. The sediment was then vortexed with 5 mL MilliQ water, recentrifuged, and the wash was combined with the collected supernatant. For the second leach, 0.1 M tetrasodium pyrophosphate was added to the sediment and placed in the rotary shaker at 35 rpm for 18 hours, before collection and washing using the same method as leach one. The third leach consisted of 50% v/v TM grade nitric acid being added to the sediment and placed in the rotary shaker at 35 rpm for 21 hours before collection and washing. The final leach started with 0.03 M potassium iodide in 50% v/v HCl being added to the sediment, followed by 45 minutes in a 70°C ultrasonic bath, with sonication applied for the first 15 minutes and the last 15 minutes, followed by collection and washing.

This protocol does not include a final digestion step to target Hg associated with refractory materials. To determine the total amount of THg in the soils, the bulk soil THg was measured by the Nippon MA-3000 Direct Mercury Analyzer (see below) and the amount associated with refractory materials was considered the total amount minus the cumulative Hg extracted from the selective leaches. The average amount of THg not bound to refractory materials was 70% ± 20% (*n*=7) for the intertidal core fractions, 80% ± 20% (*n*=6) for the tundra active layer fractions, and 90% ± 20% (*n*=5) for the tundra permafrost fractions. All soil parameters measured (i.e. sampling depth, soil carbon, soil THg, soil Fe, and soil Mn) are listed in Supplemental Table S1.

2.4 Sediment Plug Flow-Through Experiments

Influent water for these experiments was collected in the Simpson Lagoon region, to mimic natural infiltrating water through these soils. Freshwater was collected in the form of snow in April 2023 by scooping visually clean snow into clean plastic bags that were then stored in coolers and allowed to melt. They were filtered using a Hytrex cartridge filter (1 μm) into clean plastic cubitainers later in the lab. Saline water (S=26.5) was collected in July 2023 from Simpson Lagoon using a bilge pump and two in-line Hytrex cartridge filters (10 μm, 1 μm) into clean plastic cubitainers. Each of these natural waters were tested for trace metals, Hg, and DOC.. The concentrations of iron (Fe) and manganese (Mn) were negligible in the samples compared to the effluent values, with initial DOC also being comparatively low (freshwater DOC <0.001 mM; seawater DOC ~ 0.1 mM). The initial concentrations of THg were 9.4 pM and 0.33 pM for the freshwater and saline water, respectively. The initial concentrations of MeHg were 0.33 pM and <0.07 pM for the freshwater and saline water, respectively.

For the experiments, a sediment plug flow-through reactor (Pallud and Van Cappellen, 2006, Pallud et al. 2007) was used to mimic the flow of groundwater through intact sediment cores sections. Cores were 5 cm x 4.5 cm (length x diameter; Figure 2), except for three of the Elson Lagoon cores where sample material was limited and cores of length 2.5 cm were used. We acknowledge there may be slight differences in species concentrations in these cores due to their shorter length and therefore residence time; however, the concentrations still fall within the same range as the other Elson Lagoon cores.

Prior to the experiments, frozen soil core section edges were scraped using a clean ceramic blade to remove possible metal contamination. Pre-cut core sections (Elson Lagoon) were allowed to thaw to the point that the clear acrylic reactor tube could be pushed down onto the core, scraping off the thawed exterior but not disturbing the frozen middle. The excess sediment from each core section was collected and freeze dried for porosity/ice content, soil carbon, and soil THg analyses (Supplemental Table S2). The cores were then capped with 1 mm thick, 0.45 μm hydrophobic porous plates at each end (in contact with the sediment) and sealed inside the reactor by tightly screwing fitted/grooved acrylic plates with O-rings into place. This was completed before the encased core section thawed, to ensure minimal disruption to the soil structure. Intact cores (Simpson Lagoon and Drew Point) were split to the desired length using the ceramic blade and a rubber mallet (did not come into contact with cores), then processed in the same way as the pre-cut core sections.

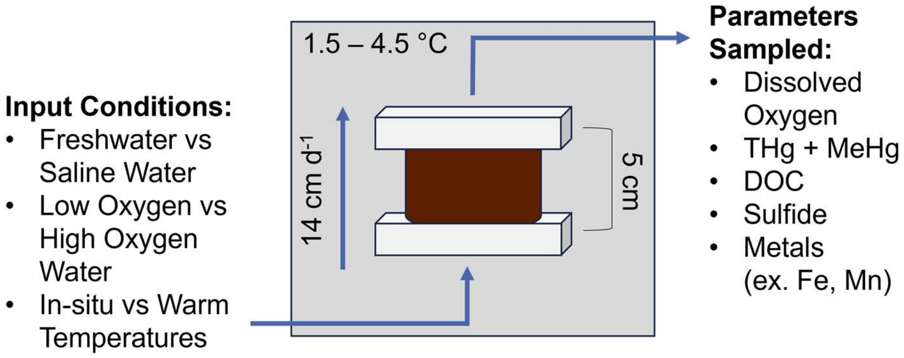

Figure 2. Design diagram of the sediment/soil plug flow-through reactor, modified from Pallud and Van Cappellen (2006). Input conditions, flow rate, and parameters samples are all described.

The chosen flow rate for these experiments was 14 cm d^{-1}, based on hydraulic conductivity measurements taken at Simpson Lagoon (Guimond et al. 2023), and was implemented via peristaltic pump. Temperature was controlled by keeping the cores in a mini-fridge at 1.5 – 4.5°C to mimic *in situ* summer groundwater temperatures along the Beaufort Sea coastline. To test for temperature impacts on Hg cycling, selected reactors were allowed to come to room temperature (20 - 22°C). Six core sections could be run in tandem, with each experiment lasting between 80 - 85 hours. Each experiment began with a certain set of conditions (ex. ~3°C, oxygenated fresh water influent), with the conditions changed at approximately 48 hours into the experiment (ex. 20°C, oxygenated saline water influent). The experimental conditions for each set of reactors can be seen in Supplemental Table S3. Oxygen concentrations were checked periodically using a Unisense Oxygen MicroOptode in a flow-through cell that was attached to the exit port tubing for analysis. The optode was calibrated every few hours using deoxygenated (via N_2 purging) and fully oxygenated water. Dissolved oxygen concentrations in the cores ranged from 4 µM to 400 µM (avg: 110 ± 70 µM) which was comparable to concentrations observed in the field (range: 8.5 – 425 µM; avg: 210 ± 130 µM). Sulfide concentrations were measured using the same methods as during the July 2023 field campaign (see above).

All collected samples were filtered through Cytiva Whatman Uniflo Syringe PTFE filters (0.45 µm). Samples for THg and MeHg were collected in acid-washed, combusted amber borosilicate glass vials with PTFE-lined caps (40 mL or 250 mL) that had been pre-charged with TM grade HCl for a final concentration of 0.2% sample volume. Additional samples for THg were collected in clear borosilicate glass vials (4 mL) prepared in the same way as the amber vials. From the amber vials, 10 mL were removed and added to sterile polypropylene centrifuge tubes and frozen for DOC analysis. For each DOC sample, three consecutive time points were combined to make an integrated DOC sample of 30 mL total. Trace metal samples were collected in HDPE vials (2 - 4 mL) that had been acid washed and pre-charged with Optima grade nitric acid, for a final concentration of 1%. Reported concentrations for THg, MeHg, and DOC are adjusted for the initial concentrations of each species (ie. measured concentration – influent water concentration = adjusted concentration). For THg, the starting fresh meltwater THg was 9.4 pM and the starting saline lagoon water THg = 0.326 pM. For MeHg, the fresh starting meltwater MeHg was 0.33 pM and the starting saline lagoon water had a MeHg concentration less than the detection limit (0.07 pM). For DOC, all initial freshwater DOC was below 0.001 mM, while the initial seawater DOC concentration was ~ 0.1 mM.

2.5 Mercury analysis

All mercury-related samples were analyzed at the University of Connecticut. MeHg samples, which encapsulates both mono- and di-methylmercury due to the preservation technique of acid (Black et al. 2009), were pre-distilled before analysis to separate the MeHg from the dissolved organic matter in the samples. The distillation was preceded by the addition of 50% H_2SO_4 and 20% KCl to aid in breaking down the natural organics complexing with the MeHg (Hammerschmidt and Fitzgerald, 2001, Balcom et al. 2015). Just before analysis, ascorbic acid (2.5%) was added and the samples were derivatized with sodium tetraethylborate (NaTEB). The samples were then analyzed using a Tekran 2700 purge and trap gas chromatographic cold vapor atomic fluorescence spectrometry (CVAFS) automated instrument (Tseng et al. 2004). Calibration was done using MeHg standard curves (Alfa Aesar, NIST) and sample concentrations were corrected based on average field blank values (avg: 0.09 pM, range: 0.00 – 0.21, *n* = 5), with laboratory blanks appearing in the same range (avg: 0.05 pM, range: 0.047 - 0.055, *n*=2). Duplicate and triplicate samples differed by less than 10%. Spike recoveries for *in situ* field samples were 71% ± 20% and were 65% ± 15% for experimental samples. The detection limit for this method is 0.07 pM based on Tseng et al. (2004) and modified slightly to match the utilized instrument. Samples are reported in their blank- and spike-corrected form (blank subtracted from value and normalized to spike recovery percentage).

THg samples were digested with BrCl overnight, followed by the addition of 12% $NH_2OH{\cdot}HCl$ to consume any remaining BrCl (Bloom and Fitzgerald, 1988). A saturated $SnCl_2$ solution was then used to convert Hg(II) to Hg(0) before analysis on a Tekran Series 2600 automated system using the dual gold pre-concentration/CVAFS method (Bloom and Fitzgerald, 1988). Sample concentrations were corrected based on field and method blanks (0.5 ± 0.2 pM, *n*=7). Spike recoveries were 111% ± 10% the expected value. The detection limit was 0.2 pM, based on the standard deviation of the instrument blanks. Samples are reported in their blank- and spike-corrected form (blank subtracted from value and normalized to spike recovery percentage).

Total soil THg was analyzed on a Nippon MA-3000 Direct Mercury Analyzer (DMA) using thermal decomposition, amalgamation cold vapor atomic absorption spectroscopy (CVAAS). Prior to analysis, samples were freeze-dried and ball-milled to ensure consistency. Approximately 200 mg of sediment were measured into pre-combusted ceramic sample boats and loaded into the analyzer. Liquid standards (THg; J.T. Baker, NIST) were used for calibration, along with the standard reference material MESS-3 (marine sediment; National Research Council of Canada (NRC)), which yielded 0.085 ± 0.001 mg/kg. This is within the range of acceptable values for MESS-3 (0.091 ± 0.009 mg/kg). The detection limit for this method is 0.01 ng Hg per gram of sediment and the relative standard deviation (RSD) was 2%.

2.6 Trace Metal analysis

Samples were analyzed for iron (^{57}Fe) and manganese (^{55}Mn) at the Woods Hole Oceanographic Plasma Mass Spectrometry Facility using an iCAP Qc inductively coupled plasma mass spectrometer (ICP-MS) in Kinetic Energy Discrimination (KED) mode. Prior to analysis, samples were diluted using 2% nitric acid (optima grade) and Indium (^{115}In) was added as an internal standard. Standard curves (8-point for Mn, 10-point for Fe) were made using a comprehensive trace element standard (Woods Hole Oceanographic Institution) and were run periodically throughout sample analysis. Sample concentrations were corrected using the preceding standard curve. Blanks (2% nitric acid + ^{115}In spike) were measured every 10 samples and averaged, excluding clear outliers. Blank values were subtracted from sample Fe and Mn concentrations. Additionally, the following trace metal certified reference materials were analyzed during each ICP-MS run to ensure correct standard curve and blank corrections were being used: seawater (NASS-7; National Research Council Canada), river water (SLRS-6; National Research Council Canada), and natural water (SRM 1640a; National Institute of Standards and Technology). The reported reference material concentrations showed good agreement with the measured values, apart from NASS-7 samples, which had considerable matrix interference, as shown by low ^{115}In yields, and are generally low in Fe and Mn concentration. SLRS-6 has a reported Fe concentration of 1.51 ± 0.06 µM, with our data yielding 1.45 ± 0.06 µM (n = 7), and a reported Mn concentration of 0.039 ± 0.002 µM, with our data yielding 0.038 ± 0.002 µM (n = 7). SRM 1640a has a reported Fe concentration of 0.66 ± 0.03 µM, with our data yielding 0.63 ± 0.03 µM (n = 7), and a reported Mn concentration of 0.74 ± 0.01 µM, with our data yielding 0.74 ± 0.04 µM (n = 7). Due to its low concentrations, NASS-7 samples are omitted as they fell close to the detection limit. Any samples showing similarly low concentrations were rerun at a higher dilution.

2.7 Carbon Analysis

Samples for DOC were analyzed at the University of Texas Marine Science Institute using a Shimatzu TOC-V CSH analyzer. Due to flocculation of DOC that occurred after collection and/or freezing, groundwater samples were acidified to a pH of 2 with TM grade concentrated HCl and sonified prior to analysis to break up flocs. Additionally, the TOC analyzer was equipped to homogenize samples during analysis using magnetic stir bars, preventing any remaining flocs from settling out. Samples collected from the sediment plug flow-through experiments did not exhibit any flocculation, likely due to lower concentrations of DOC and Fe present in the samples.

Tundra soils and intertidal sediments were prepared for soil organic carbon analysis in the same way as for THg (freeze-drying, followed by ball milling). The prepared samples were then analyzed for organic carbon via combustion at 900 - 1000°C, followed by column separation and measurement by thermal conductivity using an Elemental Microanalysis Flash EA 1112.

2.8 Statistical Tests

For the plug flow-through experiments, the sediment porosity was used to determine how long it took to displace the original sediment porewater from the core. Any samples collected before this flushing was complete were excluded from the data interpretation, due to their long-term contact with the sediments. However, these porewater fractions were analyzed to understand the THg concentrations released from the melting ice of permafrost soils. Due to sampling limitations, such as required volume for different parameters, certain species other than THg and MeHg (DOC, Fe, Mn, Sulfide, DO) were interpolated to get a full dataset to compare to the Hg concentrations measured. Interpolation was done using the polyfit function in MATLAB R2023a. All interpolations were done manually to ensure a good fit between the data and the interpolated values. An example interpolation graph can be seen in the Supplemental Materials (Supplemental Figure S1).

For all samples, comparisons between parameters were done using one-way ANOVA statistical analyses and linear regression analyses in Microsoft Excel 2021. A p-value of less than 0.05 was considered significant (95% confidence interval); however, data behind all significant results were also visually analyzed to ensure that outliers or incorrect boxing (i.e. compared groups should have a roughly similar number of samples; incorrect boxing occurs when one group has dramatically fewer samples than the others) were not creating a false correlation. The cutoff values discussed in the results section separating low to high concentrations were based on creating boxes that were relatively similar in number, except in cases where there were binary distinctions in core conditions (i.e. temperature being split into cold vs warm).

3. Results

3.1 Overview of Statistics

Comparisons between parameters were done using one-way ANOVA statistical analyses and linear regression analyses in Microsoft Excel 2021. A p-value of less than 0.05 (95% confidence interval) was considered significant. Below is a summary of the significant relationships observed by ANOVA analyses. While linear regressions were also performed, they largely confirmed the ANOVA results (Supplemental Tables S4 and S5). The major exception was salinity, which is explained below.

3.2 In Situ Groundwater Samples

3.2.1 Transects

The average THg, MeHg, DOC, Mn, and Fe concentrations in Simpson Lagoon groundwater sampled *in situ* at transects T1, T2, and T3 can be seen in Table 1, with MeHg vs THg and both compared to DOC and salinity shown in Figure 3. Contours of a selection of species measured at each of the transects can be seen in Figure 4 for T1, Figure 5 for T2, and Figure 6 for T3. In order to determine the factors controlling Hg cycling within the subterranean estuary at these locations, THg and MeHg concentrations were compared to the salinity, temperature (°C), ORP, pH, DO (μM), manganese (Mn, μM), iron (Fe, μM), DOC (mM), total dissolved nitrogen (TDN, μM), and the Fe:Mn ratio (a proxy for reducing conditions within a single site - higher ratios correlate with more reducing conditions (Hamer et al. 2020)). While sulfide was measured during the July 2023 campaign, no field samples were above the limit of detection (0.3 μM).

Transect T1 (Figure 4) THg (n=48) concentrations decreased with increasing salinity ($p < 10^{-5}$) and DOC ($p < 0.004$), Fe:Mn ratio ($p < 0.02$), and temperatures above freezing ($p < 0.03$). The MeHg for T1 (n=46) decreased with increasing salinity ($p < 10^{-6}$) and increasing ORP values ($p < 0.002$), but increased with increasing THg concentrations ($p < 10^{-6}$), increasing DOC ($p < 0.04$), higher pH ($p < 0.002$), and higher Fe:Mn ratios ($p < 0.007$). Transect T2 (Figure 5) THg (n=16) showed declines with increasing Mn ($p < 0.05$) and Fe ($p < 0.05$) concentrations. The T2 MeHg (n=15) tests showed no significant correlations with any parameter measured, even THg. Transect T3 (Figure 6) THg (n=17) decreased with increasing salinity ($p < 0.0004$) and increasing Mn ($p < 0.002$), but increased with increasing DOC ($p < 0.002$) and above freezing temperatures ($p < 0.03$). The T3 MeHg (n=16) tests showed a decrease with increasing salinity ($p = 0.05$); however, the three maximum MeHg concentrations measured at T3 (15. 2

pM, 16.5 pM, and 16.7 pM) all occurred in the top 4 DOC samples. This may indicate a possible relationship with DOC as well.

Table 1. Average concentrations of dissolved THg, MeHg, DOC, Mn, and Fe in field *in situ* groundwater samples and sediment plug flow-through experiments, as well as soil THg and soil carbon from the core sections used.

Field Transects	THg (pM)	*n*	MeHg (pM)	*n*	DOC (mM)	*n*	Mn (μM)	Fe (μM)	*n*	Soil THg (pmol/g)	Soil Carbon (mmol/g)	*n*
Transect T1	15.1 ± 3.2	48	3.2 ±3.2	46	4.4 ± 2.7	48	4.90 ± 9.70	13.3 ± 4.4	48			
Transect T2	12.1 ± 8.8	16	9.5 ± 7.6	15	4.6 ± 2.1	16	0.17 ± 0.14	7.9 ± 4.6	16			
Transect T3	18.2 ± 17.2	17	4.1 ± 6.2	16	6.4 ± 4.2	17	0.76 ± 0.82	20.6 ± 24.8	17			
Experiments												
Simpson Lagoon Permafrost	2.7 ± 5.5	141	0.30 ± 0.46	59	1.20 ± 0.75	91	0.032 ± 0.076	1.3 ± 3.0	44	310 ± 100	14.3 ± 3.6	9
Simpson Lagoon Active Layer	6.7 ± 9.2	96	0.45 ± 0.67	42	0.99 ± 0.91	70	0.062 ± 0.098	0.9 ± 2.4	37	410 ± 220	16.3 ± 3.4	6
Elson Lagoon Permafrost	1.2 ± 2.0	106	0.10 ± 0.11	49	0.88 ± 0.90	103	0.017 ± 0.032	0.9 ± 2.8	47	170 ± 50	6.4 ± 6.7	5
Drew Point Permafrost	1.3 ± 2.1	152	0.10 ± 0.10	68	0.85 ± 0.84	139	0.11 ± 0.16	0.004 ± 0.004	64	270 ± 20	9.7 ± 1.3	3

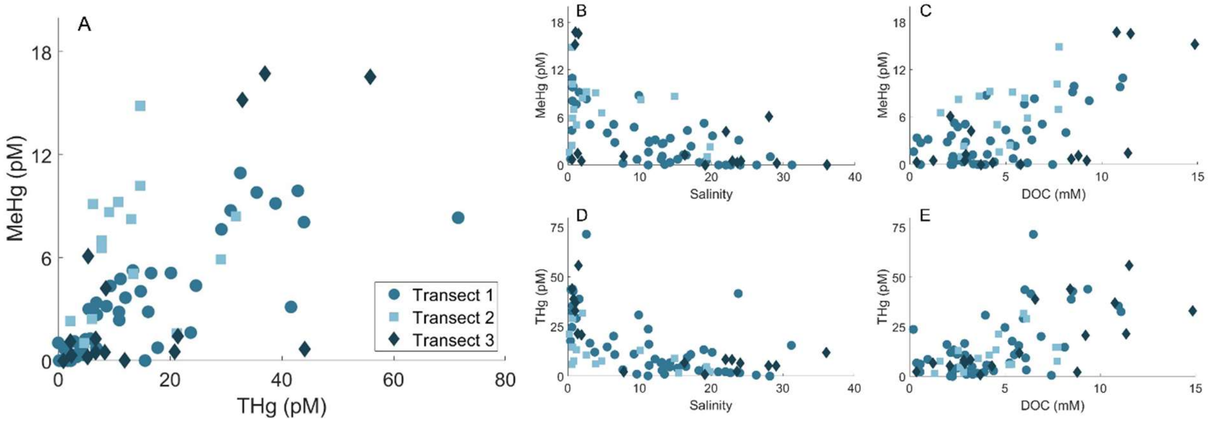

Figure 3. Groundwater concentrations of MeHg, THg, and DOC from transects T1, T2, and T3. The scatter plots show the relationship between MeHg and A) THg, B) salinity, and C) DOC, as well as THg and D) salinity and E) DOC.

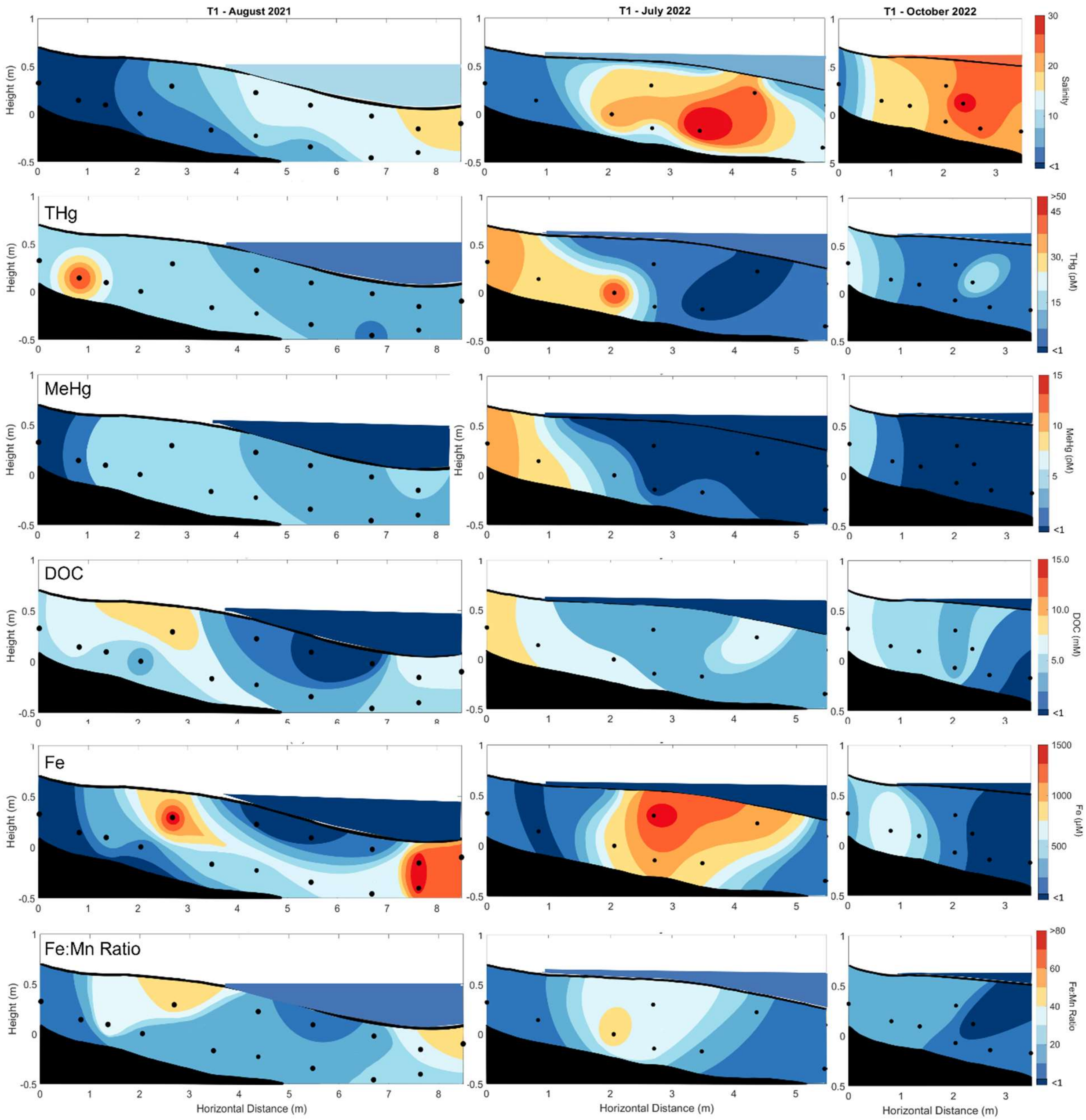

Figure 4. Contour plots showing changing salinity, THg, MeHg, DOC, Fe, and the Fe:Mn ratio in Simpson Lagoon and across the subterranean estuary at Transect T1 during the August 2021, July 2022, and October 2022 sampling campaigns. The black section at the bottom represents the ice table. The solid black line that begins at height = 0.7 m is the ground level, with contours below the line occurring in the active layer groundwater. Colors above the ground level line represent lagoon water level and conditions.

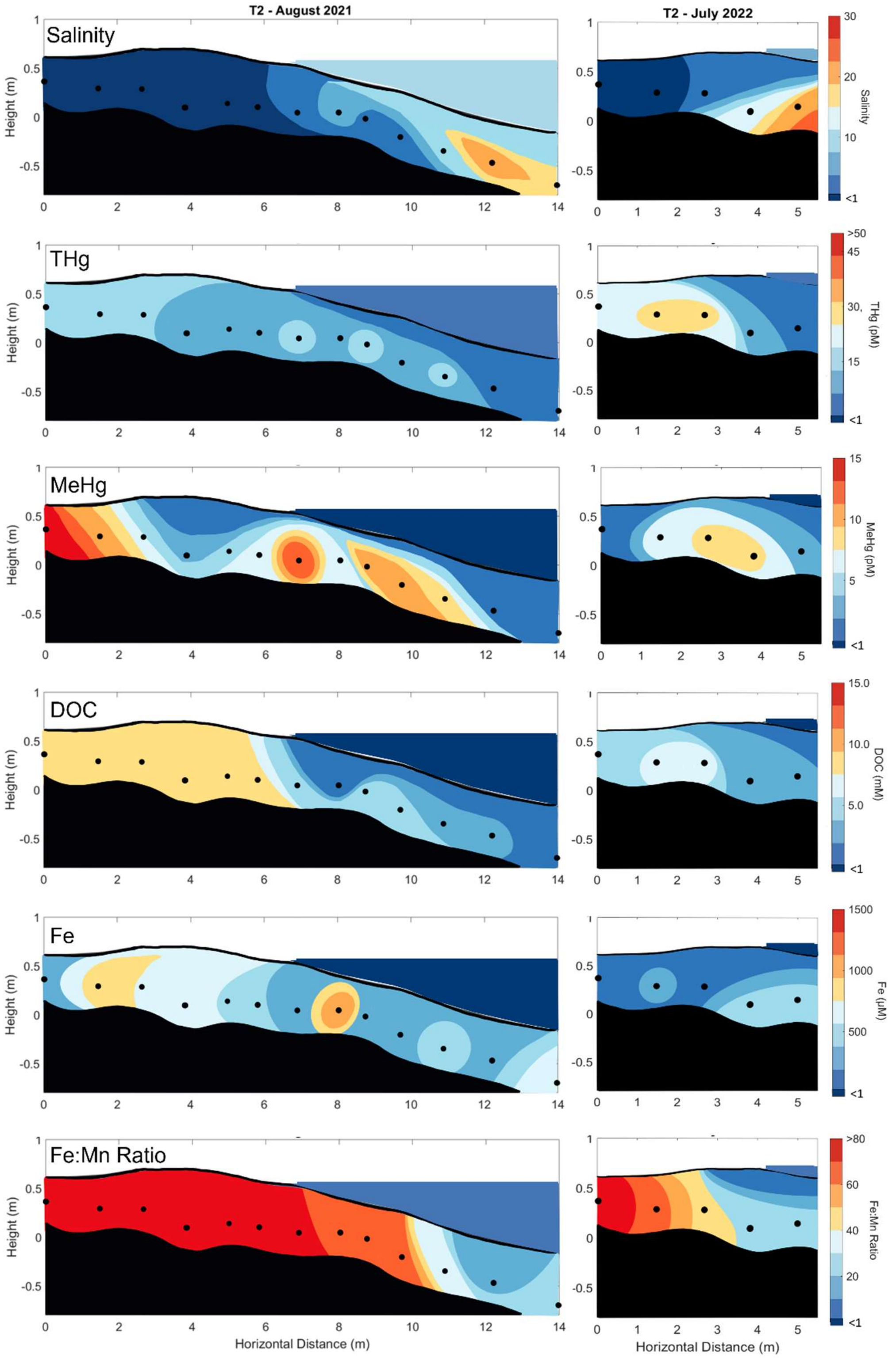

Figure 5. Contour plots showing changing salinity, THg, MeHg, DOC, Fe, and the Fe:Mn ratio in Simpson Lagoon and across the subterranean estuary at Transect T2 during the August 2021 and July 2022 sampling campaigns. The black section at the bottom represents the ice table. The solid black line that begins at height = 0.6 m is the ground level, with contours below the line occurring in the active layer groundwater. Colors above the ground level line represent lagoon water level and conditions.

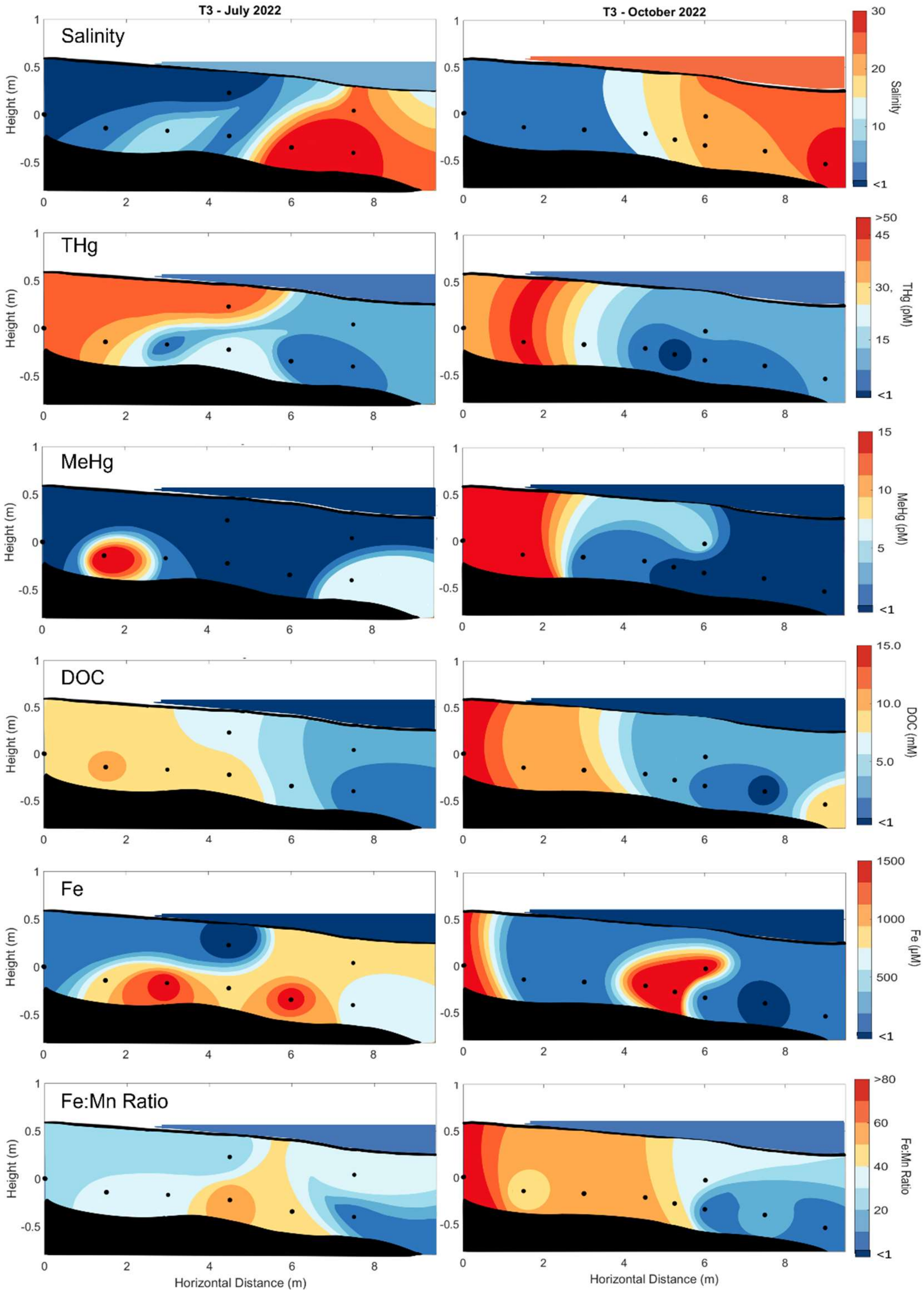

Figure 6. Contour plots showing changing salinity, THg, MeHg, DOC, Fe, and the Fe:Mn ratio in Simpson Lagoon and across the subterranean estuary at Transect T3 during the July 2022 and October 2022 sampling campaigns. The black section at the bottom represents the ice table. The solid black line that begins at height = 0.6 m is the ground level, with contours below the line occurring in the active layer groundwater. Colors above the ground level line represent lagoon water level and conditions.

3.2.2 Time Series

In July 2023, three piezometers in Transect T1 were sampled daily across four consecutive days (Figure 7), with piezometer 1 (P1) being closest to the tundra, piezometer 3 (P3) starting at the day 1 water level, and piezometer 2 (P2) situated in between. On day 3 an additional piezometer (P1.5) was installed between P1 and P2. The salinity of Simpson Lagoon increased over the period, from 11.3 on day 1, to 27.1 on day 4. The water level of the lagoon also rose approximately 20 cm over the course of the sampling period, from the base of piezometer 3 on day 1, to the base of piezometer 1 on day 4.

MeHg and DOC largely showed conservative mixing between the tundra endmember and the lagoon surface water on day one; however, THg, Fe, and Mn did not, with THg having a higher concentration at P2 than P1 (71.6 pM vs 32.6 pM). Fe shows a drop from P1 to P2, followed by a rise at P3 (507 µM → 137 µM → 567 µM) and while Mn increases steadily over the course of the transect, both Mn and Fe appear to remain largely in the sediment rather than being mobilized into the lagoon.

As the water level rose, the species dynamics changed due to the shift in the location of the salinity mixing zone, which moved farther inland over the course of the time series, as shown by P2 (Figure 7). The groundwater salinity at P2 jumps from 2.6 on day 1 to 11.3 on day 2, to 20.2 on day 3, and stabilized around 19 on day 4. DO drops from close to 100 µM on day 1 to 45 µM (13.6%) on day 2, with a concurrent drop in pH from 7.21 to 6.76. THg drops from 71 pM to 16 pM, while MeHg drops from 8.3 pM to 2.8 pM. There is also a substantial drop in DOC, from 6.5 mM to 2.0 mM. Mn and Fe, however, increase slightly over the first two days, with Mn rising from 4.3 µM to 6.1 µM and Fe rising from 137 µM to 170 µM. Interestingly, while THg, DO, DOC, Mn, and Fe all continue their respective positive/negative trends or remain somewhat stable following the change in conditions, MeHg and pH begin to return towards their day 1 levels over the final two days of the time series (Figure 7).

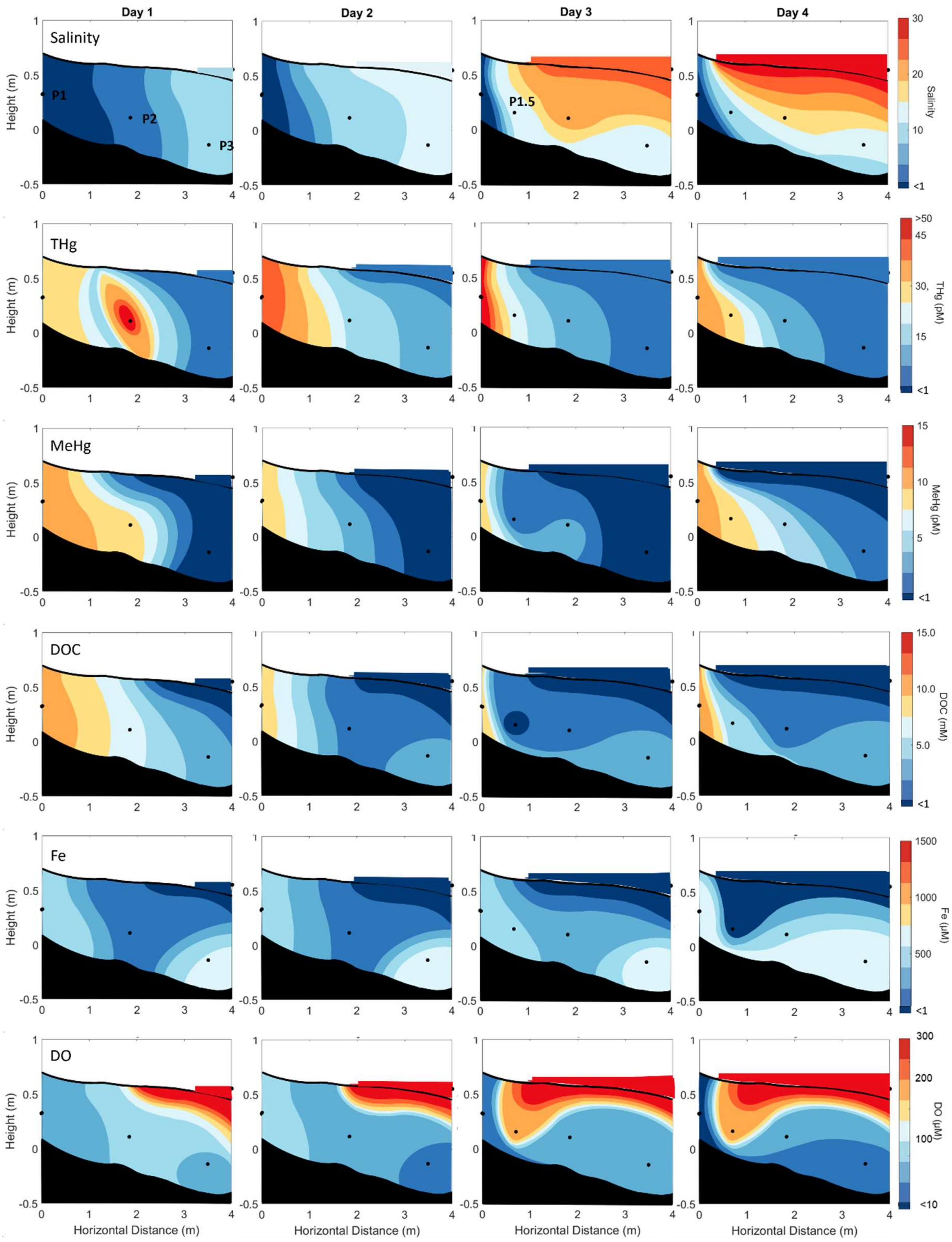

Figure 7. Contour plots showing changing salinity, THg, MeHg, DOC, Fe, and DO in Simpson Lagoon and across the subterranean estuary at Transect 1 during the July 2023 time series. The black section at the bottom represents the ice table. The solid black line that begins at height = 0.7 m is the ground level, with contours below the line occurring in the active layer groundwater. Colors above the ground level line represent lagoon water level and conditions.

3.3 Selective Leaching Experiments

Three cores were taken along Transect T1 for sediment analyses, two from the tundra (active layer + permafrost) and one from the intertidal sandy beach. Soil carbon, Mn, Fe, and THg were analyzed along the cores, with the full results shown in the supplementary materials (Supplemental Table S1). The intertidal core had the lowest average concentrations for all four parameters, with THg concentrations of 120 ± 90 pmol/g, carbon of 3.9 ± 4.0 mmol/g, Mn of 1.6 ± 1.2 µmol/g, and Fe of 220 ± 140 µmol/g. The tundra active layer (36 cm, only collected 0-23 cm) had more than double these concentrations, with THg coming to 270 ± 170 pmol/g, carbon to 13.4 ± 8.1 mmol/g, Mn to 2.3 ± 1.2 µmol/g, and Fe to 460 ± 212 µmol/g. Finally, the permafrost core (sampled from the top of the ice table at 36 cm down to 55 cm from the surface) had the highest concentrations and the least variability, with THg of 310 ± 10 pmol/g, carbon of 19.6 ± 0.2 mmol/g, Mn of 10.7 ± 4.4 µmol/g, and Fe of 670 ± 140 µmol/g.

The associations of Hg in fractions of sediment from each of these cores were also investigated, using operationally-defined leaching experiments (Fernández-Martínez and Rucandio, 2013) designed to isolate Hg associated with labile species, humic/fulvic complexes (hereafter: organic matter), crystalline oxides, and sulfide species. Refractory species consist of the remaining THg not recovered by the leaches. The species most associated with THg varied between and down the cores (Figure 8). The intertidal core showed the largest variability, both in THg content and associations. In general, the intertidal THg associated predominantly with crystalline oxides, sulfides, and refractory species, which may be a result of greater mineral content in the sandy intertidal zone as opposed to the carbon-rich tundra and permafrost soils at this site. The tundra active layer soils show an increase in THg down core, as well as an increase in the amount of THg associated with crystalline oxides and organic matter. The permafrost sediments show higher THg and greater association of THg with crystalline oxides at the top of the core, possibly due to varying active layer depths and cycling of THg and metals over time. Below 45 cm, the permafrost samples become remarkably consistent in their total concentrations and associations, with THg associating mostly with the organic fraction. There is also an increase in the proportion of THg associated with refractory species in the deeper permafrost core sections.

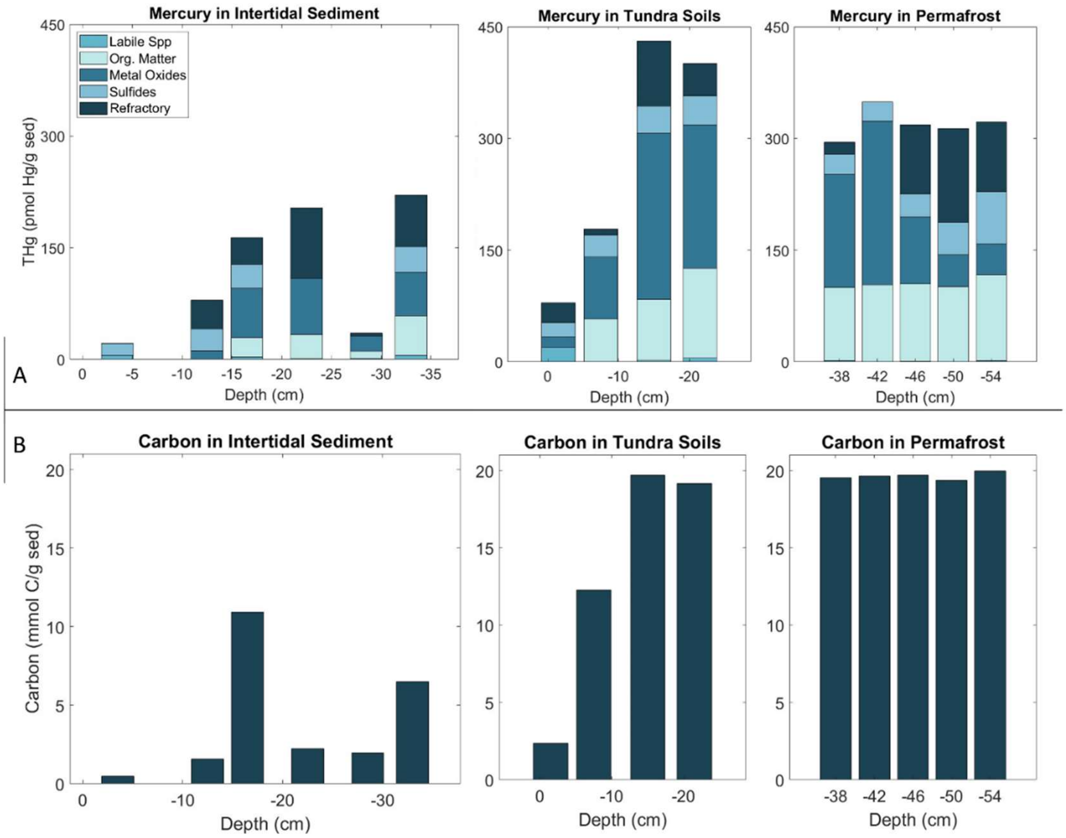

Figure 8. Results from the selective leaching of sediments from transect T1, with A) showing the associations of THg based on the amount of THg leached in each selective leach and B) showing the total amount of soil carbon associated with each core section.

3.4 Sediment Plug Groundwater Flow-Through Experiments

3.4.1 Simpson Lagoon Active Layer

Six sediment sections were used for the Simpson Lagoon tundra active layer experiments, with salinity, DO, sulfide, DOC, Mn, Fe, Fe:Mn ratio, soil carbon, and total soil THg being tested against THg and MeHg (**Figure 9**). The collection depths of the soils ranged from 2 to 17 cm below the surface (with above-soil vegetation removed), with an average porosity of 65% ± 5%, a carbon content of 16.3 ± 3.4 mmol/g (20 ± 4% weight), and a THg content of 410 ± 220 pmol/g (Supplemental Table S2). When considering the average mobilization of THg during the freshwater vs the seawater flow through, there was significant variability between core sections. Section C3A, which was the shallowest active layer section collected, leached 10 times the amount of THg as any other active layer core section, despite having relatively low soil THg and carbon. A core section taken from a different location but similar depth (C3E) did not show similarly high THg leaching rates. Omitting this high outlier, the cores had a net removal for the freshwater treatment of 1.1 ± 1.3 pM and a net removal for the saltwater treatment of -1.0 ± 1.5 pM. The outlier core did not show similarly high leaching for MeHg. Instead, the core with the highest soil carbon content, C3F, leached the most MeHg (freshwater ad.avg: 1.8 pM, saline ad.avg: 0.66 pM). The adjusted average freshwater concentration for the MeHg leached from the rest of the cores was 0.36 ± 0.77 pM and the adjusted average seawater concentration leached was 0.20 ± 0.23 pM. Leached concentrations of DOC did show a clear pattern, however, with lower concentrations following the switch to saline water (freshwater leaching: 1.3 ± 0.7 mM; seawater leaching: 0.6 ± 0.2 mM).

THg leached from the active layer cores increased with increasing DOC ($p < 10^{-7}$) and Fe:Mn ($p < 0.007$) and decreased with increasing Mn ($p < 10^{-5}$) and Fe ($p < 10^{-4}$) concentrations. At DOC concentrations greater than 0.80 mM, THg went from being retained in the cores on average (net removal: 5 ± 23 pM) to being released from the cores (leached: 6 ± 170 pM; $p < 10^{-7}$). Increasing metal concentrations caused a decline in the THg concentrations leached from the active layer cores, with Mn concentrations greater than 35 nM associated with a drop in THg from 3 ± 130 pM to -5 ± 24 pM ($p < 10^{-5}$) and Fe concentrations greater than 250 nM related to a drop in THg from 2 ± 130 pM to -5 ± 23 pM ($p < 0.0001$). Ratios of Fe:Mn above 1 (more reducing) related to an increase in the THg concentrations ($p < 0.007$). Notably, THg was strongly suppressed during the transition from fresh influent to saline influent ($p < 10^{-7}$), resulting in a significant drop in THg concentrations (fresh leaching: 5 ± 190 pM, brackish net removal: 6 ± 17 pM, saline leaching: 2 ± 28 pM - $p < 10^{-7}$).

The MeHg leached from the active layer cores increased with DOC ($p < 0.03$) and higher temperatures ($p < 0.0004$) and MeHg decreased when DO concentrations rose above 100 µM ($p < 0.01$). MeHg average concentrations rose (0.12 ± 0.11 to 0.56 ± 0.88 pM) when DOC was greater than 0.80 mM ($p < 0.03$), and fell when DO concentrations were greater than 100 µM (0.62 ± 0.87 pM to 0.09 ± 0.11 pM; $p < 0.01$). When temperatures increased, MeHg concentrations rose from net removal of 0.18 ± 0.06 pM to leaching of 0.18 ± 0.08 pM.

3.4.2 Simpson Lagoon Permafrost

Eight sediment intervals were used for the Simpson Lagoon tundra permafrost plug flow-through experiments. These sections ranged in depth from 18 cm below the surface to 50 cm below the surface, with an average porosity of 64% ± 9%, soil carbon of 14.5 ± 3.8 mmol/g (17 ± 5% weight), and soil THg content of 320 ± 100 pmol/g (Supplemental Table S2). Unlike the active layer cores, all but one of the Simpson Lagoon permafrost cores showed an increase in THg leached following the switch to saline water (freshwater net removal: 2.2 ± 3.4 pM; seawater leaching: 0.79 ± 0.48 pM), with MeHg showing the same pattern (freshwater net removal: -0.09 ± 0.44 pM; seawater leaching: 0.19 ± 0.25 pM), though with lower concentrations than observed for the active layer soils. DOC concentrations remained largely similar throughout (freshwater leaching: 1.0 ± 0.8 pM; seawater leaching: 0.9 ± 0.4 pM).

THg leached from the Simpson Lagoon permafrost cores decreased with increasing Mn ($p < 0.006$) and Fe ($p < 0.03$) concentrations. When Mn was greater than 35 nM, adjusted THg concentrations dropped from an average net removal of 3.2 to 6.2 pM ($p < 0.006$). When Fe was greater than 15 nM, the net removal of THg increased from 0.3 to 5.2 pM. THg was suppressed during the transition between fresh and saline conditions ($p < 10^{-7}$) as was observed for the active layer cores. The MeHg leached from the Simpson Lagoon permafrost cores increased with increasing DOC ($p < 0.0002$), with rising Fe concentrations ($p < 0.01$), and with higher Fe:Mn ($p < 0.015$). At DOC concentrations greater than 0.80 mM, MeHg went from being retained in the cores on average (net removal: 0.05 ± 0.27 pM) to being released from the cores (leached: 0.39 ± 0.56 pM; $p < 0.0002$). There was also an increase in MeHg concentrations when Fe concentrations were greater than 1 µM ($p < 0.01$) and when the Fe:Mn ratio was greater than 10 ($p < 0.015$). At higher temperatures, MeHg shifted from a net removal of 0.01 ± 0.27 pM to net leaching of 0.41 ± 0.42 pM ($p < 0.04$).

3.4.3 Elson Lagoon Permafrost

Five sediment sections were used for the Elson Lagoon permafrost experiments. The depths ranged from 55 cm below the surface to 350 cm below the surface, with an average porosity of 55% ± 29%, a soil carbon content of 6.4 ± 6.7 mmol/g (7.7 ± 8.2% weight), and a soil THg content of 170 ± 50 pmol/g (Supplemental Table S2). These freshly thawed soils almost always acted as a sink for THg from infiltrating natural waters, regardless of treatment, though net removal decreased once the influent became fully saline (freshwater net removal: 6.6 ± 3.0 pM; seawater net removal: 1.3 ± 1.1 pM). MeHg concentrations also increased following the transition to saline water, though concentrations were very low compared to the Simpson Lagoon soils (freshwater net removal: 0.32 ± 0.22 pM; seawater net leaching: 0.08 ± 0.23 pM). The concentrations of DOC leached from the Elson Lagoon permafrost soils were similar to those seen in Simpson Lagoon soils (freshwater leaching: 1.1 ± 1.1 mM; seawater leaching: 0.5 ± 0.2 mM).

THg leached from the Elson Lagoon permafrost soils decreased with increasing Mn ($p < 0.0003$) and Fe ($p < 0.02$) concentrations, as well as higher Fe:Mn ($p < 0.01$). An increase in Mn above 35 nM corresponded with an increase in the net removal of THg (removal of 9 ± 43 pM to 14 ± 32 pM; $p < 0.0003$), with a similar relationship exhibited for Fe concentrations above 15 nM (net removal: 9 ± 44 pM to 12 ± 42 pM; $p < 0.02$). Unlike in the Simpson Lagoon active layer samples where increases in Fe:Mn corresponded with a rise in THg, for the Elson Lagoon samples an increase in the Fe:Mn ratio over 1 corresponded with a decline in THg leaching ($p < 0.01$). However, as was observed for the Simpson Lagoon permafrost and active layer samples, a rise in salinity led to temporary increase in THg removal (net removal for fresh: 6.6 ± 3.0 pM, brackish: 8.8 ± 1.4 pM, and saline: 1.3 ± 1.1 pM; $p < 10^{-26}$).

The only parameters that significantly corresponded with MeHg concentrations leached from the Elson Lagoon permafrost samples were salinity and temperature. When the influent was fresh, the soils exhibited net removal of MeHg on average (net removal: 0.32 ± 0.22 pM). When the influent was saline, the soils leached more MeHg than it removed (leached: 0.08 ± 0.23 pM; $p < 10^{-6}$). MeHg concentrations also increased with increasing temperature (<4°C net removal: 0.45 ± 0.28 pM; >4°C leaching: 0.20 ± 0.38 pM; $p < 0.02$).

3.4.4 Drew Point Permafrost

Two sediment sections, both obtained from the same horizontally drilled core, were used for the Drew Point permafrost experiments. The depth of the core was 65 cm below the surface, with an average porosity of 80% ± 6%, a soil carbon content of 9.2 ± 1.4 mmol/g (11 ± 2% weight), and a soil THg content of 260 ± 10 pmol/g (Supplemental Table S2). The behavior of the Drew Point soils was similar to the Elson Lagoon cores, almost always acting as a sink for THg from infiltrating natural waters, regardless of treatment, though the degree of removal decreased once the influent became fully saline (freshwater net removal: 6.12 ± 0.03 pM; seawater net removal: 1.1 ± 0.1 pM). MeHg concentrations also increased following the transition to saline water in a similar range to the Elson Lagoon cores (freshwater net removal: 0.21 ± -0.02 pM; seawater leaching: 0.08 ± 0.04 pM). The concentrations of DOC leached were similar to those seen in all of the other soil types (freshwater leaching: 1.3 ± 0.2 mM; seawater leaching: 0.4 ± 0.1 mM).

Despite having fewer replicates, the THg concentrations from the Drew Point cores still showed the same pattern as the other experiments: the suppression of THg as salinity rose (net removal of fresh: 6.5 ± 2.5 pM, brackish: 8.1 ± 8.2 pM, saline: 1.1 ± 1.3 pM; $p < 10^{-9}$). THg concentrations also decreased when DO concentrations exceeded 150 μM ($p < 0.02$). The MeHg concentrations leached from the Drew Point permafrost samples increased with increasing salinity (fresh net removal: 0.21 ± 0.01 pM; saline leaching: 0.09 ± 0.01 pM; $p < 10^{-5}$) and increasing Mn concentrations over 35 nM (net removal of 0.15 ± 0.03 pM to leaching 0.08 ± 0.01 pM; $p < 0.005$).

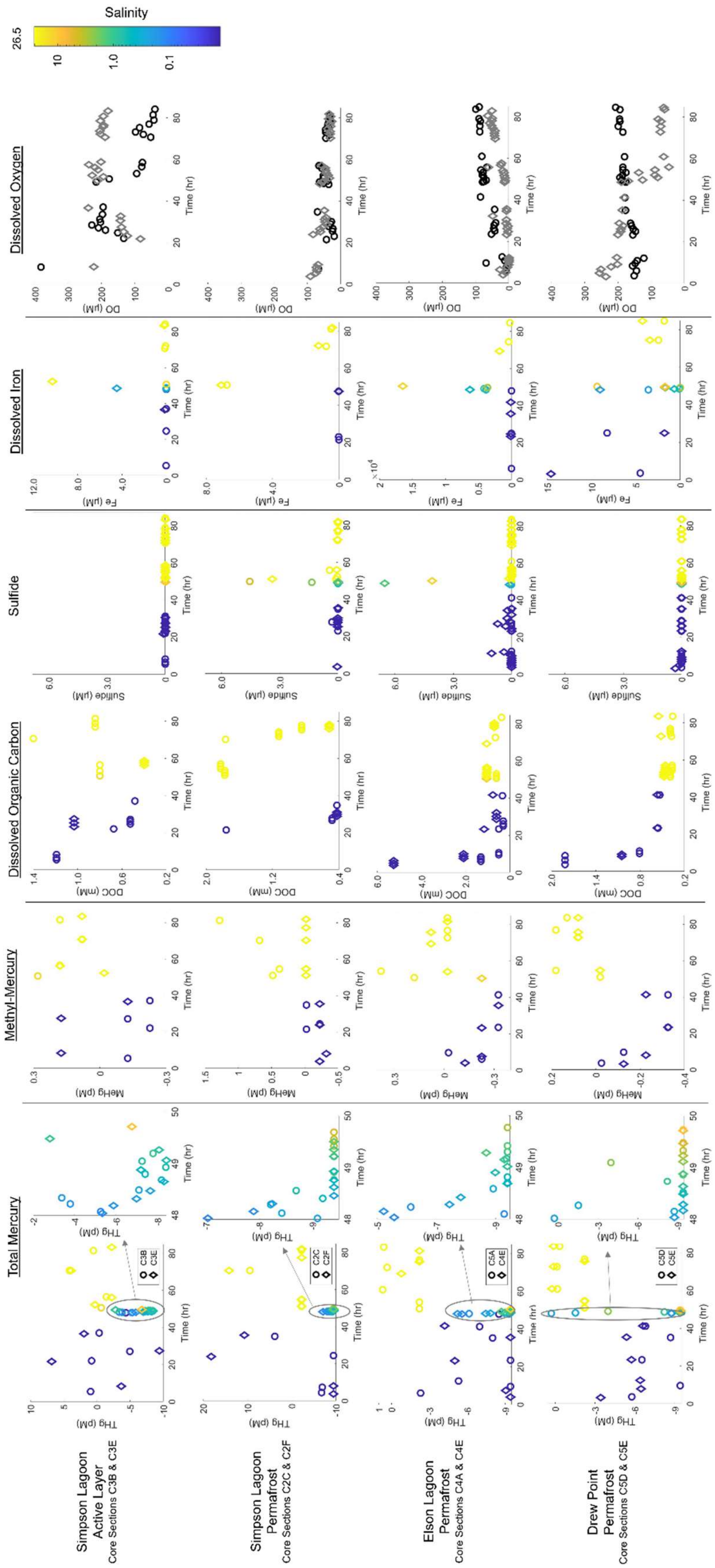

Figure 9. Influent-adjusted concentrations measured for THg, MeHg, DOC, sulfide, Fe, and DO over the course of the sediment plug flow-through experiments. Two cores from each soil type (differentiated using circle and diamond shapes) have been chosen to represent the general behavior of the species across the experiments. Salinity is shown for all dissolved species via the color map, other than DO. Given the high number of time points, DO is shown in gray-scale to allow for better differentiation between the two cores.

4. Discussion

4.1 Field Data

4.1.1 Geographic variability

Our four comprehensive field campaigns to Simpson Lagoon allow us to address questions regarding groundwater Hg changes across local geographic differences. All three transects (T1, T2, & T3) had comparable DOC, THg, and MeHg concentrations, with the species being more enriched in the freshwater reaches of the subterranean estuary as it receives active inputs from tundra vegetation. However, while T1 and T3 traversed a sandy beach, T2 was situated in a trough between two eroding polygons. T1 and T3 show relatively conservative mixing between the freshwater endmember and the saline endmember for THg and MeHg, with significant correlations between the Hg species and DOC (Figure 3 and Figure 5). The positive correlation between MeHg and THg at these transects indicates that similar mechanisms are acting on MeHg as on Hg(II). Alternatively, T2 does not show conservative mixing across the salinity gradient. Instead, there is a spike in Hg concentrations at the saline-freshwater interface (Figure 4) with concurrent spikes in Fe and Mn, which may indicate release associated with metal oxide dissolution (Luther et al. 1992, Haris-Hellal et al. 2011) or the stabilization of Hg(II) in the aqueous phase due to complexation with chloride or hydroxide ions (Powell et al. 2005, Spyropoulou et al. 2022). Additionally, the high ratios of MeHg to THg (T2: 70 ± 40%, vs T1: 20 ± 20% and T3: 25 ± 30%) and lack of correlation between MeHg and THg indicate that Hg(II) is being actively methylated at this location (Varty et al. 2020). Higher methylation rates have been associated with higher lability DOC (Kim et al. 2011, Mazrui et al. 2016), which may account for T2 having greater MeHg:THg ratios than T1 and T3, due to its position between two degrading tundra polygons.

4.1.2 Seasonal differences in THg and MeHg concentrations

Significant seasonal differences were observed between transects sampled in the summer and autumn (T1 and T3). Both transects showed notable decreases in THg concentrations when groundwater temperatures dropped below freezing, with T1 also exhibiting a similar decline for MeHg. In the case of THg, uptake and deposition by tundra plants into the soil active layer declines as the growing season comes to an end (Obrist et al. 2017, Olson et al. 2018), leading to falling concentrations of easily mobilized THg in the autumn. The reduction of MeHg is more directly tied to colder temperatures in the autumn, which lower microbial methylation rates (Lehnherr et al. 2012, Yang et al. 2016, Jonsson et al. 2022).

4.1.3 Short-term processes impacting Hg cycling

The time series from July 2023 at T1 shows the impact of a moving freshwater-saline water interface on a daily time scale. The rapid rise in salinity at P2 resulted in more reducing conditions. Although THg and MeHg sharply declined during the saline intrusion, they still exceeded their expected concentrations based on conservative mixing with the infiltrating lagoon water (THg = 16.1 pM vs 3.0 pM and MeHg = 2.85 pM vs 0.38 pM at S = 11.3), likely due to release from dissolving metal oxides (Luther et al. 1992) as we see an increase in Fe and Mn concentrations. However, while MeHg concentrations begin to re-establish the pre-existing geographical gradient by day 4, THg concentrations continue to decline and approach a conservative mixing gradient with the lagoon. This implies that there is either a reduction in a process that was releasing THg (ex. metal oxide dissolution) or an additional mechanism that is partitioning THg into the solid phase. Given the fact that DO concentrations at P2 remain <50 μM from day 2 – day 4 and Mn and Fe concentrations at P2 continue to increase over the course of the time series, it is unlikely that a reduction in metal oxide dissolution is the cause of the declining THg concentrations. As a result, there may be another mechanism that is drawing down THg.

4.2 Selective Leaching Experiments

The selective leaching experiments performed on the intertidal, active layer, and permafrost cores from T1 give insight into the associations of Hg in the solid phase (Figure 8). Only the top of the active layer had a substantial percentage of labile species (24%), which are species that are weakly sorbed to soil particle surfaces (Fernández-Martínez and Rucandio 2013). All other core sections had less than 4% of their soil THg in the labile fraction. This result indicates that freshly deposited THg is more labile than THg in older soil horizons. Additionally, the increase in THg concentration downcore in the active layer is consistent with findings by Liu et al. (2022), who observed that soil moisture redistribution during the thaw season in permafrost regions of Tibet causes a downward migration of soil Hg, leading to its accumulation at the ice table interface. A similar pattern is observed at this site. For the permafrost core, the percent Hg associated with organic material was consistently between 30 – 36%. The amount of soil carbon for the permafrost core sections was also relatively consistent (19.7 ± 0.2 mmol C g^{-1} sed). It is possible that the upper layers of frozen soil were recently part of the active layer (1 – 2 years prior), due to varying annual thaw depths, and therefore cannot be considered true permafrost. Regardless, their location at the top of the ice layer provides insight into how active layer soils change as they shift to an ice-dominated regime. The association of Hg with metal oxides decreased dramatically from the top layers of frozen soil to the bottom permafrost, while its association with sulfide minerals and refractory species increased. This implies higher long-term mobility of species associated with metal oxides, potentially due to changing redox conditions or microbial activity in groundwater which may lead to dissolution (Luther et al. 1992, Haris-Hellal et al. 2011). It also indicates that older permafrost soils may retain a substantial proportion of their Hg when thawed, given the amount associated with refractory species.

The intertidal core has greater variability, both in soil THg content and in the associations of Hg with the tested species. Overall, the intertidal sediments contain significantly less Hg and carbon. Given that these sediments are composed of a mix of sand and buried peat with no active plant inputs, it suggests limited deposition of dissolved THg in the intertidal zone, despite high groundwater concentrations from upstream. The dominant Hg associations are with metal oxides, sulfide minerals, and refractory minerals. The prevalence of the latter two species associations may be due to the difficulty in mobilizing Hg once it becomes bound with these less reactive materials.

4.3 Sediment Plug Flow-Through Experiments

4.3.1 Differences in THg and MeHg associations between varying soil types

In our experiments, significant associations between THg and DOC were observed only in the Simpson Lagoon active layer cores. Given that Hg(II) is mobilized by low molecular weight OM, which is indicative of biolabile molecules in peatlands (Tfaily et al. 2013), relatively unprocessed DOM will be more likely to mobilize Hg(II) in Arctic groundwater. Textor et al. (2019) demonstrated that DOM from carbon rich active layer soils with vegetative cover is more labile than DOM from melting permafrost soils in Alaska, which may be why we only see an association between THg and DOC in the active layer cores tested. For the permafrost cores from all three locations, high Fe and Mn concentrations correlated with lower THg concentrations; however, this is likely due to other processes related to saline intrusion, as discussed below, given that spikes in metal concentrations occurred during the freshwater-to-saline transition period (Figure 9). Consequently, differences in the quantity of THg leached from the permafrost cores has more to do with the total amount of THg found in the soils (Table 1, Figure 10), rather than differences in soil carbon, DOC, or metal concentrations.

Similar to THg, the MeHg leaching from Simpson Lagoon active layer soils correlated with DOC, likely due to the biolability of the active layer DOC molecules. In contrast to THg, however, there were notable differences between the cores from Simpson Lagoon, Elson Lagoon, and Drew Point permafrost MeHg associations. The concentrations leached from the Simpson Lagoon permafrost tended to be higher than those observed in the Elson Lagoon and Drew Point effluent, possibly due to higher concentrations of soil organic matter and THg in the Simpson Lagoon permafrost soils, which likely indicate higher soil MeHg concentrations. What is more interesting than the total amount leached is the different controls on MeHg mobilization between the sediments. Unlike the Simpson Lagoon permafrost MeHg, which mobilized significantly only at high DOC concentrations ($p < 10^{-4}$) and high Fe:Mn ratios ($p < 0.01$), the Elson Lagoon and Drew Point permafrost MeHg switched from retention to mobilization when salinity increased ($p < 10^{-5}$ for both sites). It is possible that the lower soil carbon concentrations in the Elson Lagoon and Drew Point permafrost samples, as well as the likely differences between OM deposited in peat vs lacustrine and marine sediments (MacDonald et al. 2021), led to salinity driven changes in metal oxide and sulfur species concentrations controlling MeHg mobilization in these cores, rather than DOC (Figure 10).

4.3.2 Suppression of THg upon salinity intrusion

Inorganic Hg(II) has a tendency to complex with sulfur-containing organic molecules (Lamborg et al. 2004), as shown in Figure 10, which examines the complexation behavior of Hg(II) across a range of DOC and chloride concentrations that may be observed in an Arctic subterranean estuary. The relevant Hg(II) species between pH values 6 - 8, as observed in our samples, are [Hg^{2+}], [$HgCl^{+}$] (Log K = -7.31), [$HgCl_2$] (Log K = -14.0), [$HgCl_3^{-}$] (Log K = -14.925), [$HgCl_4^{2-}$] (Log K = -15.54), [$HgOH_3^{-}$] (Log K = -21.1), and [$RS\text{-}Hg^{+}$] (Log K = -25.5) (Powell et al. 2005, Dong et al. 2010). Given the strong preference our samples should have for sulfide functional groups, based on our observed DOC concentrations, it is surprising that only the Simpson Lagoon samples show a strong correlation between the DOC and THg values. This is likely because there were other processes occurring that could not be captured by aqueous complexation dynamics alone.

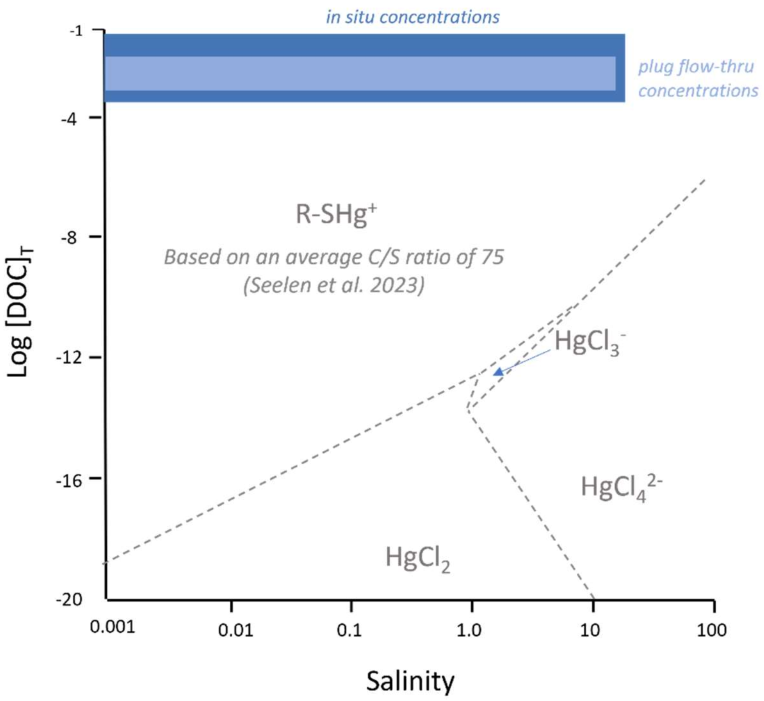

Figure 10. Speciation diagram for the dominant Hg(II) species along a range of DOC and chloride concentrations, using complexation constants from Powell et al. (2005) and Dong et al. (2010). *In situ* and experimental DOC and chloride concentration range are shown in the blue bars.

A key deviation from predicted complexation dynamics is that our core experiments revealed significant suppression of THg in the effluent during the transition from fresh to saline conditions (Figure 9), followed by an increase back to or higher than previous concentrations. This occurred in all soils tested, regardless of organic matter content. Possible explanations include the salting out of neutral DOC-associated Hg(II) species (Turner et al. 2001) or removal due to the formation of insoluble HgS minerals (Johannesson and Neumann, 2013).

While this study was not able to capture DOC concentrations at a high enough resolution to determine whether the salting out of DOC is driving this decline in THg; however, the difference in log K_d values of THg between the freshwater phase (4.7 ± 0.4) and during the transition phase (5.3 ± 0.6) matches well with the observed differences between estuarine sediment freshwater and saltwater log K_d values for THg in the literature where salting out was observed (freshwater: 4.9 ± 0.8, n = 14; saltwater: 5.3 ± 0.6, n = 12) (Li et al. 1984, Nyffeler et al. 1984, Coquery et al. 1997, Turner et al. 2001, Hammerschmidt and Fitzgerald, 2004). The second possibility is that microbial sulfate reducers (MSRs), which are known to be present in Arctic soils (Ravenschlag et al. 2001, Zhang et al. 2022), are increasing sulfide concentrations and causing deposition of HgS minerals. Evidence supporting this hypothesis includes sulfide measurements taken in several of the core experiments, where spikes in sulfide concentrations were observed during the transition phase between fresh and saline water (Figure 9). Evidence for a momentary rise in sulfide concentrations, even when below the detection limit of our probe, was seen in effluent from additional cores from Simpson Lagoon's active layer and Elson Lagoon sediment, which turned blue-green upon exposure to oxygen. This was likely due to the mobilization of colloidal vivianite (Rothe et al. 2014), which is known to degrade when sulfide concentrations increase and is easily identified by its distinct color when exposed to air (Rosenqvist, 1970, Rothe et al. 2016, Kubeneck et al. 2024).

It is likely that a combination of both mechanisms drives the initial decline in THg concentrations when exposed to higher salinity waters. Regardless, the suppression of THg is temporary, meaning that other, slower processes mobilize enough THg to bring concentrations back up. As shown in figure 10, if DOC concentrations are momentarily reduced due to salting out, Hg(II) may associate with chloride ions (Cl^-) to form a variety of stable coordination complexes (Kozin and Hansen, 2013, Spyropoulou et al. 2022). Hg(II) may also be released from metal oxides if they are subject to dissolution via reducing conditions (Luther et al. 1992, Haris-Hellal et al. 2011). In this organic rich environment, DOC will likely dominate Hg(II) complexation over chloride species (Lamborg et al. 2004), making the second mechanism more likely to dominate Hg(II) mobilization in these soils. Supporting this theory, the cores show an increase in Fe concentrations ($p < 10^{-4}$) and Mn concentrations ($p < 10^{-15}$) during active infiltration of saline water, indicative of more reducing conditions and the dissolution of metal oxides that may release Hg.

4.3.3 Mechanisms driving MeHg mobilization

Fluxes of MeHg from the cores were almost always higher following the transition to saline water than during the freshwater treatment, with the difference being statistically significant for the Elson Lagoon and Drew Point samples, but less definitive for the Simpson Lagoon sediments. In this case, freshwater and laboratory studies offer insights into why seawater intrusion appears to mobilize MeHg from Arctic soils. One possible explanation is the production of new MeHg by MSR upon the introduction of sulfate, as carried into the core by Simpson Lagoon seawater (Jeremiason et al. 2006, Myrbo et al. 2017). Additionally, the mobilization of pre-existing MeHg may be enhanced by the presence of sulfide species.

The log K values of MeHg associated with these soil sulfides ($SOC\text{-}RS^-$) and other reduced sulfur species have been determined using a variety of laboratory methods:

$CH_3Hg^+ + S^{2-} \leftrightarrow CH_3HgS^-$ (log K: 21.1)

(Schwarzenbach & Schellenberg, 1965)

$CH_3Hg^+ + SH^- \leftrightarrow CH_3HgSH$ (log K: 14.5)

(Dryssen & Wedborg, 1991)

$CH_3Hg^+ + RS^- \leftrightarrow CH_3HgSR$ (log K: 16.5)

(Dryssen & Wedborg, 1991)

$CH_3Hg^+ + SOC\text{-}RS^- \leftrightarrow CH_3HgSR\text{-}SOC$ (log K: 15.6 – 17.5)

(Reid & Rabenstein, 1981, Qian et al. 2002,
Karlsson & Skyllberg, 2003)

Unlike Hg(II), as shown in Figure 10, ions such as chloride (log K: 4.9 – 5.28; Alderighi et al. 2003) have limited ability to compete with sulfur-containing soil carbon for complexation with MeHg (Reid and Rabenstein, 1981, Alderighi et al. 2003, Qian et al. 2002, Karlsson and

Skyllberg, 2003). Additionally, while Hg(II) will fall out of solution when exposed to reduced sulfur species, MeHg has the ability to complex with these species, which have complexation constants that are closer to organic matter associated sulfur groups (Schwarzenbach and Schellenberg, 1965, Dryssen and Wedborg, 1991). As MSR begin to produce dissolved sulfide that can compete with the surface-bound carbon sulfur functional groups, MeHg may be more readily mobilized. Given the nature of aquatic complexation chemistry, this potential mobilization will also be impacted by the relative amounts of dissolved sulfide to organic sulfide. The lower quantity of soil organic carbon (Figure 11) in the Elson Lagoon and Drew Point permafrost soils likely allows more MeHg to complex with the dissolved sulfide species, exposing this dynamic in a way that was not readily apparent in the organic-rich Simpson Lagoon experiments.

Despite salinity-dependent mobilization being clearer in the lacustrine permafrost, there is evidence that the peat-derived MeHg has greater mobilization potential. As mentioned, Simpson Lagoon has higher organic matter content than Elson Lagoon and Drew Point permafrost, which is a result of their origins as tundra peat vs lacustrine sediments, respectively (Figure 11). While this also directly impacts the soil THg content of these cores, with Elson Lagoon having ~55% and Drew Point having ~87% the amount of THg seen in the Simpson Lagoon permafrost samples (Table 1), accounting for this disparity does not reconcile the lower amount of MeHg leached from the lower organic material cores. Even normalizing the leaching results of the Elson Lagoon and Drew Point cores to the Simpson Lagoon soil THg concentrations did not bring the MeHg yield above 61% of the MeHg leached from the Simpson Lagoon permafrost. Lambertsson and Nilsson (2006) noted that in brackish environments, organic matter content of soils is a better indicator of Hg methylation than total soil Hg. Our experiments support this observation, with the permafrost peat soils have higher quantity and mobilization potential of MeHg due to their higher organic matter concentrations compared to mineral soils.

4.4 Aggregate findings from experimental and field data

The sediment plug flow-through and leaching experiments provide insight into the mechanisms that may be controlling Hg cycling inthe Simpson Lagoon subterranean estuary. Significant correlations between THg and DOC were observed in transect T1, with T3 exhibiting its highest THg concentrations associated with elevated DOC values. We also see increased retention of Hg associated with soil OM in our T1 tundra active layer selective leaches at depths approaching the ice table, where the OM is likely older. Finally, the plug flow-through experiments only showed a correlation between THg and DOC in the active layer peat sediments. Together, all of these data support the conclusion that DOC that has been relatively unprocessed by microbes will be more likely to mobilize Hg(II) in Arctic groundwater.

The impact of DOC on MeHg mobilization is also seen in both the field data and the experimental data. Most MeHg in organic rich wetland soils is complexed with low molecular weight organic carbon molecules containing sulfide functional groups, such as thiols (Liem-Nguyen et al. 2017). This association with thiols, as shown above, likely explains the significant mobilization of MeHg by DOC in the organic rich Simpson Lagoon active layer and permafrost soils, as well as in the field data collected from T1 and T3 (Zhang et al. 2014, Mazrui et al. 2016). There is also evidence for the mobilization of MeHg due to seawater intrusion in both the experimental data and the field data. Although there are no significant correlations between MeHg and salinity in the Simpson Lagoon transects, based on bulk statistical analyses, the time series from T1 gives us a glimpse into how seawater intrusion is still leading to MeHg release.

While there is an initial decline in MeHg when salinity rises, there remains a non-conservative excess of MeHg that increases over the two days following saline intrusion. The reason we see this pattern in the time series data and not in bulk field analyses is due to the fact that this nonconservative release is obscured by much higher MeHg concentrations observed in the freshwater endmember. The T1 intertidal sediments that this process occurs within have low organic matter content compared to the tundra peat soils (Supplemental Table S1), and so are more comparable to the lacustrine sediment of the Elson Lagoon and Drew point cores which also showed the mobilization by sulfide and/or production by MSR of MeHg upon the introduction of seawater. Together, these field and experimental data highlight the importance of DOC in organic rich sediments and the impact of seawater-derived sulfate in lower OM-content sediments on MeHg mobilization.

There are a few major differences between the field and experimental data, largely stemming from the much shorter water residence time in the cores due to experimental design and sampling limitations. Our sediment plugs had a maximum length of 5 cm, resulting in a water residence time around 3 hours. In contrast, an environmental sample may have traveled through more than 5 m of active layer soil before being collected. Consequently, *in situ* MeHg concentrations are consistently an order of magnitude higher and THg concentrations are more than twice as high as those observed in the sediment plug flow-through experiments. The experiments also show lower concentrations of DOC, Fe, and Mn compared to *in situ* values for the same reason. Additionally, unlike our experiments, *in situ* groundwater receives new, labile inputs of Hg and DOC from overlying plant species along its flow path. As a result, it is not appropriate to use the concentrations from these experiments to estimate overall fluxes from groundwater to the Arctic Ocean. Instead, the results from the core experiments provide valuable insights into how THg and MeHg interact with different Arctic soil types and the conditions that are more likely to mobilize Hg species.

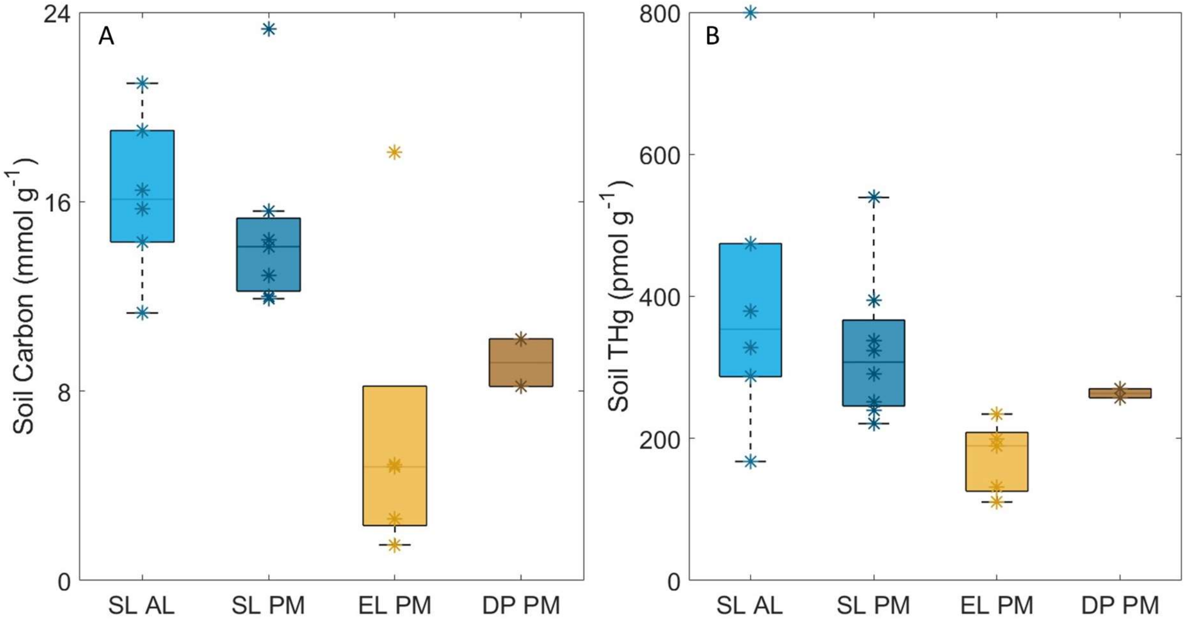

Figure 11. Box and Whisker plot of A) soil carbon and B) soil THg in core sections from the four soil types.

SL AL = Simpson Lagoon Active Layer, SL PM = Simpson Lagoon Permafrost, EL PM = Elson Lagoon Permafrost, and DP PM = Drew Point Permafrost. Boxes contain values from the 0.25 to the 0.75 quartiles, with the central mark indicating the median. Whiskers extend to values less than 1.5 the interquartile range.

4.5 Implications for Hg inputs to the Arctic Ocean from coastal erosion

Substantially more research is needed to accurately estimate Hg inputs from coastal erosion into the Arctic Ocean. The most comprehensive estimate to date is provided by Dastoor et al. (2022), who calculated THg inputs by combining coastal erosion rates with THg concentrations in active layer and permafrost soils. However, to the best of our knowledge, no studies have yet examined the behavior of Hg after the eroded soil contacts the saline waters of the Arctic Ocean.

The initial porewater collected from our plug flow-through experiments, though omitted from our time series analyses, provides insight into the first release of Hg from eroding soils. These initial concentrations were almost always higher than those observed later in the experiment, likely due to the long residence time of the porewater. Although some cores' THg porewater concentrations were over 100 pM, the average concentrations for Simpson Lagoon's active layer cores was 29 ± 24 pM, for Simpson Lagoon's permafrost cores it was 8.6 ± 9.7 pM, for Elson Lagoon's permafrost cores it was 9.3 ± 8.0 pM, and for Drew Point's permafrost cores it was 8.0 ± 2.7 pM. Using Dastoor et al.'s (2022) estimates for the volume of ice eroded with sediment annually along the pan-Arctic coastline ($0.614\ \mathrm{km^3\ ice\ y^{-1}} \rightarrow 0.565 \times 10^{12}\ \mathrm{kg\ y^{-1}}$), we estimate that 1.7 – 14.0 mol THg is released from this source annually. This is a small fraction compared to the soil THg eroding into the Arctic Ocean ($9 \times 10^4 - 26 \times 10^4\ \mathrm{mol\ y^{-1}}$; Dastoor et al. 2022); however, as our work shows, much of the soil-associated THg remains in the solid phase even when exposed to higher salinities due to the strong preference Hg(II) has for soil organic particles. Consequently, the accessibility of THg released from the melting ice means it likely has a disproportionate impact on Arctic fauna. These results also suggest that the importance of coastal erosion inputs of THg to the Arctic Ocean may be overestimated, given not all of the soil THg is likely to be dissolved. On the other hand, MeHg inputs from coastal erosion are largely ignored, while this work shows that MeHg is mobilized from the lacustrine permafrost soils by saline water, indicating that MeHg may become more accessible when these soils erode into a saline environment.

5. Conclusions: Major controls on Hg mobilization from Arctic soils and permafrost

This study has shown that the soil type will have dramatic implications for the amount of Hg leached from Arctic permafrost and the parameters controlling its release. For cases where the soil carbon is high, as shown in the Simpson Lagoon field measurements and core experiments, DOC mobilizes THg and MeHg from the sediments. However, the lability of the DOC may also be important to consider, as shown by transect T2, which received high amounts of recently generated DOC from the surrounding tundra and may have spurred uptake by microbes, as well as the fact that only the peat active layer core experiments showed a significant relationship between DOC and THg mobilization. For MeHg, a similar pattern occurred, with DOC exerting the largest control on MeHg mobilization only in the organic-rich soils from Simpson Lagoon, despite the cores from Elson Lagoon and Drew Point having comparable DOC concentrations. These findings highlight the need for more research addressing the composition of DOC leaching from Arctic soils and how it associates with Hg species.

Between sites with differing mineral and carbon compositions, total soil organic carbon was the predominant control on the overall amount of MeHg mobilized ($p < 10^{-4}$), followed closely by soil THg ($p < 0.04$). Based on our experiments, we cannot tell if this is just leaching or also microbial production, thus more work is needed to determine which of these two processes dominate in Arctic coastal groundwater. For the lacustrine permafrost sediments, which contained lower amounts of total soil carbon and tended to have net removal of dissolved THg, the impact of salinity on the cycling of sulfur and metal oxides was the most important control on THg (Figure 9) and MeHg cycling (Figure 12). Despite having lower concentrations leached than those observed for the peat sediments, the fact that infiltrating seawater can change these soils from a sink of MeHg to a source is particularly concerning in the context of rising, rapid coastal erosion in the Arctic (Nielsen et al. 2022). No work has been published regarding the fate of MeHg in eroding Arctic coastlines, with the only studies to date using THg as a proxy for MeHg content in eroding soils (Leitch, 2006, Jonsson et al. 2022); however, this work indicates that MeHg in eroding lacustrine permafrost bluffs will be mobilized upon erosion into the Beaufort Sea, rather than being quickly deposited in the sediment. This work also highlights the need for more cross-discipline studies, where both the complexation, mobilization, and microbial production of species is considered.

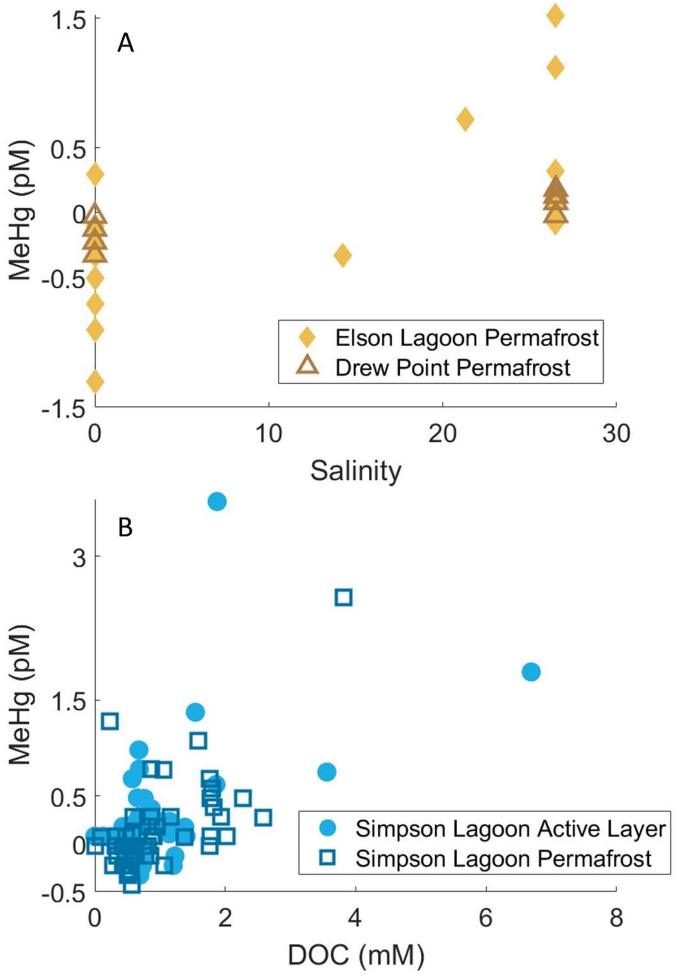

Figure 12. Scatter plots of MeHg against Salinity and DOC, the most significant parameter tested via linear regression, respectively, for A) lacustrine permafrost from Elson Lagoon (R^2: 0.41, $p < 10^{-5}$) and Drew Point (R^2: 0.75, $p < 10^{-5}$) and B) peat active layer soils (R^2: 0.27, $p < 0.0003$) and permafrost (R^2 0.42, $p < 10^{-7}$) from Simpson Lagoon - DOC.

Finally, higher temperatures led to an increase in THg and MeHg leached, in the case of both the *in situ* samples taken across seasons (T1, T3) and the experimental data. This is likely due to active inputs from plants during the growing season for THg (Obrist et al. 2017) and potentially lower K_d values at warmer temperatures, though this needs to be tested. MeHg leaches at higher temperatures due to an increase in rates of microbial methylation (Oiffer and Siciliano, 2009). This raises concerns for two reasons. First, Arctic temperatures are rising up to four times faster than the rest of the globe (Rantanen et al. 2022). Based on the results of our active layer and *in situ* samples, this will lead to higher rates of Hg(II) release and methylation, as well increased mobilization of MeHg into the Arctic Ocean from active layer soils. Second, in our warming climate, Arctic permafrost is increasingly vulnerable to degradation (IPCC, 2019, Saito et al. 2020). Not only will previously sequestered MeHg be released from recently thawed permafrost soils, but the dependence on temperature indicates that new production of MeHg within these soils is likely.

Acknowledgements

This project was funded by the National Science Foundation's Office of Polar Programs through grants 2134865 (Bullock and Charette), 1938873 (Charette), 1938820 (Cardenas and McClelland), 1656026 (McClelland), and 1854454 (Mason). Samples from Elson Lagoon and Drew Point were collected by Sasha Peterson and Emily Bristol as part of Craig Tweedie's work in Utqiagvik. Assistance with fieldwork was provided by Cansu Demir, Isabel Schaal, Julia Guimond, and Paul Henderson. Assistance with laboratory analyses was provided by Hannah Inman and Wesley Hoffman. We thank Hillcorp Alaska for providing access to field sites and resources, as well as Battelle Arctic Research Operations (via Polar Field Services) for logistical support. We also thank the Beaufort Lagoon Ecosystems Long Term Ecological Research program for sharing lab and field resources.

References

Aleku, D. L., Lazareva, O., Pichler, T. (2024). Mercury in groundwater – Source, transport and remediation. *Applied Geochemistry, 170,* 106060. https://doi.org/10.1016/j.apgeochem.2024.106060

AMAP, 2021. AMAP Assessment 2021: Mercury in the Arctic. Arctic Monitoring and Assessment Programme (AMAP), Tromsø, Norway. pg: viii - 324.

Balcom, P. H., Schartup, A. T., Mason, R. P., Chen, C. Y. (2015). Sources of water column methylmercury across multiple estuaries in the Northeast US. *Marine Chemistry, 177,* 721–730. https://doi.org/10.1016/j.marchem.2015.10.012

Babiarz, C. L., Hurley, J. P., Hoffmann, S. R., Andren, A. W., Shafer, M. M., Armstrong, D. E. (2001). Partitioning of Total Mercury and Methylmercury to the Colloidal Phase in Freshwaters. *Environmental Science & Technology, 35* (24), 4773-4782. https://doi.org/10.1021/es010895v

Basu, N., Abass, K., Dietz, R., Krümmel, E., Rautio, A., Weihe, P. (2022). The impact of mercury contamination on human health in the Arctic: A state of the science review. *Science of The Total Environment, 831,* 154793. https://doi.org/10.1016/j.scitotenv.2022.154793

Benoit, J. M., Gilmour, C. C., Mason, R. P., Heyes, A. (1999). Sulfide Controls on Mercury Speciation and Bioavailability to Methylating Bacteria in Sediment Pore Waters. *Environmental Science & Technology, 33*(6), 951-957. https://doi.org/10.1021/es9808200

Benoit, J. M., Gilmour, C. C., Heyes, A., Mason, R. P., Miller, C. L. (2003). “Geochemical and Biological Controls over Methylmercury Production and Degradation in Aquatic Ecosystems.” In *Biogeochemistry of Environmentally Important Trace Elements, ACS Symposium Series,* vol. 835, pg: 262-297. https://doi.org/10.1021/bk-2003-0835.ch019

Biskaborn, B. K., Smith, S. L., Noetzli, J., Matthes, H., Vieira, G., Streletskiy, D. A. et al. (2019). Permafrost is warming at a global scale. *Nature Communications, 10,* 264. https://doi.org/10.1038/s41467-018-08240-4

Black, F. J., Conaway, C. H., and Flegal, A. R. (2009). Stability of Dimethyl Mercury in Seawater and Its Conversion to Monomethyl Mercury. *Environmental Science & Technology, 43*(11), 4056-4062. https://doi.org/10.1021/es9001218

Bloom, N., Fitzgerald, W. F. (1988) Determination of volatile mercury species at the picogram level by low-temperature gas chromatography with cold-vapour atomic fluorescence detection. *Analytica Chimica Acta, 208*, 151–161.

Bone, S. E., Charette, M. A., Lamborg, C. H., Gonneea, M. E. (2007). Has Submarine Groundwater Discharge Been Overlooked as a Source of Mercury to Coastal Waters? *Environmental Science & Technology, 41*(9), 3090-3095. https://doi.org/10.1021/es0622453

Bristol, E. M., Connolly, C. T., Lorenson, T. D., Richmond, B. M., Ilgen, A. G., Choens, R. C., Bull, D. L., Kanevskiy, M., Iwahana, G., Jones, B. M., McClelland, J. W. (2021). Geochemistry of Coastal Permafrost and Erosion-Driven Organic Matter Fluxes to the Beaufort Sea Near Drew Point, Alaska. *Frontiers in Earth Science, 8.* https://doi.org/10.3389/feart.2020.598933

Brown, J., Jorgenson, M. T., Smith, O. P., Lee, W. “Long-term rates of coastal erosion and carbon input, Elson Lagoon, Barrow, Alaska.” In *Permafrost*. Eds: Phillips, Springman, and Arenson. Swets & Zeitlinger, 2003, pg: 101-106.

Bullock[a], E. J., Schaal, I. V., Cardenas, M. B., McClelland, J. W., Henderson, P. B., Charette, M. A. (2024[a]). Seasonality of submarine groundwater discharge to an Arctic coastal lagoon. *Limnology and Oceanography, 69* (6), 1429-1438.

Bullock[b], E. J., Mason, R., Bristol, E. M., Inman, H., Huffman, W. W., Cardenas, M. B., McClelland, J. W., Charette, M. A. (2024[b]). Methylmercury Inputs to the Arctic Ocean from Submarine Groundwater Discharge. *Submitted.*

Chiasson-Gould, S. A., Blais, J. M., Poulain, A. J. (2014). Dissolved Organic Matter Kinetically Controls Mercury Bioavailability to Bacteria. Environmental Science & Technology, 48(6), 3153-3161. https://doi.org/10.1021/es4038484

Coquery, M., Cossa, D., Sanjuan, J. (1997). Speciation and sorption of mercury in two macro-tidal estuaries. *Marine Chemistry, 58* (1-2), 213-227. https://doi.org/10.1016/S0304-4203(97)00036-4

Dastoor, A., Angot, H., Bieser, J., Christensen, J. H., Douglas, T. A., Heimbürger-Boavida, L-E., et al. (2022). Arctic mercury cycling. *Nature Reviews Earth & Environment, 3,* 270-286. https://doi.org/10.1038/s43017-022-00269-w

Déry, S. J., Stieglitz, M., Rennermalm, Å. K., Wood, E. F. (2005). The Water Budget of the Kuparuk River Basin, Alaska. Journal of Hydrometerology, 6, 633 - 655. https://doi.org/10.1175/JHM434.1

Fernández-Llamazares, A., Garteizgogeascoa, M., Basu, N., Brondizio, E. S., Cabeza, M., Martínez-Alier, J., McElwee, P., Reyes-García, V. (2020). A State-of-the-Art Review of Indigenous Peoples and Environmental Pollution. *Integrated Environmental Assessment and Management, 16*(3), 324-341. https://doi.org/10.1002/ieam.4239

Fernández-Martínez, R., Rucandio, I. (2013). Assessment of a sequential extraction method to evaluate mercury mobility and geochemistry in solid environmental samples. *Ecotoxicology and Environmental Safety, 97,* 196-203. https://doi.org/10.1016/j.ecoenv.2013.07.013

Ghimire, P. S., Tripathee, L., Zhang, Q., Guo, J., Ram, K., Huang, J., Sharma, C. M., Kang, S. (2019). Microbial mercury methylation in the cryosphere: Progress and prospects. *Science of The Total Environment, 697,* 134150. https://doi.org/10.1016/j.scitotenv.2019.134150

Gibbs, A. E., Richmond, B. M. (2015). *National Assessment of Shoreline Change—Historical Shoreline Change along the North Coast of Alaska, U.S.–Canadian Border to Icy Cape*. U.S. Geological Survey Open–File Report 2015–1048, USGS, Reston, Virginia. http://dx.doi.org/10.3133/ofr20151048

Gilmour, C. C., Podar, M., Bullock, A. L., Graham, A. M., Brown, S. D., Somenahally, A. C., Johs, A., Hurt Jr., R. A., Bailey, K. L., Elias, D. A. (2013). Mercury Methylation by Novel Microorganisms from New Environments. *Environmental Science & Technology, 47*(20), 11810-11820. https://doi.org/10.1021/es403075t

Gilmour, C. C., Bullock, A. L., McBurney, A., Podar, M., Elias, D. A. (2018). Robust Mercury Methylation across Diverse Methanogenic Archaea. *mBio, 9*(2), e02403-17. https://doi.org/10.1128/mBio.02403-17

Gong, Y., Yin, J., Zhang, T., Yin, W., Sun, L., Liang, Q., Wang, Q. (2023). Ferrous sulfide nanoparticles control mercury speciation and bioavailability to methylating bacteria in contaminated groundwater: Impacts of mercury species. *Chemical Engineering Journal, 455,* 140612. https://doi.org/10.1016/j.cej.2022.140612

Graham, A. M., Aiken, G. R., Gilmour, C. C. (2012). Dissolved Organic Matter Enhances Microbial Mercury Methylation Under Sulfidic Conditions. *Environmental Science & Technology, 46*(5), 2715-2723. https://doi.org/10.1021/es203658f

Graham, A. M., Aiken, G. R., Gilmour, C. C. (2013). Effect of Dissolved Organic Matter Source and Character on Microbial Hg Methylation in Hg–S–DOM Solutions. *Environmental Science & Technology, 47*(11), 5746-5754. https://doi.org/10.1021/es400414a

Guimond, J.A., Demir, C., Kurylyk, B. L., Walvoord, M. A., McClelland, J. W., Cardenas, M. B. (2023). Wind - modulated groundwater discharge along a microtidal Arctic coastline. *Environmental Research Letters, 18*(9), 094042. https://doi.org/10.1088/1748-9326/acf0d8

Halbach, K., Mikkelsen, Ø., Berg, T., Steinnes, E. (2017). The presence of mercury and other trace metals in surface soils in the Norwegian Arctic. *Chemosphere, 188,* 567-574. https://doi.org/10.1016/j.chemosphere.2017.09.012

Hamer, K., Gudenschwager, I., Pichler, T. (2020). Manganese (Mn) Concentrations and the Mn-Fe Relationship in Shallow Groundwater: Implications for Groundwater Monitoring. *Soil Systems, 4* (3), 49. https://doi.org/10.3390/soilsystems4030049

Hammerschmidt, C. R., Fitzgerald, W. F. (2001). Formation of artifact methylmercury during extraction from a sediment reference material. *Analytical Chemistry, 73*(24), 5930–5936. https://doi.org/10.1021/ac010721w

Hammerschmidt, C. R., Fitzgerald, W. F., Lamborg, C. H., Balcom, P. H., Visscher, P. T. (2004). Biogeochemistry of methylmercury in sediments of Long Island Sound. *Marine Chemistry, 90*(1-4), 31-52. https://doi.org/10.1016/j.marchem.2004.02.024

Harirs-Hellal, J., Grimaldi, M., Garnier-Zarli, E., Bousserrhine, N. (2011). Mercury mobilization by chemical and microbial iron oxide reduction in soils of French Guyana. *Biogeochemistry, 103,* 223-234. https://doi.org/10.1007/s10533-010-9457-y

Hellal, J., Guédron, S., Huguet, L., Schäfer, J., Laperche, V., Joulian, C., Lanceleur, L., Burnol, A., Ghestem, J-P., Garrido, F., Battaglia-Brunet, F. (2015). Mercury mobilization and speciation linked to bacterial iron oxide and sulfate reduction: A column study to mimic reactive transfer in an anoxic aquifer. *Journal of Containment Hydrology, 180,* 56-68. https://doi.org/10.1016/j.jconhyd.2015.08.001

IPCC. (2019). IPCC Special Report on the Ocean and Cryosphere in a Changing Climate [H.-O. Pörtner, D.C. Roberts, V. Masson-Delmotte, P. Zhai, M. Tignor, E. Poloczanska, K. Mintenbeck, A. Alegría, M. Nicolai, A. Okem, J. Petzold, B. Rama, N.M. Weyer (eds.)]. In press.

Jiskra, M., Sonke, J. E., Agnan, Y., Helmig, D., Obrist, D. (2019). Insights from mercury stable isotopes on terrestrial–atmosphere exchange of Hg(0) in the Arctic tundra. *Biogeosciences, 16*, 4051–4064. https://doi.org/10.5194/bg-16-4051-2019

Johannesson, K. H., Neumann, K. (2013). Geochemical cycling of mercury in a deep, confined aquifer: Insights from biogeochemical reactive transport modeling. *Geochimica et Cosmochimica Acta, 106,* 25-43. https://doi.org/10.1016/j.gca.2012.12.010

Jones, B. M., Arp, C. D. (2015). Observing a Catastrophic Thermokarst Lake Drainage in Northern Alaska. *Permafrost and Periglacial Processes, 26*(2), 119-128. https://doi.org/10.1002/ppp.1842

Jones, B., Farquharson, L. M., Baughman, C. A., Buzard, R. M., Arp, C. D., Grosse, G., et al. (2018). A decade of remotely sensed observations highlight complex processes linked to coastal permafrost bluff erosion in the Arctic. *Environmental Research Letters, 13*(11), 115001. https://doi.org/10.1088/1748-9326/aae471

Jonsson, S., Skyllberg, U., Nilsson, M. B., Westlund, P-O., Shchukarev, A., Lundberg, E., Björn, E. (2012). Mercury Methylation Rates for Geochemically Relevant HgII Species in Sediments. *Environmental Science & Technology, 46*(21), 11653-11659. https://doi.org/10.1021/es3015327

Jonsson, S., Mastromonaco, M. N., Wang, F., Bravo, A. G., Cairns, W. R. L., Chételat, J., Douglas, T. A., Lescord, G., Ukonmaanaho, L., Heimbürger-Boavida, L-E. (2022). Arctic methylmercury cycling. *Science of the Total Environment, 850,* 157445. https://doi.org/10.1016/j.scitotenv.2022.157445

Kanevskiy, M., Shur, Y., Jorgenson, M. T., Ping C-L., Michaelson, G. J., Fortier, D., Stephani, E., Dillon, M., Tumskoy, V. (2013). Ground ice in the upper permafrost of the Beaufort Sea coast of Alaska. *Cold Regions Science and Technology, 85,* 56-70. https://doi.org/10.1016/j.coldregions.2012.08.002

Kerin, E. J., Gilmour, C. C., Roden, E., Suzuki, M. T., Coates, J. D., Mason, R. P. (2006). Mercury Methylation by Dissimilatory Iron-Reducing Bacteria. *Applied and Environmental Microbiology, 72*. https://doi.org/10.1128/AEM.01602-06

Kim, M., Han, S., Gieskes, J., Deheyn, D. D. (2011). Importance of organic matter lability for monomethylmercury production in sulfate-rich marine sediments. *Science of The Total Environment, 409*(4), 778-784. https://doi.org/10.1016/j.scitotenv.2010.10.050

Kozin, L. F., Hansen, S. C. (2013). *Mercury Handbook: Chemistry, Applications, and Environmental Impact*. Royal Society of Chemistry, Cambridge, UK.

Kubeneck, L. J., Notini, L., Rothwell, K. A., Fantappiè, G., Huthwelker, T., ThomasArrigo, L. K., Kretschmar, R. (2024). Transformation of vivianite in intertidal sediments with contrasting sulfide conditions. *Geochimica et Cosmochimica Acta. 370,* 173-187. https://doi.org/10.1016/j.gca.2024.01.020

Lambertsson, L., Nilsson, M. (2006). Organic Material: The Primary Control on Mercury Methylation and Ambient Methyl Mercury Concentrations in Estuarine Sediments. *Environmental Science & Technology, 40*(6), 1822-1829. https://doi.org/10.1021/es051785h

Lamborg, C. H., Fitzgerald, W. F., Skoog, A., Visscher, P. T. (2004). The abundance and source of mercury-binding organic ligands in Long Island Sound. *Marine Chemistry, 90* (1-4), 151-163. https://doi.org/10.1016/j.marchem.2004.03.014

Lamborg, C. H., Hammerschmidt, C. R., Bowman, K. L. (2016). An examination of the role of particles in oceanic mercury cycling. *Mathematical, Physical, and Engineering Sciences, 374,* 20150297. https://doi.org/10.1098/rsta.2015.0297

Lehnherr, I., St. Louis, V.L., Emmerton, C.A., Barker, J.D., Kirk, J.L. (2012). Methylmercury Cycling in High Arctic Wetland Ponds: Sources and Sinks. Environmental Science & Technology, 46(19), 10514-10522. https://doi.org/10.1021/es300576p

Leitch, D. R. (2006). Mercury distribution in water and permafrost of the lower Mackenzie basin, their contribution to the mercury contamination in the Beaufort Sea marine ecosystem, and potential effects of climate variation. MSc Dissertation. University of Manitoba, Winnipeg, Manitoba, Canada.

Li, Y-H., Burkhardt, L., Teraoka, H. (1984). Desorption and coagulation of trace elements during estuarine mixing. *Geochimica et Cosmochimica Acta, 48* (10), 1879-1884. https://doi.org/10.1016/0016-7037(84)90371-5

Liu, Y., Wang, J., Guo, J., Wang, L., Wu, Q. (2022). Vertical distribution characteristics of soil mercury and its formation mechanism in permafrost regions: A case study of the Qinghai-Tibetan Plateau. *Journal of Environmental Sciences, 113,* 311-321. https://doi.org/10.1016/j.jes.2021.06.016

Luther, G. W., Kostka, J. E., Church, T. M., Sulzberger, B., Stumm, W. (1992). Seasonal iron cycling in the salt-marsh sedimentary environment: the importance of ligand complexes with Fe(II) and Fe(III) in the dissolution of Fe(III) minerals and pyrite, respectively. *Marine Chemistry, 40*(1-2), 81-103. https://doi.org/10.1016/0304-4203(92)90049-G

Luther, G. W., Glazer, B., Ma, S., Trouborst, R., Shultz, B. R., Druschel, G., Kraiya, C. (2003). Iron and Sulfur Chemistry in a Stratified Lake: Evidence for Iron-Rich Sulfide Complexes. *Aquatic Geochemistry, 9,* 87-110. https://doi.org/10.1023/B:AQUA.0000019466.62564.94

MacDonald, E. N., Tank, S. E., Kokelj, S. V., Froese, D. G., Hutchins, R. H. S. (2021). Permafrost-derived dissolved organic matter composition varies across permafrost end-members in the western Canadian Arctic. *Environmental Research Letters, 16,* 024036. https://doi.org/10.1088/1748-9326/abd971

Mazrui, N. M., Jonsson, S., Thota, S., Zhao, J., Mason, R. P. (2016). Enhanced availability of mercury bound to dissolved organic matter for methylation in marine sediments. *Geochimica et Cosmochimica Acta, 194,* 153-162. http://dx.doi.org/10.1016/j.gca.2016.08.019

Mehrohtra, A. S., Sedlak, D. L. (2005). Decrease in Net Mercury Methylation Rates Following Iron Amendment to Anoxic Wetland Sediment Slurries. *Environmental Science & Technology, 39*(8), 2564-2570. https://doi.org/10.1021/es049096d

Moore, W. S. (1999). The subterranean estuary: a reaction zone of ground water and sea water. *Marine Chemistry, 65*(1-2), 111-125. https://doi.org/10.1016/S0304-4203(99)00014-6

Nyffeler, U. P., Li, Y-H., Santschi, P. H. (1984). A kinetic approach to describe trace-element distribution between particles and solution in natural aquatic systems. *Geochimica et Cosmochimica et Acta, 48* (7), 1513-1522. https://doi.org/10.1016/0016-7037(84)90407-1

Nielsen, D. M., Pieper, P., Barkhordarian, A., Overduin, P., Ilyina, T., Brovkin, V., Baehr, J., Dobrynin, M. (2022). Increase in Arctic coastal erosion and its sensitivity to warming in the twenty-first century. *Nature Climate Change, 12,* 263-270. https://doi.org/10.1038/s41558-022-01281-0

Obrist, D., Agnan, Y., Jiskra, M., Olson, C. L., Colegrove, D. P., Hueber, J., Moore, C. W., Sonke, J. E., Helmig, D. (2017) Tundra uptake of atmospheric elemental mercury drives Arctic mercury pollution. *Nature, 547*, 201–204. https://doi.org/10.1038/nature22997

Oiffer, L., Siciliano, S. D. (2009). Methyl mercury production and loss in Arctic soil. *Science of The Total Environment, 407*(5), 1691-1700. https://doi.org/10.1016/j.scitotenv.2008.10.025

Olson, C., Jiskra, M., Biester, H., Chow, J., Obrist, D. (2018). Mercury in Active-Layer Tundra Soils of Alaska: Concentrations, Pools, Origins, and Spatial Distribution. *Global Biogeochemical Cycles, 32* (7), 1058-1073. https://doi.org/10.1029/2017GB005840

Pallud, C., Meile, C., Laverman, A. M., Abell, J., Van Cappellen, P. (2007). The use of flow-through sediment reactors in biogeochemical kinetics: Methodology and examples of applications. *Marine Chemistry, 106* (1-2), 256-271. https://doi.org/10.1016/j.marchem.2006.12.011

Pallud, C., Van Cappellen, P. (2006). Kinetics of microbial sulfate reduction in estuarine sediments. *Geochimica et Cosmochimica Acta, 70* (5), 1148-1162. https://doi.org/10.1016/j.gca.2005.11.002

Ping, C-L., Michaelson, G. J., Guo, L., Jorgenson, M. T., Kanevskiy, M., Shur, Y., Dou, F., Liang, J. (2011). Soil carbon and material fluxes across the eroding Alaska Beaufort Sea coastline. *Journal of Geophysical Research: Biogeosciences*, *116*(G2). https://doi.org/10.1029/2010JG001588

Rahman, M. M., Lee, Y. G., Kim, G., Lee, K., Han, S. (2013). Significance of submarine groundwater discharge in the coastal fluxes of mercury in Hampyeong Bay, Yellow Sea. *Chemosphere, 91*(3), 320-327. https://doi.org/10.1016/j.chemosphere.2012.11.052

Rantanen, M., Karpechko, A. Y., Lipponen, A., Nordling, K., Hyvärinen, O. Ruosteenoja, K., Vihma, T., Laaksonen, A. (2022). The Arctic has warmed nearly four times faster than the globe since 1979. *Nature Communications Earth & Environment, 3,* 168. https://doi.org/10.1038/s43247-022-00498-3

Ravenschlag, K., Sahm, K., Amann, R. (2001). Quantitative Molecular Analysis of the Microbial Community in Marine Arctic Sediments (Svalbard). *Applied and Environmental Microbiology, 67*. https://doi.org/10.1128/AEM.67.1.387-395.2001

Rawlinson, S.E. (1993). Surficial geology and morphology of the Alaskan central arctic coastal Plain. *Alaska Division of Geological & Geophysical Surveys,* RI 93-1, 2484. https://doi.org/10.14509/2484

Rawlins, M. A. (2021). Increasing freshwater and dissolved organic carbon flows to Northwest Alaska's Elson lagoon. *Environmental Research Letters, 16*(10), 105014. https://doi.org/10.1088/1748-9326/ac2288

Rosenqvist, I. T. (1970). Formation of vivianite in holocene clay sediments. *Lithos, 3*(4), 327-334. https://doi.org/10.1016/0024-4937(70)90039-3

Rothe, M., Frederichs, T., Eder, M., Kleeberg, A., Hupfer, M. (2014). Evidence for vivianite formation and its contribution to long-term phosphorus retention in a recent lake sediment: a novel analytical approach. *Biogeosciences, 11*(18), 5169-5180. https://doi.org/10.5194/bg-11-5169-2014

Rothe, M., Kleeberg, A., Hupfer, M. (2016). The occurrence, identification and environmental relevance of vivianite in waterlogged soils and aquatic sediments. *Earth-Science Reviews, 158,* 51-64. https://doi.org/10.1016/j.earscirev.2016.04.008

Saito, K., Machiya, H., Iwahana, G., Ohno, H., Yokohata, T. (2020). Mapping simulated circum-Arctic organic carbon, ground ice, and vulnerability of ice-rich permafrost to degradation. *Progress in Earth and Planetary Science, 7,* 31. https://doi.org/10.1186/s40645-020-00345-z

Schaefer, K., Elshorbany, Y., Jafarov, E., Schuster, P. F., Striegl, R. G., Wickland, K. P., Sunderland, E. M. (2020). Potential impacts of mercury released from thawing permafrost. *Nature Communications, 11,* 4650. https://doi.org/10.1038/s41467-020-18398-5

Schaal, I. V. (2023). Distribution and behavior of trace metals in the subterranean estuary of an Arctic coastal lagoon. MSc Thesis. Massachusetts Institute of Technology and the Woods Hole Oceanographic Institution, Cambridge and Woods Hole, MA, USA.

Schreiner, K. M., Bianchi, T. S., Eglinton, T. I., Allison, M. A., Hanna, A. J. M. (2013). Sources of terrigenous inputs to surface sediments of the Colville River Delta and Simpson's Lagoon, Beaufort Sea, Alaska. *Journal of Geophysical Research: Biogeosciences, 118*(2), 808-824. https://doi.org/10.1002/jgrg.20065

Slowey, A. J., Brown Jr., G. E. (2007). Transformations of mercury, iron, and sulfur during the reductive dissolution of iron oxyhydroxide by sulfide. *Geochimica et Cosmochimica Acta, 71*(4), 877-894. https://doi.org/10.1016/j.gca.2006.11.011

Smith, S. L., O'Neill, H. B., Isaksen, K., Noetzli, J., Romanovsky, V. E. (2022). The changing thermal state of permafrost. *Nature Reviews Earth & Environment, 3,* 10-23. https://doi.org/10.1038/s43017-021-00240-1

Spyropoulou, A. E., Lazarou, Y. G., Sapalidis, A. A., Laspidou, C. S. (2022). Geochemical modeling of mercury in coastal groundwater. *Chemosphere, 268*(1), 131609. https://doi.org/10.1016/j.chemosphere.2021.131609

Stumm, W. (1992). *Chemistry of the Solid–Water Interface*. John Wiley & Sons, Inc., New York.

Textor, S. R., Wickland, K. P., Podgorski, D. C., Johnston, S. E., Spencer, R. G. M. (2019). Dissolved Organic Carbon Turnover in Permafrost-Influenced Watersheds of Interior Alaska: Molecular Insights and the Priming Effect. *Frontiers in Earth Science, 7,* 275. https://doi.org/10.3389/feart.2019.00275

Tfaily, M. M., Hamdan, R., Corbett, J. E., Chanton, J. P., Glaser, P. H., Cooper, W. T. (2013). Investigating dissolved organic matter decomposition in northern peatlands using complimentary analytical techniques. *Geochimica et Cosmochimica Acta, 112*, 116-129. https://doi.org/10.1016/j.gca.2013.03.002

Tseng, C.-M., Hammerschmidt, C. R., Fitzgerald, W. F. (2004). Determination of methylmercury in environmental matrixes by on-line flow injection and atomic fluorescence spectrometry. Analytical Chemistry, 76, 7131–7136. https://doi.org/10.1021/ac049118e

Turner, A., Millward, G. E., Le Roux, S. M. (2001). Sediment-Water Partitioning of Inorganic Mercury in Estuaries. *Environmental Science and Technology, 35* (23), 4648-4654. https://doi.org/10.1021/es010933a

Tweedie, C. E., Aguirre, A., Cody, R., Vargas, S., Brown, J. (2012). Spatial and Temporal Dynamics of Erosion Along the Elson Lagoon Coastline near Barrow, Alaska (2002-2011). Proceedings of the Tenth International Conference on Permafrost, 425-430.

Varty, S., Lehnherr, I., St. Pierre, K., Kirk, J., Wisniewski, V. (2020). Methylmercury Transport and Fate Shows Strong Seasonal and Spatial Variability along a High Arctic Freshwater Hydrologic Continuum. *Environmental Science & Technology, 55,* 331-340. https://dx.doi.org/10.1021/acs.est.0c05051?ref=pdf

Wallschläger, D., Desai, M. V. M., Wilken, R-D. (1996). The role of humic substances in the aqueous mobilization of mercury from contaminated floodplain soils. *Water, Air, and Soil Pollution, 90,* 507-520. https://doi.org/10.1007/BF00282665

Ward, C. P., Cory, R. M. (2015). Chemical composition of dissolved organic matter draining permafrost soils. *Geochimica et Cosmochimica Acta, 167,* 63-79. https://doi.org/10.1016/j.gca.2015.07.001

Yang, Z., Fang, W., Lu, X., Sheng, G., Graham, D.E., Liang, L., Wullschleger, S.D., Gu, B. (2016). Warming increases methylmercury production in an Arctic soil. Environmental Pollution, 214, 504-509. https://doi.org/10.1016/j.envpol.2016.04.069

Zhang, T., Kucharzyk, K. H., Kim, B., Deshusses, M. A., Hsu-Kim, H. (2014). Net Methylation of Mercury in Estuarine Sediment Microcosms Amended with Dissolved, Nanoparticulate, and Microparticulate Mercuric Sulfides. *Environmental Science & Technology, 48*(16), 9133-9141. https://doi.org/10.1021/es500336j

Zhang, L., Philben, M., Taş, N., Johs, A., Yang, Z., Wullschleger, S. D., Graham, D. E., Pierce, E. M., Gu, B. (2022). Unravelling biogeochemical drivers of methylmercury production in an Arctic fen soil and a bog soil. *Environmental Pollution, 299,* 118878. https://doi.org/10.1016/j.envpol.2022.118878

Supplementary Information for Chapter 5

S1. Selective Leaching Experiments

Below (Supplemental Table S1) are the other parameters measured for the soils that were utilized during the selective leaching experiments. Please note that the Lagoon Bottom Sediment and the Kuparak River Bluff sediment were taken as grab samples. The intertidal core was a single core taken from the ground surface down to the ice table. The tundra active layer core was cut out of the tundra and the permafrost core was taken directly below where the active layer core was gathered.

Supplemental Table S1. Depth and concentrations of THg, carbon, Mn, and Fe found in soils taken from sites at Simpson Lagoon.

Core	Sampling Depth (cm)	Soil THg (pmol/g)	Soil Carbon (mmol/g)	Soil Mn[a] (µmol/g)	Soil Fe[a] (µmol/g)
Lagoon Bottom Sediment[b]	0	205	2.81	4.46	394
Kuparuk River Bluff[c]	0	104	2.15	7.10	412
Transect T1: Intertidal Active Layer Core	-3.5	22	0.47	1.00	143
	-12.5	80	1.57	0.89	134
	-16.5	164	10.96	2.18	376
	-22.5	203	2.23	1.00	
	-28.5	35	1.99	0.82	
	-33	221	6.49	3.73	
Transect T1: Tundra Active Layer Core	-1.5	80	2.35	3.55	143
	-7.5	179	12.28	0.64	519
	-15	431	19.69	2.37	555
	-21.5	401	19.16	2.75	609

Transect T1: Tundra Permafrost Core	-38	295	19.53	11.65	716
	-42	315	19.63	2.91	448
	-46	318	19.71	12.56	662
	-50	313	19.37	13.47	806
	-54	322	19.98	12.92	725

a) Total metal concentrations in soil obtained from Schaal (2023), who used the same cores.
b) Sample collected ~0.5 km from shore.
c) Sample collected from actively eroding river bluff face.

S2. Sediment Plug Flow-Through Experiments

The core sections used in the sediment plug flow-through experiments were analyzed for soil carbon, soil THg, and porosity (Supplemental Table S2). The experiments were set up so that there were set conditions for the first ~46 hours, after which the conditions were altered to test for the impact of changing salinity, oxygen levels, and temperature. Supplemental Table S3 has the experimental conditions used for each core. It should be noted that the designation “high oxygen” indicates that the influent was equilibrated with the atmosphere (≥350 μM). “Low oxygen” indicates that the influent was deoxygenated (≤ 5 μM). We do not call this condition anoxic because the readings of effluent from the low oxygen treatments were almost always greater than 5 μM. This likely represented a leak in the system, but as it could not be located and the oxygen values were still low, we refer to these treatments as low oxygen.

Supplemental Table S2. Soil depths, porosities, and concentrations of carbon and THg in core sections used for the sediment plug flow-through experiments.

Soil Type	Fraction	Depth from surface (cm)	porosity	Soil Carbon (mmol/g)	Soil THg (pmol/g)
Simpson Lagoon Permafrost	C1A	-17.8	70%	15.6	539
	C1C	-27.3	78%	14.4	324
	C2A	-24.1	66%	23.3	395
	C2B	-29.2	55%	14.1	338
	C2C	-34.3	55%	12.9	291
	C2D	-39.4	62%	11.9	252
	C2E	-44.5	56%	11.9	240

	C2F	-49.5	73%	12	221
Simpson Lagoon Active Layer	C3A	-2.2	64%	19	379
	C3B	-7.0	56%	11.3	168
	C3C	-12.1	69%	16.5	799
	C3D	-17.1	66%	14.3	474
	C3E	-2.5	67%	15.7	328
	C3F	-10.2	71%	21	287
Elson Lagoon Permafrost	C4A	-350.0	40%	1.5	111
	C4C	-250.0	13%	2.6	131
	C4E	-75.0	68%	18.1	234
	C5A	-55.0	65%	4.9	189
	C5C	-235.0	90%	4.8	199
Drew Point Permafrost	C5D	-65.0	76%	8.2	257
	C5E	-65.0	84%	10.2	270

Supplemental Table S3**.** Experimental conditions used for each core fraction for the sediment plug flow-through experiments. Conditions that were varied: salinity, oxygen level, and temperature.

		Initial Conditions			Secondary Conditions		
Soil Type	Fraction	Salinity	Oxygen Level[a]	T (°C)	Salinity	Oxygen Level[a]	T (°C)
Simpson Lagoon Permafrost	C1A	0	High	3	0	Low	3
	C1C	0	High	3	26.5	Low	3
	C2A	0	Low	3	26.5	Low	3
	C2B	0	Low	3	26.5	High	3
	C2C	0	Low	3	26.5	Low	20
	C2D	0	Low	3	26.5	High	20
	C2E	0	Low	3	26.5	Low	3

	C2F	0	Low	3	26.5	High	3
Simpson Lagoon Active Layer	C3A	0	High	3	26.5	High	3
	C3B	0	High	3	26.5	High	20
	C3C	0	High	3	26.5	Low	3
	C3D	0	High	3	26.5	Low	3
	C3E	0	High	3	26.5	High	3
	C3F	0	High	3	26.5	Low	3
Elson Lagoon Permafrost	C4A	0	High	3	26.5	High	3
	C4C	0	High	3	26.5	High	3
	C4E	0	High	3	26.5	High	3
	C5A	0	High	3	26.5	High	20
	C5C	0	High	3	26.5	High	3
Drew Point Permafrost	C5D	0	High	3	26.5	High	3
	C5E	0	High	3	26.5	Low	3

a) High oxygen levels indicate influent that was equilibrated with the atmosphere (≥350 μM). Low oxygen levels indicate influent that was deoxygenated (≤ 5 μM). We do not call this condition anoxic because the readings of effluent from the low oxygen treatments were almost always greater than 5 μM. This likely represented a leak in the system, but as it could not be located and the oxygen values were still low, we refer to these treatments as low oxygen.

S3. Statistical Tests

S3.1 Interpolation

In order to get a full data set of variables to compare to THg and MeHg measured concentrations, we interpolated measured values of DO, sulfide, Mn, Fe, and DOC using *polyfit* in MATLAB R2023a. All interpolations were adjusted manually (using the *polyfit* function options and utilizing boxing when applicable) to ensure a good fit between the measured data, observed trends, and interpolation output. Below (Supplemental Figure S2) is an example of the interpolations for the core section designated C2A, which was a Simpson Lagoon permafrost sample. Interpolated values never replaced actual measured values that were available for a particular time point. For the full number of samples measured for each parameter, see Table 1 in the main manuscript.

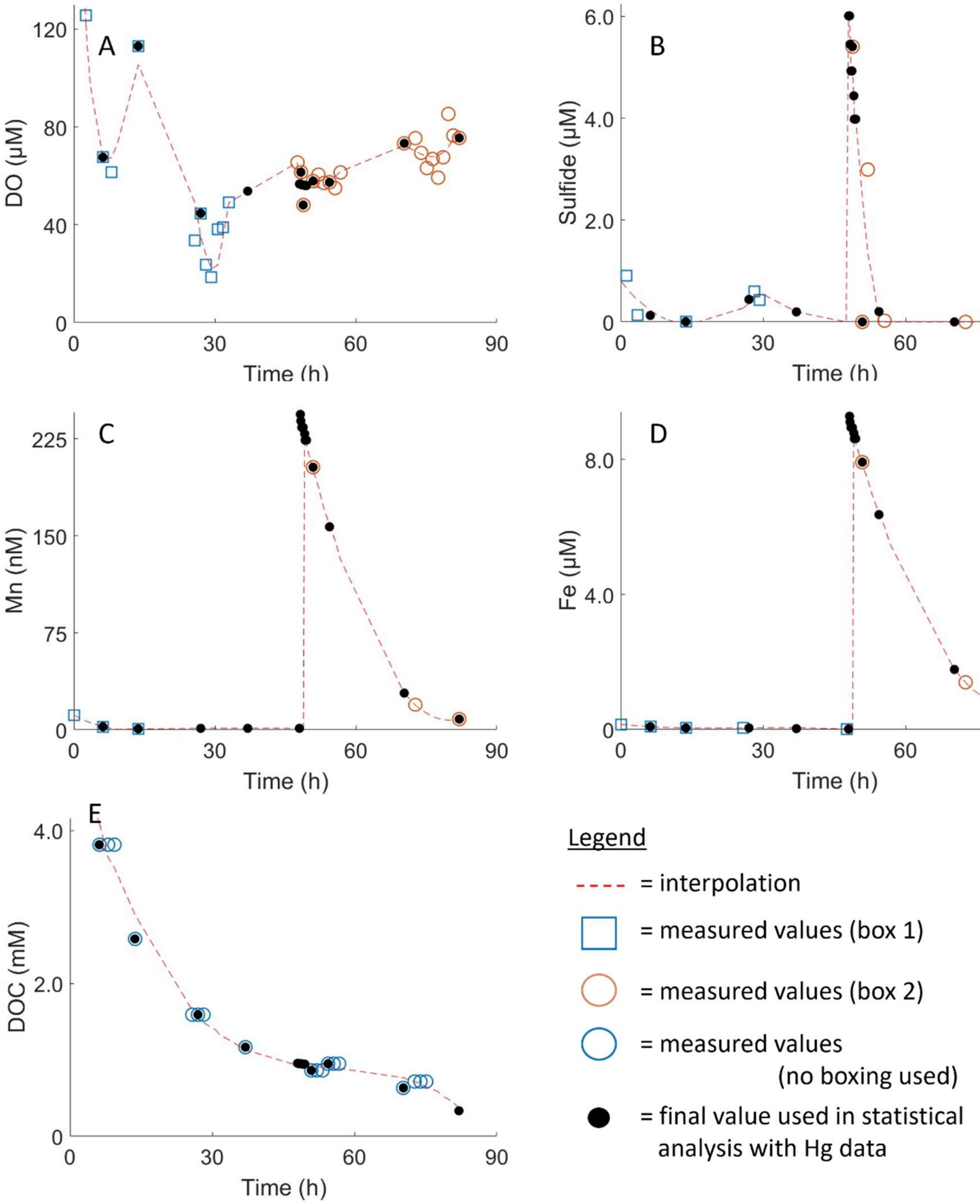

Supplemental Figure S1. An example of the interpolations produced from the results of one of the core sections used in the sediment plug flow-through experiments (C2A) for A) DO, B) sulfide, C) Mn, D) Fe, and E) DOC. Graphs with multiple symbols indicate boxing adjustments used to ensure a better fit.

S3.2 Results from Tests

Below is a summary of the significant results from the linear regressions (Supplemental Tables S4 and S5) performed on the samples and sediment plug flow-through experiment results.

Supplemental Table S4. Significant linear regression results for the *in situ* groundwater samples taken at Simpson Lagoon.

Transect	Species		Salinity	Temp	pH	ORP	DOC	Mn	Fe	Fe:Mn	TDN
T1	THg	R^2	0.34	0.14	0.1	—	0.34	—	—	0.2	—
		p	10^{-5}	0.01	0.05		10^{-5}			0.001	
	MHg	R^2	0.45	0.2	0.3	0.32	0.37	—	—	0.4	0.14
		p	10^{-6}	0.002	0.0004	0.0003	10^{-5}			10^{-5}	0.04
T2	THg	R^2	—	—	—	0.31	—	0.22	0.27	—	—
		p				0.01		0.05	0.04		
	MHg	R^2	—	—	—	—	—	—	—	—	—
		p									
T3	THg	R^2	0.56	—	—	—	0.51	0.23	—	—	—
		p	0.0005				0.001	0.05			
	MHg	R^2	0.25	—	—	—	0.38	—	—	—	—
		p	0.05				0.01				

Supplemental Table S5. Significant linear regression results for the sediment plug flow-through experiments.

Soil Type	Species		Salinity	DO	DOC	Mn	Fe:Mn
Simpson Lagoon Active Layer	THg	R^2	–	–	0.35	0.12	–
		p			10^{-10}	0.0003	
	MHg	R^2	–	0.16	0.27	–	0.17
		p		0.006	0.0003		0.005
Simpson Lagoon Permafrost	THg	R^2	0.21	–	–	–	–
		p	10^{-7}				
	MHg	R^2	–	–	0.42	–	–
		p			10^{-7}		
Elson Lagoon Permafrost	THg	R^2	0.41	–	–	0.14	–
		p	10^{-11}			0.0002	
	MHg	R^2	0.41	–	–	0.1	–
		p	10^{-5}			0.04	
Drew Point Permafrost	THg	R^2	0.51	0.11	–	–	–
		p	10^{-9}	0.02			
	MHg	R^2	0.74	–	–	–	–
		p	10^{-5}				

Chapter 6. Conclusion

Because of its harsh conditions and remote nature, baseline conditions in the Arctic remain poorly understood. Unfortunately, there is limited time to address this knowledge gap, as the Arctic Ocean is uniquely vulnerable to rapid, climate-induced change. This thesis addressed several major unresolved issues in our understanding of Arctic radium (Ra), mercury (Hg), and groundwater fluxes. By combining historical datasets, detailed sampling campaigns, and laboratory investigations, I have enhanced our understanding of terrestrial inputs to the Arctic Ocean and provided the first estimates of Hg fluxes to the Arctic Ocean from groundwater. However, much work remains to determine whether these findings are applicable on a pan-Arctic scale.

In Chapter 2, I utilized historical datasets, unpublished data, and Ra desorption experiments to estimate pan-Arctic inputs of ^{228}Ra and ^{226}Ra from rivers to the Arctic Ocean. I was able to perform desorption experiments on sediment from the Kolyma River in Siberia, which enabled the first comparison between Ra content in North American rivers' sediment and that of a Eurasian river. Stark differences were found in dissolved Ra concentrations, behavior, and Ra desorption between the two continents, emphasizing the need for more pan-Arctic scientific collaboration, since findings from Alaska and Canada may not be representative of conditions on the Eurasian continent. Future work should focus on increasing geographic variability in sampling and ensuring that the estuarine salinity gradient is represented, as flocculation or sediment settling can impact Ra concentrations. Most global Ra riverine studies estimate Ra desorption based on previous literature values, but my work shows that rivers draining watersheds with different geological features may have dramatically different Ra desorption amounts, underscoring the need for desorption experiments on river sediment at new study locations.

Chapter 3 presented the first seasonal study of submarine groundwater discharge (SGD) utilizing Ra isotopes in the Arctic. Field sampling and modeling highlighted the dominance of riverine Ra inputs immediately following the spring freshet, with diffusion and SGD being the major Ra sources following ice break-up through the ice-free period. During the ice-free period, Ra box models indicated substantial SGD inputs to Simpson Lagoon driven by wind-dependent water level changes and short term processes such as wave pumping and benthic advective flow. Future research should replicate this study in other Arctic locations with varying geologies and topographies to gain a better understanding of Arctic SGD. Additionally, more work isneeded to understand how low temperatures and high soil organic matter impact the Ra partitioning coefficient (K_d), which may have led to the low dissolved groundwater Ra activities observed at our field site.

Chapter 4 applied the SGD fluxes from Chapter 3 to total mercury (THg) and methylmercury (MeHg) measured during concurrent field campaigns to Simpson Lagoon. I demonstrated that THg inputs are largely dependent on groundwater fluxes and are similar to river inputs during the post-freshet ice-free period. However, MeHg showed a strong seasonal dependence, with warmer temperatures in the summer driving higher concentrations of MeHg in Simpson Lagoon groundwater. This results in SGD inputs of MeHg far exceeding riverine inputs in the summer and, to a lesser extent, in autumn. If this trend holds along the entire Arctic coastline, MeHg inputs from groundwater could significantly influence our understanding of microbial MeHg production in the Arctic Ocean water column. More work is needed to measure

THg and MeHg concentrations in Arctic coastal groundwater and SGD water fluxes in both North America and Eurasia to determine whether SGD is truly a major source of MeHg to the Arctic Ocean.

Finally, Chapter 5 investigated the species controlling THg and MeHg partitioning in Arctic subterranean estuaries using field data from Simpson Lagoon and soil cores from Simpson Lagoon and two other sites along the Beaufort Sea Alaskan coast (Elson Lagoon and Drew Point). I found that organic matter content in soils is a major control on the dissolved species influencing Hg mobilization. In soils of peat origin with high organic matter content, dissolved organic carbon (DOC) was the species most affiliated with dissolved THg and MeHg. However, in lacustrine permafrost soils with lower soil carbon content, salinity impacted mobilization more than DOC, likely due to seawater-derived sulfate leading to increased sulfide concentrations and an associated reduction and dissolution of metal oxides. The study revealed that the type of permafrost soil significantly impacts the quantity of THg and MeHg leached from soils, as well as the controls on their mobilization.

However, the work in Chapter 5 does not encompass the majority of soil types found across the Pan-Arctic coastline. While it lays a strong foundation for future studies, extended sampling efforts are needed, focusing on areas with contrasting geologies and coastal conditions. Future research should investigate soil characteristics along the Eurasian Arctic coastline, which may receive different inputs of Hg.

This thesis lays a solid foundation for future investigations into Hg and Ra in the Arctic. It provides a robust, seasonal and interannual perspective on Ra and Hg cycling in an Arctic coastal system, exploring geographic variability both on a small kilometer scale and across the Beaufort Sea coastline. This work also demonstrates the benefits of combining laboratory experiments with extensive field datasets to elucidate underlying processes. Nonetheless, the novelty of these studies means that conclusions regarding Pan-Arctic cycling of these species require further investigation, particularly in areas of the Arctic coastline with differing soil characteristics and geologies.